Western Boundary Dynamics in the Arabian Sea

Clément Vic

THÈSE / UNIVERSITÉ DE BRETAGNE OCCIDENTALE
sous le sceau de l'Université européenne de Bretagne

pour obtenir le titre de
DOCTEUR DE L'UNIVERSITÉ DE BRETAGNE OCCIDENTALE
Mention : Océanographie Physique
École Doctorale des Sciences de la Mer

présentée par
Clément VIC
Préparée au
Laboratoire de Physique des Océans,
UMR 6523 – CNRS – Ifremer – IRD - UBO

Western Boundary Dynamics in the Arabian Sea

Thèse soutenue le 12 novembre 2015
devant le jury composé de :

Laurent MEMERY
Directeur de Recherche CNRS, LEMAR, Brest
Président du jury
Yves MOREL
Directeur de Recherche CNRS, LEGOS, Toulouse
Rapporteur
Jérôme VIALARD
Directeur de Recherche IRD, LOCEAN, Paris
Rapporteur
Jeroen MOLEMAKER
Associate Researcher, UCLA, Los Angeles
Examinateur
Guillaume ROULLET
Maître de Conférences, UBO, Brest
Co-directeur de thèse
Xavier CAPET
Chargé de Recherche CNRS, LOCEAN, Paris
Co-directeur de thèse
Xavier CARTON
Professeur, UBO, Brest
Co-directeur de thèse

Western boundary dynamics in the Arabian Sea

Clément Vic

sous la direction de :

Guillaume Roullet, Maître de Conférences - UBO
Xavier Capet, Chargé de Recherche - CNRS
Xavier Carton, Professeur - UBO

Manuscrit de thèse, préparée au :

Laboratoire de Physique des Océans,

UMR 6523, CNRS/Ifremer/IRD/UBO,
6 Avenue Le Gorgeu, 29200 Brest, France.

Remerciements

A leur arrivée, les navigateurs solitaires commencent toujours par remercier les gens à terre pour leur soutien et leur accompagnement dans leur projet, sans qui rien n'est possible. Le travail de thèse peut parfois s'apparenter à une traversée en solitaire, avec une préparation hâtive, des amarres larguées très tôt et immanquablement quelques escales techniques pour pénurie d'inspiration ou avarie de bonne humeur ! Heureusement, j'ai été entouré d'une équipe qui a su me guider et me confier les clés du bateau ! Merci tout d'abord à mes directeurs de thèse, Guillaume pour les innombrables discussions physiques et métaphysiques, ta confiance, ton enthousiasme, et ta bonne inspiration de m'envoyer en Californie quelques temps; Xavier Carton, pour ta bienveillance, ta confiance et tes relectures express; Xavier Capet pour tes conseils toujours pertinents, ta rigueur très instructive, et tes nombreuses corrections approfondies de mon travail. Merci aux rapporteurs (Yves Morel et Jérôme Vialard) et examinateur (Jeroen Molemaker) d'avoir accepté de rapporter sur mon travail, pour vos critiques constructives et vos encouragements. Merci particulièrement à Jeroen pour ton accueil et ton encadrement à UCLA. Merci à Laurent Memery d'avoir accepté de présider. Un merci particulier à Anne-Marie Tréguier qui m'a mis le pied à l'étrier en stage de M2 et m'a soutenu dans ma recherche de thèse. Merci à Jonathan Gula et Lionel Renault pour votre accueil à UCLA, les discussions scientifiques et vos coups de main techniques. Merci à la Direction Générale de l'Armement et la Région Bretagne d'avoir soutenu financièrement cette thèse. Enfin, merci au soutien administratif, Gilberte pour les ordres de mission et Elisabeth pour les affaires de l'école doctorale.

Abstract

This PhD aims to investigate some western boundary processes in the Arabian Sea. Namely, we focused on three phenomena : the life cycle of the so-called Great Whirl, a persistent mesoscale eddy; the dynamics of the Persian Gulf outflow, a marginal sea dense outflow; and the seasonal Oman upwelling, a coastal upwelling forced by summer monsoonal winds. The cornerstone of all these phenomena is their location at a western boundary, which makes them being influenced by both local forcing (e.g., monsoonal winds) and remote forcing (Rossby waves and drifting eddies). Specifically, the latter is expected to impact the western boundary dynamics since the low latitude of the Arabian Sea implies a fast westward propagation of long Rossby waves and eddies. Moreover, waves are continously excited by the reversing monsoonal winds. We designed numerical experiments of different complexity using a primitive equation model that allowed to either realistically simulate the dynamics in the Arabian Sea or to isolate some processes.

Major findings can be summarized as follows : (i) The Great Whirl life cycle is found to be significantly paced by annual Rossby waves, although the strong monsoonal wind stress curl is of major importance to sustain the structure. (ii) The Persian Gulf Water (PGW) spreading in the Gulf of Oman and the northern Arabian Sea can be explained by the stirring done by mesoscale eddies entering the Gulf. These remotely formed surface intensified mesoscale eddies propagate into the Gulf and interact with the topography. These frictional interactions produce intense vorticity strips at the boundary that detach and roll up in the interior, forming submesoscale coherent vortices (SCV). These SCV trap PGW initially located on the slope and redistribute it in the interior. This mechanism of transport ultimately produces mixing that explains the rather large-scale gradient of salinity in the Gulf. (iii) We find that the dynamics of the seasonal upwelling off Oman contrasts with the more deeply studied Eastern Boundary Upwelling Systems (EBUS). In particular, Rossby waves, propagating offshore in EBUS vs. onshore in this western boundary upwelling, are found to modulate the wind driven upwelling and its sea surface temperature response.

Overall, these results appear to be rather specific to the western Arabian Sea. The short zonal extent and the low-latitude of the Arabian Sea, as well as the seasonally reversing wind forcing are the distinguishing features of this region. Fast waves and drifting eddies and their interactions with the western boundary significantly shape the turbulent regimes of the western Arabian Sea.

Résumé

Le but de cette thèse est d'analyser plusieurs phénomènes de bord ouest de la Mer d'Arabie. Nous nous sommes concentrés sur trois phénomènes en particulier : le cycle de vie d'un tourbillon de mésoéchelle persistant, le Great Whirl; la dynamique d'un écoulement d'eau dense (*outflow*) formée dans une mer adjacente, l'outflow du Golfe Persique; et une remontée d'eau profonde (*upwelling*) saisonnière dans la zone côtière d'Oman. Le point commun entre ces phénomènes est leur localisation sur un bord ouest océanique. Ils sont donc influencés par des forçages locaux (notamment les vents de mousson) et des forçages à distance (ondes de Rossby et tourbillons dérivant vers l'ouest). En particulier, ces derniers vont jouer un rôle particulier car la Mer d'Arabie est située à basses latitudes, ce qui implique une propagation rapide des ondes longues et tourbillons. De plus, des ondes sont continuellement excitées par le régime saisonnier des moussons. Nous avons mis au point des expériences numériques de différentes complexités en utilisant un modèle aux équations primitives. Ces expériences permettent soit de simuler de manière réaliste la dynamique complexe de la Mer d'Arabie, soit d'isoler un processus en particulier.

Les résultats principaux peuvent se résumer comme suit : (i) le cycle de vie du Great Whirl est significativement impacté par les ondes de Rossby annuelles. Le rotationnel de la tension de vent joue un role important dans le maintien, le renforcement et la barotropisation du tourbillon. (ii) La dispersion de l'Eau du Golfe Persique (*Persian Gulf Water*, PGW) est déterminée par le mélange induit par les tourbillons de mésoéchelle. Précisément, ces tourbillons entrent dans le Golfe d'Oman (où se déverse la PGW), et interagissent avec la topographie. Ces interactions frictionnelles produisent des bandes de vorticité très intenses dans la couche limite du fond. Celles-ci sont arrachées et forment des tourbillons de sous-mésoéchelle. Ces tourbillons capturent de la PGW initialement située sur la pente continentale et la redistribuent dans le Golfe d'Oman. Ce mécanisme donne finalement lieu à du mélange, permettant d'expliquer le gradient de salinité climatologique observé en profondeur. (iii) La dynamique de l'upwelling saisonnier au large d'Oman contraste fortement avec la dynamique des upwellings de bord est (*Eastern Boundary Upwelling Systems*, EBUS) plus largement étudiés. En effet, les ondes de Rossby se propagent vers le large dans les EBUS et vers la côte dans l'upwelling de bord ouest d'Oman. Ces ondes modulent la réponse en temperature de l'upwelling forcé par le vent.

Dans l'ensemble, ces résultats sont relativement spécifiques à la Mer d'Arabie. La faible extension zonale et la basse latitude de la Mer d'Arabie, ainsi que le régime de mousson des vents saisonniers en font une région particulière. La propagation rapide des ondes et tourbillons, et leurs interactions avec le bord ouest façonnent les régimes de turbulence de la Mer d'Arabie.

Contents

Chapter 1

Introduction

Contents

1.1 General Background on the Arabian Sea

In this section, we review the essential characteristics of the Arabian Sea circulation. In the next section, we detail specific features (Rossby waves, marginal seas outflows and upwellings) of the oceanic dynamics that are of particular interest in the western Arabian Sea.

1.1.1 Once Upon a Time ...

Geomorphology

The Arabian Sea is commonly defined as the western part of the Indian Ocean, extending from the west coast of India to the east coast of Africa. Its northern boundary is made up of the Arabian Peninsula (Oman and Yemen) and the Iran and Pakistan coasts. Notice that the presence of continents at such low latitudes ($\sim 25°$N) is specific to the Indian Ocean and changes the atmospheric circulation[1]. There is no material southern boundary and studying the Arabian Sea in terms of ocean currents may involve a knowledge of the Indian Ocean's equatorial dynamics. There are two major basins in the Arabian Sea separated by the Carlsberg Ridge that extends in a northwest-southeast direction. North of the Carlsberg Ridge, the Arabian basin bathymetry reaches 4600 m and has its eastern limit with the Chagos-Laccadive Plateau. South of the Ridge, the Somali basin extends southward of the equator and bathymetry reaches 5200 m (see Figure 1.1).

One of the specific features of the Arabian Sea is the presence of two marginal seas which connect to it through narrow straits. The Persian Gulf connects with the Gulf of Oman through the Strait of Hormuz, and the Red Sea connects with the Gulf of Aden through the Strait of Bab el Mandeb. These two semi-enclosed seas are of crucial importance in the water mass description of the Arabian Sea. In both seas evaporation exceeds precipitation, which favours the formation of saline waters that are injected at certain depths in the Arabian Sea. They can be found far from their source, even in the Mozambique channel for the Red Sea Water (Beal et al., 2000).

History

The Arabian Sea was firstly described centuries ago by European navigators who passed by its numerous ports of call on the *Route of Spices*, discovered by Vasco da Gama[2]. At this early time in the navigation history, navigators had already noticed the importance of

[1] The regime of Trade Winds developed in the Atlantic and in the Pacific does not exist in the Indian Ocean.

[2] (1460 or 1469 – 24 December 1524) was a Portuguese explorer, one of the most successful in the Age of Discovery and the commander of the first ships to sail directly from Europe to India (landed in 1498).

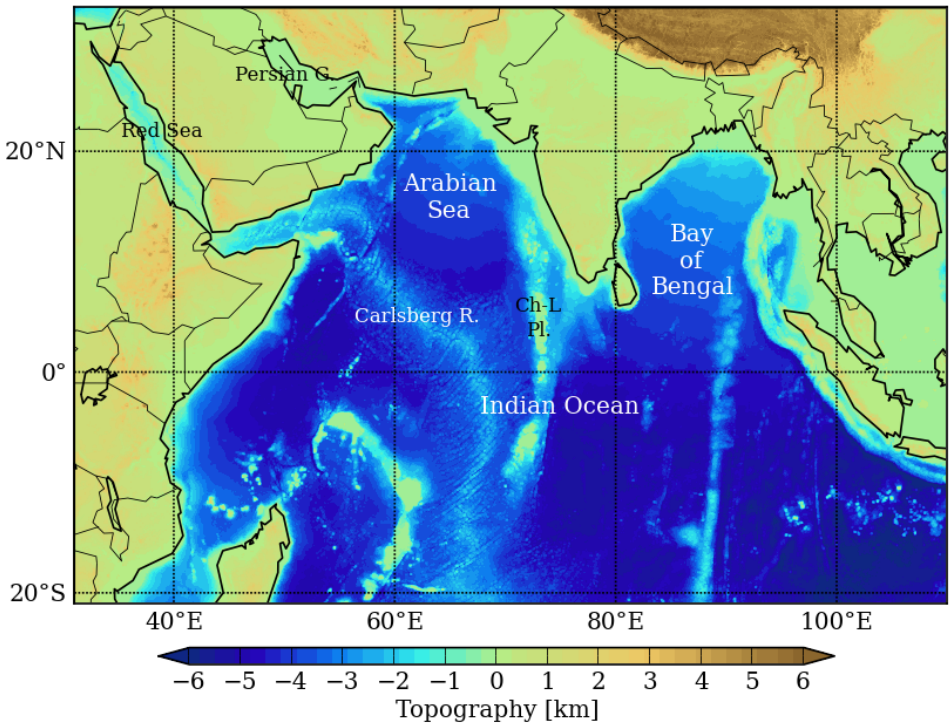

Figure 1.1: Topography of the Indian Ocean and the Indian Continent (dataset is ETOPO2, Smith and Sandwell, 1997). Ch-L Pl. stands for Chagos-Laccadive Plateau.

the seasonal winds and currents in the Indian Ocean. Subrahmanyam (1998) relates that in 1511, half of the fleet of Vasco da Gama remained blocked in Mozambique because they missed the southwest monsoon (downwind on their route) to cross the Arabian Sea. Indeed, even if there are many possible ethymologies[3] of the word *monsoon*, it certainly comes from the Portuguese *monção*, itself from the Arabic *mawsim* which means *season*. One of the first maritime and meteorological description made for navigation needs was written by Findlay (1876). The seasonal reversal of the winds along the northeast-southwest axis is described and the southwest monsoon was observed to be the strongest and longest as opposed to the northeast monsoon, as suggested by the observations in Figure 1.2.

The seasonal shift of the winds is perhaps the most distinguishing feature of the Arabian Sea forcing mechanisms, as compared to other oceanic basins (e.g., Atlantic and Pacific) whose subtropical and subpolar gyres do not experience such a reversing stress at seasonal time scales. Understanding its effect on oceanic currents has been the starting point of observational research projects since the 1970's (e.g., Wyrtki, 1973; Fieux and Stommel, 1977; Schott, 1983). Furthermore, ocean-atmosphere interactions during monsoons are known to be strong and to influence the variability of inland precipitations (Izumo et al., 2008) with high societal impacts.

[3]Oxford English Dictionary

TABLE OF THE WINDS ON THE EAST COAST OF INDIA.

	22°—20° N.		20°—15° N.		15°—10° N.		10°—5° N.		5°—0° N.	
	Days.	Days.	Days.	Days.	Days.	Days.	Days.	Days.	Days.	Days.
	N.E.	S.W.	N.E.	S.W.	N.E.	S.W.	N.E.	S.W.	N.E.	S.W.
January ..	17	6	21	2	23	1	20	1	19	3
February .	11	11	13	6	19	3	22	1	16	2
March	4	18*	7	15	18	5	13	0	15	2
April	2	24	2	22*	6	12	6	11	4	14
May.....	1	25	1	24	3	21*	1	23*	0	19*
June	0	28	1	27	0	29	1	25	0	24
July	2	24	1	27	0	30	0	28	0	24
August ..	0	28	1	24	0	24	1	22	0	18
September.	6	14	1	18	0	23	0	26	1	18
October ..	9	6†	12	6†	8	10	6	16	4	14
November.	11	6	25	2	21	2†	10	6	5	14
December.	27	0	26	1	24	1	15	3†	12	11

* Setting in of the S.W. monsoon. † Ending of the S.W. monsoon.

Figure 1.2: Table from Findlay (1876) showing the number of days per month during which the wind blows from the southwest (S.W.) and the northeast (N.E.) at the east coast of India (similar wind statistics were observed at the east African coast, not shown).

1.1.2 Ocean Dynamics

Climatology of winds

Observing the monthly climatological wind stress and wind stress curl fields in Figure 1.3, one clearly notices two distinct periods of sustained winds. The *Southwest Monsoon* (SWM) roughly begins between May and June, reaches its peak in July and fades out during September. The winds are moist and warm as coming from the equatorial band where moist air convection is high (Lee et al., 2000). The strongest winds are blowing from the coast of Somalia to Pakistan. This steady wind jet is known as the *Findlater Jet* (Findlater, 1969). Its maximum can reach a sustained value of 12 $\mathrm{m\,s^{-1}}$ and forms a line where the wind curl changes sign (the so-called *zero wind curl line*), being negative on its right side and positive on the coastal left side.

The *Northeast Monsoon* (NEM) starts blowing in November, reaches its peak in January and vanishes in March. The winds are formed of dry and cool air coming from the mountains of the Asian continent. The maximum wind speed is about 8 $\mathrm{m\,s^{-1}}$ offshore the Arabian Peninsula. Although less intensified than during the SWM, wind stress curl patterns are reversed, being negative on the northern Arabian Sea and positive southward. Notice that the reversal of the wind stress curl between the monsoons may impact the large scale circulation, the Ekman pumping and the Sverdrup transport, as suggested by Godfrey and Golding (1981); Bruce (1983).

The intermonsoon periods, refered to as the *Spring Intermonsoon* and *Fall Intermonsoon* (SIM and FIM, March – May and September – November, respectively, Lee et al., 2000), are transition stages between the SWM and the NEM. Wind stress and wind stress curl patterns are reminiscent of the latest monsoon.

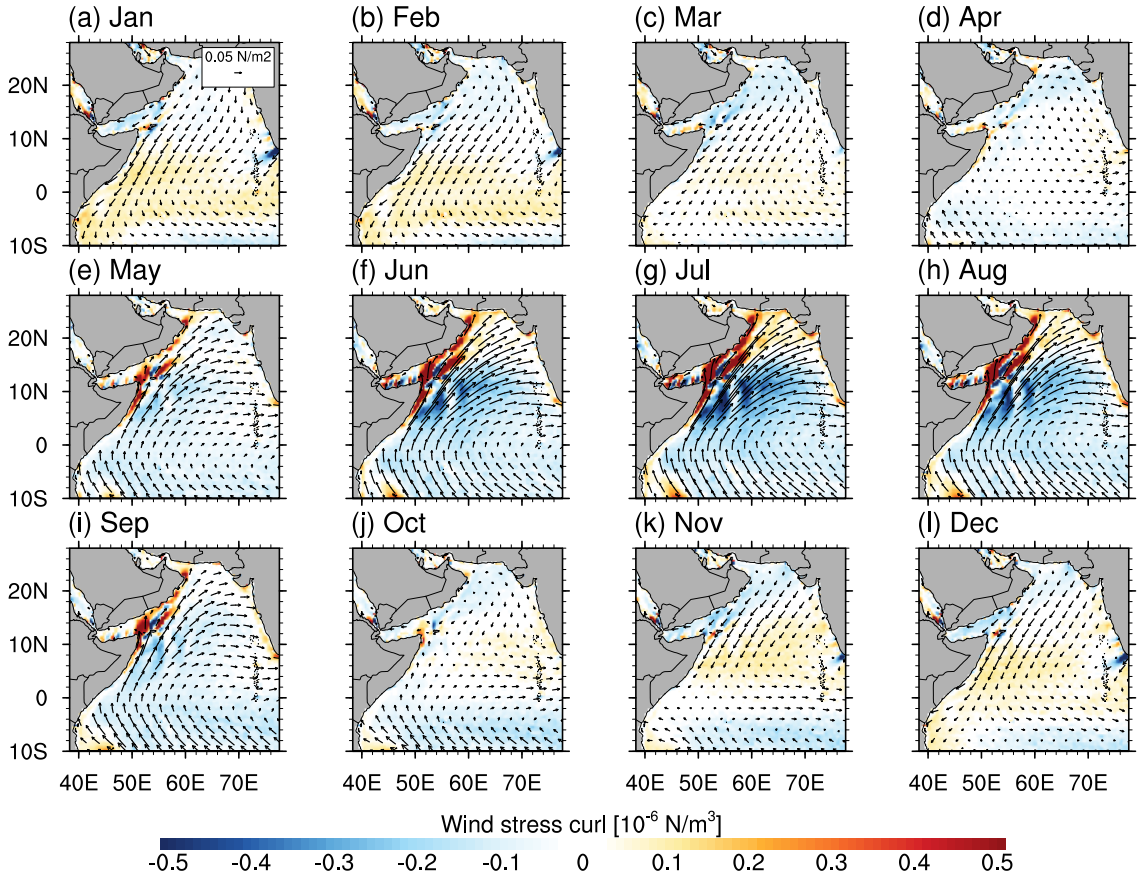

Figure 1.3: Monthly climatology of wind stress (arrows) and wind stress curl (colors) derived from QuikSCAT data for the period September 1999 – October 2009 (QuikSCOW climatology, Risien and Chelton, 2008).

Evidence for associated oceanic motions

There is gathered evidence for an oceanic direct response to seasonal winds (Bruce, 1983; McCreary et al., 1993; Lee et al., 2000; Schott and McCreary, 2001). Observations off the Somali coast early revealed the existence of a wind-driven coastal upwelling (Schott, 1983) occuring only during the SWM. Further north, off the Omani coast, the same seasonal atmospheric jet also forces an upwelling (Elliott and Savidge, 1990). Moreover, studies based on observations converge toward a predominance of the Ekman pumping in the mixed-layer depth of the Arabian Sea (Bauer et al., 1991; Hastenrath and Greischar, 1991), thus depending mostly on the seasonal wind stress curl. Maybe the most striking feature of the seasonality of the oceanic circulation is the reversal of the Somali Current. This western boundary current settled at the African coast heads northeastward during the SWM and southwestward during the NEM (Schott, 1983; Luther and O'Brien, 1985).

As examined by Shetye et al. (1994), the circulation in the Arabian Sea follows seasonally the large-scale wind stress and wind stress curl patterns, being anticyclonic during

the SWM and cyclonic during the NEM (Figure 1.3). Notice that mesoscale eddies dominate the circulation in the inner basin and are ubiquitous in the western basin (Flagg and Kim, 1998; Carton et al., 2012). Periods between monsoons do not show any distinguishing feature in terms of wind forcing. The associated oceanic circulation is often seen in litterature as undergoing a transition between the evanescence of the ending monsoon and the onset of the following (Lee et al., 2000). This is why we will only describe the circulation during the two monsoon periods.

Southwest monsoon circulation

Starting at the onset of the SWM, the circulation is steady in boreal summer under the influence of strong winds. It shows little intraseasonal variations expect through internal variability (e.g., in upwellings, Vialard et al., 2012). Here we describe the circulation in the Arabian Sea, starting from the equator and going northward at the coast, following the path of the main currents. Those currents are roughly represented on the schematic map of Figure 1.4.

The Somali Current (SC) is fed by the South Equatorial Current (SEC) that is deflected northward when reaching the north of Madagascar and meeting the North East Madagascar Current (NEMC). Then deflected northeastward, NEMC meets the East African Coastal Current (EACC), which directly supplies the SC. The SC is the strongest current observed during this period, transporting about 20 Sv in the upper 500 m on 50-100 km width (Schott et al., 1990). As explained by Schott and McCreary (2001), a meridional flow can not freely cross the equator because it has to change the sign of its potential vorticity when changing hemisphere. The SC is thus deflected sharply to the right and separates into two branches, one of them crossing back the equator, forming the Southern Gyre (SG) and the other recirculating in the interior basin. Interestingly, the winds are upwelling favourable near the Somali coast in the northern hemisphere (Schott and Quadfasel, 1982). As such, the downwind upwelling jet prolongates the SC northward.

At the northern end of the SC, a highly energetic large anticyclonic eddy develops. The so-called *Great Whirl* (GW) has been observed at a quasi steady position between 5°N and 10°N from the end of May until the end of September. Its radius has been observed to evolve between 350 km in early June 1995 and 540 km in September 1995 (Beal and Donohue, 2013). The onset of the GW has been controversed in literature for decades. Authors invoke instability of current, local forcing due to the persistent strong wind or remote forcing due to waves. Firstly, Schott and Quadfasel (1982) observed westward propagating signals after the onset of the SWM, interpreted as first-mode Rossby wave which were reflected at the coast into shortest modes. The first-mode Rossby waves were

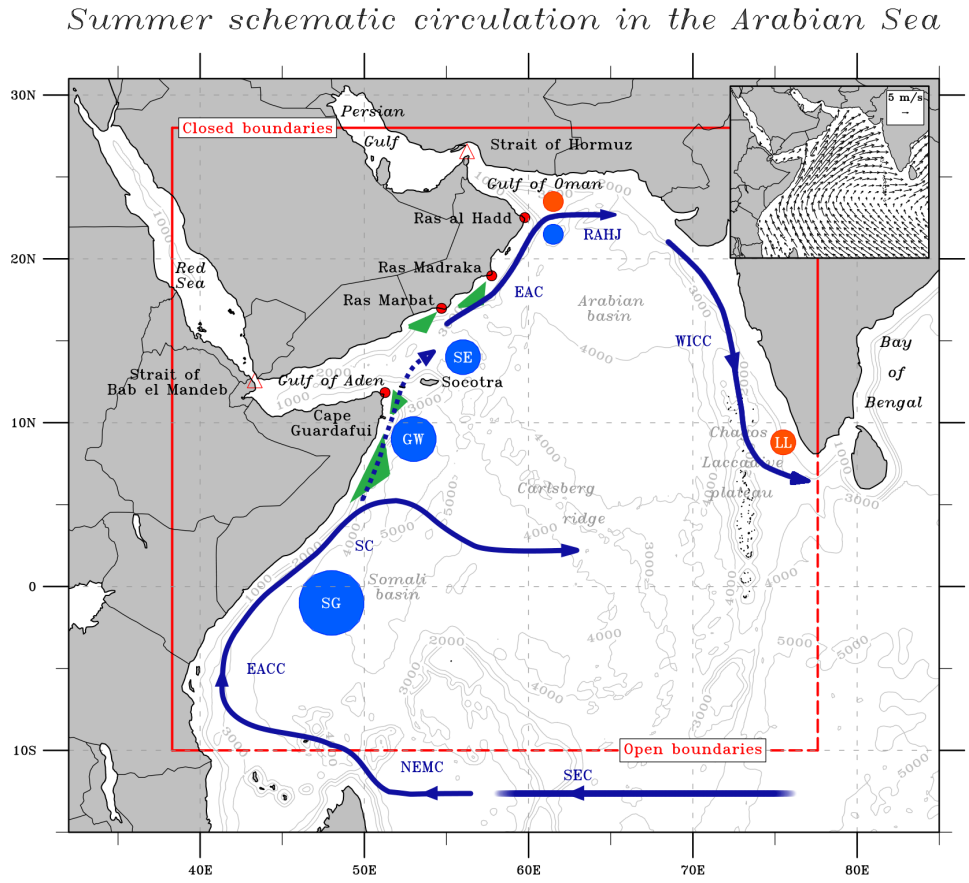

Figure 1.4: Schematic map of the summer monsoon (SWM) surface circulation in the Arabian Sea. The blue (resp. orange) disks are persistant anticyclones (resp. cyclones) and the green areas are the coastal upwelling regions. The major currents and steady eddies are coarsely localised and abbreviated this way (from the north to the south) : Ras Al Hadd Jet (RAHJ), East Arabian Current (EAC), West Indian Coastal Current (WICC), Socotra Eddy (SE), Great Whirl (GW), Laccadive Low (LL), Somalia Current (SC), Southern Gyre (SG), East African Coastal Current (EACC), North East Madagascar Current (NEMC) and South Equatorial Current (SEC). The inset at the top-right corner is the average wind field in July at the peak of the SWM. Red lines are the boundaries of a realistic model used in this dissertation and described in Chapter 2.

assessed to be excited by the strong anticyclonic curl of the wind stress. Then, a numerical study of McCreary et al. (1993) highlighted the arrival of annual Rossby waves from the tip of India which could be a remote forcing of many structures at the western boundary of the basin. The influence of the slanted coast and Socotra Island on the western boundary current instabilities are also discussed in McCreary and Kundu (1988); Luther and O'Brien (1989). The review of Schott and McCreary (2001) concluded on a domination of local forcing into the generation of the GW. Soon after, Wirth et al. (2002) proposed a new point of view in examining the GW as a western boundary current instability. As opposed to this, the analysis of 18 years of satellite data on sea surface height allows Beal and Donohue (2013) to observe the propagating anomaly signal reaching the coast before the

onset of the wind and the settlement of the SC, then swirling into what becomes the GW. However, this article brings back together former theories with the observation of the GW enhancement with the winds at the onset of the SWM in June. Moreover, its northen flank position seems to be constrained by the zero wind curl along the axis of the Findlater jet. The collapse of the GW is not clear either. It seems to move southwestward under the influence of flanking cyclones (Beal and Donohue, 2013) but it can also disapear by mechanisms of internal instabilities (Jensen, 1993; Wirth et al., 2002). Observations of water masses on a particular year show that it can merge with the Socotra Eddy, another remarkable steady anticyclonic eddy north of Socotra (Fischer et al., 1996).

The termination of the SC is not well defined as it is overwhelmed by the GW (as suggested by dotted lines in Figure 1.4). However, evidences of coastal upwellings on both sides of the GW implies a coastal jet prolongating the SC northward, through the passage between Socotra and the Horn of Africa (Cape Guardafui).

Also forced by the wind, the East Arabian Current (EAC) has not a very marked pathway and mesoscale eddies dominate the dynamics in the north Arabian Sea (Flagg and Kim, 1998; Kim et al., 2001; Carton et al., 2012). Upwelling favourable winds create wedges of cold waters off the protruding capes (Ras Madraka, Ras Marbat, ...). The flow leaves the coast at the end of the Omani coast in the Ras Al Hadd Jet (RAHJ, Böhm et al., 1999). The West Indian Coastal Current (WICC) flows southward along the Indian coast and exits the Arabian Sea at the tip of India (Shetye et al., 1990).

Northeast monsoon circulation

The NEM winds start blowing in November from the north of the basin and largely extend to the south in December. Then they are quasi-steady until the beginning of March (Figure 1.3). The wind stress curl in the Arabian Sea changes sign and the circulation is roughly inversed (Lee et al., 2000). Here we comment on the circulation summarized on the schematic map in Figure 1.5. Literature about the circulation during the NEM is poorer than during the SWM. A plausible explanation is that dynamics in this period do not develop remarkable steady features such as upwellings or persistent eddies as the Great Whirl.

The Arabian basin is still fed by the SEC but is also fed from the tip of India by a current resulting from the NEM in the Bay of Bengal. This flow is divided into two branches, one flowing along the coast in the WICC (notice that this current also reverses, Shetye et al., 1991) and the other going westward in large paths towards the Somali coast and forming the SC. The SC flows southward and is tilted to the left when crossing the equator. It merges the steady EACC to supply the South Equatorial Countercurrent (SECC, Schott and McCreary, 2001). The circulation in the north of the Arabian Sea

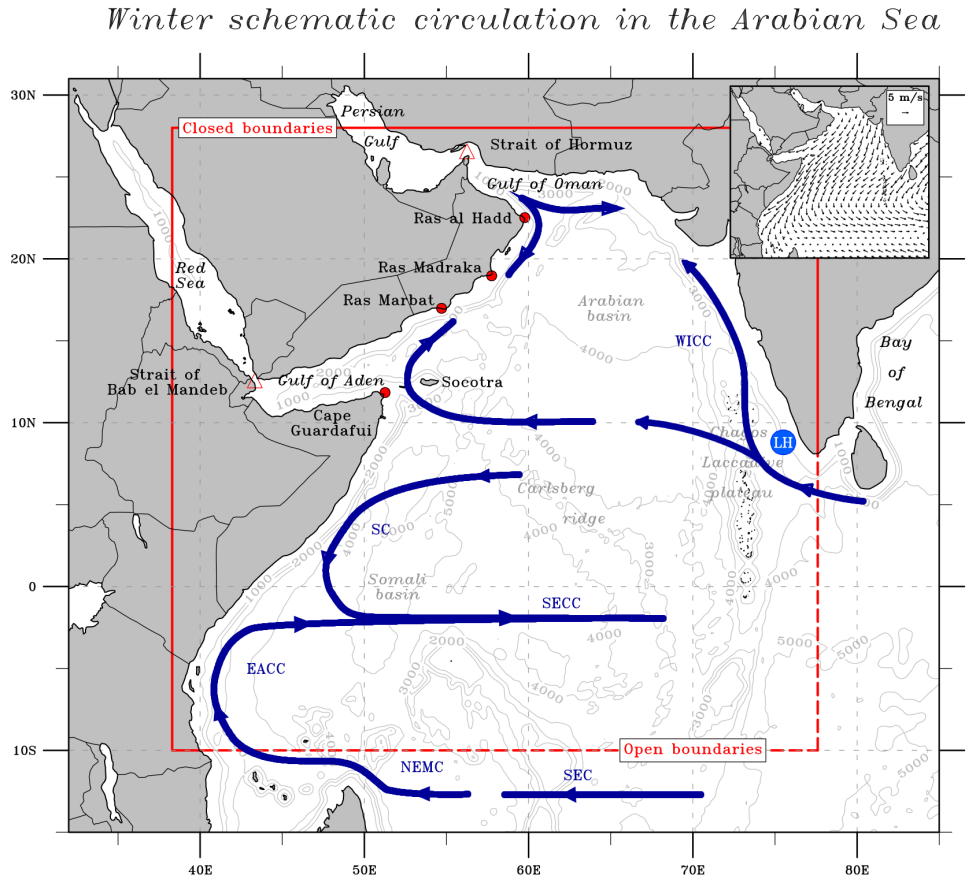

Figure 1.5: Same as figure 1.4 but for the winter monsoon (NEM). New abbreviations are : Laccadive High (LH), South Equatorial Counter Current (SECC). The inset at the top-right corner is the average wind field in January, at the peak of the NEM.

is still dominated by mesoscale eddies and the mean flow is westward with a downwelling along the Omani coast (Shi et al., 2000).

1.2 Oceanic Variability in the Western Arabian Sea

In this section, we put forward three phenomena occuring in the western Arabian Sea. These phenomena could interact which each other and some of them are not well understood yet. Therefore, they make the cornerstones of each chapter of this dissertation.

1.2.1 Rossby Waves

Theory

Geophysical fluid dynamics can be studied through different sets of equations, all of them derived from the Navier-Stokes equations. They differ by their level of complexity, either depending on the analytical framework (i.e., shallow-water vs. continously stratified) or depending on the dynamical assumptions (i.e., quasi-geostrophic vs. primitive equations). Quasi-geostrophic equations hold for motions characterized by :

- A small Rossby number, $Ro = U/f_0 L \ll 1$, where U and L are the velocity and length scales of motion and f_0 is a reference Coriolis parameter. This means that the flow is in near-geostrophic balance.

- A scale of motion that is not significantly larger than the deformation scale, i.e., an order one Burger number $Bu = (R_d/L)^2 \sim 1$. $R_d = NH/f_0$ for the continously stratified case, with H the ocean depth. $N^2 = -(g/\rho_0)\partial_z \rho$ is the Brunt-Väisälä frequency that measures stratification, where g is the acceleration of gravity, ρ is the seawater density and ρ_0 is a reference density.

A common practice in physics to study a system described by a set of equations is to start with simplifying the equations, often in linearizing them for the unforced problem. Following the textbook *Ocean Dynamics* (Olbers et al., 2012, section 8.2.), the linearized quasi-geostrophic equation (in potential vorticity form) for the stream function ψ can be written as :

$$\frac{\partial}{\partial t}\left[\nabla_h^2 \psi + \frac{\partial}{\partial z}\left(\frac{f_0^2}{N^2}\frac{\partial \psi}{\partial z}\right)\right] + \beta \frac{\partial \psi}{\partial x} = 0 \tag{1.1}$$

Assuming a separation of vertical and horizontal structures $\psi(x, y, z, t) = \phi_n(z)\tilde{\psi}(x, y, t)$, one gets for the horizontal structure :

$$\nabla_h^2 \frac{\partial \tilde{\psi}}{\partial t} - \frac{1}{R_n}\frac{\partial \tilde{\psi}}{\partial t} + \beta \frac{\partial \tilde{\psi}}{\partial x} = 0 \tag{1.2}$$

with R_n the Rossby radius[4] of mode n. Looking for wave-like solutions of Eq. 1.2 in the form $\tilde{\psi} = \tilde{\psi}_0 \exp[i(kx + ly - \omega t)]$, where ω is the angular frequency ($\omega = 2\pi f$) and k and l are the wavenumbers in the zonal and meridional directions respectively, yields the dispersion relation :

$$\omega = -\frac{\beta k}{k^2 + l^2 + R_n^{-2}} \tag{1.3}$$

Equation 1.3 is the dispersion relation of the so-called Rossby waves (theory derived in the atmosphere by Rossby, 1940), solutions of the linearized and unforced quasi-geostrophic equations. Rossby waves (hereafter RW) owe their existence to the variation of the Coriolis frequency with latitude (β). In the following, we will refer to RW as the first baroclinic mode ($n = 1$) as this mode contains most of the surface kinetic energy (Wunsch, 1997), except in equatorial bands.

Observation

RW are associated with pressure perturbations ($\psi = p/(f_0\rho_0)$ in the quasi-geostrophic framework, thus in Eqs. 1.1 and 1.2), which can be measured with *in situ* sensors in the atmosphere. Pressure anomalies in the ocean are much more difficult to measure due to the dominating static signal. However, they are associated with sea surface height anomalies. Moreover, for the first baroclinic mode, sea surface height anomalies are mirrored as pycnocline (that can be approximated by the thermocline) depth variations of the opposite sign. The order of magnitude of the pycnocline depth anomalies is about three times larger than the surface height anomalies; a deviation of +2 cm (resp. -2 cm) in sea surface height gives a deviation of -20 m (resp. +20 m) in the thermocline (LeBlond and Mysak, 1981). The thermocline displacement is measurable with *in situ* instruments and historically, RW have been first detected by arrays of currentmeters (White, 1977; Schott and Quadfasel, 1982; Kessler, 1990). However, their slow propagation speeds ($O(1-10$ cm s^{-1})) and long wavelengths ($O(100-1000$ km)) require sustained observational systems covering large areas.

The development of satellite altimetry since the beginning of the 1990s (e.g., TOPEX/-POSEIDON mission, Fu et al., 1994) has made the continuous observation of sea surface height with a global coverage possible, at a resolution allowing to measure sea surface height with a precision of 2 cm (Le Traon and Ogor, 1998). Horizontal resolution, limited by the satellite swath width and instantaneous coverage, is comprised between 1/3° and 1/4° (∼30 km at mid latitudes). It allows observing signals with an order of magnitude in $O(R_d)$. The RW scale is thus within the range of observation using altimetry. Since the beginning of the era of satellite altimetry, they were continously detected in every

[4]Note that the *Rossby radius* or *deformation scale* R_d is often refered to as the characteristic scale of mode $n = 1$ (if the mode is not specified).

oceanic basin. Local observations were first made in the South Atlantic (Le Traon and Minster, 1993) and basin-wide and global characterizations followed (e.g., Chelton and Schlax, 1996; Polito and Cornillon, 1997).

Why are Rossby Waves important?

From Eq. 1.3, we deduce that for a positive frequency ω, the zonal wavenumber k must be negative. The zonal phase propagation component of RW is hence westward. This implies that RW are a mechanism for transporting information from eastern boundaries and the inner basin towards western boundaries. Anderson and Gill (1975); Anderson et al. (1979) studied the spin-up of a stratified ocean at rest, suddenly forced by wind stress. They found that the adjustment can be explained by RW processes, rapidly propagating westward and leaving a near-equilibrium state behind (eastward). Furthermore, the structure of the western boundary current appears to be set by the superposition of RW. More generally, changes in wind stress and atmospheric buoyancy forcing are integrated by the ocean through RW propagation mechanisms.

Basically, two mechanisms are involved in the excitation of RW (Fu and Qiu, 2002) : wind stress curl fluctuations and eastern boundary perturbations. Using a linear shallow-water model in the Pacific forced by eastern boundary anomalies in sea surface height and wind stress curl, Fu and Qiu (2002) find that wind stress curl fluctuations are the principal source of forcing at mid and high latitudes whereas eastern boundary signals are the main RW forcing at low latitudes. RW are considered to be the primary response of the ocean to atmospheric forcing, at temporal scales varying between seasons to interannual. Indeed, they contribute significantly to the adjustment of climate (e.g., propagation of El Niño in the Pacific, Jacobs et al., 1994). RW are also found to modulate biological activity, as they can be tracked in ocean color data (Cipollini et al., 2001).

Why are Rossby Waves important in the Arabian Sea?

We recall in the previous paragraph that oceanic RW are a mean to propagate changes in atmospheric forcing. We also presented in Section 1.1.2 a distinguishing feature of the Arabian Sea, which is the seasonal reversing of monsoonal winds (wind stress and wind stress curl, Figure 1.3). As such, RW are expected to play a key role in the Arabian Sea oceanic adjustment to these seasonal forcing, as early examined by Lighthill (1969) in the northern Indian Ocean (Arabian Sea and Bay of Bengal).

The fastest baroclinic RW have the lowest frequencies and longest wavelengths. They are of particular interest since they propagate the bulk of the oceanic response to atmospheric forcing (for the first baroclinic mode, thus the principal movement of the thermocline, Wunsch, 1997, 2011) and have the property to be non-dispersive (i.e., the westward

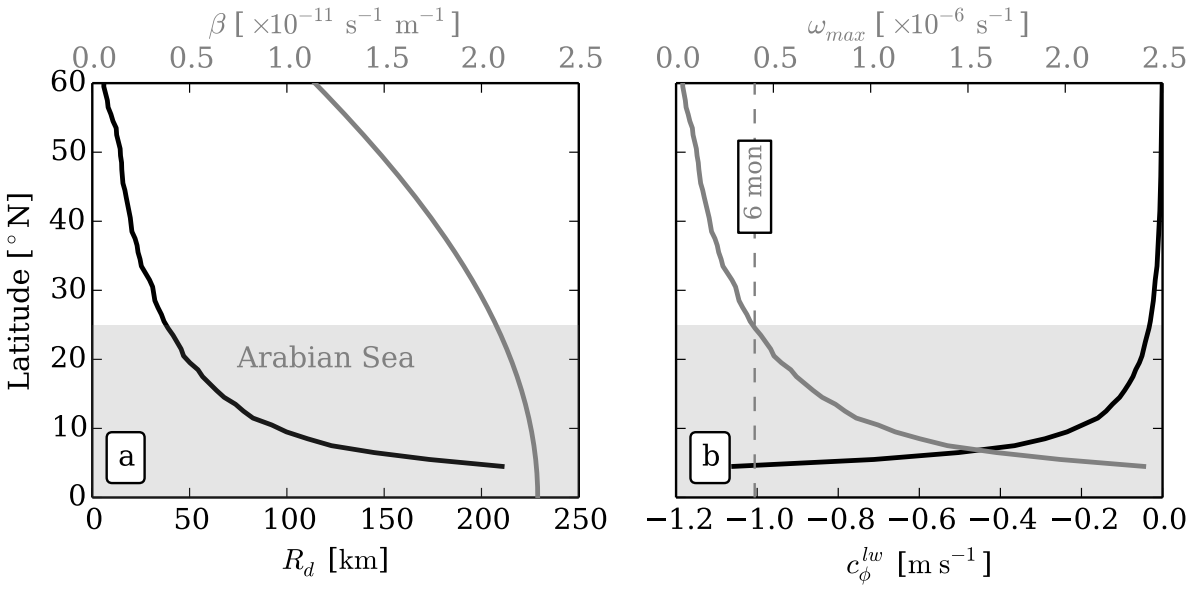

Figure 1.6: (a) Zonally averaged first baroclinic radius of deformation R_d (black) and β (gray) as functions of latitude in the northern hemisphere. R_d is computed using the WKB approximation, similarly to Chelton et al. (1998), $R_d \sim \frac{1}{|f|\pi}\int_{-H}^{0} N(z)\,\mathrm{d}z$, where $N^2(z) = -\frac{g}{\rho_0}\frac{\partial \rho}{\partial z}$ is the Brunt-Väisälä frequency computed with the World Ocean Atlas (release 2013, WOA13) temperature and salinity (Antonov et al., 2010; Locarnini et al., 2010) (dataset available at `https://www.nodc.noaa.gov/OC5/woa13/`). (b) Rossby wave phase speed in the long wave approximation $c_\phi^{lw} = -\beta R_d^2$ (black) and maximum frequency allowed at a given latitude ω_{max} (gray). The dashed line corresponds to the semi-annual frequency. In both panels, the gray area embeds the Arabian Sea latitudes.

component of phase speed is independent of wavelength). From Eq. 1.3, their phase speed c_ϕ^{lw} is often approximated as :

$$c_\phi^{lw} = \frac{\omega}{k}\bigg|_{k \ll R_d^{-2}} \sim -\beta R_d^2 \tag{1.4}$$

The Arabian Sea is situated at low latitudes (< 25°N) where both β and R_d are maximum (R_d is maximum due to the minimum Coriolis frequency and the maximum of stratification, Chelton et al., 1998). Figure 1.6a highlights this dependence of β and R_d to latitude in the Northern Hemisphere, computed with the same method as Chelton et al. (1998) (see the caption for details on the computation). As a consequence, long RW travel at a high speed compared to mid and high latitudes (Figure 1.6b). Figure 1.7a shows specifically c_ϕ^{lw} in the Arabian Sea. Brandt et al. (2002) use hydrographic data and altimetric sea surface height to reveal the existence of annual RW radiated from the tip of India at 8°N. Mode 1 has an estimated phase speed of 38 cm s^{-1}, in the range of values computed in the linear theory (~ 40 cm s^{-1}, Figures 1.6a and 1.7a).

Another distinguishing feature of the Arabian Sea is its relatively small zonal extent (2800 km from the tip of India to the Somali coast, vs. ∼5000 km in the North Atlantic and ∼8000 km in the Pacific), which, associated with high phase speed, allows long RW

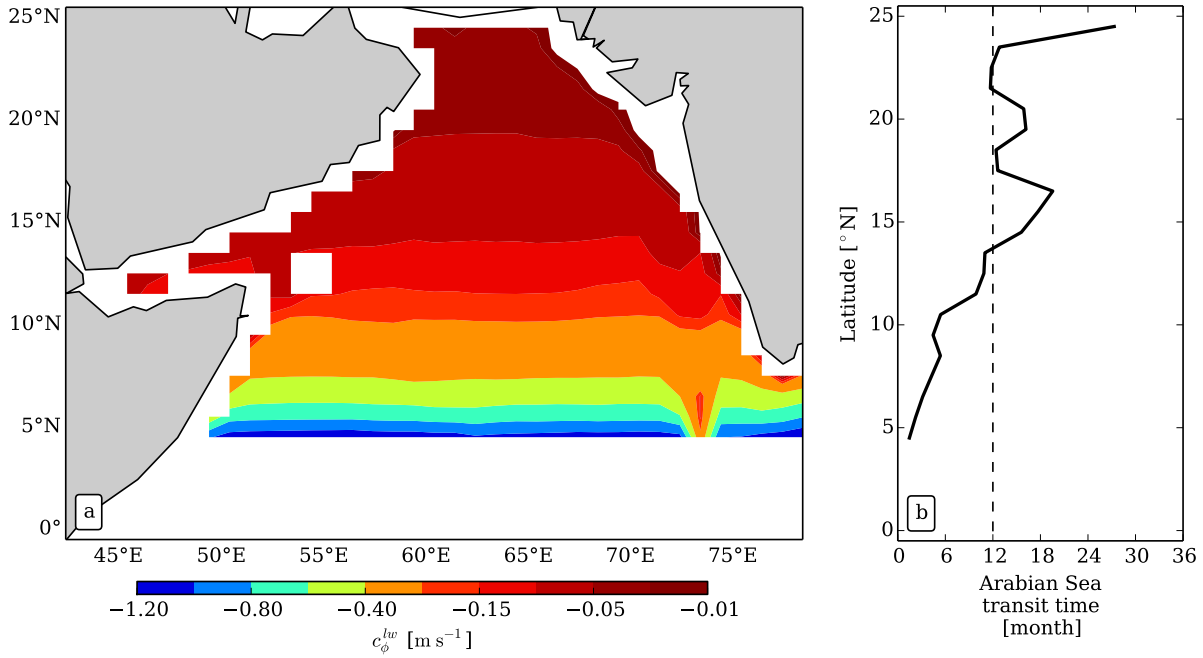

Figure 1.7: (a) Rossby wave phase speed in the the long wave approximation $c_\phi^{lw} = -\beta R_d^2$ (R_d is computed using the WKB method with the WOA13 temperature and salinity, as in Figure 1.6). Notice that the colorscale is nonlinear. (b) Time for a long Rossby wave travelling at c_ϕ^{lw} to cross the Arabian Sea at each latitude. Dashed line indicates a transit time of one year.

to rapidly cross the basin. Indeed, transit time has an order of magnitude of months to seasons (Figure 1.7b), whereas transit time at mid and high latitudes in the Atlantic or in the Pacific have interannual scales (10-20 years at 40°N in the Atlantic, Figure 9 in Wunsch, 2011). This supports the idea that waves act to rapidly adjust the seasonal monsoonal forcing[5]. Furthermore, from Eq. 1.3, one can find that a maximum frequency exists for a given set of parameters (R_d, β) :

$$\omega_{max} = \frac{\beta R_d}{2} \tag{1.5}$$

This frequency ω_{max} is represented in Figure 1.6b as a function of latitude. It illustrates that the lower the latitudes, the higher frequencies can be excited. This further supports that time scales involved with RW processes at mid and high latitudes are preferentially annual to interannual whereas they can be much shorter at low latitudes.

Ambiguities and clarification

Here we point out two ambiguous questions that may bother the reader, and explain how we deal with them in the dissertation.

[5]We do not focus on interannual and decadal variability in the Arabian Sea, which is part of a larger scale system involving the whole Indian Ocean (e.g., *Indian Ocean Dipole* mode of variability, Saji et al., 1999).

1. *Rossby Waves vs. Forced Waves.* In the current section, we first derive theoretical aspects on RW, emphasizing on the fact that they are the solutions of the unforced linear quasi-geostrophic equations, i.e., they are *free waves*. Then we have reviewed that RW were a mean to integrate and propagate atmospheric forcing. The question that follows is : should they be considered as *forced waves*? Chelton and Schlax (1996) considered that the westward propagation of wave-like motions are unforced, in the sense that waves are not continously forced along their propagation (no evidence for resonance), although their characteristics may be altered. Soon after, Qiu et al. (1997) separated two types of waves, free and forced (both called RW), depending whether they emerge from eastern boundaries (spontaneously generated and *free*) or they are generated by wind anomalies (*forced*). Their major result is that the nature of the generation of RW may influence their propagation speed. In this dissertation, in the spirit of Qiu et al. (1997), we will refer to *Rossby waves* all wave-like motions, linear (with a propagation speed consistent with the linear theory) or not, and whatever the generation mechanism is.

2. *Rossby Waves vs. Eddies.* Since the development of satellite altimetry, oceanographers firstly focused (mainly) on RW (1990's). In the 2000's, in parallel of the development of high resolution models resolving mesoscale turbulence, they became more interested in tracking eddy-like features in altimetry (e.g., Morrow et al., 2004; Chelton et al., 2007). Sea surface height has to be filtered to remove the background field encoding the basin-wide circulation, in order to isolate eddies. They were found to propagate in the open ocean (except in the Antarctic Circumpolar Current) at the phase speed of long baroclinic RW c_ϕ^{lw}. This finding raised an unresolved debate on the nature of the signals observed, waves vs. eddies (e.g., Polito and Sato, 2015, and references therein). We will not participate in this debate and just consider the influence of remotely forced signals propagating westward (generalized β-effect) on the western Arabian Sea dynamics. This westward drift, associated with the intensified circulation at the western boundary, increases the level of Eddy Kinetic Energy (EKE) in the western Arabian Sea (Figure 1.8). The mesoscale circulation is at least one order of magnitude more energetic in the western part of the bassin than in its eastern part (Figure 1.8). It is expected to significantly impact the outflow and upwelling dynamics.

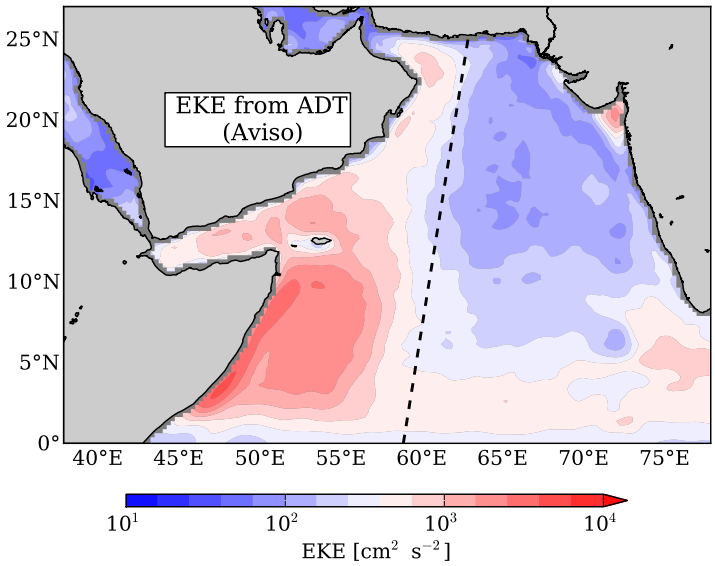

Figure 1.8: Surface Eddy Kinetic Energy (EKE) computed on the period 1993-2010 with geostrophic currents derived from Aviso's Absolute Dynamics Topography (ADT). The black dotted line separates the energetic western part of the Arabian Sea from its more quiescent eastern part.

Summary of Section 1.2.1 Rossby Waves

- The Arabian Sea low latitudes imply a fast propagation of Rossby waves. They are a mean to adjust the ocean dynamics to the seasonal variability of atmospheric forcing.
- Mainly travelling westward, Rossby waves and eddies, generated in the inner basin or at the eastern boundary, are expected to impact the dynamics in the western Arabian Sea, noticeably the spreading of outflows and seasonal upwellings.

1.2.2 Marginal Seas Outflows

Background

The Arabian Sea connects with two marginal seas, the Red Sea and the Persian Gulf, through narrow straits, the Strait of Bab el Mandeb and the Strait of Hormuz respectively (see Figure 1.5 for geographical information). In both seas evaporation exceeds precipitation and dense, salty and warm waters are formed (see the review of Bower et al., 2000). These waters spread in the Arabian Sea, and more precisely in the Gulf of Aden and in the Gulf of Oman respectively. They have strong signatures in salinity climatological maps, around their equilibrium depths, namely 250 m and 600 m (Figure 1.9).

Dense water outflows are likely to play an important role in the overturning circulation

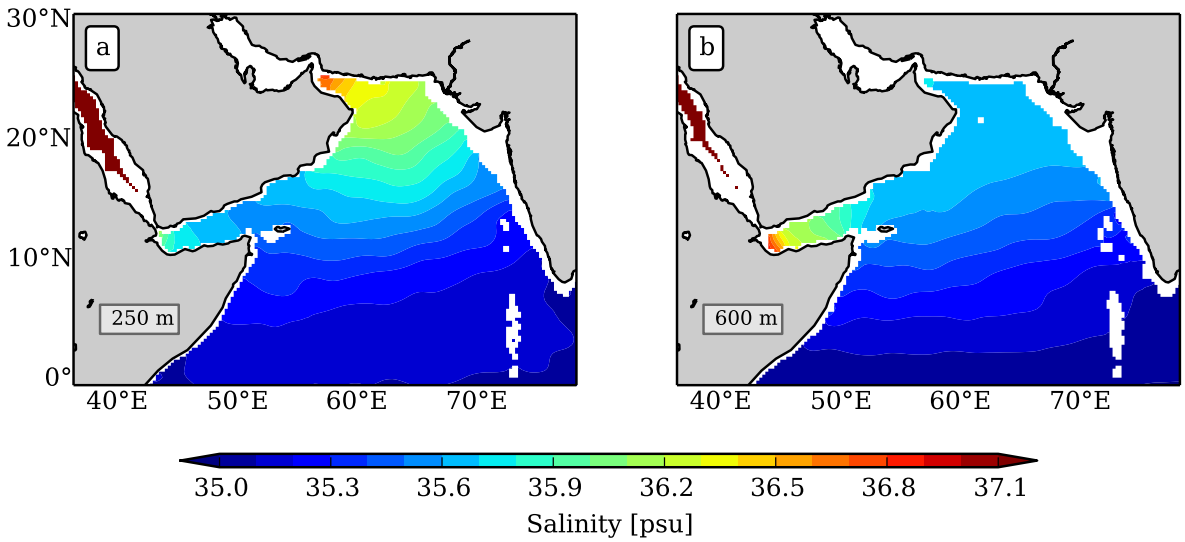

Figure 1.9: Salinity maps in the Arabian Sea at (a) 250 m showing the Persian Gulf outflow signature and (b) 600 m showing the Red Sea outflow signature. Dataset is the World Ocean Atlas, release 2013 (WOA2013, Antonov et al., 2010; Locarnini et al., 2010) at 1/4° of horizontal resolution.

thus in the Earth climate system (review of Legg et al., 2009). In fact, they deliver specific water masses formed in marginal seas in the open ocean. As such, understanding the dynamics of outflows and in particular how water masses are spread is of primary importance. Dynamics of outflows involves a wide range of processes, from the descent and entrainment of ambient water to the formation of eddies containing outflow waters, as illustrated in Figure 1.10. Thus, it has been studied through many perspectives, including laminar buoyancy-driven flows (e.g., Griffiths, 1986; Price and O'Neil Baringer, 1994), turbulent mixing (e.g., Baringer and Price, 1997), and eddy formation (e.g., the so-called "meddies" containing Mediterranean Sea Water). The latter can be either due to shear instability and detachment of a slope current (e.g., D'Asaro, 1988; Bower et al., 1997), balanced adjustment of a weakly stratified fluid into a stratified ocean (McWilliams, 1988) or mixed barotropic/baroclinic instability of a slope current (e.g., Cherubin et al., 2000).

Although the Red Sea outflow has been deeply studied using both observational *in situ* data (Bower et al., 2002, 2005; Peters et al., 2005; Peters and Johns, 2005; Bower and Furey, 2012) and numerical models (Özgökmen et al., 2003; Ilıcak et al., 2011), the Persian Gulf outflow is poorly documented. Part of this dissertation (Chapter 4) is dedicated to the study of the Persian Gulf outflow. In the following, we give an overview of our current understanding of the Persian Gulf outflow. Then we review some of the processes occuring in the Red Sea outflow and explain why we expect similarities in the Persian Gulf outflow. In Appendix A, we present another outflow problem that is the Congo River outflow[6]. The objective is the same than for the Persian Gulf outflow, which is the understanding

[6]This work has been mainly done during my Master II's internship at the Laboratoire de Physique des Océans, under the supervision of Anne-Marie Tréguier.

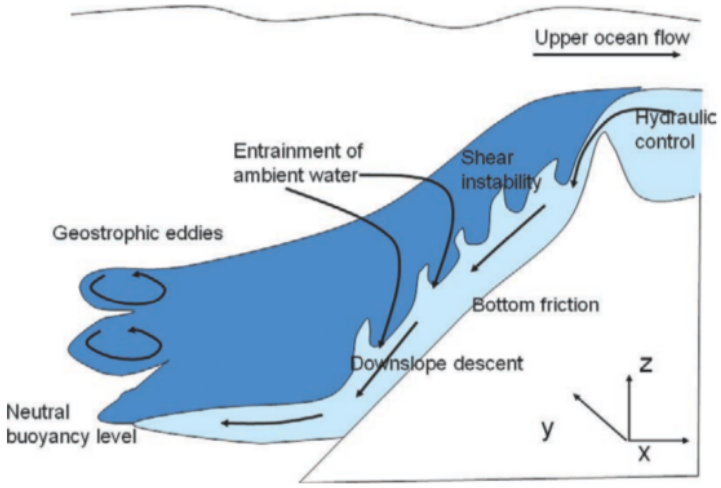

Figure 1.10: Figure from Legg et al. (2009). Schematic illustrating the physical processes acting in overflows.

of the spreading of outflowing waters. However, this outflow dynamics strongly contrasts with the Persian Gulf and the Red Sea outflows.

Current knowledge of the Persian Gulf outflow

The Persian Gulf has been early revealed to be an evaporation basin (Privett, 1959). However, the first experiment that measured the water mass exchanges in the Strait of Hormuz was carried out *recently*, compared to other outflows (Brewer and Dyrssen, 1985, mention a *"classical Mediterranean type of circulation"*, i.e., a two-layer flow at the Strait, with light inflowing waters in the upper layer and dense outflowing waters in the bottom layer). An extensive survey of the Persian Gulf carried out by the NOAA[7] confirmed the existence of a two-layer flow in the Strait (Reynolds, 1993). Two distinct campaigns sampled Persian Gulf Water (PGW) in the Gulf of Oman, contained in small scale structures (in the submesoscale range), but none of them could conclude on their formation process and no footprint of a slope current is mentioned (Banse, 1997; Senjyu et al., 1998). Banse (1997) insists on the turbulent nature of the outflow and on the chaotic spreading of PGW infered from salinity and oxygen casts : *"Rules about this variability could not be recognized"*. Using repeated conductivity-temperature-depth (CTD) and expendable bathythermograph (XBT) measurements in the Gulf of Oman, Bower et al. (2000) were the first to sample PGW extensively. Measurements reveal a vein of saline (37.5-38 psu) waters at ∼200 m depth along the southern boundary of the Gulf.

The GOGP-99 campaign (Golfe d'Oman Golfe Persique), carried out in 1999 by the

[7]The National Oceanic and Atmospheric Administration (NOAA) conducted an extensive survey in the Persian Gulf after the Gulf War (1990-1991) to monitore the spread of crude oil discharged by Iraq against Kuwait.

Service Hydrographique et Océanographique de la Marine (SHOM), provides a good sampling of the water mass structure in the Strait of Hormuz and in the Gulf of Oman (Pous et al., 2004a,b). The main conclusions obtained from those data analyses are : (i) strong mixing occurs in the near Strait plume, whose variability is dominated by short time scales (∼1 month); (ii) a slope current located near 200-250 m depth is observed to veer seaward at Ras-Al-Hadd (a cape on its way) and (iii) mesoscale variability may influence the spreading of PGW. Examining Argo floats trajectories, L'Hégaret et al. (2013) highlight the influence of the mesoscale surface-intensified circulation (reaching 700 m) on the PGW seaward expelling from the slope current. However, all these observational studies acknowledge the lack of repeated sampling with a sufficient spatio-temporal coverage to draw a consistent picture on the fate of the PGW. Besides, literature on the Red Sea outflow could give us insight on the PGW spread, as the geomorphological frames and dynamics of these outflows share similarities : they both spread into confined gulfs dominated by mesoscale circulation of gulf-wide, westward travelling eddies (e.g., Ilıcak et al., 2011; Bower and Furey, 2012; Carton et al., 2012).

Lessons from the Red Sea outflow literature

Classic literature on outflow problems cited above (e.g., Price and O'Neil Baringer, 1994) is mostly derived for waters outflowing in relatively quiescent environments. This means that the background eddy activity is considered to be low enough not to influence the buoyancy-driven dynamics of the slope current, i.e., the assumption is made that the surrounding flow is at rest. This assumption is justified by the fact that the studied outflows (mainly, Mediterranean outflow, Denmark Strait Overflow, Faroe Bank channel outflows, Ross and Weddell Seas outflows) are situated (i) far from western boundary intensified circulation and (ii) at depths where the surface intensified mesoscale circulation has no signature (cf Table 1.1). To the contrary, the Red Sea outflow and the Persian Gulf outflow (i) are situated on western boundaries and (ii) equilibrate at shallow depths (notice that strait depths are also slightly shallower). For comparison, surface EKE near the Strait of Gibraltar is less than 100 $cm^2\ s^{-2}$ whereas it reaches more than 1000 $cm^2\ s^{-2}$ in the western Arabian Sea (EKE derived from satellite altimetry, Ducet et al., 2000).

Bower and Furey (2012) sum up the effect of (i) and (ii) in comparing the Red Sea outflow with the Mediterranean outflow : *"The observations contain little evidence of features that have been shown previously to be important in the spreading of Mediterranean Outflow Water (MOW) in the North Atlantic, namely a wall-bounded subsurface jet (the Mediterranean Undercurrent) and submesoscale coherent lenses containing a core of MOW ("meddies"). This is attributed to the fact that the Red Sea Outflow Water enters the open ocean on a western boundary. High background eddy kinetic energy typical*

Table 1.1: Sill depth and equilibrium depth of some of the world ocean outflows, see Legg et al. (2009) for additional properties.

	Sill depth [m]	Equilibrium depth [m]
Faroe Bank	800	3000
Denmark Strait	500	1600
Ross Sea	600	>3000
Weddell Sea	500	2000
Mediterranean Sea	300	800-1000
Red Sea	200	600-800
Persian Gulf	100	200-300

of western boundary regimes will tend to shear apart submesoscale eddies and boundary undercurrents." The modelling study of Ilıcak et al. (2011) has similar conclusions and specifically shows that the spreading of Red Sea waters is dominated by the stirring done by surface intensified mesoscale eddies.

Summary of Section 1.2.2 Marginal Seas Outflows

- The Red Sea and the Persian Gulf feed the western Arabian Sea with dense salty outflows.
- Because they are situated at a western boundary and equilibrate at shallow depths, their dynamics is known/expected (Red Sea/Persian Gulf outflow) to be influenced by incoming eddies propagating into the Gulf of Aden/Gulf of Oman.
- Details on how eddies spread the Persian Gulf outflow are unknown.

1.2.3 Western Boundary Coastal Upwellings

Background

During the summer monsoon, the winds are dominantly northeastward near the western boundary of the Arabian Sea (Figure 1.3). As such, they drive upwellings off the coasts of Somalia and Oman through Ekman divergence mechanism (Schott and McCreary, 2001). The atmospheric jet crossing the Arabian Sea (Findlater Jet) leaves a region of strong positive wind curl shoreward, reinforcing the upwelling through Ekman pumping. Figure 1.11 shows climatological sea surface temperature (SST) in January and July. SST is clearly reduced all along the Arabian Sea western boundary (compared to offshore values) in July (Figure 1.11b) and reveals wind driven upwellings. During the winter monsoon, the winds reverse and are downwelling favorable in this area.

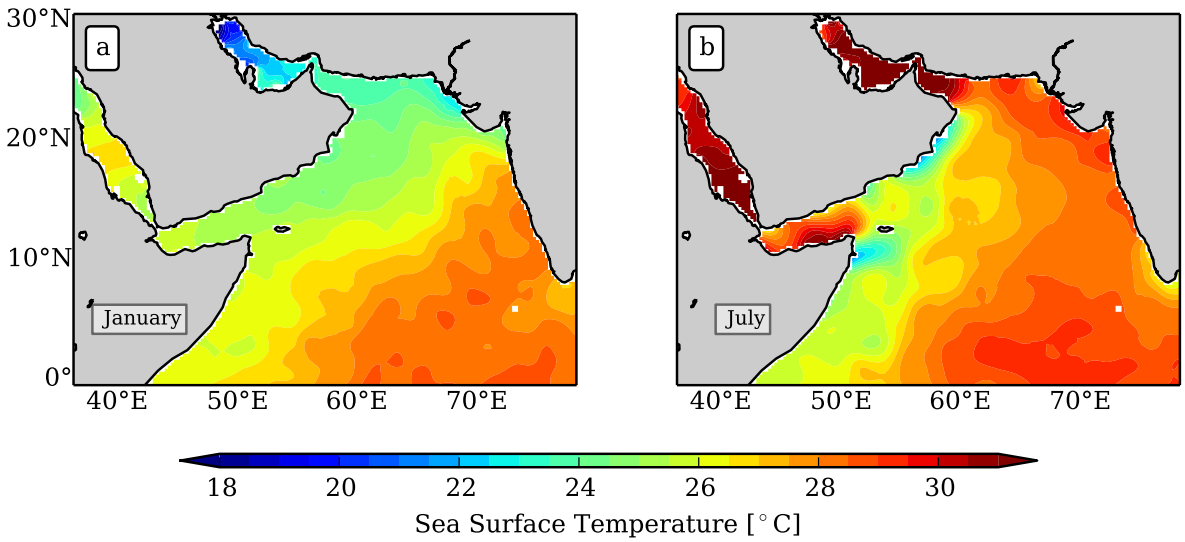

Figure 1.11: Sea surface temperature maps in the Arabian Sea in (a) January and (b) July. Seasonal upwellings are visible along the coasts of Somalia and along the Arabian Peninsula in July. Dataset is the World Ocean Atlas, release 2013 (WOA2013, Antonov et al., 2010; Locarnini et al., 2010) at 1/4° of horizontal resolution.

Arabian Sea upwellings are particularly important in driving a summer phytoplankton bloom (Resplandy et al., 2011). They also play a major role in ocean-atmosphere interactions during the monsoon (Vecchi et al., 2004) and strongly impact the mixed layer heat budget (de Boyer Montégut et al., 2007). Furtermore, they influence Indian rainfall variability (Izumo et al., 2008), triggering strong societal consequences. In coupled ocean-atmosphere general circulation models, warm biases along eastern boundaries (where major upwelling systems take place but are not properly resolved due to the coarse resolution) were shown to be responsible for uncertainties and biases in precipitations (Large and Danabasoglu, 2006). We can expect a similar significance of the Arabian Sea upwellings, especially for the monsoon rainfall variability which is still modestly predictable.

Despite their importance, the Somali and Oman upwelling structures remain poorly documented (Shi et al., 2000) and no comprehensive study has been dedicated to the understanding of their dynamics. In Chapter 5 we investigate the Oman upwelling system and in the following we briefly introduce why we expect a different regime than in eastern boundary upwelling systems.

Why are western boundary upwellings specific?

The Somali and the Oman upwellings have specific features making them fundamentally different from more deeply studied Eastern Boundary Upwelling Systems (EBUS, Canary, Benguela, Peru-Chile and California upwelling systems, see the review of Capet et al.,

2008a). In fact, the Somali and the Oman upwellings are (i) active only seasonally and (ii) coupled with a very intense and turbulent surface circulation linked with their position on a western boundary (Elliott and Savidge, 1990, on the Oman upwelling). EBUS show less seasonal fluctuations and are dynamically more isolated because of their position on eastern boundaries. Schematically, as explained in Section 1.2.1, turbulence generated at eastern boundaries is radiated westward, whereas western boundaries receive turbulent features generated in the inner basin. Specifically in EBUS, mesoscale turbulence[8], whose strength is measured by eddy kinetic energy, is continously radiated offshore due to β (Kelly et al., 1998). On the contrary, in western boundary upwellings, the locally generated mesoscale turbulence is trapped, thus increasing the eddy kinetic energy of the system. Furthermore, we expect the Arabian Sea upwellings to be influenced by remotely forced signals. More specifically, the interaction of incoming Rossby Waves with a western boundary current system has been suggested by McCreary and Kundu (1985) for the upwelling off Somalia. It has also been highlighted by Marchesiello et al. (2000) for the East Australian Current associated upwelling : *"At eastern boundaries, coastal upwelling currents leak consistently offshore by means of the radiation of Rossby waves [...] At western boundaries, according to McCreary and Kundu (1985), the same mechanism does not occur since the Rossby waves propagate onshore"*. However, the impact of Rossby waves on SST during upwelling events has not been precisely quantified yet and still deserves a particular attention.

Summary of Section 1.2.3 Western Boundary Coastal Upwellings

- Summer monsoonal winds trigger upwellings along the western boundary of the Arabian Sea (Somalia and Oman).
- Western boundary upwellings are poorly studied and their dynamics is expected to differ significantly from eastern boundary upwellings (Rossby waves propagating onshore).
- Impacts on oceanic heat balance and ocean-atmosphere interactions should be strong.

[8] mainly comprised of eddies generated by baroclinic instability of the upwelling jet (Marchesiello et al., 2003).

1.3 Aims of the PhD

In this general introduction, we highlighted that the western Arabian Sea is dynamically complex. Three main processes are expected to play an important role in the variability of the dynamics : Rossby waves, and westward (thus, onshore) drifting of remotely generated mesoscale turbulence, marginal seas outflows and western boundary upwellings. Figure 1.12 summarizes these processes and illustrates the fact that they are stronly suspected to interact with each other. Those interactions are conceptually rather simple to figure out (e.g., interaction of the Oman upwelling with remotely forced turbulence) but specific treatments lack and a lot of issues remain unresolved. This PhD dissertation aims at adressing this issues.

Our main investigation tool is numerical modelling. It allows to either reproduce the full dynamics in its whole complexity or to isolate specific mechanisms. Thus, we believe that this tool is specifically well designed for studying the interactions between processes. Chapter 2 describes the numerical framework we use in this dissertation.

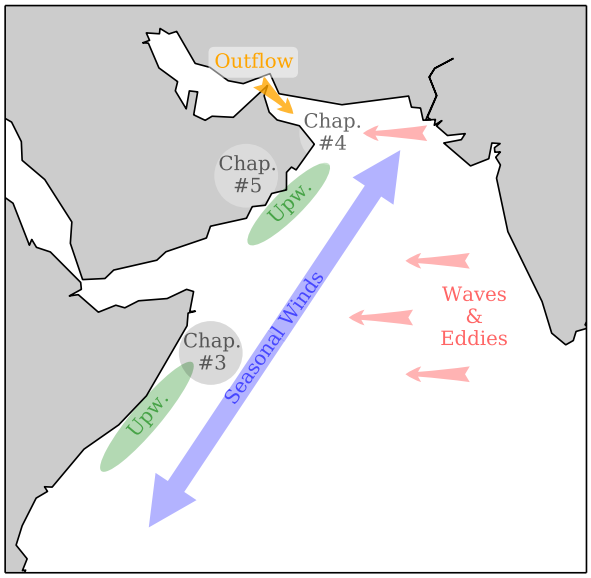

Figure 1.12: Schematic summarizing the different dynamical features of the western Arabian Sea presented in the introduction of this dissertation (Rossby waves, outflows and upwellings) and showing the topics of investigation of each chapter in their geographical and dynamical contexts.

The first issue we tackle is related to the life cycle of the dominating mesoscale structure in the Arabian Sea, namely, the Great Whirl, which has been introduced in Section 1.1.2. This anticyclone remains at a quasi steady place along the coast of Somalia during the Southwest (summer) Monsoon. The onset, reinforcement and demise of this structure remain unexplained, and influences of local forcing (wind stress and wind stress curl) vs. remote forcing (Rossby waves) is still debated. We address these questions in Chapter 3. Results were published in the Journal of Geophysical Research (Vic et al.,

2014b). We notably find that Rossby waves significantly pace the life cycle of the Great Whirl and quantify the wind-driven intensification of the eddy. Far from being exclusive to this eddy, the results give insights on remote influences on mesoscale dynamics further north in the area (as recently illustrated by L'Hégaret et al., 2015).

The general question of how Persian Gulf Water spreads in the Gulf of Oman is addressed in Chapter 4. We investigate how remotely formed mesoscale eddies propagating into the Gulf of Oman interact with the outflow. Their basin-wide size makes them interact with the topography leading to the formation of submesoscales participating actively to the spreading of outflowing waters.

Dynamics of the upwelling off Oman is investigated in Chapter 5. The philosophy of this study is to characterize the upwelling (focusing on the vertical structure of temperature and currents, and energy conversion) in regards to deeply studied eastern boundary upwelling systems and to bring points of comparison. Specifically, we investigate how Rossby waves influence the upwelling and the surface layer heat budget. Rossby waves are found to modulate the sea surface temperature response to wind forcing.

To summarize, the guideline of this dissertation is to analyse turbulent processes in the western Arabian Sea under the assumption that the western boundary brings dynamical complexity. Namely, different processes are interacting with each other unlike in eastern boundary systems that are more isolated.

Chapter 2

Numerical Framework

Contents

2.1 Model and Configuration

In this section we briefly present the essential characteristics of the Regional Oceanic Modeling System (ROMS) as well as numerical options used in the configuration set up. For a complete description of the model, the reader is refered to Shchepetkin and McWilliams (2005); Penven et al. (2006); Debreu et al. (2012) and further technical information can be found on the ROMS-AGRIF website[1]. We willingly do not extend much on the configuration set up as it is done in a *classic* way, regarding the history of regional modeling studies using ROMS (e.g., Marchesiello et al., 2003; Penven et al., 2005; Capet et al., 2008b; Mason et al., 2011). By *classic* we mean that the ocean is forced by the atmosphere (there is no coupling) and that surface and boundary conditions are provided by climatological observational (or reanalysed) datasets. The spirit of this modeling strategy is to study the balanced oceanic response to atmospheric forcing. On the contrary, I pay more attention to the procedure of an offline one-way nesting done on the northwestern Arabian Sea (section 2.2).

2.1.1 The Regional Oceanic Modeling System

Physics

ROMS solves the primitive equations on a curvilinear terrain-following coordinate system (called σ coordinates). The three primary assumptions required to derive the primitive equations from the Navier-Stokes equations are (i) the Boussinesq approximation, (ii) the hydrostatic approximation and (iii) the incompressibility of the fluid :

- The Boussinesq approximation states that density variations are sufficiently small to be neglected in the Navier-Stokes equations, except in the gravity force. An underlying assumption is that inertia (horizontal acceleration of fluid motions) is far less than gravity [2].

- The hydrostatic approximation comes from the assumption that the ocean is a thin layer of fluid with horizontal scales dominating over vertical scales. As such, variations of pressure p on the vertical are only due to changes in density ρ (not to inertial motions), so $\partial_z p = -\rho g$ (g is the acceleration of gravity).

- Incompressibility of fluid relies on the assumption that the mass of a particle does not vary with pressure. This leads to simplify the continuity equation to a non-divergence condition of the fluid velocity, $\partial_x u + \partial_y v + \partial_z w = 0$. This diagnostic

[1] `http://www.romsagrif.org/index.php/documentation`

[2] One may verify that this is trivial, considering a variation of fluid velocity of 1 $\mathrm{m\,s^{-1}}$ over 1 h (already a substantial acceleration in the scales we model) gives an acceleration in $O(10^{-4}\ \mathrm{m\,s^{-2}}) \ll g = O(10\ \mathrm{m\,s^{-2}})$

equation allows to infer the vertical velocity w from the horizontal velocity (u, v), which are determined by the prognostic equations of momentum.

Primitive equations are thus composed of the conservation of horizontal momentum, hydrostatic balance, incompressibility of fluid, an equation of state for seawater linking temperature and salinity to density at a given depth and transport equations for tracers. Dynamics in a given basin is forced at the surface by the atmosphere (wind stress, freshwater flux and heating) and at open boundaries by currents associated with temperature and salinity properties.

Numerics

The primitive equations are discretized horizontally on the Arakawa C-grid that is well suited to solve problems with horizontal resolution smaller than the first radius of deformation (Arakawa and Lamb, 1977), hence motions we are interested in (meso to submesoscale). Discretization on the vertical is done on a staggered grid with distinct ρ and w levels (called the Lorenz discretization). Equations are written in flux form, allowing to limit the number of averaging operations while ensuring a better conservation of momentum and tracers. Temporal discretization uses a split-explicit time step with leap-frog predictor and 3$^{\text{rd}}$ order Adams-Moulton corrector (Shchepetkin and McWilliams, 2005). Barotropic equations are solved using a smaller time step than the full 3D equations (baroclinic). Without going into details, the idea is to propagate the barotropic equations several times between two baroclinic time steps[3] before reinjecting prognostic variables ($\eta, \overline{u}, \overline{v}$, $\bar{\cdot}$ denotes a vertical average) in the baroclinic equations. In order to avoid aliasing due to the high frequency propagation of the barotropic equations, η,$\overline{u}$ and $\overline{v}$ are averaged over one baroclinic time step before being reinjected (Shchepetkin and McWilliams, 2005).

The advection scheme is 3$^{\text{rd}}$ order upstream biased. It allows the generation of steep gradients (ubiquitous features at scales smaller than the mesoscale) while being diffusive implicitely at a scale of a few grid points (Shchepetkin and McWilliams, 1998). As the implicit diffusion is commonly assessed to be sufficient, explicit lateral viscosity is not needed (unlike in centered schemes), except in sponge layers near the open boundaries. The advection operator can be split into a purely advective part and a diffusive part. The latter is naturally along σ coordinates, producing a spurious (not physical) mixing, sometimes in a diapycnal direction (where σ levels are the most tilted, over sloping topography). For tracers (temperature and salinity), it can be rotated along geopotentials

[3]In practice, the ratio of the baroclinic/barotropic time step is tighted to the wave speed of internal/external gravity waves, that is $\sqrt{g'h}/\sqrt{gH}$, H and h being the ocean depth and the thickness of the *equivalent depth*, and g' being the reduced gravity (in shallow-water models). Considering $g' = O(10^{-3}g)$ and $h = O(10^{-1}H)$ gives a ratio in $O(10^{-2})$.

(Marchesiello et al., 2009) or isopycnals (Lemarié et al., 2012) to better conserve water mass properties. This can be of crucial importance for long term integration in regions with wide water mass spectra near the bottom topography (e.g., outflows).

Open boundary conditions are treated using a mixed active/passive scheme (Marchesiello et al., 2001). Larger-scale information $(u, v, \overline{u}, \overline{v}, T, S, \eta)$ is prescribed to force the model, while dynamics generated in the model is allowed to radiate outside. The explicit lateral viscosity increases smoothly close to the lateral open boundaries to fade out the reflection of internal signals.

The turbulent closure scheme mostly used[4] to parameterize subgrid-scale vertical mixing is the K-Profile Planetary (KPP) boundary layer (surface and bottom) scheme (Large et al., 1994) connected to an interior mixing scheme. It produces vertical viscosity coefficient (entering the momentum equations) and vertical diffusion coefficient for potential temperature and salinity. The boundary layer depth (often called *mixed-layer depth*) varies with surface momentum and buoyancy forcing and is determined by comparing a bulk Richardson number ($Ri = N^2/(\partial_z u)^2$, N being the Brunt-Väisälä frequency, measuring stratification) to a critical value. At the base (top) of the surface (bottom) boundary layer, both diffusivity and its gradient are forced to match the interior values. In the interior, vertical diffusivity is computed taking into account three processes generating vertical mixing : vertical shear instability, internal wave breaking and hydrostatic instability (convective adjustment). Note that there is no tide in the simulations so that there is diapycnal mixing induced by breaking tidal internal waves.

2.1.2 The Arabian Sea Configuration

Running ROMS requires a grid (coordinates and associated metrics), surface and optionally boundary forcing and an initial state (T, S and horizontal velocity field). For the Arabian Sea configuration, all these fields were built using Penven et al. (2008)'s pre-processing tools.

Grid and initial state

The grid extends meridionally from 10°S to 28°N and zonally from 38.3°E to 77.6°E (Figure 2.1). It covers the whole Arabian Sea and partly encompasses marginal seas (Red Sea and Persian Gulf). Dynamical connections between both hemispheres are important in the Indian Ocean (e.g., Lighthill, 1969). As such, the study of the Arabian Sea requires to resolve the dynamics as far south as 10°S to properly model these exchanges, occuring mainly through the cross-equatorial Somali Current (Schott et al., 1990). The

[4]Generalized Length Scale (GLS) scheme is also available.

choice of representing partially adjacent seas (thus not fully resolving their dynamics) is a compromise in terms of computation cost. In fact, embedding the whole Red Sea (resp. Persian Gulf) would have led to enlarge the grid importantly westward (resp. northward), unfortunately filling it mostly with land points (useless information but still entering the computation). These compromises allow to barely model the exchanges although we keep in mind that Red Sea and Persian Gulf outflows are poorly resolved in the parent simulation. The grid has 640×640 horizontal ρ-points and 56 σ-levels on the vertical. The mean horizontal resolution is 6.6 km and the vertical resolution varies between 2 m at the surface to 500 m at the bottom above the deepest bathymetry (5403 m). Stretching occurs only on the surface layers above $h_c = 300$ m, with stretching parameters $\theta_s = 6.5$ (surface) and $\theta_b = 0$ (bottom). We use the parameter Vtransform=2 which provides a better repartition of levels below the thermocline.

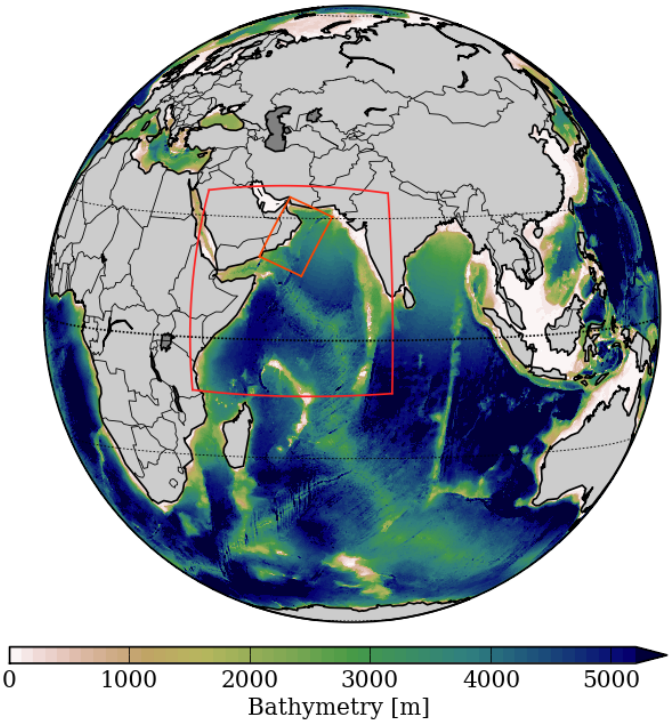

Figure 2.1: Bathymetry of the Indian Ocean (ETOPO2 dataset, Smith and Sandwell, 1997). Dashed black lines are the equator and tropics of Cancer (23°N) and Capricorne (23°S). Red and orange rectangles are the parent and child configuration domains respectively. Child configuration set up is presented in section 2.2.

The bathymetry comes from ETOPO2 dataset (Smith and Sandwell, 1997) at 2' of horizontal resolution, interpolated on the model grid. To avoid too steep gradients in the topography that may lead to pressure gradient errors (Beckmann and Haidvogel, 1993), the bathymetry h is smoothed under the constraint $\delta h/2h < 0.2$. More generally, for numerical consistency of the solution, one may avoid to introduce forcing with spatial scales near or under the grid point size. In fact, the smallest spatial scales resolved are at

a few grid points so forcing below this scale is meaningless. Here, the effective resolution of the bathymetry dataset ($\sim$ 3.7 km around mean latitude) is less than the model resolution (6.6 km) and thus requires some smoothing[5].

Initial state is at rest ($u, v, \overline{u}, \overline{v}, \eta = 0$) and (T, S) are derived from the monthly climatology World Ocean Atlas 2009 (WOA09, Antonov et al., 2010; Locarnini et al., 2010) in January.

Surface and lateral boundary forcing

We chose to force the simulation with climatological fields (no interannual variability) to focus on the intrinsic variability of the ocean. Moreover, the monsoon regime of the Arabian Sea is typically an ocean-atmosphere coupled phenomenon (Vecchi et al., 2004) involving interannual feedbacks (Beal et al., 2013). Hence, adding interannual atmospheric forcing with no oceanic feedback would lead to get an unbalanced oceanic solution at intra-annual scales. Wind stress comes from the Scatterometer Climatology of Ocean Winds (QuikSCOW) data set (Risien and Chelton, 2008), computed on 122 months (September 1999 to October 2009) of QuikSCAT scatterometer data with a horizontal resolution of 1/4°. This climatology contains persistent small-scale features (Chelton et al., 2004) such as island corner acceleration near Socotra Island and resolves the influence of orography of the Arabian Peninsula (capes in Oman) and the Horn of Africa. Such accelerations have been shown to influence importantly the onshore upwelling dynamics of the US West Coast (Renault et al., 2015) and we expect similar significance for the Oman upwelling (Chapter 5). Atmospheric fluxes (net heat flux, short wave radiation and freshwater flux, evaporation minus precipitation) come from the in-situ International Comprehensive Ocean Atmosphere Dataset (ICOADS) at 1/2° of resolution (Worley et al., 2005). Eastern and southern boundaries are forced $(u, v, \overline{u}, \overline{v}, \eta)$ with Simple Ocean Data Assimilation (SODA) data set release 2.1.6 [Carton et al., 2000]. To get temporal consistency between forcings, we computed a monthly climatology from this dataset on almost the same period as QuikSCOW. Northern (in the Persian Gulf) and western (in the Red Sea) boundaries are closed.

According to Dai and Trenberth (2002) who have listed the 200 most important rivers in the world and their mean rate of flow, the major freshwater discharge in our configuration domain is brought by the Indus River (Pakistan) and represents an average of 0.0033 Sv (104 $km^3\,yr^{-1}$ = 3300 $m^3\,s^{-1}$). This is not much compared to the major rivers inflows (for instance, the Congo River rate of flow, 2nd largest in the world, is 40000 $m^3\,s^{-1}$, cf Appendix A). Actually, the major rivers which take source in the Himalaya Moutains

[5]Bathymetry is seen here as a forcing but it is also true for wind issues near the coast : the so-called *blind zone* for satellites implies an extrapolation that involves small spatial scales, both in the wind field and in the oceanic response (e.g., Desbiolles et al., 2014)

mainly discharge in the Bay of Bengal. Therefore we consider that the impact of river inflows can be neglected.

Numerical options

We mainly kept the basic options offered in the ROMS-AGRIF release of ROMS. Given the diffusivity of the advection scheme, no explicit lateral viscosity nor tracer diffusivity is added. We have tested the sensitivity of the salt tongue in the northern Arabian Sea (due to the spread of the Persian Gulf outflow) to the tracer advection scheme. We tested the genuine 3$^{\text{rd}}$ order upstream biased scheme (UP3) and its variants, whose diffusion parts are rotated, either along geopotentials (RSUP3-GEO, Marchesiello et al., 2009) or along isopycnals (RSUP3-ISO, Lemarié et al., 2012). UP3 severely alters the hydrological properties of the salt tongue (similarly to the results by Couvelard et al., 2008), whereas RSUP3-GEO and RSUP3-ISO better conserve properties on yearly time scales. We finally chose RSUP3-GEO which was less expensive than RSUP3-ISO[6]. The background vertical mixing is set to zero for momentum and tracers. Sponge layers near open boundaries have a width of 150 km (25 grid points) with a maximum diffusivity of 1000 $\text{m}^2\,\text{s}^{-1}$. The bottom stress is linear, $\boldsymbol{\tau}_b = -\rho_0 C_D \boldsymbol{u}$ with a drag coefficient $C_D = 3\,10^{-4}$ $\text{m}\,\text{s}^{-1}$ (default value). In Chapter 4 we discuss the impact of the bottom stress parameterization on the dynamics of boundary layers.

Computational performances

ROMS is efficiently parallelized for distributed memory and message-passing interface (MPI) architectures. Computational resources were provided by the Pôle de Calcul Intensif pour la Mer (CAPARMOR cluster) at Ifremer, Brest, France. We use a two-dimensional partitioning into subdomains and 64 processors were used for the parent simulation. An adjustement stage of $\sim$ 10 days, consisting in the radiation of gravity waves generated by the wind *burst* (given the state of rest of the ocean), requires a small time step (100 s). Then a time step of 500 s is used, requiring about 20 wall-clock hours to complete a year's simulation.

2.2 Nesting Procedure

The nesting procedure is one-way and offline and follows Mason et al. (2010). This means that the high resolution *child* simulation is forced at lateral boundaries by the coarser resolution *parent* solution but has no feedback on it. Moreover, the child simulation is

[6] At the time we ran the simulation (Fall 2012), RSUP3-ISO still had bugs and was indecently expensive.

run independently of the parent one. The one-way procedure only allows *downscaling* effects (instead of *downscaling* and *upscaling* effects in two-way nesting procedures) but presents highest flexibility in terms of grid dimensions and orientations (the grid can be rotated to maximise the ratio of ocean to land points) and in computational resources. All tools used to build grid and forcing variables are derived from Jeroen Molemaker's *Roms2roms* toolbox[7]. Although surface forcing is done in a classic way, using the same datasets as in the parent solution, the grid and boundary forcing files necessitate particular attention.

Grid and initial state

The grid is rotated clockwise 22° compared to the parent grid (both grids in Figure 2.1) to maximise the number of ocean points. As we are particularly interested in the Persian Gulf outflow and the Oman upwelling, the grid orientation and dimension is a compromise to cover the whole Gulf of Oman including the Strait of Hormuz and the Oman coast until Yemen (Figure 2.2 for geographical information). The grid has $502 \times 702 \times 56$ ρ-points and the horizontal resolution is 2 km, approximately one third of the parent resolution. This grid refinement coefficient ($\Delta x_{parent}/\Delta x_{child} = 3.3$) is in the standards for regional nestings (ranging from 2 to 5, according to Debreu and Blayo, 2008). Stretching parameters for vertical distribution of σ-levels are the same as in the parent configuration.

Bathymetry is from the SRTM30-plus dataset at 30' ($\sim$ 1 km) of resolution[8]. It is based on the Sandwell and Smith (2009) global 1-minute grid corrected by higher resolution data wherever available (local depth soundings, Becker et al., 2009). A Gaussian smoothing with a width of $4 \times \Delta x$ is applied to avoid aliasing as Δx is greater than the bathymetry resolution. Then, to avoid pressure gradient errors caused by too steep topography gradients, bathymetry is smoothed under the constraint $\Delta h/2h < 0.2$ (same as in the parent configuration). Special treatment is required near the boundaries to match the parent and child bathymetries. Indeed, higher resolution of the dataset (SRTM-30 resolution is 4 times higher than ETOPO2) increases the steepness of the continental shelf and isolated seamounts for instance, leading to depth mismatches between parent and child grids. This becomes a problem where bathymetry mismatches lie along open boundaries. To recover continuity of the bathymetry, a correction is applied following Mason et al. (2010) :

$$h_{child} = \alpha h_{child} + (1 - \alpha) h_{iparent}, \tag{2.1}$$

where h_{child} and $h_{iparent}$ are the child bathymetry and parent bathymetry interpolated on the child grid respectively. α is a function of the distance to lateral boundaries, varying

[7] available at `http://molemaker.org/software.html`
[8] available at `http://topex.ucsd.edu/WWW_html/srtm30_plus.html`

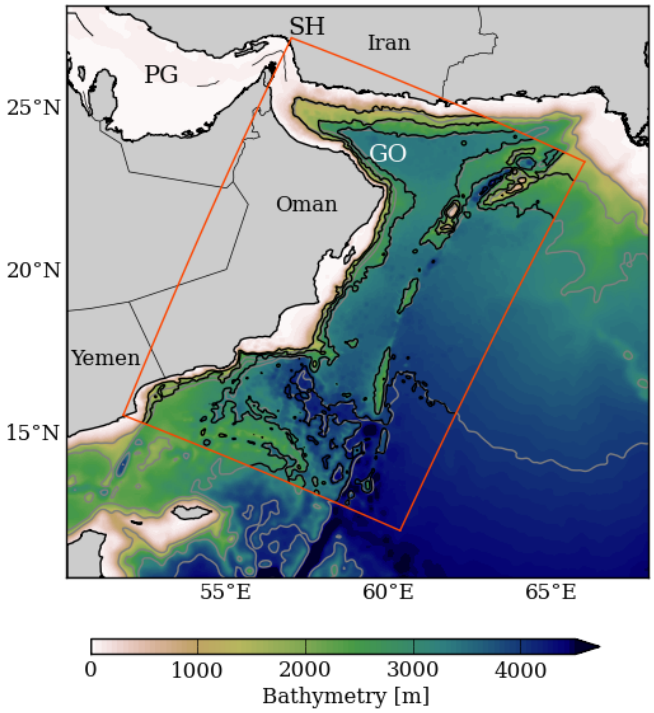

Figure 2.2: Bathymetry of the parent and child domains (inside and outside orange rectangle, respectively). Gray (black) lines are the parent (child) grid bathymetry isolines 1000, 2000, 3000 and 4000 m. Inside the child domain, the bathymetry near the boundaries is matched to the parent grid bathymetry, following the procedure in Mason et al. (2010). GO, PG and SH stand for Gulf of Oman, Persian Gulf and Strait of Hormuz respectively.

between 0 at the boundaries to 1 in the interior[9]. Figure 2.2 illustrates how the match is done for some isobaths (1000, 2000, 3000 and 4000 m).

The interpolation process used to build the 3D initial state is generic to interpolate data from a ROMS grid to another ROMS grid. It is therefore employed to build the lateral boundary forcing files (next paragraph). It consists in three separated stages at a given time step. First, all variables are horizontally interpolated from the parent to the child grid at each level (still in the parent σ-coordinate system). Second, all 3D variables are vertically interpolated from the parent σ-coordinates to z-coordinates. Lastly, they are interpolated from z-coordinates to the child σ-coordinates. If there is no parent information available at a given point (often near the bottom where bathymetries may mismatch in the interior), a *nearest neighbour* extrapolation is done to fill gaps while avoiding creation of potential extrema.

Lateral boundary forcing

The child simulation is forced at the northern, southern and eastern boundaries by the parent simulation with a 10-day frequency. We use the same procedure for interpolation as shown precedently (horizontal, then $\sigma_{parent} \rightarrow z \rightarrow \sigma_{child}$ interpolation) at each time

[9]In practice, α is a tanh with a characteristic decay scale of 50 km.

step. To ensure volume conservation inside the child domain, baroclinic and barotropic normal velocities $(u_\perp, \overline{u}_\perp)$ are corrected :

$$(u_\perp, \overline{u}_\perp) = (u_\perp, \overline{u}_\perp) - \int_\Gamma (u_\perp, \overline{u}_\perp) \cdot h \, \mathrm{d}\Gamma \Big/ \int_\Gamma h \, \mathrm{d}\Gamma \tag{2.2}$$

where Γ follows the northern, southern and eastern boundaries and h is the water depth. Consequently, the net inflow through these boundaries is zero.

At the western boundary, ocean points are confined to the Strait of Hormuz (SH) in a shallow region ($< 100\,\mathrm{m}$, Figure 2.2). As the parent outflow is not satisfactory in terms of hydrology and volume transport, we build synthetic boundary forcing fields $(T, S, \zeta, u, v, \bar{u}, \bar{v})$ representative of the Persian Gulf outflow in the SH. The only data in the SH that has a sufficient temporal coverage to depict an annual cycle are the Acoustic Doppler Current Profilers (ADCPs) moored during the period December 1996 – March 1998 (Johns et al., 2003). Other cruises were conducted in regions embedding the SH but they are too temporally sparse for our purpose (e.g., Pous et al., 2004a). We use this data to assess *a posteriori* the validity of the prescribed boundary forcing regarding the modeled outflow in the Gulf of Oman. Given the sparseness of the data, we build our synthetic forcing on the following assumptions :

1. There is no tangential velocity at the boundary, $u_\parallel = 0$;
2. the analytical profiles of T–S and $u_\perp$ depend only on time and on the vertical (horizontally homogeneous at the boundary, modulo a geostrophic correction);
3. we assume a two-layer flow as most commonly observed, surface inflow in the Persian Gulf and deep outflow to the Gulf of Oman (e.g., Bower et al., 2000);
4. the total transport through the boundary is zero. Indeed, even if the Persian Gulf is an evaporative basin and thus a net inflow should balance this evaporative loss, it is less than 0.02 Sv (Johns et al., 2003) and thus we neglect it.

Figure 7 in Johns et al. (2003) illustrates the annual cycle in T–S properties. We build the boundary variables in 4 stages :

1. We use these data to define two linear vertical profiles associated with two seasons (January–June and July–December). Synoptic cruise observations may overestimate the mean velocities in the SH (Figure 10 in Johns et al., 2003) and we rather define velocity profiles that are coherent with integrated transport in both layers (Bower et al., 2000; Johns et al., 2003).
2. After interpolating these profiles on the child grid, we compute the gradient of η (sea surface height) that balances geostrophically the surface flow. Then we constrain

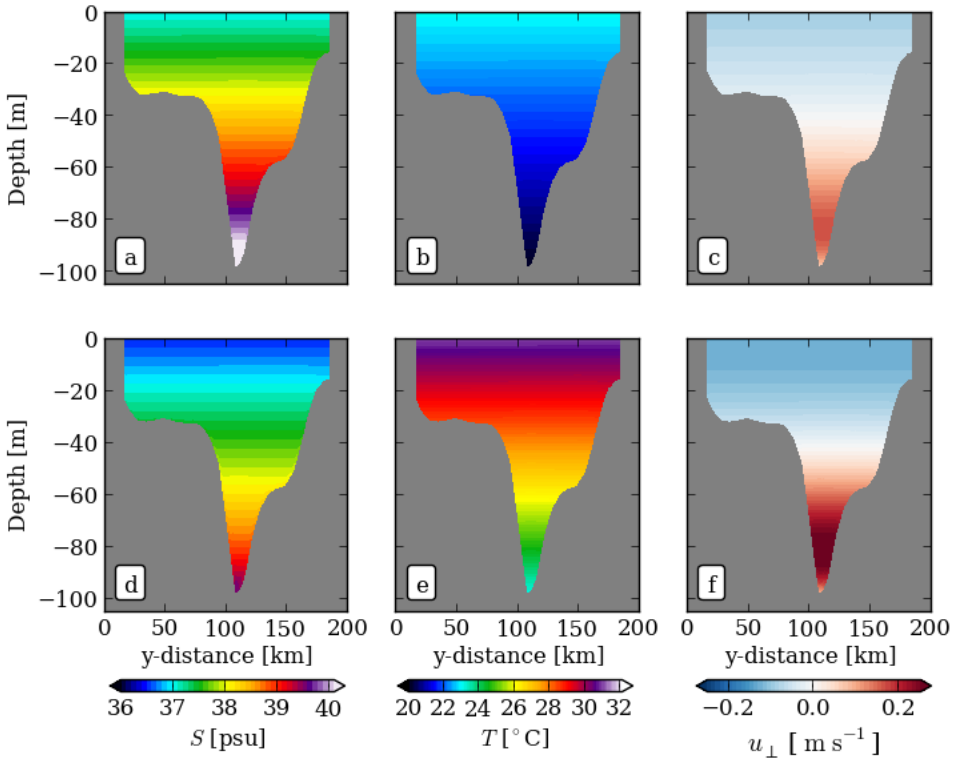

Figure 2.3: Synthetic northwestern boundary forcing for the child simulation : (left) salinity S, (middle) temperature T and (right) normal velocity $u_\perp$. Top (bottom) panels represent variables at date 01/01 (07/01). Temporal interpolation is done following Equation 2.3 to get variables at all dates.

the mean value of η to be equal to the mean of other boundaries at the same time (to avoid having pressure gradients between boundaries that would generate large-scale flow). S is also modified to account for a balanced thermal-wind flow in the interior.

3. We enforce the total transport to be zero by removing the mean velocity through the boundary to baroclinic and barotropic velocities (Equation 2.2). Figure 2.3 presents the synthetic variables at the western boundary of the child grid.

4. Lastly, we interpolate temporally between the two profiles to get any variable $X(t)$ every 10 days :

$$X(t) = \frac{X_{01/01}}{2}\left[1 + \cos\left(\frac{2\pi}{nt}t\right)\right] + \frac{X_{07/01}}{2}\left[1 - \cos\left(\frac{2\pi}{nt}t\right)\right], \tag{2.3}$$

where $X_{01/01}$ and $X_{07/01}$ are variables at dates 01/01 and 07/01 and nt is the number of days in a year (360 in ROMS).

2.3 Post-processing Lagrangian Diagnostics

In order to get a Lagrangian perspective on the fate of the Persian Gulf outflow, we released synthetic particles in the outflow (Chapter 4). The code used is *Pyticles*[10], developed by Jonathan Gula. *Pyticles* is a Python/Fortran hybrid parallelized code for Lagrangian particles 3D advection. Processing is offline, using the 3D velocity field outputs from simulations to advect particles. It has been used to illustrate and quantify the submesoscale vertical pump in filaments (Gula et al., 2014). In this section, I give some general characteristics of the code and describe the parameters we use.

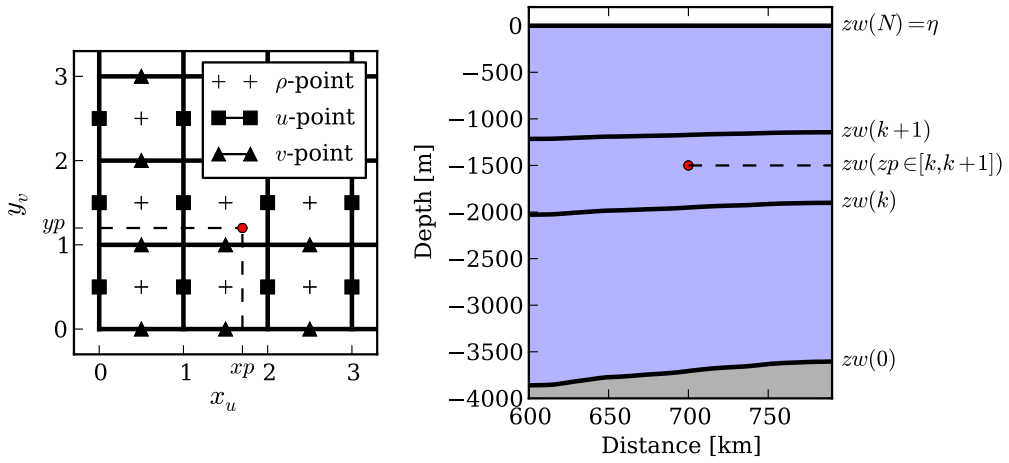

Figure 2.4: Particle (left) horizontal and (right) vertical coordinates (xp, yp, zp). The red point represents a particle. xp coordinate is on the u-grid, yp coordinate is on the v-grid (horizontal C-grid) and zp coordinate is on the w-levels.

A patch of particles is initialized[11] in the model coordinates system (x_u,y_v,σ), where x_u and y_v are coordinates on u- and v-grid respectively. Each particle is described by its position (xp, yp, zp) at a given time t (Figure 2.4 shows the coordinate system). The 3D velocity field is extracted from simulation outputs with a given frequency (the higher the better) and is linearly interpolated in time between two outputs with a higher frequency. We use the child simulation outputs at a 12 h-frequency and interpolate 100 times between two outputs. As such, the velocity field is updated every ∼7 minutes. The interpolation frequency is chosen following the reasoning that particles must not cross more than a grid cell between two time steps to ensure the continuity of trajectories (this is especially important near fronts). As the maximum horizontal velocity in the simulation is $u_{max} = 1.7\ \mathrm{m\,s^{-1}}$ and the grid size is $\Delta x = 2$ km, the maximum time step required to verify this condition is $\Delta t = \Delta x / u_{max} \sim 20$ minutes.

[10] available at `http://web.atmos.ucla.edu/~gula/2/codes.php`

[11] The code can be either used in a *continous injection* mode with particles being added continously or with an initial patch.

The timestepping uses a 4^{th} order Runge-Kutta (RK4) scheme. Although more expensive than Adams methods (same family of predictor-corrector algorithms) of comparable order, Runge-Kutta methods are more stable and accurate (Kuzmin, 2010). As advection of particles requires both stability and accuracy (at the expense of higher computational cost), RK4 method is particularly well suited. In space, linear interpolation of the velocity field is performed at each particle location. More complex interpolation schemes are implemented (cubic, spline, WENO) but they do not provide substantial changes (regarding Jonathan Gula's experience with the code).

The simulation consists in the mere advection of particles continuously injected in the Strait of Hormuz during 2 years to cover the seasonal cycle of the outflow. Figure 2.5 illustrates how the distribution of particles looks like after a sufficient time of integration for particles to populate to whole Gulf of Oman.

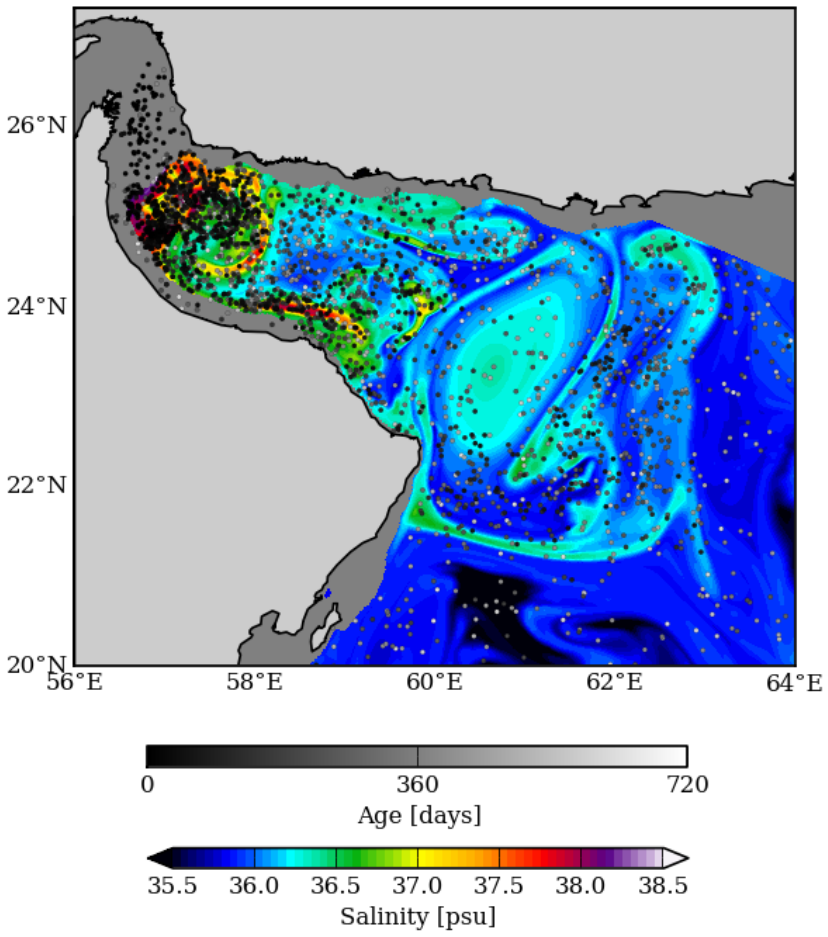

Figure 2.5: Snapshot of particles distribution after almost 2 years of integration superimposed on salinity at 150 m. 399 Particles are released every 12 h in the Strait of Hormuz. We only keep particles that "live" more than 10 days (meaning that they do not go back to the strait in surface layers) and with a salinity greater than 38.5 psu (ensuring they are in the outflow). We only plot $1/20^{th}$ of particles for clarity of the map. The age of particles (shades of grey) is the time spent in the bassin since their release.

Chapter 3

Mesoscale Dynamics in the Western Arabian Sea

Contents

3.1 Introduction

In Chapter 1, we presented an important feature of the Arabian Sea that is the reversing seasonal wind forcing. We also explained why Rossby waves play an important role in the Arabian Sea. The dynamics of the western Arabian Sea thus involves local forcing by the wind and remote forcing by the waves. In this chapter, we investigate the dynamics of a particular structure, the Great Whirl, which involves both mechanisms in ways that we clarify in article Vic et al. (2014b). The Great Whirl is a well-known persistent mesoscale anticyclone off the coast of Somalia during the summer monsoon. Its onset has been controversial for decades. On the one hand, some authors claim dominating local forcing mechanism (instability of the Somali Current or forcing by the strong negative wind stress curl, Schott, 1983; Luther and O'Brien, 1989; Wirth et al., 2002). On the other hand, a tight link between the arrival of a downwelling Rossby wave at the African coast and the onset of the Great Whirl has been observed (Schott and Quadfasel, 1982; McCreary et al., 1993; Beal and Donohue, 2013). Moreover, the sustainment of the eddy and its demise remain poorly studied. Using the numerical simulations described in Chapter 2, we find that the arrival of the downwelling Rossby wave is indeed significant in setting the onset of the Great Whirl (position and time). Nonetheless, the wind stress curl is of primary importance to reinforce the eddy. We also found that the collapse of the Great Whirl is linked with the arrival of an upwelling Rossby wave.

In a more general perspective than the life cycle of a single eddy, the results give insight into the importance of the wind stress curl and Rossby waves to impact mesoscale dynamics in the Arabian Sea. Recently, L'Hégaret (2015) and L'Hégaret et al. (2015) specifically analyzed how strong wind stress curl can reinforce eddies that have the same polarity.

These results are rather specific to the Arabian Sea, which has a short zonal extent and is situated at low latitudes. They contrast with the general functioning of large-scale subtropical and subpolar oceanic gyres. In short, these gyres are forced by large-scale winds, setting the oceanic gyre circulation and in particular the eastern and western boundary currents. These boundary currents are known to be unstable (baroclinic instability often seems to dominate) and account for the production of the majority of mesoscale eddies (Spall, 2000; Smith, 2007; Tulloch et al., 2011). Waves and winds are not known to be significant in the mesoscale variability.

3.2 Article Published in Journal of Geophysical Research

AGU PUBLICATIONS

JGR

Journal of Geophysical Research: Oceans

RESEARCH ARTICLE
10.1002/2014JC009857

Mesoscale dynamics in the Arabian Sea and a focus on the Great Whirl life cycle: A numerical investigation using ROMS

C. Vic[1], G. Roullet[1], X. Carton[1], and X. Capet[2]

[1]Laboratoire de Physique des Océans, UMR 6523, CNRS/Ifremer/IRD/UBO, Brest, France, [2]IPSL/LOCEAN, UMR 7159, CNRS/UPMC/IRD/MNHN, 4 Place Jussieu, Paris, France

Key Points:
- ROMS simulation of the Arabian Sea at 6 km of resolution
- Characterization of the Great Whirl life cycle
- Assessment of the Rossby waves influence on the Great Whirl life cycle

Correspondence to:
C. Vic,
clement.vic@univ-brest.fr

Citation:
Vic, C., G. Roullet, X. Carton, and X. Capet (2014), Mesoscale dynamics in the Arabian Sea and a focus on the Great Whirl life cycle: A numerical investigation using ROMS, *J. Geophys. Res. Oceans*, *119*, 6422–6443, doi:10.1002/2014JC009857.

Received 27 JAN 2014
Accepted 3 SEP 2014
Accepted article online 9 SEP 2014
Published online 22 SEP 2014

Abstract The Great Whirl (GW) is a persistent anticyclonic mesoscale eddy that is observed seasonally in the Arabian Sea during a period embedding the 3 months of the southwest monsoon (June–July–August) at a quasi-steady location. Its dynamics remain unclear despite it being one of the largest coherent vortices in the world ocean. Realistic regional numerical experiments using ROMS are performed to investigate the life cycle of the GW, which is not well resolved by sparse available in situ measurements in the region. Using a set of sensitivity experiments and an accurate temporal characterization of the eddy properties (including position, radius, depth, and vorticity) we (i) confirm the role of basin-scale downwelling Rossby waves in the GW generation, (ii) clarify the role of the monsoonal strong anticyclonic wind in its maintenance and barotropization, and (iii) suggest a connection between basin-scale Rossby wave dynamics and GW collapse.

1. Introduction

The circulation in the Arabian Sea is highly seasonal due to the reversing winds in the region, blowing mainly from the southwest in summer (southwest monsoon, SWM, commonly occurring from June to August) and from the northeast in winter (northeast monsoon, NEM, from December to February) [*Bruce*, 1983]. The basin circulation mainly follows the large-scale wind stress curl pattern, being cyclonic during the NEM and anticyclonic during the SWM [*Shetye et al.*, 1994]. Circulations during the spring and fall intermonsoons (SIM, from March to May and FIM, from September to November, respectively) are often interpreted as relaxation of wind forced circulations during the monsoons [*Lee et al.*, 2000].

The western boundary current along the Eastern African Coast, between the equator and 4−9°N (depending on the season), known as the Somali Current (SC), also reverses [*Schott*, 1983]. This seasonal shift of the currents is a distinguishing feature of the Arabian Sea due to the wind seasonality (the word *monsoon* comes from the Portuguese *monção*, itself from the Arabic *mawsim* which means *season*). To first order, it can be explained by the low latitude of the region, which implies a rapid adjustment of the dynamics by planetary waves [*Lighthill*, 1969]. It has however recently been shown that retroaction at interannual time scales exist [*Beal et al.*, 2013]. During the SWM, the SC flows northward and is accompanied by a coastal upwelling triggered by the winds parallel to the coast (Figure 1).

At the northern end of the SC, during the SWM, a remarkable mesoscale anticyclonic eddy has been observed with in situ [*Leetmaa et al.*, 1982; *Schott and Quadfasel*, 1982; *Wirth et al.*, 2002] and satellite [*Schott*, 1983; *Beal and Donohue*, 2013] data. The position of the so-called Great Whirl (as first described by sailors), located close to the Somali coast between 5°N and 10°N and embedded in the very turbulent environment of the western boundary upwelling (winds blow parallel to the coast in a direction triggering upwelling), is quasi-steady from the onset of the monsoon until the end of October, about 1 month after the end of the SWM. Being the dominant persistent mesoscale structure of the region, it has been studied for decades.

The onset of the GW, its life cycle, and the mechanisms underlying its collapse are issues which have received attention, but which are not yet totally resolved. In particular, the respective role of local forcing by the wind versus remote effects induced by Rossby waves remains to be settled. *Schott and Quadfasel* [1982] observed in situ westward propagating signals after the onset of the SWM, which they interpreted as a possible first-mode Rossby wave that reflects at the coast into shorter modes and leads to the formation of

AGU Journal of Geophysical Research: Oceans 10.1002/2014JC009857

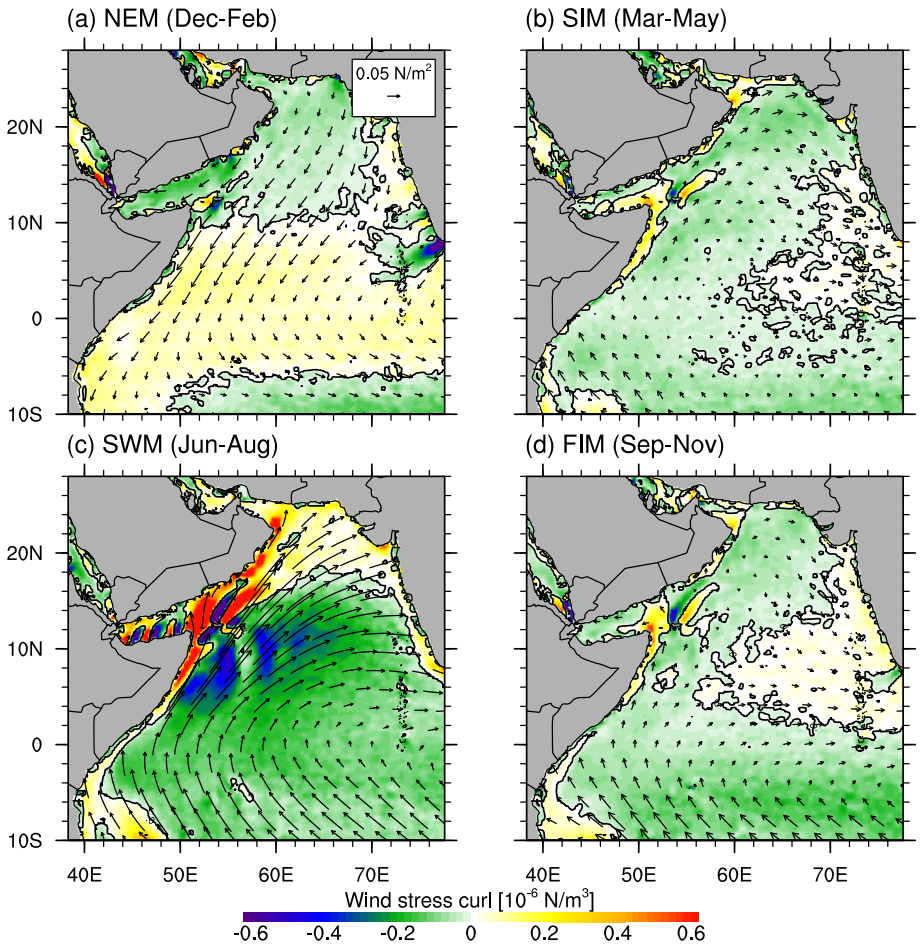

Figure 1. Wind stress (arrows) and wind stress curl (contours) derived from QuikSCAT climatology (see Table 1 for details) and averaged for the periods (a) NEM (December–February), (b) SIM (March–May), (c) SWM (June–August), and (d) FIM (September–November). Black contour is the zero wind stress curl.

eddies at the boundary. A numerical study of *McCreary et al.* [1993] highlighted the arrival of annual Rossby waves from the tip of India which could be a remote forcing of many structures at the western boundary of the basin. This has recently been confirmed by the analysis of 18 years of satellite data that shows positive sea surface height anomalies reaching the coast and then swirling into what becomes the GW [*Beal and Donohue*, 2013]. In a more general framework, the importance of wave-like signals emerging from the eastern side of the basin in the dynamics of the Arabian Sea has also been highlighted by *Kim et al.* [2001] and *Rao et al.* [2010] and is consistent with the low-latitude planetary wave dynamics, e.g., in terms of high propagation speed [*Lighthill*, 1969].

On the other hand, the wind has often been considered as the dominant forcing of the GW because the eddy is located where the wind stress curl is the most negative, hence anticyclonic favorable [*Schott*, 1983; *Luther and O'Brien*, 1989]. The review of *Schott and McCreary* [2001] concluded that local forcing dominates the generation and variability of the GW. The Findlater Jet is defined as the monsoonal southwesterly wind maximum in the Arabian Sea [*Findlater*, 1969]. It is characterized by a zero wind stress curl along its axis that separate the two regions of different wind stress curl polarity (negative southward and positive northward). The position of the GW seems to be constrained by this change of wind stress curl sign and is confined in the southern area [*Schott and McCreary*, 2001; *Beal et al.*, 2013, their Figure 8]. The winds can also play a remote role in reinforcing the waves during their propagation across the Arabian basin [*Brandt et al.*, 2002].

AGU Journal of Geophysical Research: Oceans 10.1002/2014JC009857

The GW has also been considered as a manifestation of the local western boundary current instability regime [*Wirth et al*., 2002]. The influence of the slanted coastline (roughly southwest-northeast) and the presence of Socotra Island on this regime have also been discussed in *McCreary and Kundu* [1988] and *Luther and O'Brien* [1989]. Their geomorphological constraint could also play a role in the steadiness of the eddy.

Finally, the collapse of the GW is not clear either. Prior to collapse, it sometimes moves southwestward seemingly under the influence of flanking cyclones before interacting with the equatorial dynamics [*Beal and Donohue*, 2013]. Other mechanisms have also been proposed such as internal instabilities [*Jensen*, 1993; *Wirth et al*., 2002] and merging with the Socotra Eddy, another remarkable steady anticyclonic eddy north of Socotra [*Fischer et al*., 1996].

In the present paper, we focus on the GW life cycle that is a key aspect of the mesoscale dynamics of the Arabian Sea, successively addressing the issues of generation, persistence, and collapse of the eddy. The use of a numerical model allows a consistent spatiotemporal view contrary to in situ measurements that are sparse in the region. In the next section, we present the model and the Arabian Sea configuration used here, along with a brief assessment of the simulation and a description of the seasonal dynamics as seen in the model. Then we focus on the GW life cycle before disentangling the role of remote versus local forcing on the regional dynamics using experiments that have been designed in such a way that those forcings can be independently switched off.

2. The ROMS Model

We use the version 3.0 of the Regional Ocean Modelling System - Agrif [ROMS, see *Shchepetkin and McWilliams*, 2005 for a complete description] (branch of ROMS developed by the Institut de Recherche pour le Développement [IRD] and INRIA; information can be found at http://www.romsagrif.org/). ROMS solves the primitive equations on an orthogonal curvilinear coordinates system. Its vertical component is terrain-following to better represent the effect of topography on the fluid. The advection scheme is third-order upstream-biased which acts as a subgrid-scale closure and allows not to add physical explicit eddy viscosity nor tracer diffusivity in the interior of the domain. The diffusive part of the advection scheme is rotated along the iso-geopotential surfaces to avoid spurious diapycnal mixing [*Marchesiello et al*., 2009]. Subgrid-scale vertical mixing processes are parameterized using the K-profile parameterization (KPP) boundary formulation [*Large et al*., 1994].

2.1. The Reference Arabian Sea Configuration

The grid has 640×640×56 points covering the Arabian Sea and a part of its adjacent seas, the Red Sea, and the Persian Gulf (10°S–28°N, 38.3°E–77.6°E, domain represented in Figure 2). The horizontal resolution is $1/16^\circ$ which corresponds to ∼6.6 km. We use stretching parameters θ_s=6.5 and θ_b=0 [*Haidvogel and Beckmann*, 1999] and the newly defined function of the vertical levels (Vtransform=2) which allows a more homogeneous distribution than the original function [*Lemarié et al*., 2012]. The minimum depth at which stretching occurs is defined with the parameter h_c = 300 m. It ensures a good representation of outflows in the shallow straits [depth less than 200 m, *Bower et al*., 2000] as well as in the interior basin. Bathymetry is taken from ETOPO2 data set [*Smith and Sandwell*, 1997]. It is smoothed under the constraint $\Delta h/2h < 0.2$ and the minimum depth represented is 15 m. Southern and eastern boundaries are open whereas northern (Persian Gulf) and western (Red Sea) boundaries are closed.

We use climatological forcing to investigate the proper seasonal and interannual variability of the ocean. Information on the data sets used for the forcing of the model and the validation is sum up in Table 1. Wind stress is taken from the Scatterometer Climatology of Ocean Winds (SCOW) data set [*Risien and Chelton*, 2008], computed on 122 months (September 1999 to October 2009) of QuikSCAT scatterometer data with a resolution of $1/4^\circ$. This climatology contains small-scale features [*Chelton et al*., 2004] such as island corner acceleration near Socotra Island and resolves the persistent influence of orography of the Arabian Peninsula and the Horn of Africa. Air-sea fluxes are taken from the in situ International Comprehensive Ocean Atmosphere Dataset (ICOADS) at $1/2^\circ$ of resolution [*Worley et al*., 2005]. Boundaries are forced with Simple Ocean Data Assimilation (SODA) data set release 2.1.6 [*Carton et al*., 2000]. To get temporal consistency between forcings, we computed a monthly climatology from this data set on nearly the same period as QuickSCOW.

AGU Journal of Geophysical Research: Oceans 10.1002/2014JC009857

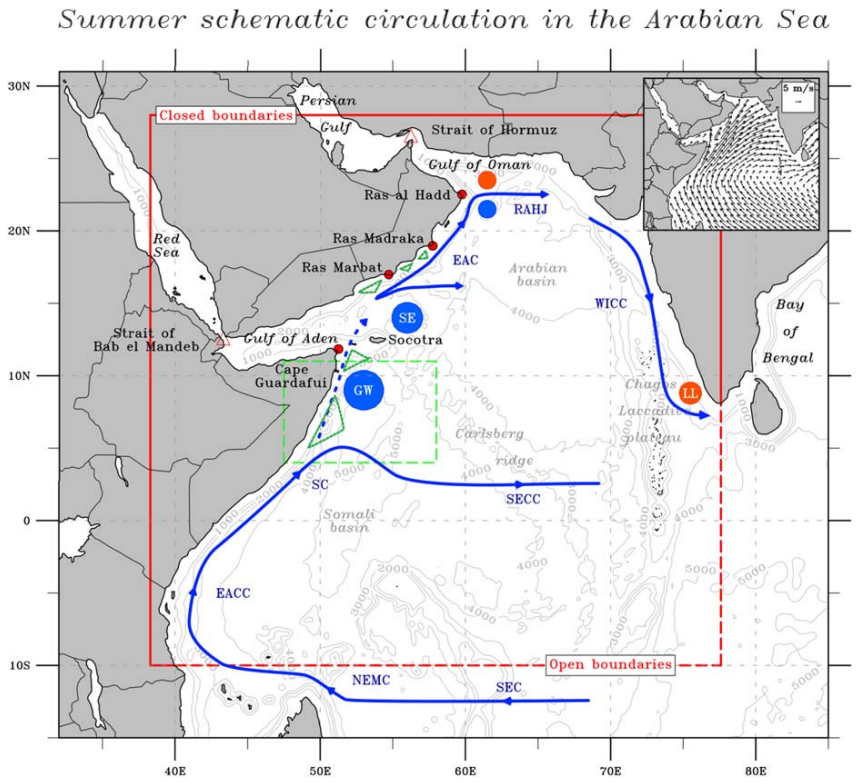

Figure 2. Schematic of the summer surface circulation in the Arabian Sea. The main source for the current paths is the reviews of *Schott and McCreary* [2001] and *Schott et al.* [2009] updated with *Beal et al.* [2013]. Green contoured wedges are the upwelling regions and blue (resp. orange) disks are nearly persistent anticyclones (resp. cyclones) during the SWM. The red lines represent the boundaries of the configuration used, plain lines are closed boundaries, and dashed lines are open boundaries. The inset at the top-right corner represents the climatological wind field in July at the peak of the SWM monsoon. The major currents and steady eddies are coarsely localized and abbreviated this way (from the north to the south): Ras Al Hadd Jet (RAHJ), East Arabian Current (EAC), West Indian Coastal Current (WICC), Socotra Eddy (SE), Great Whirl (GW), Laccadive Low (LL), Somalia Current (SC), South Equatorial Counter Current (SECC), East African Coastal Current (EACC), North East Madagascar Current (NEMC), and South Equatorial Current (SEC). The green dashed rectangle is the area over which surface kinetic energy is averaged in Figure 4c.

Table 1. Description of Data Sets Used for Forcing and Validation of the Model

Data Set	Resolution	Description
ETOPO2	1/30°	Global topography data set [*Smith and Sandwell*, 1997]. http://www.ngdc.noaa.gov/mgg/global/global.html
WOA09	1°	World Ocean Atlas, climatological fields of in situ temperature [*Locarnini et al.*, 2010] and salinity [*Antonov et al.*, 2010]. http://www.nodc.noaa.gov/OC5/WOA09/pr_woa09.html
SCOW	1/4°	Climatology of wind stress from QuickSCAT computed for the period September 1999 to October 2009 [*Risien and Chelton*, 2008]. Used to force the model. http://cioss.coas.oregonstate.edu/scow/
SODA	1/2°	Simple Ocean Data Assimilation data set, release 2.1.6 [*Carton et al.*, 2000], climatology computed on the same period as SCOW. Used to force the model at open boundaries. http://soda.tamu.edu/data.htm
ICOADS	1/2°	International Comprehensive Ocean Atmosphere Dataset [*Worley et al.*, 2005], in situ climatology. Air-sea fluxes used to force the model. http://icoads.noaa.gov/products.html
Aviso	1/3°	Absolute Dynamic Topography [*Rio and Hernandez*, 2004]. Variance computed for the same period as SCOW. http://www.aviso.oceanobs.com/en/data.html
OSTIA	1/20°	Operational Sea Surface Temperature and Sea Ice Analysis Seasonal climatology computed on period 2000–2008 [*Stark et al.*, 2007] http://podaac.jpl.nasa.gov/dataset/UKMO-L4HRfnd-GLOB-OSTIA
GDP	1/2°	Global Drifter Program (Satellite-tracked surface drifting buoys) [*Lumpkin and Johnson*, 2013]. http://www.aoml.noaa.gov/phod/dac/index.php

AGU Journal of Geophysical Research: Oceans 10.1002/2014JC009857

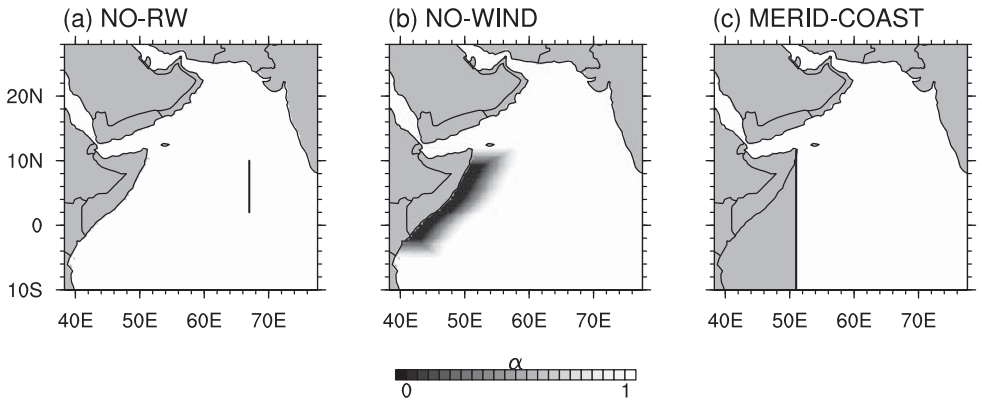

Figure 3. (a) The NO-RW domain with the wall in black line. (b) The damping function α by which is multiplied the reference wind stress in the domain for experiment NO-WIND (damping is linear). (c) The domain of the MERID-COAST experiment, black line is the new coastline.

The ocean is initially at rest, with temperature and salinity fields taken from the World Ocean Atlas 2009 data set [WOA09, *Antonov et al.*, 2010; *Locarnini et al.*, 2010] at 1° of resolution, in January (beginning of the simulation). This is our reference simulation (REF).

2.2. Sensitivity Experiments

In order to evaluate the impact of local and remote forcing on the GW life cycle, we set up sensitivity experiments to separate the role of different forcings. We ran each experiment for 10 years following 2 years of dynamical spin-up. All configuration parameters are identical to those of the reference simulation.

2.2.1. The NO-RW Experiment

The NO-RW experiment is designed to impede the propagation of long Rossby waves into the Arabian Sea by insulating the western basin from Rossby waves with a meridional wall at 67°E between 2°N and 10°N (Figure 3a). The physical consequence is the confinement of the western part of the basin from nearly any signal generated at the eastern side. Therefore, we ensure that the dynamics in the western Arabian Sea is nearly locally driven.

2.2.2. The NO-WIND Experiment

The NO-WIND experiment is designed to prevent the GW from being forced by local wind stress and wind stress curl (strongly negative) during the SWM (extended from May to September). The wind is linearly smoothed from its original value at 550 km (5° of longitude) from the coast to zero at 330 km (3° of longitude) from the coast. The smoothing is done over this relatively large area in order to avoid the creation of strong localized spurious Ekman pumping. The smoothing operator $\alpha(x, y, t)$ is defined as

$$(\tau^x_{\text{NO-WIND}}, \tau^y_{\text{NO-WIND}}) = \alpha \times (\tau^x_{\text{REF}}, \tau^y_{\text{REF}}), \quad (1)$$

(τ^x, τ^y) being the wind stress in the zonal and meridional directions. α is shown for the period May–September in Figure 3b.

2.2.3. The MERID-COAST Experiment

The influence of a slanted coastline on the reflection of waves at the western boundary and on the gyre circulation has been discussed by *Cane and Gent* [1984] and *McCreary and Kundu* [1988] but little has been said on its impact on the GW drift. To assess its importance, we set up the experiment MERID-COAST by setting a meridional coastline at the western boundary passing through Cape Guardafui (Figure 3c).

2.3. Evaluation of the Model and Description of the Basin Dynamics

Here we perform a comparison of the model solution with observed fields in order to evaluate the degree of confidence we can give to the diagnostics described further on. This includes an assessment of the Arabian Sea dynamics so as to better understand the processes governing the GW life cycle.

Figure 4 shows domain averaged kinetic energy at the surface and at 2000 m, and kinetic energy averaged near the western boundary encompassing the upwelling region (see legend for details). This is a good proxy to visualize the spin-up stage of the model. Starting from rest, we consider that the spin-up is done after

AGU Journal of Geophysical Research: Oceans 10.1002/2014JC009857

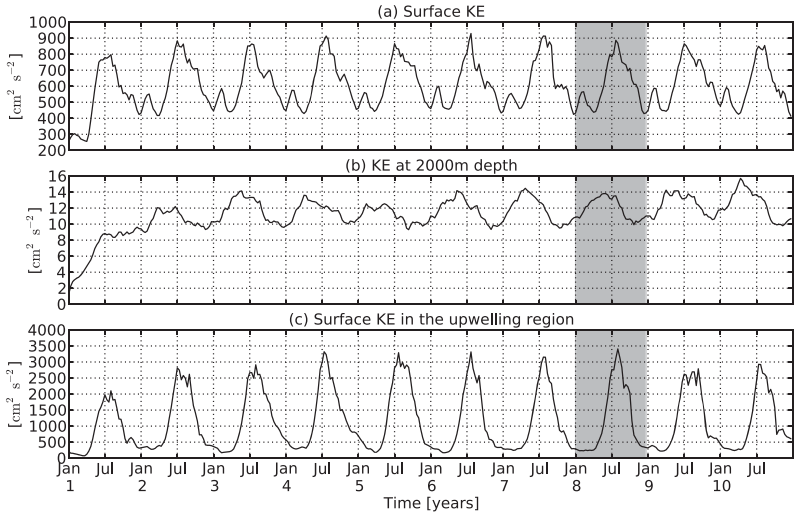

Figure 4. Kinetic energy (KE) averaged (a) at the surface on the whole domain, (b) at 2000 m depth on the whole domain, and (c) at the surface on the upwelling area marked in green dashed line in Figure 2. Year 8 is shadowed in gray to emphasize the normality of this year in terms of energetics as we take it to display typical scenario of the GW life cycle in Figure 8.

the first 2 years as there is no significant trend even at depth where the dynamics takes more time to reach an equilibrium. Consequently, all further diagnostics will be performed using the last 8 years of the simulation. Figure 4 also highlights a strong seasonal variability with the SWM (peak of the monsoon in July) dynamics being nearly twice as energetic as the NEM (centered in January) dynamics at the surface and even six times more energetic at the western boundary, consistent with a strong Ekman response to wind forcing [*Beal et al*., 2013]. The seasonal variability is also observed at 2000 m depth but with a less well-defined cycle. During the SWM, the kinetic energy extrema in the upwelling area (Figure 4c) arise at different dates and have different amplitudes depending on the year, although it should be noted that the forcing is climatological. This is due to intrinsic interannual variability associated with the chaotic nature of the forced turbulent flow [*Wirth et al*., 2002; *Penduff et al*., 2011].

As we noticed previously, the regional dynamics is highly seasonal due to the influence of monsoonal wind forcing. For this reason, we compute seasonal means based on the four periods NEM, SIM, SWM, and FIM, as commonly done in this region [e.g., *Resplandy et al*., 2011]. Figure 5 compares the climatology of Sea Surface Temperature (SST) computed over 8 years for the model with the SST from the Operational Sea Surface Temperature and Sea Ice Analysis product [OSTIA, *Stark et al*., 2007, see Table 1]. The OSTIA data set, delivered by the Met Office, has a horizontal resolution of $1/20^\circ$ and combines infrared and microwave satellites data as well as in situ data. Superimposed on these fields are the model and the *Lumpkin and Johnson* [2013] surface velocity climatologies (see Table 1). This data set uses quality controlled data from drogued drifters of the Global Drifter Program (GDP) from 1979 to June 2012. The general distribution of the model and OSTIA SSTs agree well in the interior of the domain during all seasons. The seasonal cycle is well represented in simulations north of 5°N, with large-scale patterns of colder SST during the NEM (a and b) and warmer SST during the SWM (e and f). This seasonal variability is seemingly driven by air-sea exchanges [*Vecchi et al*., 2004]. The coastal wind-driven upwellings off the Somali and Oman coasts [*Shi et al*., 2000] are spatially and seasonally consistent between model and observations during the SWM and the FIM. The minimum temperature in the Somali upwelling area is about 17°C, consistent with *Schott and McCreary* [2001]. The largest discrepancies appear in the adjacent seas during summer with a warm bias of the model of approximately 2°C. As these seas are not entirely represented in the domain, thermodynamical processes are partial and may account for those differences. Nonetheless, this may not influence much the inner dynamics of the Arabian Sea since the gulfs behind Hormuz and Bab El Mandeb straits, the Gulf of Oman and Gulf of Aden (see Figure 2 for geographical information), do not exhibit SST anomalies. The other bias appears at the equator during the SWM where the model surface water is approximately 1.5°C colder than the OSTIA SST. We diagnose that this anomaly comes from the open southern boundary according to the 3-D analysis of the velocity field.

AGU Journal of Geophysical Research: Oceans 10.1002/2014JC009857

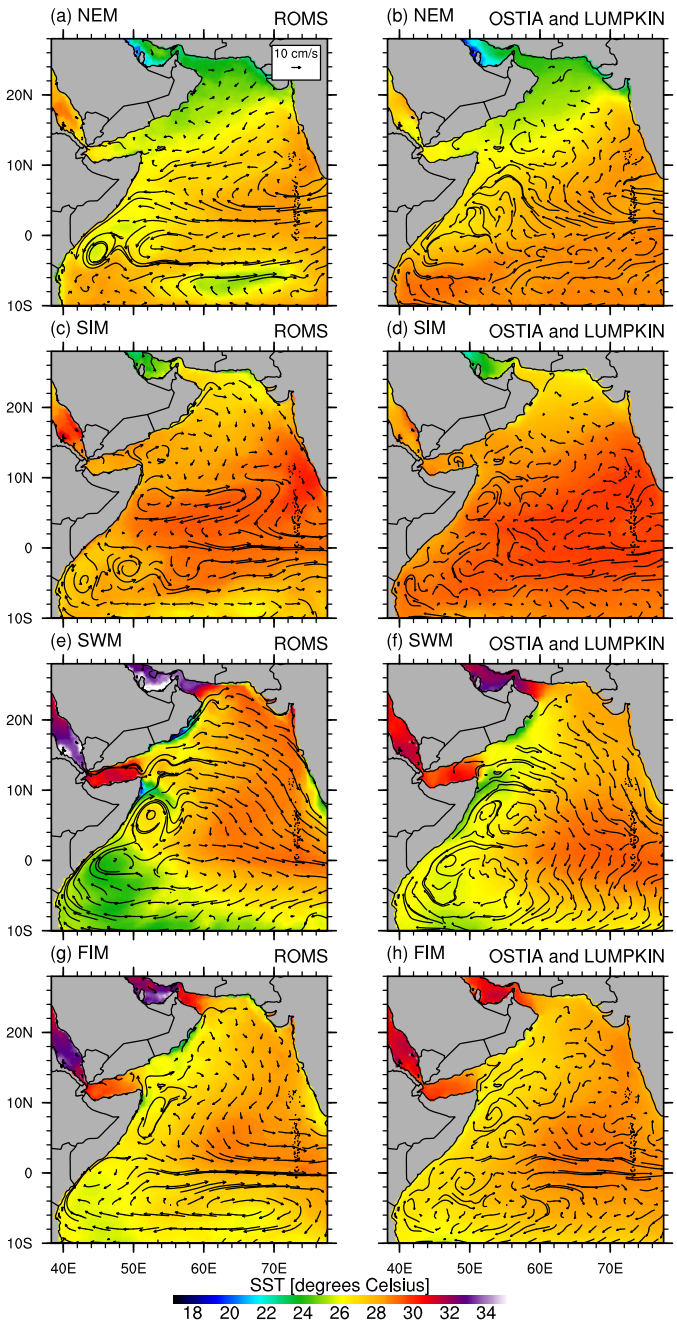

Figure 5. Climatology of Sea Surface Temperature (SST) and surface velocity computed for (left) the model and (right) OSTIA (SST) and the *Lumpkin and Johnson* [2013] surface drifter climatology for each season (from top to bottom: NEM, SIM, SWM, and FIM).

Because the Ekman component of the velocity is of primary importance in the Arabian Sea [*Hastenrath and Greischar*, 1991; *Beal et al.*, 2013], we choose to compare the total velocity of the model with the observations rather than just the geostrophic component (derived from the sea surface height both in model and altimetry) as commonly done in model studies [e.g., *Mason et al.*, 2011]. Another reason for this choice is that our model encompasses the equatorial band where estimating geostrophic velocity is difficult. To this end, we use the *Lumpkin and Johnson* [2013] surface drifter climatology that has been recently used in the region [*Beal et al.*, 2013]. We find that the large-scale circulation agrees well during both monsoons, with the major zonal currents adequately represented. In addition to these qualitative comparisons, we compare the model SC structure with the equatorial observations of *Schott et al.* [1990]. Based on 2 years of an array of six moorings at 0° latitude between the coast and 175 km offshore, they computed a northward flow of 21 Sv ($1Sv=10^6 m^3 s^{-1}$) between the surface and 500 m for the period 1 June to 13 September. Taking the same area and time window, we find a SC mean transport of 23.1 Sv (std dev 3.2 Sv) for the 8 last years of simulation, in good agreement with *Schott et al.* [1990].

Mesoscale persistent structures at seasonal scales are effectively conserved in those climatologies, and the dominant imprint is the one of the GW close to the Somali coast at approximately 7°N during SWM. This is present in both the model and the in situ data, surrounded by a cold tongue of upwelled water [*Schott and McCreary*, 2001]. The model slightly overestimates horizontal velocities compared to drifter's climatology. This may partly be due to the low resolution of the latter (~50km), for which mesoscale features are crudely resolved owing to a deformation radius of ~140km in the region [*Chelton et al.*, 1998]. The Southern Gyre [recirculation of the SC, *Schott et al.*, 1990] south of the GW centered at the latitude of the equator is also represented in the model.

AGU Journal of Geophysical Research: Oceans 10.1002/2014JC009857

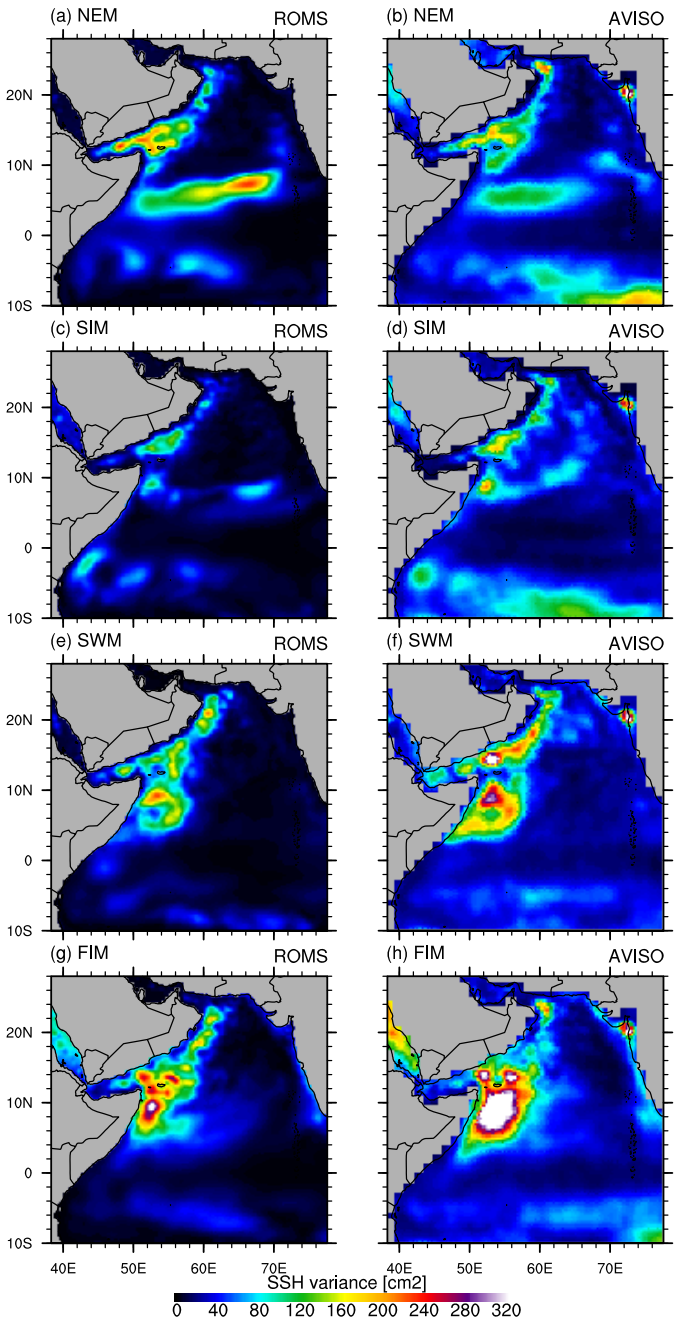

Figure 6. Sea surface height (SSH) variance for (left) the 8 years of simulation and (right) 10 years of MADT Aviso data (same period than the QuickSCOW climatology).

Figure 6 shows the sea surface height (SSH) variance computed over the last 8 years of the model simulation and the Aviso satellite altimetry-derived Absolute Dynamic Topography [ADP, *Rio and Hernandez*, 2004] variance computed on the same period as the SCOW wind forcing (Table 1). Here SSH variance is preferred over Eddy Kinetic Energy (EKE) because the geostrophic assumption [e.g., *Penven et al*., 2005] is not valid in part of our computation domain. Therefore, we rather use the SSH variance as an integrated proxy for available potential energy, thus EKE in a geostrophic turbulence framework [*Rhines*, 1979]. Global patterns show a strong seasonality that is very similar in the model and in the data except at latitudes south of 5°S, maybe due to inadequacies related to the forcing field at the southern boundary as previously noticed. We remark that for all seasons, the SSH variance is maximum at the western boundary, as expected from the basin large-scale circulation. During the NEM, the strong zonal strip of large SSH variance is consistent with the traveling of Rossby waves that emerges from the tip of India [*Brandt et al*., 2002], presumably created by a downwelling coastal Kelvin wave in the Bay of Bengal [*Rao et al*., 2010]. The SWM SSH variance underscores enhanced differences between the ocean interior and western boundary dynamics. The rapid onset of the SC is often interpreted in terms of reflection of long equatorial Rossby waves into short eastward Rossby waves [slowly propagating and accounting for the dynamics in a narrow coastal band, *Lighthill*, 1969; *Anderson and Gill*, 1975]. The enhanced energy level and variability can thus be attributed to Rossby wave-driven motions. The wind stress in the Arabian Sea is also found to be geographically and temporally at its peak (Figure 1). Hence, the wind work on the ocean circulation is maximum, implicitly forcing turbulent motions [*Hughes and Wilson*, 2008, and references therein]. The presence of a local minimum surrounded by a ring of elevated SSH variance reveals the position of the GW center which is relatively steady

AGU Journal of Geophysical Research: Oceans 10.1002/2014JC009857

over much of the SWM period. Model (7°17′N, 52°54′E) and data (6°53′N, 53°00′E) GW positions are in close agreement (the Aviso resolution at this latitude is ∼36km, thus the difference is of the order of one or two pixels), separated by approximately 45 km. Surprisingly, the largest pattern of SSH variance is reached during the FIM which is a season of low forcing by the wind, being a transition period between monsoons. SSH variance is representative of the level of geostrophic turbulence, itself essentially triggered by instability of the main currents [*Smith*, 2007]. During the SWM, seasonally steady currents set up and are fed by the constant wind stress field. After the end of the monsoon, the relaxing of the wind during the FIM leads to destabilization of the currents [*Lee et al*., 2000] thus to an enhancement of the geostrophic turbulence. SSH variance in our solution is generally lower than in the observations. We attribute this to the fact that interannual and intraseasonal (less than the monthly frequency) variabilities in the forcings (atmospheric and oceanic) are absent. Additional sources of variability would in particular contribute to displacements of the GW away from its mean location and enhance SSH variance levels in its vicinity.

We have also calculated EKE of the region and found high values within the upwelling area, reaching local values of 3000cm^{2}s^{-2} both in Aviso and the model, compatible with EKE generation of western boundary currents [*Ducet et al*., 2000]. As mentioned in section 1, this is substantially more than the EKE generated in the four major EBUS which is lower than 250cm^{2}s^{-2} [*Capet et al*., 2008]. Another particularity of this western boundary upwelling is that the maxima of EKE are very close to the coast (less than 100 km) whereas they are farther offshore in EBUS (more than 300 km from the coast). In the latter, the distance is attributed to the generation of small-scale eddy activity that undergoes an inverse cascade while moving westward, thus contributing to a maximum of geostrophic EKE offshore [*Kelly et al*., 1998]. In the Somali upwelling, eddying structures are prevented from moving westward by the coast, hence EKE remains concentrated nearshore.

This evaluation step helps us gain confidence in the realism of the simulated Arabian Sea circulation and eddy activity. Apart from discrepancies with observations near the southern boundary of the domain, the main large-scale currents are well represented and the global level of energy is consistent with satellite measurements. Importantly, excellent model-data agreement is achieved in terms of SSH variance patterns, including the location of the local minimum associated with the GW center (Figures 6e and 6f).

3. Dynamics of the Great Whirl

In this section, we describe the GW dynamics and show that it follows a well-defined life cycle on seasonal time scales, with some year-to-year variability, arising due to nonlinear interactions in our climatologically forced simulations [*Marchesiello et al*., 2003].

3.1. A Rossby Wave Linked With the Onset of the Great Whirl

We start by examining the remotely forced Rossby waves present in our reference simulation. Figures 7a, 7c, and 7e represent SSH at 7.5°N as a function of time and longitude in the model and in the observations. They reveal the clear annual propagation of planetary waves that have been identified as first and second baroclinic modes of long Rossby waves [*Subrahmanyam et al*., 2001] that are continuously reinforced by the wind while traveling along the basin [*Brandt et al*., 2002]. The typical phase speed in the model is 35cms^{-1}. It can be compared to the theoretical long Rossby wave speed c_ϕ:

$$c_\phi = -\beta R_d^2 = -\beta (c_1/f)^2 = -\frac{\beta}{\pi^2 f^2}\left(\int_{-H}^{0} N(z)\,\mathrm{d}z\right)^2 \quad (2)$$

where f and β are the planetary vorticity and its gradient, N is the Brunt-Vaisala frequency, and H is the ocean depth. $R_d = c_1/f$ is the first baroclinic Rossby radius of deformation where we use the WKB approximation to deduce the wave speed for c_1 [see e.g., *Chelton et al*., 1998]. Using equation (2), we find c_ϕ=44cms^{-1} which is close to the 38cms^{-1} found in *Brandt et al*. [2002] with the actual stratification. The discrepancy between the observed and the estimated model phase speed can be attributed to the modulation by the wind [*Subrahmanyam et al*., 2001], which can arise from the background flow velocity that induces a Doppler effect while propagating in the second half of the basin at the beginning of the SIM (Figure 5). The attenuation of the signal between 55°E and the coast is presumably related to the reflected signal into shorter waves which adds higher frequency noise to the original signal. In fact, according to *Cane and Gent* [1984], the long

AGU Journal of Geophysical Research: Oceans 10.1002/2014JC009857

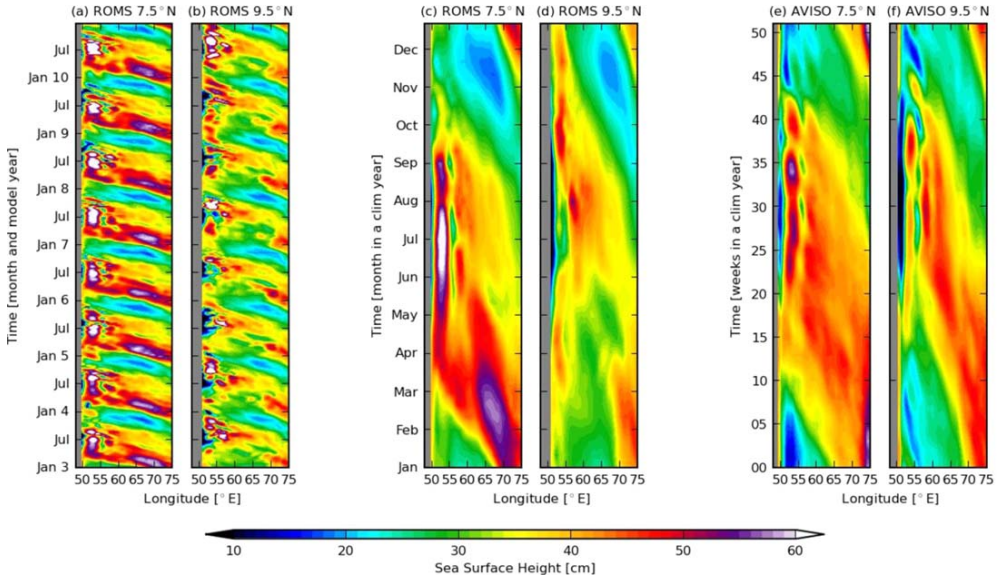

Figure 7. Hovmöller diagram of sea surface height (SSH) in the model at (a, c) 7.5°N and (b, d) 9.5°N on (Figures 7a, 7b) the last 8 years of simulation and (Figures 7c, 7d) for a climatological year (mean of years 3–8). (e, f) Aviso climatological SSH computed for years 1999–2009 (same period as forcing wind stress SCOW in the model). Aviso mean SSH has been shifted to match ROMS mean SSH to make plots comparable.

equatorial Rossby waves reaching a western boundary are reflected into eastward propagating Kelvin waves and short Rossby waves.

In this longitudinal band, we see during spring and summer the local maxima in SSH. In the interior of the basin, they are characteristic of downwelling Rossby waves, and at the coast from May to September it is the footprint of the GW. Although only qualitative, these elements indicate that our simulation produces realistic Rossby wave activity, the spring pulse being primarily generated by the eastern boundary condition with important modulations in the Arabian Sea.

3.2. Mature Stage of the Great Whirl

Figure 8 shows 10 day averaged SSH anomalies at different dates (on which the 10 day averages are centered) during year 8 of the simulation (whose energetics is comparable to the other years, as emphasized in the gray areas in Figure 4). It illustrates the typical scenario of the GW life cycle in the model, although there are some lags between different years in the various stages of the life cycle (onset, growth, and collapse), due to an intrinsic year-to-year variability. This figure can be examined alongside Figures 9 and 10 which present time series of the GW climatological attributes (latitude and longitude, SSH anomaly, radius, vorticity, and depth) in REF and the sensitivity runs. In this section, we focus on the REF simulation (black lines in Figures 9 and 10). The radius is computed by taking the area inside the contour of SSH anomaly of +6cm; then assuming that the GW geometry is circular, we obtain the equivalent radius. The choice of the contour ensures that a closed contour representative of the GW is defined at each time step. The value of the radius is therefore not absolute, as it depends on the chosen SSH level, but has a time-relative value that allows a quantitative comparison. The last feature displayed is the surface vertical relative vorticity $<\zeta> = <\partial_x v - \partial_y u>$, nondimensionalized by the local Coriolis frequency f, where $<\cdot> = \frac{1}{S}\int\int_S \cdot dS$ and S is the GW surface area (inside contour of SSH anomaly of 6 cm). The GW depth h is defined as being the depth at which the kinetic energy of the upper water column equals 75% of the kinetic energy of the whole water column:

$$\int_{-h}^{0} <\frac{1}{2}\mathbf{u}^2> dz = 0.75 \int_{-H}^{0} <\frac{1}{2}\mathbf{u}^2> dz \quad (3)$$

where H is the depth of the ocean and $\mathbf{u}=(u,v)$ is the horizontal velocity field. Again, h has no absolute signification but the 75% value has been chosen to ensure that the bulk of the eddy energy is captured. Superimposed with dashed line is the time-integrated Ekman pumping vertical velocity over the GW area:

AGU Journal of Geophysical Research: Oceans 10.1002/2014JC009857

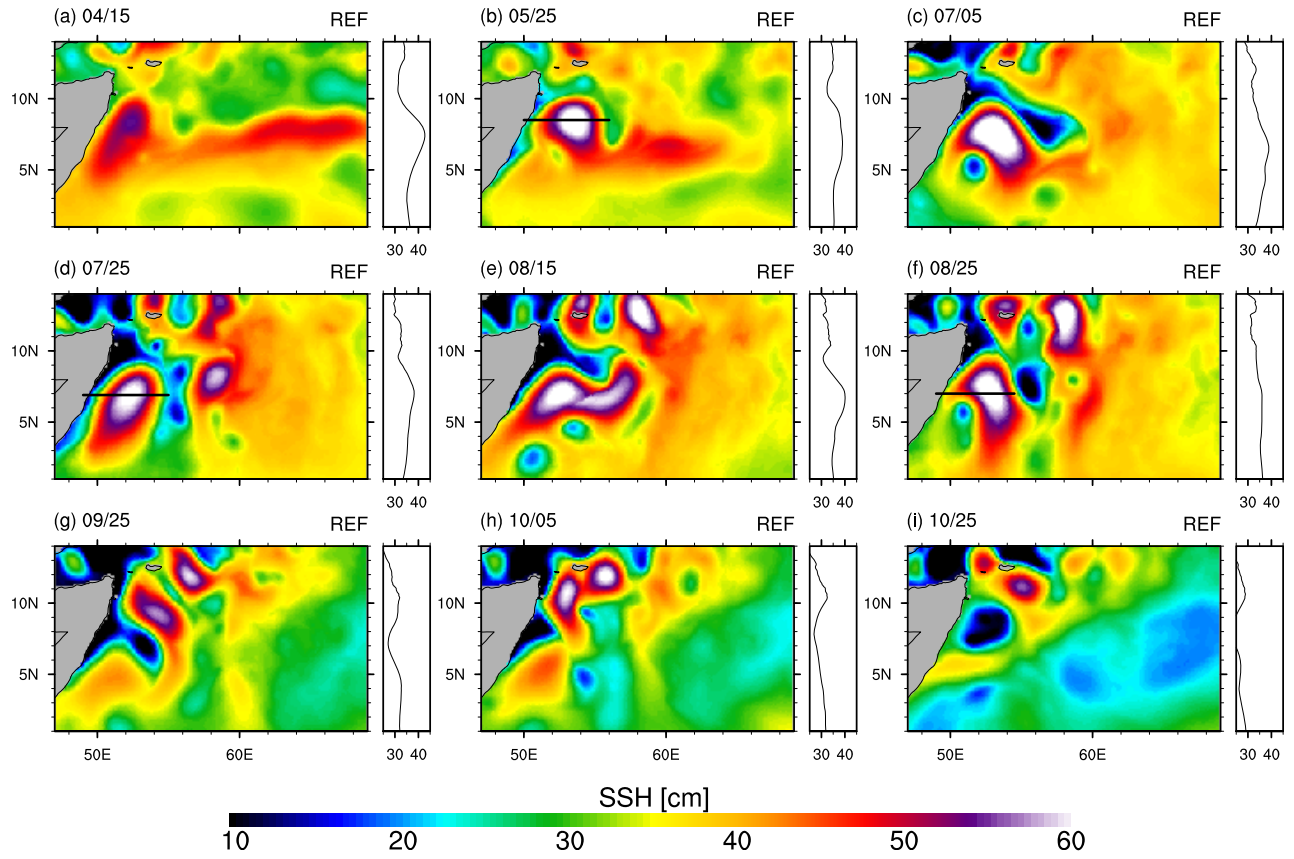

Figure 8. Sea surface height at year 8 averaged on 10 days centered on each date marked above figures. Zonal mean is computed for each figure and displayed on its right side. Black lines represent locations of sections in Figure 11. Colorbar is the same as Figure 7.

$$h_{Ek}(t) = \int_{t_0}^{t} \left[\frac{<\nabla \times \boldsymbol{\tau}(t') >}{\rho f_0} + \frac{\beta < \tau^x >}{\rho f_0^2} \right] \mathrm{d}t' + h(t_0) \tag{4}$$

where $\boldsymbol{\tau} = (\tau^x, \tau^y)$ is the wind stress, ρ is the mean water density in the Ekman layer, and t_0 is 15 May. It corresponds to the depth of a layer forced solely by the Ekman pumping.

On 15 April (Figure 8a, on both the map and the zonal mean), we see the arrival of the Rossby wave at the coast, identified as a positive SSH anomaly roughly between 5°N and 10°N (also seen in Figures 7c and 7d). As mentioned before, the local SSH maximum around position (8°N, 52°E) is modulated by the superimposition of the incident and reflected waves. This is noticeable in Figures 7a and 7c in spring. From 25 May onward, the positive SSH anomaly seemingly trapped at the coast starts to swirl anticyclonically and gains negative vorticity (seen from 15 May onward in Figure 9e).

The GW reaches its most coherent state after the onset of the SWM at the beginning of June. On the 5 July snapshot, the eddy is seen in its commonly associated environment, flanked by two cyclones and by a cold filament of coastally upwelled water on its northern side [*Beal and Donohue*, 2013]. A close examination of the SSH field at a temporal resolution of 2 days (not shown) indicates that the flanking cyclones that surround the GW during the SWM originate from this mesoscale filament. The GW pulls the upwelled waters off the coast at its northern side, forming cyclones that detach from the pool of cold water as also observed in EBUS [*Mason et al.*, 2011, their Figure 7]. Their positions tend to evolve rapidly, and sometimes another anticyclone is found eastward of the GW on the other side of the cold wedge.

The Ekman forced depression of sea level at the coast (seen clearly on 25 July in Figure 8 as well as in Figures 7c and 7d) reveals the geostrophic path of the SC, flowing northeastward during the upwelling season of the SWM. The location of the GW is quasi-steady (Figures 9a and 9b) while its radius and its SSH

AGU Journal of Geophysical Research: Oceans 10.1002/2014JC009857

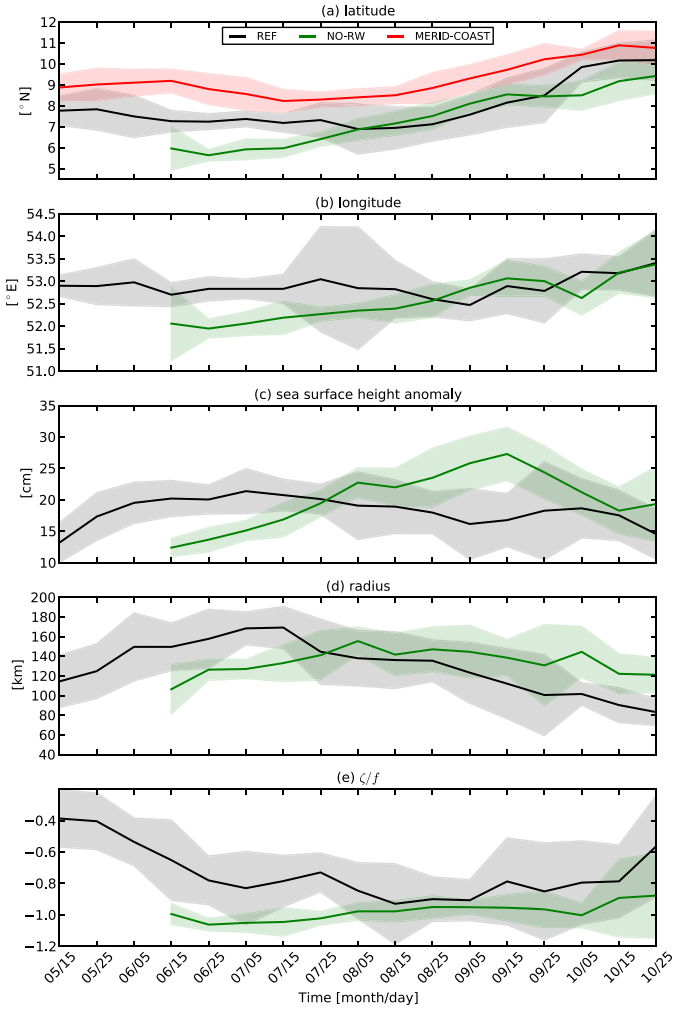

Figure 9. Temporal series of (a) latitude and (b) longitude of the Great Whirl center defined as the (c) local maximum of sea surface height anomaly, (d) radius, and (e) surface averaged relative vorticity nondimensionalized by the local Coriolis frequency. Shaded areas represent one standard deviation on each part of the mean. Standard deviation is computed by taking the biased estimator over eight realizations (8 years). Black line is for the REF simulation, green line for the NO-RW simulation, and red line for the MERID-COAST simulation.

anomaly increase until 5 July (Figures 9c and 9d), at which point they both start decreasing while the width to height aspect ratio of the GW remains relatively constant (not shown). The steadiness of this ratio is coherent with the constant surface velocity seen in Figure 11.

We see in the model the arrival of a second downwelling Rossby wave transporting another SSH maximum at 9.5°N (Figures 7b and 7d and in SSH zonal mean, Figures 8c–8e) in mid-July although it is not as clear in the data (Figure 7f). The presence of the wind curl maximum in this area (Figure 1) and at this time (Figure 10b, representative of the wind stress curl evolution in the GW vicinity) reinforces the positive anomaly at 57°E [as observed earlier in the season in *Brandt et al.*, 2002]. The highest interannual variability is found during this stage (largest standard deviation). We interpret this as a manifestation of the interannual variability of the Rossby wave itself (this is confirmed in further sensitivity experiment where Rossby waves are shut off). For instance, years 7 and 8 show a difference of 10cm in SSH (Figure 7), thus inducing different perturbations on the GW. Moreover, the SSH standard deviation also increases because of merging phenomena between anticyclones occurring at different times. The depth of the model GW dramatically increases from 50 m to 300 m, in agreement with the cruise observations of *Beal and Donohue* [2013] where the strongest surface intensified currents reach deeper than 200 m. This depth increase is also confirmed by the velocity and temperature sections of Figure 11. Thermal wind, deduced from the isopycnal slope, is observed to reach deep in the water column. We discuss the reasons accounting for this deepening in section 3.4.

During all years but one, the GW merges with the positive SSH anomaly (Figure 8e) that could be identified as the Socotra eddy [*Beal and Donohue*, 2013]. The resulting anticyclone migrates northward (Figure 9a, 15 August onward). The odd year displays a low decrease of the GW southward of the cold upwelling wedge, which seems to prevent northern merging. Even if the scenario described in this section is observed most of the years, lags exist between all these phases. The standard deviation from the mean accounts for this intrinsic interannual variability.

3.3. Dynamical Balance

It has been shown that, at a global scale [*Maximenko and Niiler*, 2006] and at a regional scale [*Penven et al.*, 2014], taking into account the effects of inertia reduce the error between geostrophic velocity from

AGU Journal of Geophysical Research: Oceans 10.1002/2014JC009857

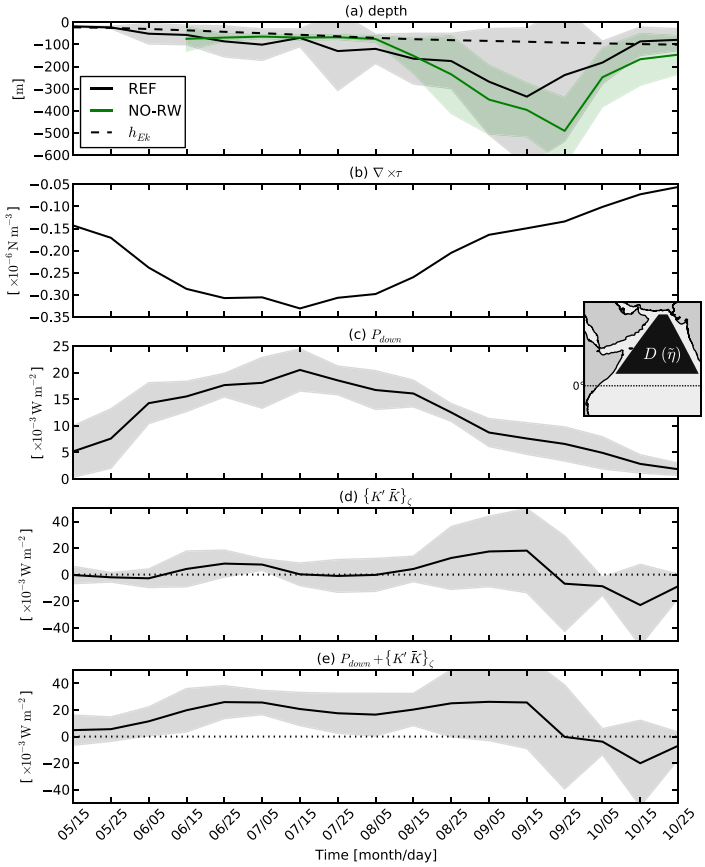

Figure 10. Temporal series of (a) depth (see text for computation), (b) wind stress curl averaged on the GW surface, (c) energy input by the wind acting to maintain the local anomaly of sea surface height [P_{down}, same notation as in *Roquet et al.*, 2011], (d) transfer term between kinetic energy of the baroclinic flow and kinetic energy of the barotropic flow, and (e) is the sum of Figures 10c and 10d. Shaded areas represent one standard deviation on each part of the mean (biased estimator). Black line is for the REF simulation and green line for the NO-RW simulation. The dashed line in Figure 10a represents the deepening of the surface layer due to Ekman pumping (see text for details). The black trapezoid area on the inset map in Figure 10c is the area over which is computed the anomaly of sea surface height $\bar{\eta}$.

altimetry and direct in situ measurements [as observed in *Fratantoni*, 2001]. In the case of anticyclonic eddies, neglecting inertia may lead to a 40% underestimate of the velocity [*Penven et al.*, 2014]. The GW is nested in a western boundary where inertia is found to play a major role in dynamical balances. Moreover, nonlinear effects are expected to actively contribute to the dynamics as revealed by the local Rossby number $|\zeta/f|$, which is often greater than 0.5 during the GW life cycle (Figure 9e). Thus, we assess if the GW obeys a cyclostrophic regime (supposing axisymmetry of the eddy):

$$-fu_\theta = -g\frac{\partial \eta}{\partial r} + \frac{u_\theta^2}{r} \tag{5}$$

where u_θ is the azimuthal velocity, η is the SSH, r is the distance to the center of the eddy, and g is the acceleration of gravity.

Figure 12 shows the evolution of the different terms in equation (5) as well as the absolute value of the residual (i.e., $|-fu_\theta + g\partial\eta/\partial r - u_\theta^2/r|$). All terms are azimuthally averaged around the eddy center at each time step. The dominant balance all along the GW life cycle is geostrophic. However, the inertial term sometimes reaches 30% of either the Coriolis acceleration or the pressure gradient. This departure from geostrophy is to be expected considering the local Rossby number ($|\zeta/f| > 0.5$, Figure 9e). It is noticeable that all the terms are maximum around the peak of the monsoon when the wind stress curl is maximum (around 15 July, see Figure 10b). This adds support to a massive energy input into the GW by the wind stress curl, an assumption that will be tested in section 4.2.

AGU Journal of Geophysical Research: Oceans 10.1002/2014JC009857

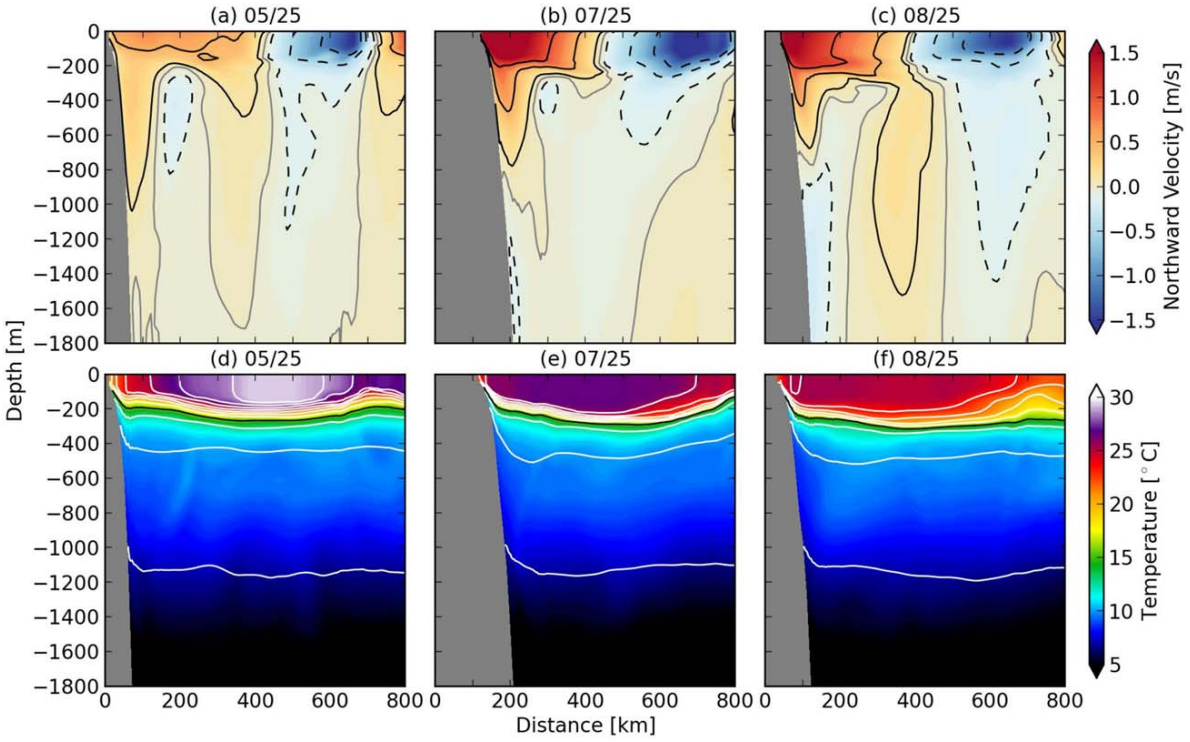

Figure 11. Velocity and temperature zonal sections in the Great Whirl core at locations of black lines in Figure 8. Black plain (resp. dashed) lines are contours of positive (resp. negative) velocity $\pm 0.1, 0.5, 1 \mathrm{ms}^{-1}$ around $0 \mathrm{ms}^{-1}$ gray line. White lines in temperature parts represent isopycnals with CI = 0.5.

Before September, the residual is less than 10% of the amplitude of the Coriolis acceleration within 250 km from the eddy center, thus confirming the validity of the cyclostrophic balance. Farther away, the hypothesis of axisymmetry is not necessarily valid and radial velocity may come into play in the balance. From the beginning of September onward, the residual slightly increases, sometimes being comparable to the inertial term. Although the main balance is still geostrophic, acceleration of velocity ($\partial u_\theta / \partial t$) may become important. This is consistent with the slowing down of the GW seen through the decrease in relative vorticity (Figure 9e).

3.4. Discussion on the Great Whirl Depth Evolution

We use the kinetic energy criterion (equation (3)) as a proxy to define the GW depth because it accurately reveals its deepening observed in sections such as shown in Figure 11. However, the reasons for the deepening observed during almost the whole eddy life cycle are not explained in the literature. In this section, we perform diagnostics on the wind input of energy to the GW and on internal kinetic energy transfers, then we comment on the mechanism of barotropization.

The wind can enhance the level of barotropic energy through wind work $\mathbf{u} \cdot \tau$. Following *Roquet et al.* [2011], we compute the fraction of that wind work that contributes to maintaining (or producing) a local anomaly of sea surface height relative to its surrounding, and hence can reinforce the GW barotropic energy:

$$P_{down} = -\rho_0 g < \tilde{\eta}\, w_{Ek} > \quad (6)$$

where $w_{Ek} = \nabla \times \left(\frac{\tau}{\rho_0 f}\right)$ and $\tilde{\cdot}$ denotes a deviation from areal and yearly averaging performed over a domain D that covers our entire region of interest including that occupied by the GW at any given time (precisely D has a trapezoid shape defined by the vertices 24°N,63.4°E; 24°N,66.1°E; 4°N,76.1°E; 4°N,48.7°E, see inset map in Figure 10c). Results are not sensitive to the particular choice of D unless D is made so small that it only covers the GW area. Using sea level deviations from the areal mean over D ensures that the barotropic energy input we compute is not biased by the fact that w_{Ek} time and space averaged over our regional domain may not be exactly zero (computed over the entire domain D, P_{down} vanishes).

AGU Journal of Geophysical Research: Oceans 10.1002/2014JC009857

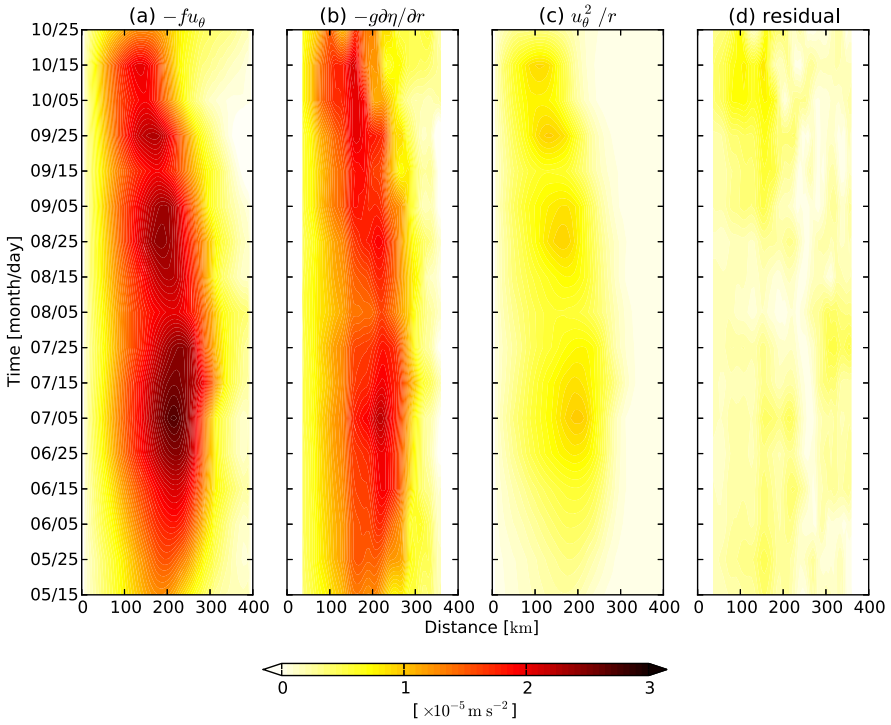

Figure 12. Different terms of the cyclostrophic balance (see equation (5)) azimuthally averaged around the GW center on years 2–8. (a) The Coriolis acceleration $-fu_\theta$, (b) the surface pressure gradient $-g\partial\eta/\partial r$, (c) the inertial term u_θ^2/r, and (d) the absolute residual $|-fu_\theta+g\partial\eta/\partial r-u_\theta^2/r|$. The derivative of SSH $\partial\eta/\partial r$ has been spatially low-pass filtered using a Lanczos filter with cutoff frequency at the grid scale to suppress noisy patterns due to differentiation.

Haney et al. [2001] studied the kinetic energy transformation between the vertical shear flow (i.e., baroclinic) and the vertical mean flow (i.e., barotropic) in California Current eddies. They find that these nonlinear processes of kinetic energy transformation are of crucial importance to account for the barotropization of eddies. The transformation of kinetic energy from the baroclinic flow (u', v') to the barotropic flow $(\bar{u}, \bar{v})$ can be written as follows:

$$\{K'\bar{K}\}=\{K'\bar{K}\}_\zeta+\{K'\bar{K}\}_\delta \tag{7}$$

with

$$\{K'\bar{K}\}_\zeta = \rho_0 H < \overline{\bar{\zeta}'(\bar{u}v'-\bar{v}u')} > \tag{8}$$

$$\{K'\bar{K}\}_\delta = -\rho_0 H < \overline{\bar{\nabla}\cdot\mathbf{u}(\bar{u}u'+\bar{v}v')} > \tag{9}$$

where H is still the total depth of the ocean and ρ_0 is a mean density. The overbar denotes a depth averaged quantity ($\bar{=}\frac{1}{H}\int_{-H}^{0}\cdot dz$) and prime is the deviation from it. $\{K'\bar{K}\}_\zeta$ is the conversion term associated with the baroclinic vorticity and $\{K'\bar{K}\}_\delta$ is linked to the flow divergence. If $\{K'\bar{K}\} > 0$, kinetic energy is transferred from the baroclinic to the barotropic flow, thus increasing the deep ocean energy. When the flow obeys quasi-geostrophy, the exchange term associated with flow divergence ($\{K'\bar{K}\}_\delta$) is at least one order of magnitude smaller than the exchange term containing the relative vorticity ($\{K'\bar{K}\}_\zeta$). We also find this to be true for the GW, with mean values of $\{K'\bar{K}\}_\zeta$ around 4×10^{-3}Wm^{-2} and $\{K'\bar{K}\}_\delta$ smaller by a factor 11. Hence, we ignore $\{K'\bar{K}\}_\delta$ in our analysis.

Figures 10c and 10d show the time series of P_{down} and $\{K'\bar{K}\}_\zeta$, respectively, during the GW life cycle, i.e., the two key sources of energy for the barotropic mode. In Figure 10e, a strong correlation is found between the evolutions of the sum of both terms and GW depth: the deepening of the GW is associated with a plateau in the energy input (from 5 June to 15 September); then the reduction of the energy input coincides with a shallowing of the GW (presumably as a result of dissipation which we do not compute here).

AGU Journal of Geophysical Research: Oceans 10.1002/2014JC009857

Examination of the separate contribution of each term in the evolution of the GW depth suggests to consider two stages during the deepening of the eddy. First, from 15 May to 15 August, the depth increases with a rate compatible with the integrated Ekman pumping being the dominant driver (Figure 10a). P_{down} is greater than $\{K'\bar{K}\}_\zeta$, confirming the leading role of the wind stress curl in the deepening of the eddy. The second stage is from 15 August to 15–25 September where the GW keeps deepening (plausibly at a faster rate but the range of uncertainty is quite large) but with the baroclinic to barotropic kinetic energy conversion term as the dominant source of energy, especially in September.

From 25 September on, the GW suddenly shallows. P_{down} is still positive at this time but is small in amplitude compared to $\{K'\bar{K}\}_\zeta$ that is now negative, revealing an extraction of energy from the barotropic mode. *Wiin-Nielsen* [1962] gives a simple interpretation of the sign of this term using a two-layer quasi-geostrophic framework. When $\{K'\bar{K}\}_\zeta < 0$, there is warm advection in the region of cyclonic vorticity ($\zeta' > 0$) or cold advection in the region of anticyclonic vorticity ($\zeta' < 0$). Over the GW area, $\zeta' < 0$ in the surface layer, thus there must be an input of cold water in the GW area. It may not be coincidental that the rapid change of sign of $\{K'\bar{K}\}_\zeta$ takes place at the time of arrival of an upwelling Rossby wave (Figures 7c and 7d). We discuss this further in the following section.

Overall, we must recognize that these diagnostics offer a caveat in the interpretation due to the important error bar on $\{K'\bar{K}\}_\zeta$.

3.5. Collapse of the Great Whirl

The physical processes at play in the GW demise are still debated, as noted in section 1 (internal instability, merging, interaction with the equatorial band, etc.). The GW is commonly observable for more than a month after the monsoonal winds switch off at the end of September. This is also the case in the REF simulation for which the GW can be tracked until the end of October (Figure 9).

At the end of September, the GW has started weakening; its size and intensity jointly decrease while it moves northward at speed $\sim$7kmd^{-1} (Figure 9) through advection by the SC, the interactions with surrounding eddies and the self-induced advection by interaction with the boundary (discussed in section 4.3). Its position is not limited by the zero wind curl line at this time as the Findlater jet is not active anymore during the FIM. The GW is also affected by an upwelling Rossby wave that reaches longitude 58°E and enters the GW influence area. It is noticeable in the Hovmöller diagram (Figures 7c and 7d) and signals concur between latitudes 7.5°N and 9.5°N [*Rao et al*., 2010]. Aviso data (Figures 7e and 7f) confirm the presence of this wave with very close timing and propagation speed, although amplitude is slightly reduced. At the beginning of October, this wave strengthens (Figures 8h and 8i, snapshot and zonal mean), imprinting a negative SSH anomaly shift to the entire zone, hence reducing the GW area and thus decreasing its radius. The propagation of this wave is closely observed in a 1993–2011 climatology of Aviso SSH anomaly in Figure 7c in *Beal et al*. [2013]. The characteristics of the GW show this loss of energy is through the damping of vorticity and the decrease of both the radius and the SSH anomaly. The upwelling triggered by this wave acts in favor of a shallowing of the eddy (Figure 10a). The Ekman depth does not evolve much and stays at the level it had at the end of the SWM, reflecting the inability of the wind to explain the eddy vertical extension at this stage. At the end of October, the Rossby wave has imposed a shift of roughly -5cm in SSH to the whole area (zonal means in Figures 8g–8i), which may contribute to the development of cyclonic eddies as seen on 25 October snapshot. The GW keeps shrinking and is not distinguishable after November for most of the years, in agreement with *Beal and Donohue* [2013].

Overall, our numerical solution suggests that the annual upwelling Rossby wave crossing the basin and reaching the coast during the FIM plays a crucial role in the GW collapse. We do not see in our model any sign of internal instability. The GW decays progressively toward the end of the SWM and somewhat more abruptly after the end of October, presumably under the influence of an upwelling Rossby wave. The weakening of the GW before the arrival of this wave is attributed to interactions with its highly turbulent environment which probably plays a role over the entire collapse period.

4. Local Versus Remote Forcing

We now further elaborate on the role of Rossby waves, local wind, and slanted coastline on the GW life cycle, especially on the generation and collapse mechanisms. We use the three sensitivity experiments presented in section 2.2 to isolate each of the effect.

AGU Journal of Geophysical Research: Oceans 10.1002/2014JC009857

As reviewed in section 1, there is no definite conclusion on the role of local (wind-induced eddy or current instability) and remote (planetary wave) forcing into the generation mechanisms. Before going into the results of the sensitivity experiments, we prior dismiss the possibility that parallel flow instabilities are implicated in the generation. When the GW is generated, there is no evidence in the model for a well-defined energetic current that could destabilize baroclinically. In fact, the SC starts to flow northward when the monsoonal winds start blowing, more than a month after the GW generation. We thus exclude baroclinic instability for the GW generation mechanism. This is consistent with *Smith* [2007] and *Tulloch et al.* [2011] who demonstrated that low-latitude flows are poorly inclined to baroclinic instability. Scaling analysis for the lateral shear maximum U''_{max} of the SC at 5°N at the end of May (during the generation stage of the GW) gives $U''_{max} \sim 5 \times 10^{-12} m^{-1} s^{-1}$ while the β-effect modulated by the current orientation is $\beta \cos\phi = 1.5 \times 10^{-11} m^{-1} s^{-1}$, where $\phi \sim 45°$ is the angle between the current and the zonal direction. This indicates that the SC does not undergo a change of sign of $\beta \cos\phi - U''$. As such, the Rayleigh-Kuo inflection point criterion is not satisfied [e.g., *Vallis*, 2006] and the SC is not barotropically unstable at this time.

4.1. The NO-RW Experiment

The typical GW evolution in the NO-RW experiment is illustrated in Figures 13a–13f, again for year 8. On 15 April, we observe the blocking of the Rossby wave at the artificial wall, leaving a smoother SSH field on the western side in comparison with the REF simulation. At the beginning of July, 1 month after the onset of the monsoon, the anticyclonic structure that will evolve into the GW (Figure 13b, 5 July) has a shape resembling that for REF between 15 April and 25 May (Figures 8a and 8b). Therefore, the GW onset is delayed by approximately 2 months when Rossby waves are shut off. Statistically, the positive SSH anomaly gets its circular shape and starts swirling only around 15 June onward; we therefore calculate statistics for the NO-RW experiment from this date onward in Figure 9. This eddy is enhanced in its anticyclonic swirl (Figure 9e) by the wind curl, which provides negative vorticity throughout the SWM. During the following month, this anomaly strengthens and has roughly the same characteristics as in the REF simulation, albeit with a lag of 1–2 months in the GW life cycle (the lag slightly decreases as the season goes on).

During the growing phase, the position of the GW is also shifted ~250 km to the southeast compared to REF. For this reason, we can unambiguously attribute the settlement of the GW at its characteristic position to the Rossby wave arrival at the coast. As a matter of fact, this phase-locking is absent in the NO-RW experiment, which explains the discrepancies. This is another argument in favor of the importance of this signal for the growth of the GW [supported by satellite observations of *Beal and Donohue*, 2013] against a wind-induced generation of the eddy.

A more general observation concerns the standard deviations of all the characteristics of the GW that are noticeably decreased in the NO-RW experiment compared to the REF simulation. As this simulation is to first order only forced by the wind west of the frontier, the fate of the GW is more deterministic, isolated from remotely forced signals which could perturb its life cycle. As a consequence, it keeps growing much longer than in REF. This is observed in the SSH anomaly and radius evolution (Figures 9c and 9d) that increase continuously under the influence of the wind without any merging or modulation by other signals. The vorticity is also higher and less variable than in REF as it is only forced by the local negative wind curl (this is likely linked with the slowly varying forcing [1 month of temporal resolution] and accounting for atmospheric synoptic variability could lead to smaller temporal scales in the ocean variability [*Desbiolles et al.*, 2014]) (Figure 9e). As standard deviations in the time series account for the interannual variability (deviation from the climatological mean), we attribute a strong part of year-to-year variability of the GW to the Rossby waves.

The GW collapse is also observed later because the eddy is not perturbed by the incoming upwelling Rossby wave emerging from the east of the basin. It should be noted that the blocking of this wave appears to be only partial (Figures 13e–13f), but it delays and strongly reduces the amplitude of the wave. The GW is still observable on snapshot 5 November and eventually disappears 20–30 days later than in REF. Furthermore, Figures 9c, 9d, and 9e demonstrate that the GW in NO-RW is stronger than in REF during its last month of existence (i.e., October). This behavior confirms that Rossby wave dynamics have a major impact on the GW collapse.

4.2. The NO-WIND Experiment

This experiment shows reduced interannual variability and a less intense coastal forcing, promoting a more linear response of the ocean over a wide area. The basic scenario is displayed in Figures 13g–13i. The

AGU Journal of Geophysical Research: Oceans 10.1002/2014JC009857

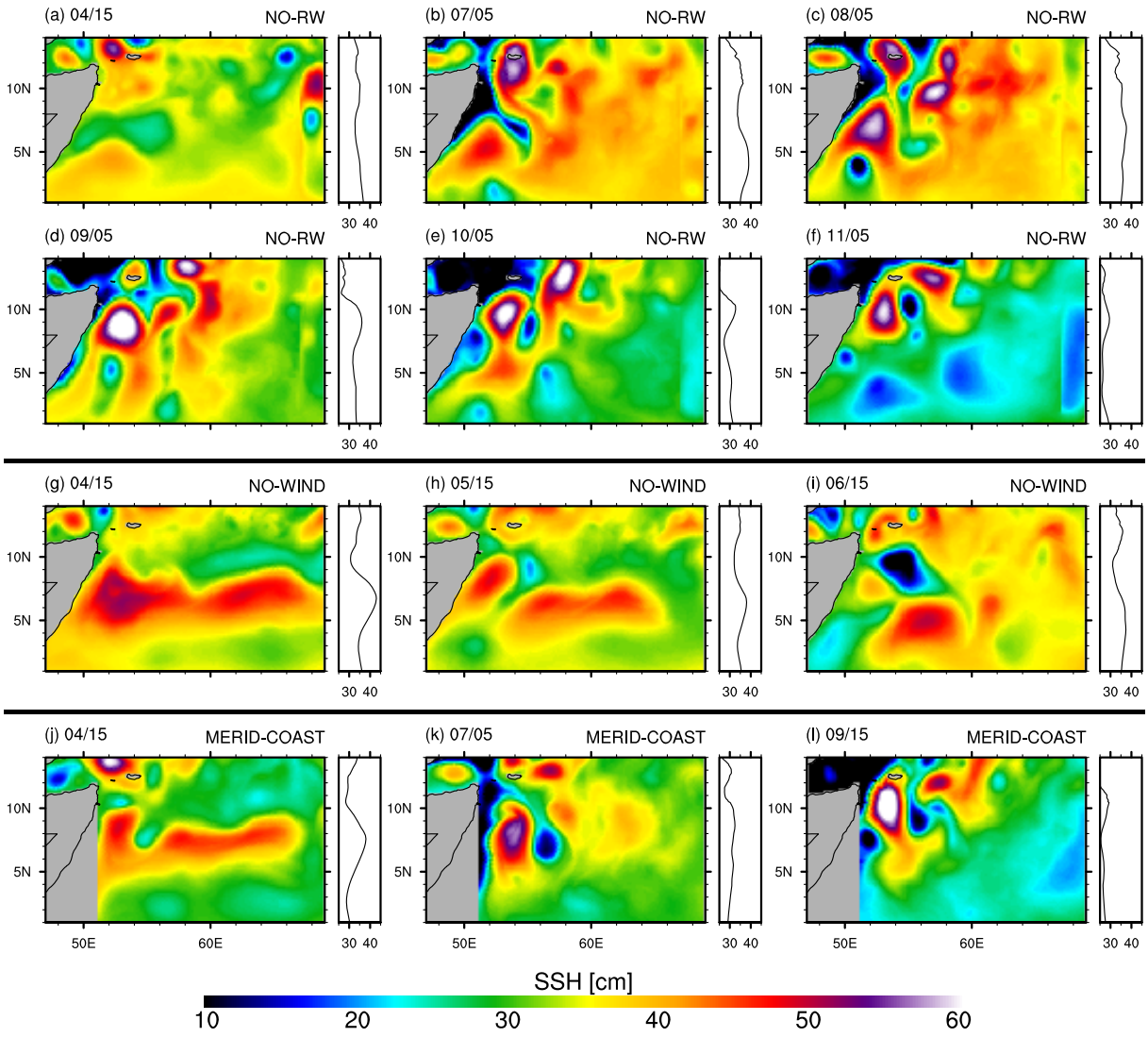

Figure 13. Same as Figure 8 but for experiments (a–f) NO-RW, (g–i) NO-WIND, and (j–l) MERID-COAST.

Rossby wave signal, identified through a local maximum of SSH, reaches the coast between the end of March and the beginning of April, before swirling anticyclonically close to the coast to become the GW. Until mid-April, there is no qualitative difference between the REF and NO-WIND mean ocean states. General patterns of the snapshot on 15 April (Figures 8a and 13g) are very similar. Differences occur after mid-May as the wind is damped sufficiently. The enhancement of the Rossby wave by the wind does not occur and the signal gradually attenuates until reaching the coast. Therefore, we observe a decrease in the GW intensity before its rapid disappearance among other ephemeral small eddying patterns. This highlights the role of the local winds as a source of negative vorticity driving the evolution of the GW and in particular its growth. Incidentally, statistics cannot easily be computed for the more diffuse shape of the GW (as done for REF and NO-RW, see Figure 9). The strong negative SSH anomaly visible on 15 June (Figure 13i) is the consequence of the wind damping which occurs a 100 km offshore of this anomaly. In this situation, the cyclone is reinforced by the positive wind curl artificially induced by the damping.

4.3. The MERID-COAST Experiment

Once generated and stabilized by the monsoonal winds, the GW remains quasi-stationary during more than 3 months. This temporal and geographical steadiness is unusual and does not occur in the open ocean as

AGU Journal of Geophysical Research: Oceans 10.1002/2014JC009857

the longest satellite-tracked eddies always move westward [*Chelton et al*., 2007]. The local geomorphology with the almost 45°-oriented coastline could influence the eddy drift as modeled by *McCreary and Kundu* [1988] in a very simplified numerical setup.

Eddy drift is determined by several processes: (i) the westward dominated drift at the long Rossby wave speed βR_d^2, modulated by an equatorward (resp. poleward) deflection for anticyclones (resp. cyclones) [*Morrow et al*., 2004]; (ii) advection by the mean currents; (iii) interactions with surrounding eddies [e.g., *Carton*, 2001], and (iv) self-induced advection by interaction with a boundary in the vicinity of a coast [e.g., *Carton et al*., 2013]. The GW is subject to all of these processes and the slant of the coast relative to the meridional direction primarily affects (i) and (iv). The MERID-COAST experiment is designed to assess the relative importance of this slanted coastline.

Figure 9a shows the climatological latitude of the GW in the MERID-COAST experiment. Longitude is not presented because it is overly affected by the coastline modification and therefore not comparable with the other experiments. The GW position is shifted to the north by approximately 1.5° from the REF experiment but undergoes the same northward translation from August onward. The Rossby wave reaches the coast further north than in REF, thus also settling the GW position northward. However, it obviously does not affect the fate of the eddy drift. Hence, we conclude that the slanted coastline has a limited impact on the GW drift.

Interestingly, MERID-COAST confirms that until the end of the monsoonal winds in early September, the northern flank of the GW cannot cross the zero wind curl line. Therefore, this certainly accounts for the steadiness of the GW position during the monsoon, regardless of fluctuations attributed to eddy-eddy interactions. After the end of the monsoon, the GW is more isolated and its northward drift is more likely due to a combination of advection by the SC and self-advection of the eddy by interacting with the boundary; (ii) and (iv) becoming the dominant processes among those enumerated in the preceding paragraph.

5. Summary

In this paper, we presented a ROMS regional simulation of the Arabian Sea circulation, climatologically forced at a horizontal resolution allowing for an adequate representation of mesoscale dynamics. After approximately 2 years, the model reaches statistical equilibrium and exhibits a marked interannual variability of intrinsic origin. Overall, the characteristic seasonality of the regional dynamics due to monsoonal winds in the Indian Ocean is well represented in the model. This therefore gives us confidence in the model for use to investigate the southwest monsoon dynamics, particularly its dominant mesoscale structure, the GW.

We precisely characterize the life cycle of the GW. We confirm the preconditioning effect of an annual downwelling Rossby wave. This wave exerts a major influence on the GW initial phase (location and timing of initiation), as suggested by *McCreary et al*. [1993] and observed by *Beal and Donohue* [2013]. The roles of the strong wind stress and anticyclonic wind stress curl remain crucial to explain the maintenance and the barotropization of the eddy. In fact, we found that although the strong Ekman pumping can explain the deepening of the eddy during the early stage of the monsoon, nonlinear kinetic energy transfer from the baroclinic flow to the barotropic flow may come into play to redistribute the input of surface energy by the wind stress curl into the deeper layers. The sudden shallowing of the GW at the end of its life cycle is compatible with the arrival of an upwelling Rossby wave. Nonetheless, this diagnostic of kinetic energy transfer appeared to be difficult to interpret in terms of water mass exchanges as proposed by *Wiin-Nielsen* [1962] and *Haney et al*. [2001] and investigation on the GW deepening is not closed.

An examination of the different terms constituting the cyclostrophic balance reveals that inertia is important for the GW dynamical structure, reaching 30% of the geostrophic terms.

The GW sits in a very turbulent western boundary upwelling region and detaches cyclones from the northern cold filament of upwelled water that circles it. Cyclones move around it and interact, leading to intraseasonal and interannual variability in its position. After the shutoff of the monsoonal winds, the GW starts to shrink during the FIM when the EKE is found to be at its peak, revealing a strongly turbulent environment. It is then mainly influenced by its interaction with surrounding eddies and the coast and self-induced advection by interaction with the boundary, causing it to drift northward. The arrival of an annual upwelling

AGU Journal of Geophysical Research: Oceans 10.1002/2014JC009857

Rossby wave at the end of October causes the collapse of the GW, which then dramatically shrinks and finally disappears.

A parallel could be made with the Loop Current Eddies where a dominant anticyclone dominates a turbulent environment made of smaller cyclones. As in the study of *Chérubin et al*. [2006], we suggest that the stability of the GW and its interaction with surrounding eddies could be studied by taking into account its baroclinic structure.

Sensitivity tests confirm the importance of Rossby waves to pace the GW life cycle. When Rossby waves are shut off, the GW onset is delayed by almost 2 months and its position is shifted by ∼250 km southward. The GW collapse is also delayed by approximately 1 month. The role of these waves has been generally underestimated in comparison to the role of local high winds. However, their importance in interacting with eddies is not that surprising since *Polito and Liu* [2003] qualified the annual and semiannual Rossby waves are among the most energetic of the planetary waves. However, when the wind is shut off, the GW disappears rapidly after its onset. This also confirms the crucial importance of the wind stress and wind stress curl to energetize the GW. Finally, the role of the slanted coastline is found to be negligible in the GW drift as the eddy gradually undergoes the same northward translation as modeled in the reference experiment.

Acknowledgments
The authors are grateful to A. Colin de Verdière (LPO, UBO) for the instructive comment on the wave-driven dynamical adjustment to the monsoon onset. All data set used in this work were downloaded from the internet addresses mentioned in Table 1. Simulations were performed on the computing center Caparmor at Ifremer. CV is supported by the Direction Générale de l'Armement (DGA) and the Région Bretagne in the form of a PhD scholarship. This study is a contribution to the French ANR Synbios. The authors also acknowledge Matthew Thomas (LPO, Ifremer) for his comments and corrections and two anonymous reviewers for their thorough remarks.

References

Anderson, D. L., and A. Gill (1975), Spin-up of a stratified ocean, with applications to upwelling, *Deep Sea Res. Oceanogr. Abstr.*, *22*(9), 583–596.
Antonov, J., D. Seidov, T. Boyer, R. Locarnini, A. Mishonov, H. Garcia, O. Baranova, M. Zweng, and D. Johnson (2010), *World Ocean Atlas 2009,* vol. 2, *Salinity*, *NOAA Atlas NESDIS 69*, U.S. Gov. Printing Office, Washington, D. C.
Beal, L., and K. Donohue (2013), The Great Whirl: Observations of its seasonal development and interannual variability, *J. Geophys. Res. Oceans*, *118*, 1–13, doi:10.1029/2012JC008198.
Beal, L., V. Hormann, R. Lumpkin, and G. Foltz (2013), The response of the surface circulation of the Arabian Sea to monsoonal forcing, *J. Phys. Oceanogr.*, *43*(9), 2008–2022, doi:10.1175/JPO-D-13-033.1.
Bower, A. S., H. D. Hunt, and J. F. Price (2000), Character and dynamics of the Red Sea and Persian Gulf outflows, *J. Geophys. Res.*, *105*(C3), 6387–6414, doi:10.1029/1999JC900297.
Brandt, P., L. Stramma, F. Schott, J. Fischer, M. Dengler, and D. Quadfasel (2002), Annual Rossby waves in the Arabian Sea from TOPEX/POSEIDON altimeter and in situ data, *Deep Sea Res., Part II*, *49*(7), 1197–1210, doi:10.1016/S0967-0645(01)00166-7.
Bruce, J. (1983), The wind field in the western Indian Ocean and the related ocean circulation, *Mon. Weather Rev.*, *111*(7), 1442–1452.
Cane, M. A., and P. R. Gent (1984), Reflection of low-frequency equatorial waves at arbitrary western boundaries, *J. Mar. Res.*, *42*(3), 487–502.
Capet, X., F. Colas, J. McWilliams, P. Penven, and P. Marchesiello (2008), Eddies in eastern boundary subtropical upwelling systems, in *Ocean Modeling in an Eddying Regime*, edited by M. W. Hecht and H. Hasumi, pp. 131–147, AGU, Washington, D. C., doi:10.1029/177GM10.
Carton, J., G. Chepurin, X. Cao, and B. Giese (2000), A simple ocean data assimilation analysis of the global upper ocean 1950-95. Part I: Methodology, *J. Phys. Oceanogr.*, *30*(2), 294–309.
Carton, X. (2001), Hydrodynamical modeling of oceanic vortices, *Surv. Geophys.*, *22*(3), 179–263, doi:10.1023/A:1013779219578.
Carton, X., B. Le Cann, A. Serpette, and J. Dubert (2013), Interactions of surface and deep anticyclonic eddies in the Bay of Biscay, *J. Mar. Syst.*, *109*, S45–S59.
Chelton, D., R. DeSzoeke, M. Schlax, K. El Naggar, and N. Siwertz (1998), Geographical variability of the first baroclinic Rossby radius of deformation, *J. Phys. Oceanogr.*, *28*(3), 433–460.
Chelton, D., M. Schlax, M. Freilich, and R. Milliff (2004), Satellite measurements reveal persistent small-scale features in ocean winds, *Science*, *303*(5660), 978–983, doi:10.1126/science.1091901.
Chelton, D. B., M. G. Schlax, R. M. Samelson, and R. A. de Szoeke (2007), Global observations of large oceanic eddies, *Geophys. Res. Lett.*, *34*, L15606, doi:10.1029/2007GL030812.
Chérubin, L. M., Y. Morel, and E. P. Chassignet (2006), Loop Current ring shedding: The formation of cyclones and the effect of topography, *J. Phys. Oceanogr.*, *36*(4), 569–591, doi:10.1175/JPO2871.1.
Desbiolles, F., B. Blanke, and A. Bentamy (2014), Short-term upwelling events at the western African coast related to synoptic atmospheric structures as derived from satellite observations, *J. Geophys. Res. Oceans*, *119*, 461–483, doi:10.1002/2013JC009278.
Ducet, N., P.-Y. Le Traon, and G. Reverdin (2000), Global high-resolution mapping of ocean circulation from TOPEX/Poseidon and ERS-1 and-2, *J. Geophys. Res.*, *105*(C8), 19,477–19,498, doi:10.1029/2000JC900063.
Findlater, J. (1969), A major low-level air current near the Indian Ocean during the northern summer, *Q. J. R. Meteorol. Soc.*, *95*(404), 362–380, doi:10.1002/qj.49709540409.
Fischer, J., F. Schott, and L. Stramma (1996), Currents and transports of the Great Whirl-Socotra Gyre system during the summer monsoon, August 1993, *J. Geophys. Res.*, *101*(C2), 3573–3587, doi:10.1029/95JC03617.
Fratantoni, D. M. (2001), North Atlantic surface circulation during the 1990's observed with satellite-tracked drifters, *J. Geophys. Res.*, *106*(C10), 22,067–22,093.
Haidvogel, D. B., and A. Beckmann (1999), *Numerical Ocean Circulation Modeling*, vol. 344, Imp. Coll. Press, London, U. K.
Haney, R. L., R. A. Hale, and D. E. Dietrich (2001), Offshore propagation of eddy kinetic energy in the California Current, *J. Geophys. Res.*, *106*(C6), 11,709–11,717.
Hastenrath, S., and L. Greischar (1991), The monsoonal current regimes of the tropical Indian Ocean: Observed surface flow fields and their geostrophic and wind-driven components, *J. Geophys. Res.*, *96*(C7), 12,619–12,633, doi:10.1029/91JC00997.
Hughes, C. W., and C. Wilson (2008), Wind work on the geostrophic ocean circulation: An observational study of the effect of small scales in the wind stress, *J. Geophys. Res.*, *113*, C02016, doi:10.1029/2007JC004371.
Jensen, T. G. (1993), Equatorial variability and resonance in a wind-driven Indian Ocean model, *J. Geophys. Res.*, *98*(C12), 22,533–22,552, doi:10.1029/93JC02565.

AGU Journal of Geophysical Research: Oceans 10.1002/2014JC009857

Kelly, K. A., R. C. Beardsley, R. Limeburner, K. H. Brink, J. D. Paduan, and T. K. Chereskin (1998), Variability of the near-surface eddy kinetic energy in the California Current based on altimetric, drifter, and moored current data, *J. Geophys. Res.*, *103*(C6), 13,067–13,083.

Kim, H.-S., C. N. Flagg, and S. D. Howden (2001), Northern Arabian Sea variability from TOPEX/POSEIDON altimetry data: An extension of the US JGOFS/ONR shipboard ADCP study, *Deep Sea Res., Part II*, *48*(6), 1069–1096, doi:10.1016/S0967-0645(00)00131-4.

Large, W., J. McWilliams, and S. Doney (1994), Oceanic vertical mixing: A review and a model with a nonlocal boundary layer parameterization, *Rev. Geophys.*, *32*(4), 363–403, doi:10.1029/94RG01872.

Lee, C., B. Jones, K. Brink, and A. Fischer (2000), The upper-ocean response to monsoonal forcing in the Arabian Sea: Seasonal and spatial variability, *Deep Sea Res., Part II*, *47*(7), 1177–1226, doi:10.1016/S0967-0645(99)00141-1.

Leetmaa, A., D. Quadfasel, and D. Wilson (1982), Development of the flow field during the onset of the Somali Current, 1979, *J. Phys. Oceanogr.*, *12*(12), 1325–1342.

Lemarié, F., J. Kurian, A. F. Shchepetkin, M. Jeroen Molemaker, F. Colas, and J. C. McWilliams (2012), Are there inescapable issues prohibiting the use of terrain-following coordinates in climate models?, *Ocean Modell.*, *42*, 57–79.

Lighthill, M. J. (1969), Dynamic response of the Indian Ocean to onset of the southwest monsoon, *Philos. Trans. R. Soc. London A*, *265*(1159), 45–92, doi:10.1098/rsta.1969.0040.

Locarnini, R., A. Mishonov, J. Antonov, T. Boyer, H. Garcia, O. Baranova, M. Zweng, and D. Johnson (2010), *World Ocean Atlas 2009,* vol. 1, *Temperature*, U.S. Gov. Print. Off., Washington, D. C.

Lumpkin, R., and G. C. Johnson (2013), Global ocean surface velocities from drifters: Mean, variance, El Nino–Southern Oscillation response, and seasonal cycle, *J. Geophys. Res. Oceans*, *118*, 2992–3006, doi:10.1002/jgrc.20210.

Luther, M. E., and J. J. O'Brien (1989), Modelling the variability in the Somali Current, in *Mesoscale/Synoptic Coherent Structures in Geophysical Turbulence*, pp. 373–386, Elsevier, Amsterdam.

Marchesiello, P., J. McWilliams, and A. Shchepetkin (2003), Equilibrium structure and dynamics of the California Current System, *J. Phys. Oceanogr.*, *33*(4), 753–783.

Marchesiello, P., L. Debreu, and X. Couvelard (2009), Spurious diapycnal mixing in terrain-following coordinate models: The problem and a solution, *Ocean Modell.*, *26*(3), 156–169, doi:10.1016/j.ocemod.2008.09.004.

Mason, E., F. Colas, J. Molemaker, A. F. Shchepetkin, C. Troupin, J. C. McWilliams, and P. Sangrà (2011), Seasonal variability of the Canary Current: A numerical study, *J. Geophys. Res.*, *116*, C06001, doi:10.1029/2010JC006665.

Maximenko, N., and P. Niiler (2006), Mean surface circulation of the global ocean inferred from satellite altimeter and drifter data, paper presented at Symposium on 15 Years of Progress in Radar Altimetry, European Space Agency Spec. Publ., ESA Publication Division, Noordwijk, Netherlands.

McCreary, J., and P. Kundu (1988), A numerical investigation of the Somali Current during the Southwest Monsoon, *J. Mar. Res.*, *46*(1), 25–58, doi:10.1357/002224088785113711.

McCreary, J., P. Kundu, and R. Molinari (1993), A numerical investigation of dynamics, thermodynamics and mixed-layer processes in the Indian Ocean, *Prog. Oceanogr.*, *31*(3), 181–244, doi:10.1016/0079-6611(93)90002-U.

Morrow, R., F. Birol, D. Griffin, and J. Sudre (2004), Divergent pathways of cyclonic and anti-cyclonic ocean eddies, *Geophys. Res. Lett.*, *31*, L24311, doi:10.1029/2004GL020974.

Penduff, T., M. Juza, B. Barnier, J. Zika, W. K. Dewar, A.-M. Treguier, J.-M. Molines, and N. Audiffren (2011), Sea level expression of intrinsic and forced ocean variabilities at interannual time scales, *J. Clim.*, *24*(21), 5652–5670.

Penven, P., V. Echevin, J. Pasapera, F. Colas, and J. Tam (2005), Average circulation, seasonal cycle, and mesoscale dynamics of the Peru Current System: A modeling approach, *J. Geophys. Res.*, *110*, C10021, doi:10.1029/2005JC002945.

Penven, P., I. Halo, S. Pous, and L. Marié (2014), Cyclogeostrophic balance in the Mozambique Channel, *J. Geophys. Res. Oceans*, *119*, 1054–1067, doi:10.1002/2013JC009528.

Polito, P. S., and W. T. Liu (2003), Global characterization of Rossby waves at several spectral bands, *J. Geophys. Res.*, *108*(C1), 3018, doi:10.1029/2000JC000607.

Rao, R., G. Kumar, M. Ravichandran, A. Rao, V. Gopalakrishna, and P. Thadathil (2010), Interannual variability of Kelvin wave propagation in the wave guides of the equatorial Indian Ocean, the coastal Bay of Bengal and the southeastern Arabian Sea during 1993–2006, *Deep Sea Res., Part I*, *57*(1), 1–13, doi:10.1016/j.dsr.2009.10.008.

Resplandy, L., M. Lévy, G. Madec, S. Pous, O. Aumont, and D. Kumar (2011), Contribution of mesoscale processes to nutrient budgets in the Arabian Sea, *J. Geophys. Res.*, *116*, C11007, doi:10.1029/2011JC007006.

Rhines, P. B. (1979), Geostrophic turbulence, *Annu. Rev. Fluid Mech.*, *11*(1), 401–441.

Rio, M., and F. Hernandez (2004), A mean dynamic topography computed over the world ocean from altimetry, in situ measurements, and a geoid model, *J. Geophys. Res*, *109*, C12032, doi:10.1029/2003JC002226.

Risien, C., and D. Chelton (2008), A global climatology of surface wind and wind stress fields from eight years of QuikSCAT scatterometer data, *J. Phys. Oceanogr.*, *38*(11), 2379–2413, doi:10.1175/2008JPO3881.1.

Roquet, F., C. Wunsch, and G. Madec (2011), On the patterns of wind-power input to the ocean circulation, *J. Phys. Oceanogr.*, *41*(12), 2328–2342.

Schott, F. (1983), Monsoon response of the Somali Current and associated upwelling, *Prog. Oceanogr.*, *12*(3), 357–381, doi:10.1016/0079-6611(83)90014-9.

Schott, F., and J. McCreary (2001), The monsoon circulation of the Indian Ocean, *Prog. Oceanogr.*, *51*(1), 1–123, doi:10.1016/S0079-6611(01)00083-0.

Schott, F., and D. R. Quadfasel (1982), Variability of the Somali Current system during the onset of the southwest monsoon, 1979, *J. Phys. Oceanogr.*, *12*(12), 1343–1357.

Schott, F., J. C. Swallow, and M. Fieux (1990), The Somali Current at the equator: Annual cycle of currents and transports in the upper 1000 m and connection to neighbouring latitudes, *Deep Sea Res., Part A*, *37*(12), 1825–1848, doi:10.1016/0198-0149(90)90080-F.

Schott, F. A., S.-P. Xie, and J. P. McCreary (2009), Indian ocean circulation and climate variability, *Rev. Geophys.*, *47*(1), doi:10.1029/2007RG000245.

Shchepetkin, A., and J. McWilliams (2005), The regional oceanic modeling system (roms): A split-explicit, free-surface, topography-following-coordinate oceanic model, *Ocean Modell.*, *9*(4), 347–404, doi:10.1016/j.ocemod.2004.08.002.

Shetye, S., A. Gouveia, and S. Shenoi (1994), Circulation and water masses of the Arabian Sea, *J. Earth Syst. Sci.*, *103*(2), 107–123, doi:10.1007/BF02839532.

Shi, W., J. M. Morrison, E. Böhm, and V. Manghnani (2000), The Oman upwelling zone during 1993, 1994 and 1995, *Deep Sea Res., Part II*, *47*(7), 1227–1247, doi:10.1016/S0967-0645(99)00142-3.

AGU Journal of Geophysical Research: Oceans 10.1002/2014JC009857

Smith, K. S. (2007), The geography of linear baroclinic instability in Earth's oceans, *J. Mar. Res.*, *65*(5), 655–683, doi:10.1357/002224007783649484.

Smith, W., and D. Sandwell (1997), Global sea floor topography from satellite altimetry and ship depth soundings, *Science*, *277*(5334), 1956–1962, doi:10.1126/science.277.5334.1956.

Stark, J. D., C. J. Donlon, M. J. Martin, and M. E. McCulloch (2007), OSTIA: An operational, high resolution, real time, global sea surface temperature analysis system, in *OCEANS 2007-Europe*, pp. 1–4, Proceedings of Oceans '07 IEEE Conference, 'Marine Challenges: Coastline to Deep Sea', 18–21 June, Aberdeen, U. K.

Subrahmanyam, B., I. Robinson, J. Blundell, and P. Challenor (2001), Indian Ocean Rossby waves observed in TOPEX/POSEIDON altimeter data and in model simulations, *Int. J. Remote Sens.*, *22*(1), 141–167, doi:10.1080/014311601750038893.

Tulloch, R., J. Marshall, C. Hill, and K. S. Smith (2011), Scales, growth rates, and spectral fluxes of baroclinic instability in the ocean, *J. Phys. Oceanogr.*, *41*(6), 1057–1076.

Vallis, G. K. (2006), *Atmospheric and Oceanic Fluid Dynamics: Fundamentals and Large-Scale Circulation*, Cambridge Univ. Press, Cambridge, U. K.

Vecchi, G., S. Xie, and A. Fischer (2004), Ocean-atmosphere covariability in the western Arabian Sea, *J. Clim.*, *17*(6), 1213–1224.

Wiin-Nielsen, A. (1962), On transformation of kinetic energy between the vertical shear flow and the vertical mean flow in the atmosphere, *Mon. Weather Rev*, *90*(8), 311–323.

Wirth, A., J. Willebrand, and F. Schott (2002), Variability of the Great Whirl from observations and models, *Deep Sea Res., Part II*, *49*(7), 1279–1295, doi:10.1016/S0967-0645(01)00165-5.

Worley, S., S. Woodruff, R. Reynolds, S. Lubker, and N. Lott (2005), ICOADS release 2.1 data and products, *Int. J. Climatol.*, *25*(7), 823–842, doi:10.1002/joc.1166.

Chapter 4

On the Fate of the Persian Gulf Outflow

Contents

4.1 Introduction

In many marginal seas[1], atmospheric conditions favor the formation of dense waters, either due to an excess of evaporation over precipitation or due to strong cooling. Dense water outflows are an important part of the climate system as they are a mean to export heat, salt, chemical and biological tracers in open oceans, thus to join the general circulation. Consequently, the fate of outflows near the straits where strong mixing occurs, and far from the strait where eddies often form, has been an important subject of investigation for decades. For instance, the Gravity Current Entrainment Climate Process Team, established by the U.S. Climate Variability and Predictability (CLIVAR) Program, had the goal to improve the parameterization of outflows in general circulation models (Legg et al., 2009).

The Mediterranean outflow has been the most studied outflow. The first Mediterranean water eddy (Meddy) was sampled in the 1970's (McDowell and Rossby, 1978). Since then, some generation mechanisms for these lenses have been discussed (see Section 1.2.2). Figure 4.1, taken from the Woods Hole 1997 summer school report illustrates the *mechanism of Meddy formation*. The arrow going from the Mediterranean Sea to the Atlantic, is surrounded by wiggling lines evoking turbulent processes. It summarizes how complex the mechanism of formation is, involving small scale processes such as mixing, entrainment and convection. All these processes occur at depths making them difficult to sample.

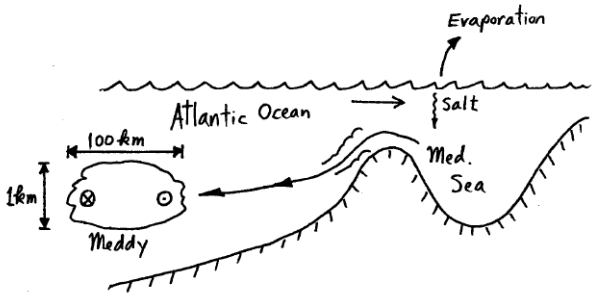

Figure 4.1: Cartoon from the Woods Hole Oceanographic Institution 1997 summer school report (Meacham, 1997). The original caption is "Mechanism of Meddy formation".

Two outflows spread in the Arabian Sea, from the Red Sea and the Persian Gulf. The Red Sea outflow has been more studied than the Persian Gulf outflow and recent findings converge towards a domination of stirring by surface intensified mesoscale eddies to explain the spreading of Red Sea Water (Bower et al., 2002; Ilıcak et al., 2011; Bower and Furey, 2012). As discussed in Chapter 1, we expect a similar contribution of mesoscale eddies to spread Persian Gulf Water (PGW). This has been recently revealed by Argo

[1] *marginal* is used to contrast with major oceanic basins (Atlantic, Pacific and Indian Oceans).

floats (L'Hégaret et al., 2013). In the following article (Vic et al., 2015), we discuss the spreading of PGW. It involves a new process (not described in an outflow context) that is the interaction of eddy with topography leading to the generation of submesoscale coherent vortices (SCV, named following McWilliams, 1985) trapping PGW. This modelling work is inspired by the recent research on the interactions of flows with topography carried out at UCLA (Molemaker et al., 2015; Gula et al., 2015a,b, and ongoing work by Kaushik Srinivasan). Some idealized experiments isolate the eddy-topography interactions and would deserve further investigation. Namely, the shear instability involved in the formation of SCV is different whether a cyclone or an anticyclone impinges on the slope and details of the instability are not fully understood yet. Sensitivity of the SCV size and intensity to the resolution and sensitivity of the formation process to the slope angle would also require further investigation.

4.2 Article Published in Journal of Geophysical Research

AGU PUBLICATIONS

JGR

Journal of Geophysical Research: Oceans

RESEARCH ARTICLE
10.1002/2015JC011033

Key Points:
- Eddy-topography interactions produce submesoscale coherent vortices (SCVs)
- Background mesoscale eddies in the Gulf of Oman participate to the spreading of Persian Gulf Water
- PGW is spread by small-scale turbulence resulting from eddy-topography interactions

Correspondence to:
C. Vic,
clement.vic@univ-brest.fr

Citation:
Vic, C., G. Roullet, X. Capet, X. Carton, M. J. Molemaker, and J. Gula (2015), Eddy-topography interactions and the fate of the Persian Gulf Outflow, *J. Geophys. Res. Oceans*, *120*, 6700–6717, doi:10.1002/2015JC011033.

Received 8 JUN 2015
Accepted 15 SEP 2015
Accepted article online 21 SEP 2015
Published online 15 OCT 2015

Eddy-topography interactions and the fate of the Persian Gulf Outflow

C. Vic[1], G. Roullet[1], X. Capet[2], X. Carton[1], M. J. Molemaker[3], and J. Gula[1]

[1]Laboratoire de Physique des Océans, UMR 6523, CNRS/Ifremer/IRD/UBO, Brest, France, [2]IPSL/LOCEAN, UMR 7159, CNRS/UPMC/IRD/MNHN, Paris, France, [3]Department of Atmospheric and Oceanic Sciences, University of California, Los Angeles, California, USA

Abstract The Persian Gulf feeds a warm and salty outflow in the Gulf of Oman (northern Arabian Sea). The salt climatological distribution is relatively smooth in the Gulf of Oman, and the signature of a slope current carrying salty waters is difficult to distinguish hundreds of kilometers past the Strait of Hormuz, in contrast to other outflows of the world ocean. This study focuses on the mechanisms involved in the spreading of Persian Gulf Water (PGW) in the Gulf of Oman, using a regional primitive equation numerical simulation. The authors show that the dispersion of PGW occurs through a regime that is distinct from, for example, the one responsible for the Mediterranean outflow dispersion. The background mesoscale eddy field is energetic and participates actively to the spreading of PGW. Remotely formed eddies propagate into the Gulf of Oman and interact with the topography, leading to submesoscales formation and PGW shedding. Eddy-topography interactions are isolated in idealized simulations and reveal the formation of intense frictional boundary layers, generating submesoscale coherent vortices (SCVs). Interactions take place at depths encompassing the PGW depth, thus SCVs trap PGW and contribute to its redistribution from the boundaries to the interior of the Gulf of Oman. The overall efficiency of these processes is confirmed by a strong contribution of eddy salt fluxes in the interior of the basin, and is quantified using particle statistics. It is found to be a highly dispersive regime, with an approximated eddy diffusivity of $\sim$1700 $m^2\ s^{-1}$.

1. Introduction

Dense water outflows are a major component of the Earth climate system. They deliver water masses into the global ocean, whose properties have been transformed in marginal seas. How these waters spread and mix is an important and delicate subject. It involves a series of processes over a wide range of scales that combine their effects in ways unique to each outflow (e.g., review of *Legg et al.* [2009]). While each outflow is different, broad categories can be distinguished. Three of the main outflows, the Mediterranean and Faroe Bank channel outflows and the Denmark Strait overflow, take place in regions with low background eddy activity. In addition, they have a relatively deep equilibrium depth (>600 m). In these deep and relatively quiescent environments, intrinsic instabilities of the outflows are a fundamental ingredient of their dispersal which takes place over hundreds or thousands of kilometers. An example is the spread of Mediterranean water by Meddies that are generated along the Iberian slope. This outflow regime has been the subject of numerous process studies in the past [e.g., *Griffiths*, 1986; *Price and O'Neil Baringer*, 1994; *Wirth*, 2009]. A different dynamical regime is to be expected when an external source of mesoscale turbulence is present and outflow waters can be passively stirred by mesoscale eddies.

Persian Gulf Water (PGW) is formed in the Persian Gulf and is delivered to the Gulf of Oman through the Strait of Hormuz (see the geographic setting in Figure 1). Initially, it has a large temperature (T) and salinity (S) signature [*Bower et al.*, 2000]. Gulf of Oman climatologies are characterized by subsurface T,S maxima at around 250 m depth where Gulf eddy energy is relatively high, and smooth horizontal T,S gradients around that depth [see *Carton et al.*, 2012, Appendix] and in particular the quasi absence of a T,S signature along the southern Gulf side where PGW would be transported within a continental slope current resulting from the gravitational adjustment of the outflow.

The Persian Gulf Outflow differs from most outflows that it equilibrates at a relatively shallow depth in an energetic environment (located at a western boundary). Figure 2 shows Eddy Available Potential Energy (EAPE) in the three outflow environments mentioned earlier and in the Gulf of Oman. EAPE has been shown

AGU Journal of Geophysical Research: Oceans 10.1002/2015JC011033

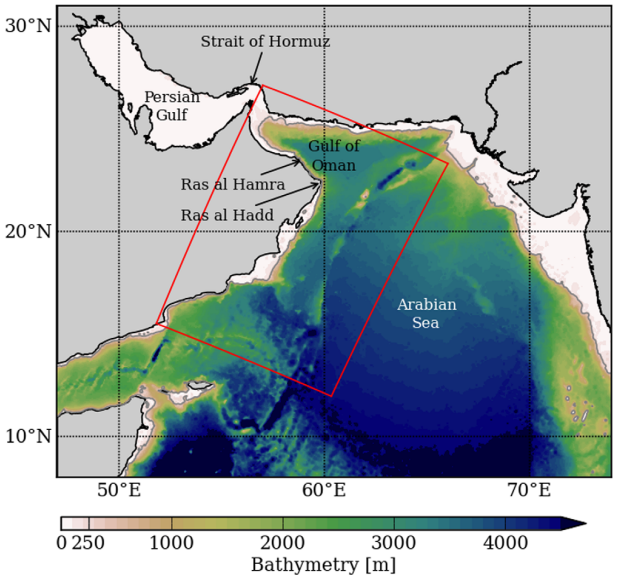

Figure 1. Bathymetry in the Arabian Sea and Persian Gulf derived from ETOPO2 [*Smith and Sandwell*, 1997]. The red rectangle represents the child domain. The parent domain encompasses the area covered by the map.

to be a good proxy to quantify the intensity of mesoscale turbulence in the ocean interior [*Roullet et al.*, 2014]. It reveals intense eddy activity in the Gulf of Oman around the PGW equilibrium depth (EAPE $\sim 800\,\mathrm{cm^2\,s^{-2}}$ corresponds to a mean current speed standard deviation, i.e., eddy mean speed, of $40\,\mathrm{cm\,s^{-1}}$) and confirms that the other outflow regions are quiescent in comparison. Similar to the spread of Red Sea Water in the Gulf of Aden [*Ilicak et al.*, 2011; *Bower and Furey*, 2012], background mesoscale activity may play an important role in the rapid dispersal of PGW in the Gulf of Oman. Although this has been partially observed in the latter region (using Argo floats in *L'Hégaret et al.* [2013]), the details of the dispersal phase are unknown.

Surface-intensified mesoscale eddies in the Gulf of Oman have a strong imprint until depths greater than the outflow equilibrium depth (circulation at 700 m depth is highly correlated with the surface circulation) [*Carton et al.*, 2012]. As such, outflow-eddy interactions are to be expected

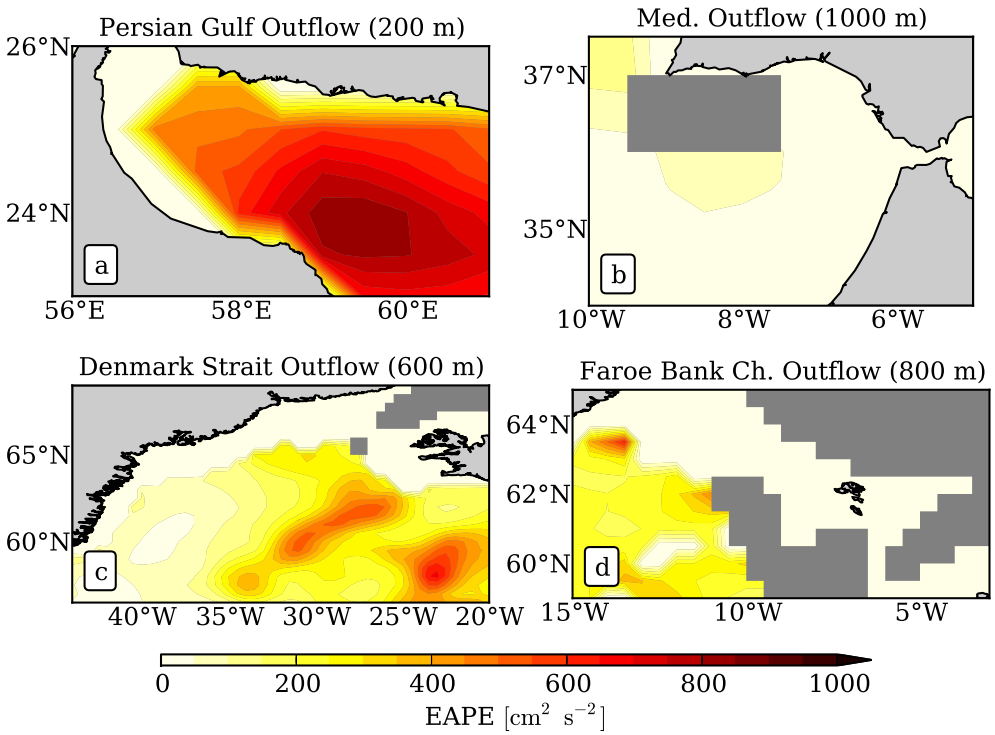

Figure 2. Eddy Available Potential Energy (EAPE) derived from Argo floats (data set described in *Roullet et al.* [2014]) in (a) the Persian Gulf Outflow environment at 200 m depth, (b) the Mediterranean Outflow environment at 1000 m depth, (c) the Denmark Strait Outflow environment at 600 m, and (d) the Faroe Bank Channel Outflow at 800 m. Depths are chosen to be the equilibrium depths of these outflows following *Price and O'Neil Baringer* [1994].

AGU Journal of Geophysical Research: Oceans 10.1002/2015JC011033

[*L'Hégaret et al*., 2013]. Moreover, the relative narrowness of the Gulf associated with the β-driven westward drift of eddies causes the latter to interact with the topography. Interactions of eddies with topography has received significant attention in idealized contexts. Simplest models with vertical walls as lateral boundaries are useful to study eddy drift, leakage, and decay. A richer variety of processes is present in models with a realistic geomorphology. Noticeably, eddy-topography interactions often produce smaller-scale vortices with an opposite polarity ("bursting" effect) [*Robinson*, 1991; *Akuetevi and Wirth*, 2015] and allow the generation of coastally trapped waves [e.g., *Sutyrin and Grimshaw*, 2010]. An inviscid well-known mechanism involved in the generation of a cyclone when a surface-intensified anticyclone encounters a shelf is the off-shelf advection of waters with high potential vorticity [*Frolov et al*., 2004; *Sutyrin and Grimshaw*, 2010]. The resulting eddy is also surface-intensified. In contrast, the viscous response at smaller scales implies the formation of a frictional bottom boundary layer, preferentially on the continental slope. It is found to be a preferred site for strong lateral shears to develop and shear instability to occur, hence generating subsurface vortices [*Oey and Zhang*, 2004; *Molemaker et al*., 2015]. We will see that frictional boundary layers play an important role in the dispersion of PGW.

In this study, we describe the spreading of dense PGW beyond the initial phase of gravitational equilibration and investigate the processes at play, using primitive equation numerical simulations. Our results suggest that PGW is efficiently transferred from the boundaries into the Gulf interior where it is rapidly stirred and mixed by mesoscale eddies. In this study, we show that the transfer from the boundaries is the result of submesoscale turbulent structures. Submesoscale turbulence is energized by the interaction of mesoscale eddies with the sloping sides of the Gulf (as opposed to internally generated by the outflow). Thus, both mesoscale and accompanying, frictionally generated, submesoscale eddies conspire to enhance PGW dispersion.

The outline of this paper is as follows. After presenting our investigation tools (section 2), we use the results of a realistic numerical experiment to get phenomenological insight in the dynamics (section 3). We find that PGW is often trapped into submesoscale coherent vortices and that the spread of PGW in the Gulf of Oman may be explained by the cross-Gulf transport of these structures. Idealized numerical experiments, in which the outflow is absent, are presented in section 4. They allow us to confirm that the outflow is not implicated in the formation of the submesoscale vortices. In contrast, they result from the detachment of frictional boundary layers that are found over the continental slope and are associated with mesoscale eddies. In section 5, we assess the efficiency of eddy-topography interactions in diffusing salinity in the Gulf of Oman using both Eulerian and Lagrangian perspectives. Main conclusions of this study are drawn in section 6.

2. Numerical Framework

We use the Regional Oceanic Modelling System (ROMS) [*Shchepetkin and McWilliams*, 2005] in two different configurations. In the following sections 2.1 and 2.2, we describe the setups used as well as interesting dynamical features in the realistic simulation.

2.1. Realistic Configuration

An off-line one-way nested configuration with a 2 km horizontal resolution is set up from a parent solution described in *Vic et al*. [2014] at 6.6 km resolution. The nesting approach follows the procedure of *Mason et al*. [2010]. The domain is shown in Figure 1. For consistency, the atmospheric forcing is monthly and climatological, identical to the data sets used to force the parent solution [*Vic et al*., 2014, Table 1]. We use the SCOW climatology of wind stress [*Risien and Chelton*, 2008] and the ICOADS climatology for heat and freshwater fluxes [*Worley et al*., 2005]. We changed the bathymetry data set from ETOPO2 [*Smith and Sandwell*, 1997] to the Shuttle Radar Topography Mission data set (SRTM30-plus) [*Becker et al*., 2009] for improved spatial resolution (30″ instead of 2′). Coordinate parameters and numerical operators are the same as in the parent solution, except for the tracer advection scheme whose diffusive part is rotated along isopycnals for a better conservation of tracer properties [*Lemarié et al*., 2012]. Open boundary conditions are extracted from the parent solution (years 3–6; the nested configuration was thus run for 4 years) except for the northwestern boundary, situated in the Strait of Hormuz (Figure 1). We carefully tuned the northwestern boundary conditions to have a realistic representation of the outflow properties (barely resolved in the parent solution) using an analytical boundary forcing based on moored Acoustic Doppler Current Profilers (ADCPs)

AGU Journal of Geophysical Research: Oceans 10.1002/2015JC011033

Table 1. Description of the Sensitivity Tests on Bottom Stress Parameterizations[a]

Type	C_D	$\langle\tau\rangle$ ($\times10^{-3}$ N m^{-2})	std(u_{bottom}) (cm s^{-1})
Linear	3.0×10^{-4} m s^{-1}	12.4	4.7
Linear	6.0×10^{-4} m s^{-1}	17.1 (+38%)	3.3 (−30%)
Quadratic	2.5×10^{-3}	8.7	5.1
Quadratic	5.0×10^{-3}	12.2 (+40%)	4.2 (−18%)
Quadratic with Von Karman C_D	Varying	7.9	5.1

[a] $\langle\tau\rangle$ is the temporally averaged bottom stress and std(u_{bottom}) is the standard deviation of the zonal velocity in the bottom layer (we only monitor u because eddy-topography interactions mainly arise in the zonal direction).

and temperature-salinity measurements in the Strait, including a seasonal cycle (measurements described in *Johns et al.* [2003]). This choice deliberately impedes the exploration of intermittent PGW outflow [*Banse*, 1997; *Thoppil and Hogan*, 2009]. We will see that high-frequency fluctuations in the outflow at the Hormuz Strait are not needed to produce a rich variability downstream.

Figure 3 compares Sea Surface Temperature (SST) and geostrophic EKE of observational data sets with the modeled solution. Although not an extensive evaluation, these comparisons confirm the models ability to produce realistic solutions. The SST snapshots (modeled and from the Moderate Resolution Imaging Spectroradiometer, MODIS) underline comparable variability throughout the domain and very similar frontal features from the coastal upwelling area (Arabian Peninsula) to the north of the domain. In the Gulf of Oman, the presence of a mesoscale eddy is characteristic of the observed dynamics [e.g., *Pous et al.*, 2004]. A warm bias is noticeable in the Persian Gulf [*Vic et al.*, 2014] but does not affect the nested simulation as the northwestern boundary is constructed directly from observational data. EKE is derived from the Absolute Dynamic Topography at 1/4° resolution from Aviso. It is found to be slightly higher (by 20% within the domain area) in ROMS although currents have been spatially filtered (Gaussian filtering at 35 km, following *Capet et al.* [2008]) to remove the energy contained in the submesoscale range that is absent in Aviso data.

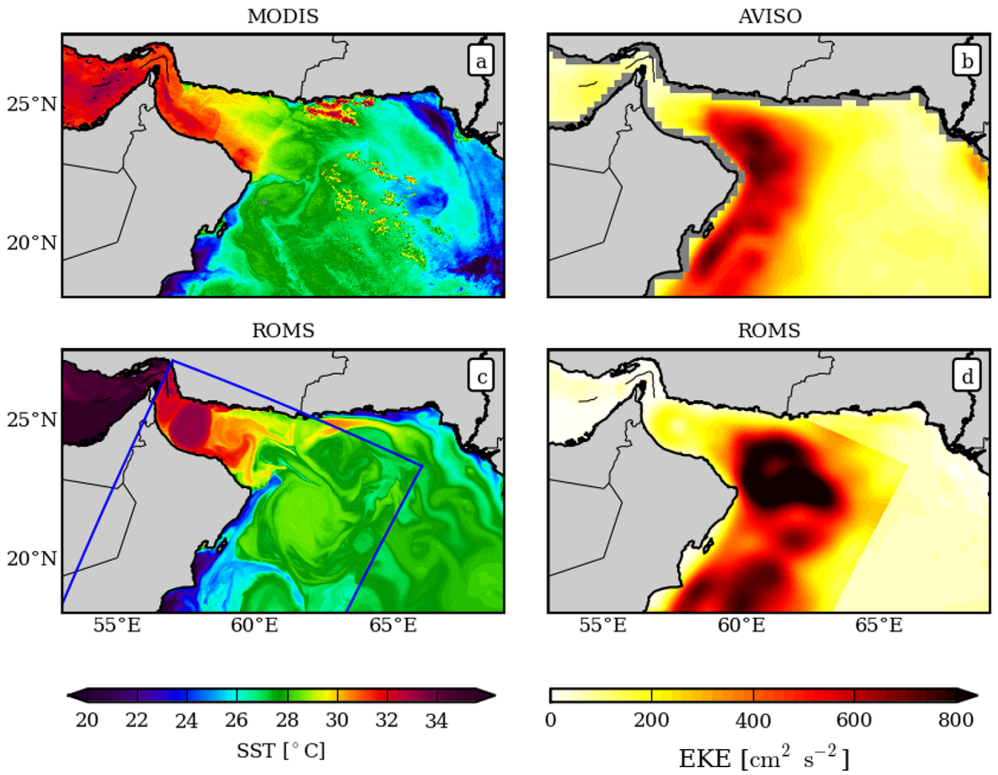

Figure 3. (left) Sea Surface Temperature (SST) from (a) MODIS and (c) the parent and nested (inside the blue rectangle) simulations at for the same period (September). (right) Surface Eddy Kinetic Energy (EKE) derived (b) from Aviso Absolute Dynamic Topography at 1/4° resolution and (c) from almost 4 years of simulation. Currents have been low-pass filtered using a Gaussian spatial filter with 35 km half width following *Capet et al.* [2008].

AGU Journal of Geophysical Research: Oceans 10.1002/2015JC011033

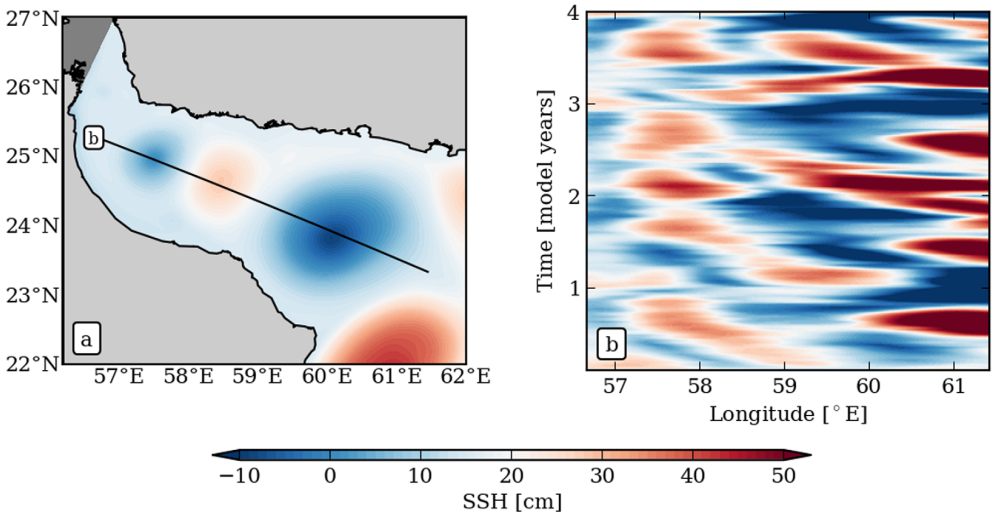

Figure 4. (a) Ten day average map of SSH in the model. (b) Hovmoller diagram of SSH through the 4 years of simulation along the track shown in Figure 4a.

Nonetheless, ranges of variability fit well and confirm that the northwestern Arabian Sea turbulent activity is energetic. The maximum of EKE is situated off Ras al Hadd and is seemingly associated with the seasonal Ras al Hadd jet and surrounding mesoscale eddies [*Böhm et al*., 1999]. The EKE reduction toward the end of the Gulf is due to the mesoscale eddy decay as they slowly progress westward as we shall see below.

Figure 4a shows Sea Surface Height (SSH) in the Gulf of Oman and reveals a typical situation with several mesoscale eddies present. Their polarity (cyclones and anticyclones are associated with SSH minima and maxima, respectively) alternates here but this is not always the case. Figure 4b reveals the origin of these eddies, coming from the northern Arabian Sea. Once they enter in the Gulf, they are trapped and invariably migrate westward as seen across paths of almost constant SSH. Eddy diameters (∼80−120 km) are similar to the full width of the Gulf. As such, the Gulf of Oman acts as an "eddy-guide" for their propagation (a similar situation is found in the Gulf of Aden) [*Bower and Furey*, 2012]. Mesoscale eddies see their intensity (visible in the amplitude of SSH) decreasing westward. They finally reach the back of the Gulf where they ultimately dissipate, mainly through frictional effects. Cyclones and anticyclones propagate through the Gulf in a chaotic manner, i.e., we could not discern any recurrent pattern. In particular, we found no seasonal preference in polarity. This indicates the fundamentally turbulent nature of the circulation. In the back of the Gulf, around 57.5°E (Figure 4b), there is a tendency for anticyclones to dominate. The time scale for alternating is between 2 and 6 months. This switch has previously been noticed in satellite altimetry (empirical orthogonal function analysis in *L'Hégaret* [2015]). Hence, by its western position in the Arabian Sea, the Gulf of Oman is continuously forced by remotely formed eddies. Because of the configuration of the Gulf, eddies cannot escape and, as a result, dominate the circulation.

2.2. Idealized Configuration

In order to isolate the interaction of mesoscale eddies with topography, we set up a simplified Gulf of Oman configuration that deliberately omits the outflow. Simplifications also include alongshore invariance of the bathymetry so that flow-topography interactions are easier to analyze. The domain size, the bathymetry profile, and the stratification are realistic (World Ocean Atlas, release 2009). The experiments consist of the free-decay evolution of two horizontally Gaussian-shaped mesoscale eddies that are initially in thermal-wind balance. They are surface-intensified and their kinetic energy vanishes at depth (a similar setup is used in *Wei and Wang* [2009, Figure 1]). We define each eddy by its center position (x_0, y_0), its surface temperature anomaly T_s' (no salinity anomaly), its radius R, and its depth range D. We define the temperature field associated with the eddy (prime denotes deviation from the background stratification) as follows:

AGU Journal of Geophysical Research: Oceans 10.1002/2015JC011033

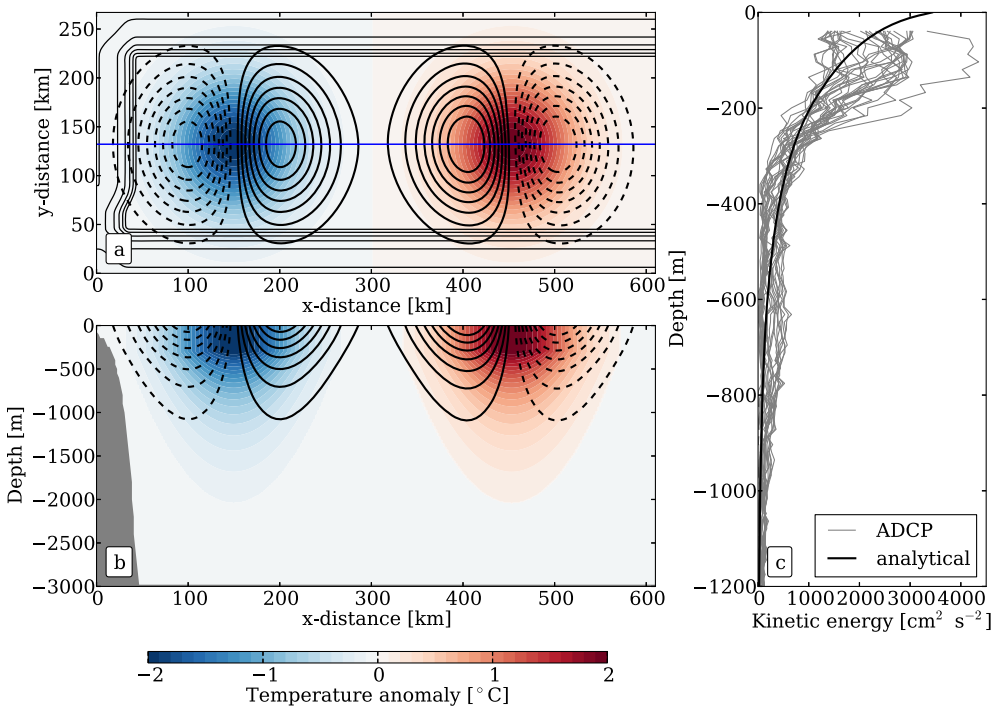

Figure 5. Characteristics of the synthetic cyclone and anticyclone initializing the simulations. Figures 5a and 5b show temperature anomaly (mean vertical background profile has been removed) and contours of meridional velocity from ±10 to ±70 cm s^{-1} with CI = 10 cm s^{-1} (dashed lines are negative values). In Figure 5a, thin black lines are contours of bathymetry and the blue line is the location of the section in Figure 5b. Figure 5c shows kinetic energy profiles in the core of the eddies (black thick line) and derived from ADCP measurements in a mesoscale eddy (gray thin lines, Physindien-2011 cruise) [*L'Hégaret*, 2015].

$$\begin{cases} T'(x,y,z) = T'_s G(x,y), & \text{if } z > \delta \\ T'(x,y,z) = T'_s G(x,y) \exp(-z/D), & \text{if } z < \delta \end{cases}, \tag{1}$$

where $G(x,y) = \exp\left(-\frac{(x-x_0)^2+(y-y_0)^2}{R^2}\right)$ and $\delta = 300$ m. We then compute η (SSH) and (u, v) (horizontal velocity) in two phases. First, we assume that each eddy is isolated and that its associated pressure field does not reach the bottom. Hydrostatic balance integrated over the water column allows us to deduce η. Second, we assume a geostrophic balance to compute the velocity field:

$$\begin{cases} u(x,y,z) = \dfrac{g}{\rho_0 f}\displaystyle\int_\eta^z \partial_y \rho + \underbrace{u(x,y,\eta)}_{=-(g/f)\partial_y \eta} \\ v(x,y,z) = -\dfrac{g}{\rho_0 f}\displaystyle\int_\eta^z \partial_x \rho + \underbrace{v(x,y,\eta)}_{=(g/f)\partial_x \eta} \end{cases}. \tag{2}$$

Figures 5a and 5b show horizontal and vertical sections of temperature and anomaly and meridional velocity across the cyclone and the anticyclone. As we are particularly interested in the role of eddies in the Gulf of Oman, we ensure that the vertical structure of simulated eddies in terms of velocity is consistent with local eddies. To do so, we adjust the vertical structure of the temperature anomaly, hence also the velocity profiles of the analytical eddies to match the observations (Figure 5). In fact, we can compare the vertical kinetic energy profiles at the position of the surface velocity maximum for the synthetic eddy and for a mesoscale eddy sampled in the Gulf of Oman during the Physindien-2011 cruise [*L'Hégaret*, 2015] carried out by the Service Hydrographique et Océanographique de la Marine (SHOM and ADCP measurements). Figure 5c exhibits a fair agreement between the two. It also reveals significant velocities at depth (e.g., 30 cm s^{-1} at 500 m). After migrating westward due to beta drift, the eddy evolution is governed by mutual interaction and topographic influence.

AGU Journal of Geophysical Research: Oceans 10.1002/2015JC011033

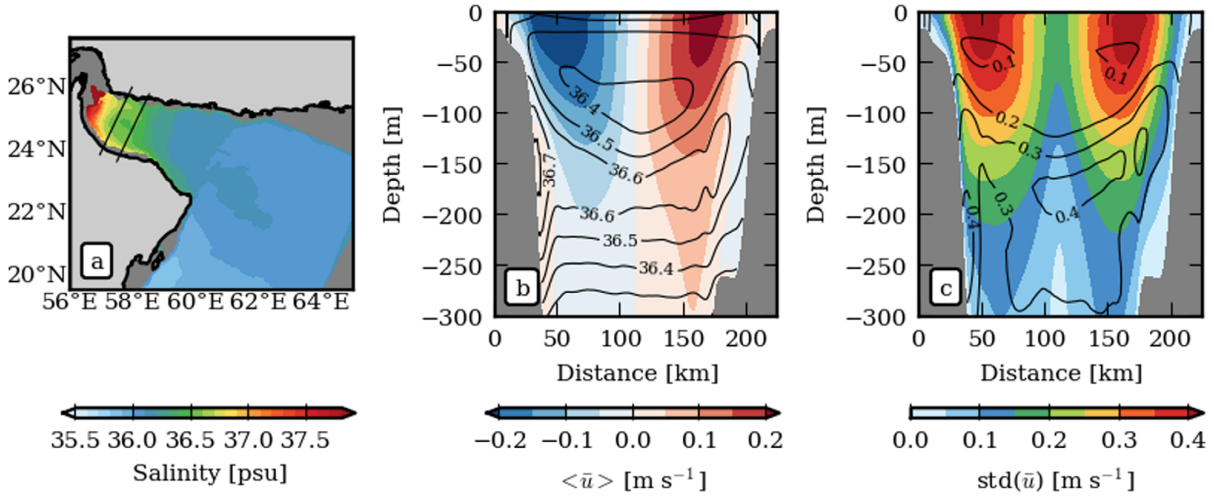

Figure 6. (a) Map of salinity averaged in time (4 years) and vertically between 100 and 250 m. (b, c) Vertical sections of along-gulf velocity (colors) and salinity (black contours) averaged in the along-gulf direction between the two thin black lines in Figure 6a. Figure 6b are time means (4 years) and Figure 6c are standard deviations (biased estimator).

3. Phenomenology

In this section, we analyze the fate of the modeled outflow in the realistic simulation.

3.1. Mean Structure

The dense PGW cascades down the continental shelf break (∼100 km downstream from the Strait, Figure 1). We do not analyze this phase, which involves small-scale turbulence processes that are not properly represented in our model. The outflow reaches a depth of equal density at which point the flow is hydrostatic and geostrophically balanced, and the outflow establishes itself with the coast on its right, as expected from a density current in the northern hemisphere. Figure 6a shows salinity averaged during the 4 years of simulation between 100 and 250 m. It reveals a salty plume with a maximum located on the right of the Gulf close to the Strait of Hormuz but there is no significant variation of salinity across the Gulf further away. This plume morphology is also found in observations [*Carton et al.*, 2012]. Figure 6b shows salinity and along-gulf velocity averaged in the along-gulf direction and in time ($\bar{\cdot}$ is an along-gulf average and $\langle\cdot\rangle$ is a time average). Figure 6c is the same for standard deviations. The dominant signal is the dipolar velocity structure corresponding to a surface-intensified eddy with a diameter of ∼100 km. After 4 years of averaging, the remaining polarity is anticyclonic, corresponding to a slight dominance of positive SSH at this longitude in Figure 4. However, the standard deviation dominates the mean, consistent with the alternating presence of cyclones and anticyclones.

The salinity local maximum hugs the coast and is associated with a maximum in velocity. This gravity current is characterized by a mean speed of $\langle\bar{u}\rangle \sim 0.05-0.1\,\mathrm{m\,s^{-1}}$, comparable to the *Nof*'s [1983] speed $u_g = g'\alpha/f = 0.13\,\mathrm{m\,s^{-1}}$, where g' is the reduced gravity and α is the slope of topography evaluated using the section shown in Figure 6b. Note that the Nof speed does not account for frictional processes which may explain the discrepancy. The mean salinity of the current is $\langle\bar{S}\rangle \sim 36.8$ psu (slightly less than synoptic measurements, 37 psu) [*Pous et al.*, 2004]. The level of equilibration of PGW (100–250 m) is also slightly shallower than observed (150–300 m) [*Pous et al.*, 2004]. We attribute this to the imperfect representation of the frictional Ekman bottom layer (the downslope movement of density currents is strongly constrained by the vertical resolution at depth) [*Laanaia et al.*, 2010] and gravitational adjustment as a whole is a difficult process to reproduce [*Peters et al.*, 2005]. As in the observations [*Carton et al.*, 2012], the mean salinity distribution is smooth, in particular in the cross-Gulf direction, with maximum salinity values located between 100 and 250 m throughout the gulf. There are two maxima in salt variability that are located in the slope current and in the interior ($\mathrm{std}(\bar{S}) = 0.4$ psu). This suggests that the slope current, bringing saline waters, displays a strong temporal variability and that saline water may be injected in the inner basin. This is supported by the weak imprint of the density current. Salinity at the boundary is only 0.3 psu higher than in the interior. For comparison, salinity contrast for the Mediterranean outflow is larger than 0.6 psu [*Legg et al.*, 2009].

AGU Journal of Geophysical Research: Oceans 10.1002/2015JC011033

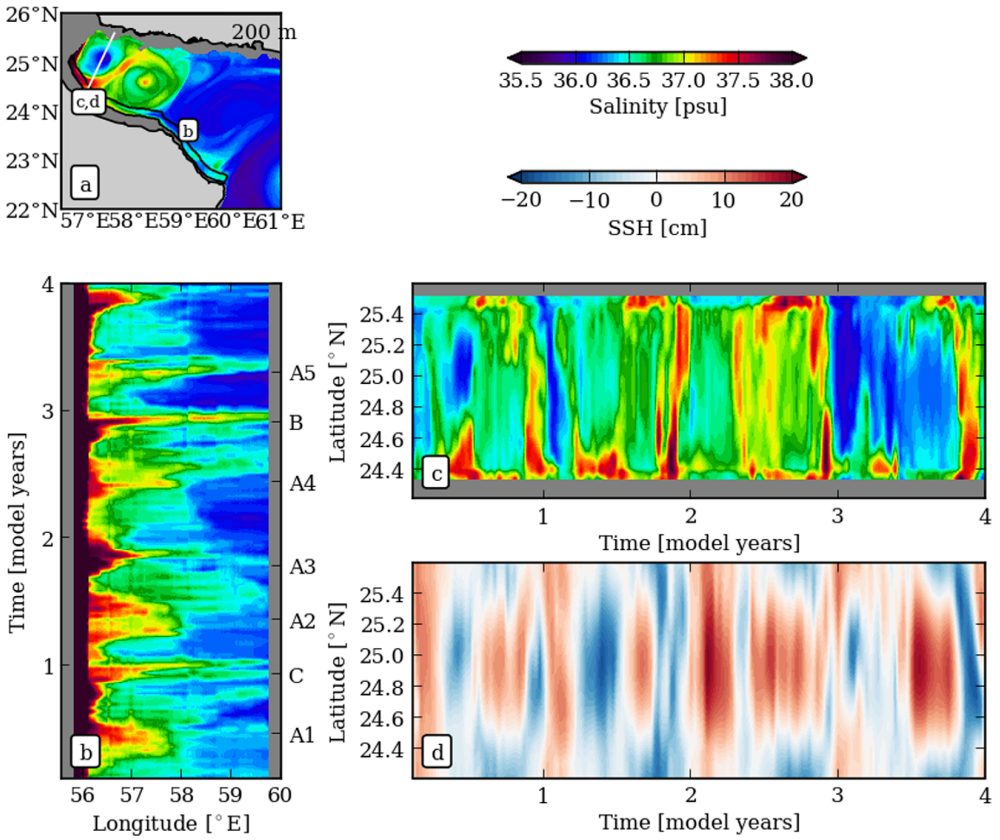

Figure 7. (a) Salinity map at 200 m averaged on 10 days. (b) Longitude-time diagram of salinity (depth averaged between 100 and 250 m and cross-shore integrated from the coastline to 20 km offshore) along the path of PGW delimited by black lines in Figure 7a. (c, d) Latitude-time diagram of salinity (depth averaged between 100 and 250 m) and sea surface height, respectively, at the section shown as white line in Figure 7a.

The mean salinity structure in the far field (downstream from Ras al Hamra, Figure 1) exhibits a very low imprint of PGW (anomalies are less than 0.1 psu) and there is no imprint of a density current. This supports that PGW has been almost completely diluted at this location.

3.2. Intermittency of the Slope Current

Figure 7 makes use of the 4 years of simulation to quantify the salinity distribution evolution in the Gulf of Oman. Salinity in Figure 7b is depth averaged between 100 and 250 m and cross-shore integrated over a 20 km wide strip ($\sim R_d/2$, typical of the slope current width, R_d being the deformation radius). Salinity in Figure 7c is depth averaged between 100 and 250 m. These figures illustrate the spatiotemporal variability of the salt content in the PGW current (Figure 7b) and through a cross-basin section (Figure 7c). The southern filament (that may be associated with the slope current) exhibits a very strong intermittence: salinity in the coastal range, upstream of Ras al Hamra (longitude $<58.5°$E), varies between 36 and 38 psu. Values above 37 psu are characteristic of PGW [*Pous et al.*, 2004] and peak approximately twice a year. This is not related to the boundary forcing as the seasonal variability in salinity is weak (maximum is always above at 39.5 psu). It thus has to be the result of another process, which is the intermittent interaction of the coastal undercurrent with the mesoscale eddy field.

Figure 7d shows SSH on the same line as the section in Figure 7c. Latitude-time diagrams (Figures 7c and 7d) show the alternating presence of PGW along the northern (resp. southern) coast depending on whether an anticyclone (resp. a cyclone) occupies the end of the Gulf. This strongly suggests a steering of PGW by mesoscale turbulence. Similar latitude-time diagrams at locations downstream of Ras al Hamra (not shown) reveal the same steering of PGW, and very diluted waters (salinity $\sim$36.1 psu) occasionally reaching the Gulf

AGU Journal of Geophysical Research: Oceans 10.1002/2015JC011033

entrance. This variability in outflowing water paths driven by mesoscale eddies is similar to the fate of the Red Sea Water outflowing in the Gulf of Aden [*Ilicak et al*., 2011].

A close examination of the salinity field at a temporal resolution of 12 h allows to focus on some particular events. Events labeled *Ai* ($i \in 1 \ldots 5$, Figure 7b) correspond to detachments of PGW from the southern coast propagating into the interior (dynamical characteristics are discussed in the next section 3.3). They are associated with the presence of a cyclone that seemingly sheds the saline water seaward. Similar events occur on the northern coast when an anticyclone lies at the back of the Gulf. These events break the slope current, expel PGW seaward, and efficiently redistribute PGW into the basin interior (in coherence with the salinity standard deviation maximum in the interior in Figure 6). They are season-lasting events, relying on surface-intensified eddies to imprint their dynamics at depth. Hence, they provide a hint of explanation for horizontally isotropic plumes of PGW seen on climatological fields in the Gulf of Oman. Events labeled *B* and *C* (also in Figure 7c), respectively, correspond to a "reattachment" and a flush of PGW. They are characterized by a salinity maximum at the southern boundary corresponding to a continuous saline filament heading to the entrance of the Gulf. These events are rarely observed and the slope current is almost always discontinuous.

3.3. Submesoscale Coherent Vortices Contain PGW

The realistic simulation shows a rich diversity of situations in terms of PGW distribution and turbulent features containing PGW. Figure 8 presents a typical event (from the family of events *Ai* in Figure 7 identified above) occurring in the simulation that helps to understand this spread. A cyclone fills the Gulf of Oman downstream of Ras al Hamra. It can be identified by means of a positive core of vertical relative vorticity ($\zeta = \partial_x v - \partial_y u \sim 0.5f$, (u, v) is the horizontal velocity) and a maximum in density (Figures 8a and 8b). The mean radius of deformation in this region is $R_d = 41$ km and the eddy diameter is 120 km $\sim 3\,R_d$, i.e., in the mesoscale range. The cyclone is energetic with a maximum velocity at 200 m of 0.5 m s^{-1}. Its deep-reaching flow field (isopycnal tilts reach 1000 m) is consistent with *Carton et al*. [2012], who showed a strong correlation between a float trajectory at 700 m and geostrophic surface circulation derived from altimetry.

Around the rim of the cyclone, five small patches of negative vorticity are present. They correspond to Submesoscale Coherent Vortices (SCV) [*McWilliams*, 1985] with horizontal length scales less than R_d (between $R_d/2$ and R_d). Their vertical extension is consistent with that of the *Peddy* (standing for *Persian Gulf Eddy*, similarly to *Meddy*) sampled by *Senjyu et al*. [1998]. The SCV core vorticity reaches $O(-f)$, consistent with the high intensity of such submesoscale structures. Embedded within the SCVs are anomalously high values of salinity (Figures 8c and 8f), hence revealing PGW. The core of PGW in this section is shallower than its mean because it is contained into a mesoscale cyclonic structure, thus having tilted isopycnals upward (this vertical shift of PGW position depending on the polarity of the structure has been noticed in cruise and Argo floats observations in *L'Hégaret et al*. [2015]). Interestingly, at the period of formation of the SCV (Figure 8f), there is no exact colocalization of the hydrological (salinity) and dynamical (vorticity) cores. In fact, the patch of positive anomaly of salinity is more diffuse horizontally and vertically than the vorticity core. To confirm the robustness of this visual feature, we compute the Probability Density Functions (PDFs) of the depth of relative vorticity maximum and the depth of salinity maximum through all water columns in an area covering the Gulf of Oman, during a period of 20 days encompassing the snapshot in Figure 8 (see the caption of Figure 9 for details on the computation). PDFs in Figure 9 show that the vorticity maximum is found around 125–150 m (we investigate the processes responsible for this subsurface vorticity maximum in section 4) whereas the salinity maximum have mainly three distinct peaks, between 100 and 275 m, depending on the location of PGW (in fact, a shift in PGW depth is noticed whether it is embedded in a cyclone or an anticyclone, and PGW core also deepens downstream from the Strait). Indeed, vorticity and PGW cores are seemingly decorrelated. This is a clue to infer on the passive role of the slope current in the formation of SCVs (further arguments on spatiotemporal scales involved are discussed in section 4.2). Instability of the current would have led to a colocalization of hydrological and dynamical cores (e.g., saline Levantine Intermediate Water spread through SCVs generated by an undercurrent detachment) [*Bosse et al*., 2015].

The coherence of the structures ($\zeta/f \sim -1$) allows to infer a mechanism of transport of PGW seaward as entrained in a rotation around the central mesoscale eddy (see velocity field in Figure 8d). This kind of

AGU Journal of Geophysical Research: Oceans 10.1002/2015JC011033

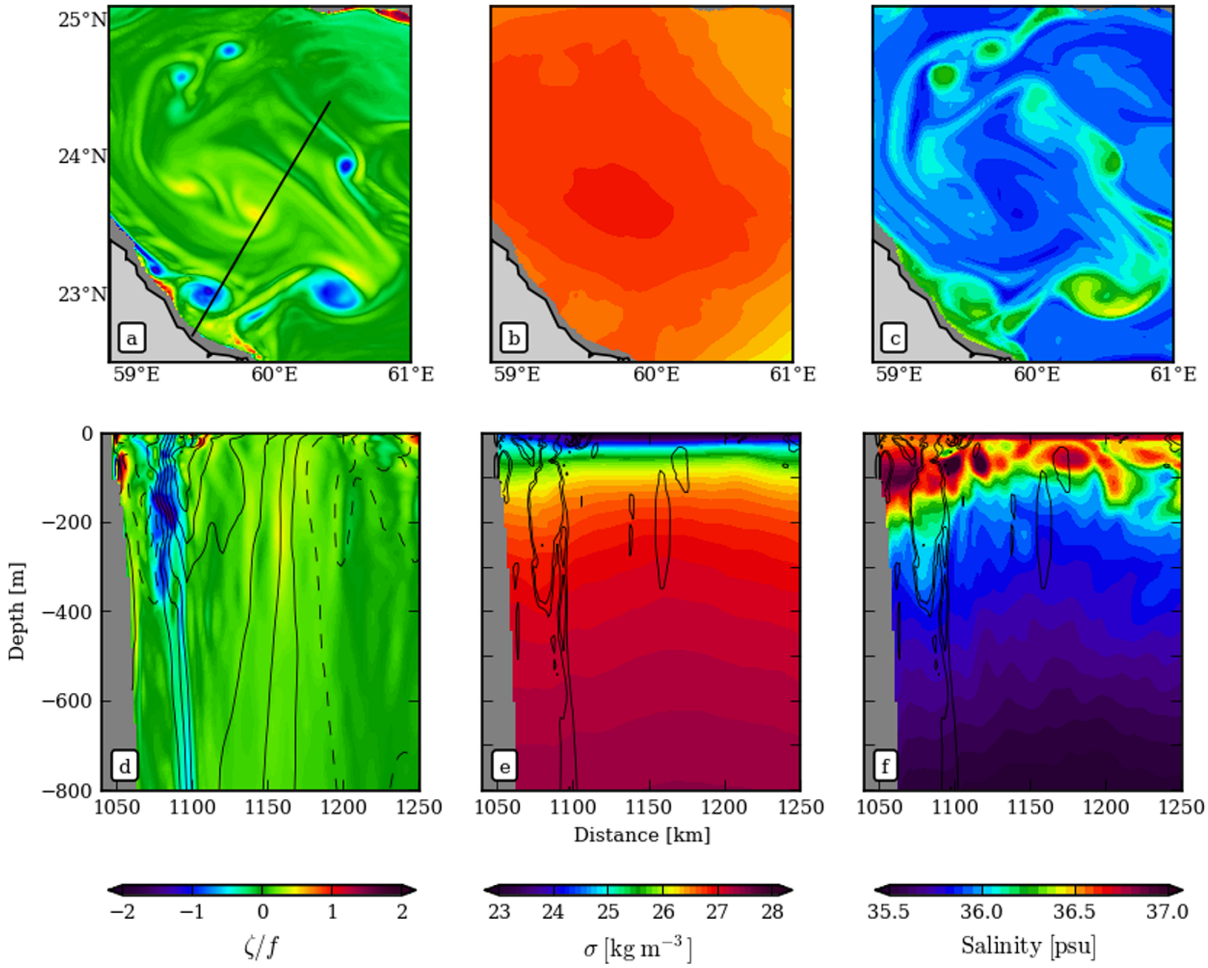

Figure 8. (top) Maps at 200 m and (bottom) sections of (left) relative vorticity ζ nondimensionalized by the planetary vorticity f, (middle) density, and (right) salinity. The black line in Figure 8a is the location of the sections. Black contours in Figure 8d are cross-section velocity ranging from -0.5 to $0.5\,\mathrm{m\,s^{-1}}$ with CI $= 0.1\,\mathrm{m\,s^{-1}}$ (negative values are dashed). Black contours in Figures 8e and 8f are ζ/f ($\pm 0.4, 0.6$).

trajectory has been reported with a mode water SCV around a mesoscale anticyclone in the Atlantic [*Reverdin et al*., 2009]. However, SCVs in the model rapidly collapse and coherent structures cannot be tracked longer than 10 days in the simulation. We attribute this short life cycle to the strong deformation field (shear s and strain σ) in the vicinity of mesoscale eddies (Figure 10). In fact, although we have $s, \sigma < \zeta$ in SCVs (confirming their coherence as rotating structures), the magnitude of the mesoscale shear and strain is comparable with SCV vorticity values. As such, they compete with it and tend to damage the submesoscale structures.

4. Processes at Play

In this section, we evidence how the kind of SCVs described previously can arise from interactions of mesoscale eddies with topography. We did several idealized experiments and present the most interesting results.

4.1. Vorticity Production on the Slope

Figure 11 shows maps and a section of relative vorticity for a snapshot of an idealized experiment. We recall that the experiment is initialized with two opposite polarity mesoscale eddies representative of the ones encountered in the Gulf of Oman. At the surface, the dominant feature is thus the mesoscale dipole with

AGU Journal of Geophysical Research: Oceans 10.1002/2015JC011033

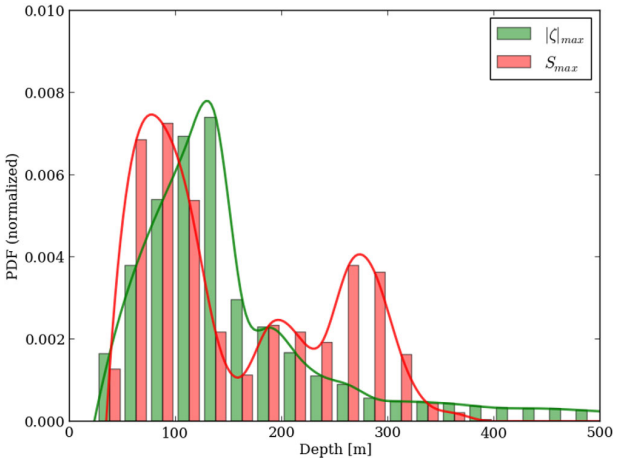

Figure 9. Probability density functions (PDFs) of the depth of (green histogram) relative vorticity maximum $|\zeta|_{max}$ and (red histogram) salinity maximum S_{max}, computed on 20 days around snapshot in Figure 8, in an area covering the Gulf of Oman (between vertices 23.8°N, 56.6°E; 26.5°N, 57.8°E; 25.2°N, 61.2°E; 22.5°N, 59.7°E). Depth is binned from 25 to 800 m with a constant bin width of 25 m (x axis is cut at 500 m). Lines are cubic splines interpolations between histogram rectangles.

core vorticity values of $\sim\pm 0.5f$ (similar to the ones realistically simulated). At depth, the footprint of the dipole is noticeable and each mesoscale eddy is surrounded by some smaller eddies of opposite polarity whose sizes ($\leq R_d$) and vorticity amplitudes ($|\zeta/f| \sim 1$) are typical of SCVs. Note that these SCVs exist in a subsurface layer and have no surface signature.

Below 150 m, a very thin layer of high vorticity $|\zeta/f| > 1$ develops where mesoscale eddies encounter the continental slope. Vorticity in the boundary layer has an opposed polarity to the eddy dragging on the slope. It is generated as the velocity field slows down toward the shore due to friction in the boundary layer. Vorticity would probably be even larger in a higher-resolution simulation as found in *Molemaker et al.* [2015] because the vorticity intensity depends on the width of the frictional layer. Vorticity strips are shed from the continental slope at the edge of their "parent" mesoscale eddies and suddenly roll up into SCVs (Figure 11b, $x \sim 350$ km). Instability of those vorticity strips carrying horizontal velocity shears is discussed in section 4.2. Notice that we characterize these vortices as submesoscales as their diameters are in the range ~35–40 km, thus slightly less or comparable to R_d.

Similar processes are discussed in *D'Asaro* [1988] and *Molemaker et al.* [2015] of the formation of a frictional boundary layer at depth. A key difference here is that friction acts on mesoscale eddy velocities instead of a boundary current (upwelling undercurrent for instance). Another difference is that detachment does not require a topographic irregularity like a cape or a canyon. Here rotation of the flow around mesoscale structures implies that currents are in some places oriented across the continental slope which promotes detachment, in the same fashion as in *Oey and Zhang* [2004] and *Akuetevi and Wirth* [2015]. Among the eddy-topography interaction processes described in the introduction, the dominating one in our simulation is thus the frictional formation of boundary layers and the relaxation of smaller-scale eddies.

To test the hypotheses that vorticity is produced: (i) on the continental slope, and (ii) due to bottom friction (the model vertical boundary layer implies a horizontal shear layer [*Molemaker et al.*, 2015, Figure 7]), we ran two experiments with and without bottom stress. We use a linear bottom stress with a drag coefficient $C_D^{lin} = 3\,10^{-4}\,\mathrm{m\,s^{-1}}$ (similar to what is commonly used) [e.g., *Dong et al.*, 2007]. Sensitivity to the bottom stress parameterization is tested in the next section 4.2. Figures 12a and 12b present the enstrophy horizontal spectra $\zeta^2/2$ as a function of depth for both experiments, computed on the same rectangular box ($x \in [46\,\mathrm{km}; 457\,\mathrm{km}], y \in [49\,\mathrm{km}; 217\,\mathrm{km}]$) and averaged over the same period (between days 45 and 75 to allow for the eddies to interact with the topography while keeping a sufficient level of energy because the system is freely decaying). The global picture matches what is expected from geostrophic turbulence in the ocean: enstrophy is mostly contained in surface-intensified structures with a scale of 2–3 R_d (mesoscale eddies in this case) and vanishes with depth at a given wave number. Looking more specifically at isoline −7 in Figure 12a reveals a positive anomaly of enstrophy between 200 and 800 m. An interior source of enstrophy at scales smaller than or equal to R_d is thus located on the continental slope. The simulation without bottom stress does not exhibit the same enstrophy creation at depth (Figure 12b). Moreover, neither frictional boundary layer nor SCV are observed, in agreement with similar experiments carried out in *Oey and Zhang* [2004]. Enstrophy is monotonically decreasing with depth for all wave numbers. The ratio of the two enstrophy power density spectra quantifies this fundamental difference to be an order of magnitude greater (Figure 12c) and validate hypotheses (i) and (ii).

AGU Journal of Geophysical Research: Oceans 10.1002/2015JC011033

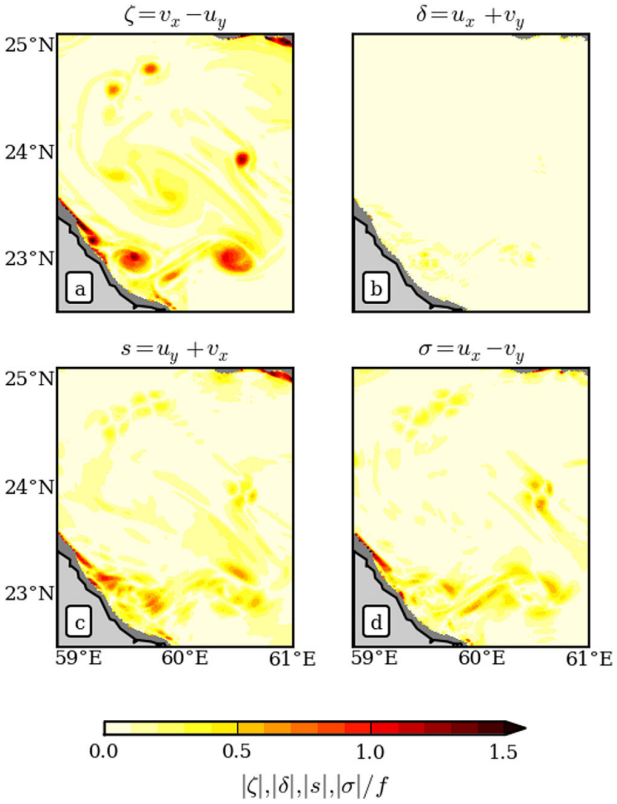

Figure 10. Maps at 200 m of the absolute value of (a) relative vorticity $|\zeta|/f$, (b) divergence $|\delta|/f$, (c) shear $|s|/f$, and (d) strain $|\sigma|/f$. All fields are computed at the same time, identical to Figure 8.

4.2. Generation of SCVs

We observe both cyclonic and anticyclonic SCVs in the realistic (although not precisely quantified, we observe a slight preference for anticyclones) and in the idealized simulations. The polarity of an SCV is opposed to the polarity of its *parent* mesoscale eddy that has dragged on the slope. Mechanisms leading to the formation of vortical structures emerging from intense frictional boundary layers was first observed by *D'Asaro* [1988] and has recently been revisited using high-resolution models [*Dewar et al.*, 2015; *Gula et al.*, 2015; *Molemaker et al.*, 2015]. They involve different instability processes depending on the polarity of the boundary layer.

The case of anticyclonic boundary layers has been studied in the context of the California Undercurrent [*Molemaker et al.*, 2015; *Dewar et al.*, 2015]. Flowing poleward along the US West Coast, it generates negative vorticity in the boundary layer. With a sufficient resolution, vorticity in the boundary layer becomes larger than f and instigates centrifugal instability when the flow separates from the slope. While our simulation does no justice to the details of evolving centrifugal instability and subsequent mixing of momentum due to the limitations of resolution and the hydrostatic assumption, the flow does quickly adjust to a state that is subcritical. Negative vorticity values that are lower than $-f$ are routinely generated in frictional boundary layers. These values are diluted to satisfy $\zeta > -f$ as soon as vorticity strips detach from the stabilizing continental slope. We argue that the same mechanism occurs in our simulations when a mesoscale cyclone drags on the continental slope and generates anticyclonic SCVs (Figure 8).

The cyclonic case has been studied on the cyclonic side of the Gulf Stream at the exit of the Florida Strait [*Gula et al.*, 2015]. The Gulf Stream drags on the continental slope on its left, generating positive vorticity by friction. After separation of the flow from the slope, the vorticity filament becomes unstable and rolls up into a string of cyclonic submesoscale vortices. *Gula et al.* [2015] show that barotropic instability, thus linked with the instability of a horizontal shear flow, is the main process generating those vortices.

Another potential candidate for the generation of eddies in the realistic simulation could be the baroclinic instability of the slope current [*Griffiths*, 1986]. The linear stability analysis of a slope current [*Stephens*, 1997] applied to the intermittent slope current in our simulation gives a maximum growth rate of $\sim 0.12\, U/R_d$ corresponding to a wavelength of $\sim 2\pi R_d/0.7$ (using a continental slope of 0.02, mean value upstream Ras al Hamra). With a slope current that reaches $U \sim 0.3\,\mathrm{m\,s^{-1}}$ and $R_d = 41$ km, this gives a growth rate of 1/13 days^{-1} and a wavelength of 360 km. These spatiotemporal scales are incompatible with SCVs and we therefore reject this as a generation mechanism of SVCs.

4.3. Sensitivity to the Bottom Stress Parameterization

The development of frictional layers in the simulations occurs when an eddy drags on the bottom slope. The strength of the friction depends on how the bottom stress τ_b is parameterized in ROMS. We are able to use either a linear bottom stress $\tau_b = \rho_0 C_D^{lin} \boldsymbol{u}$ or a quadratic bottom stress $\tau_b = \rho_0 C_D^{quad} ||\boldsymbol{u}|| \boldsymbol{u}$ where ρ_0 is a

AGU Journal of Geophysical Research: Oceans 10.1002/2015JC011033

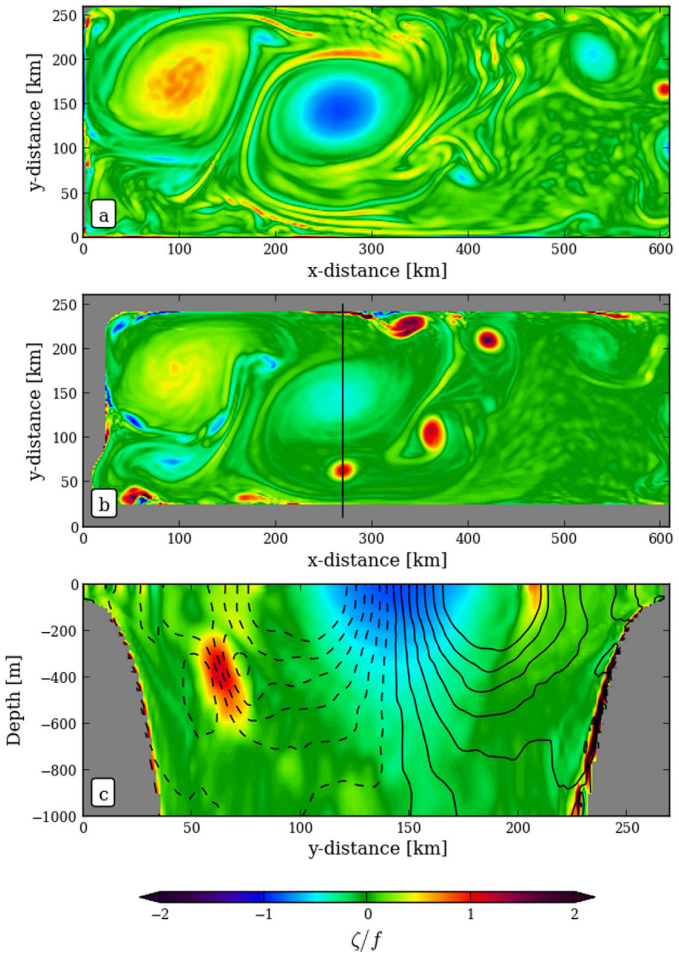

Figure 11. Snapshot maps and section of relative vorticity ζ/f in the idealized experiment with linear bottom stress. Maps are (a) at the surface and (b) at 400 m. Black line in Figure 11b indicates location of section in Figure 11c. Black contours in Figure 11c are cross-section velocity ranging from -0.6 to 0.6 m s^{-1} with CI = 0.1 m s^{-1} (negative values are dashed).

reference density, C_D is a drag coefficient, and $\boldsymbol{u}$ is the horizontal velocity. In the linear formulation, C_D is constant. In the quadratic formulation, it can be constant or vary with the thickness of the lowest layer of the grid Δz_b. This uses the Von Karman-Prandtl logarithmic formulation $C_D^{VonKarman} = \left(\frac{\kappa}{\log(\Delta z_b/z_r)}\right)^2$ where $\kappa = 0.41$ is the Von Karman constant and z_r is the roughness parameter usually taken in the range $O(10^{-2} - 10^{-3}\,\mathrm{m})$.

We made several simulations with linear and quadratic bottom stresses and varying C_D. Experiments are described in Table 1. The first observation we made is that neither the nature of the parameterization (linear or quadratic) nor the value of C_D changes qualitatively the eddy-topography interactions. Formation of frictional boundary layers is still present and roll-up of vorticity strips into vortices in the interior occurs as soon as a drag is parameterized. The evolution of the bottom stress is very similar in all cases (Figure 13). A peak occurs at the beginning of the simulation when the velocity field is dramatically damped in the bottom level (initialization does not take into account a reduction of velocity in the bottom level). Then the bottom stress decreases and fluctuates around its mean value from day 20 onward. An interesting point is that the mean bottom stress increases with C_D (Table 1) but with a smaller rate: doubling C_D only increases $\langle ||\boldsymbol{\tau}|| \rangle$ by 38% (linear case) and 40% (quadratic case). It also reduces the bottom layer velocity standard deviation std(u_{bottom}) by comparable factors. This suggests that the bottom stress is not very sensitive to the drag coefficient itself. The Von Karman formulation of the drag coefficient does not really impact the bottom stress

AGU Journal of Geophysical Research: Oceans 10.1002/2015JC011033

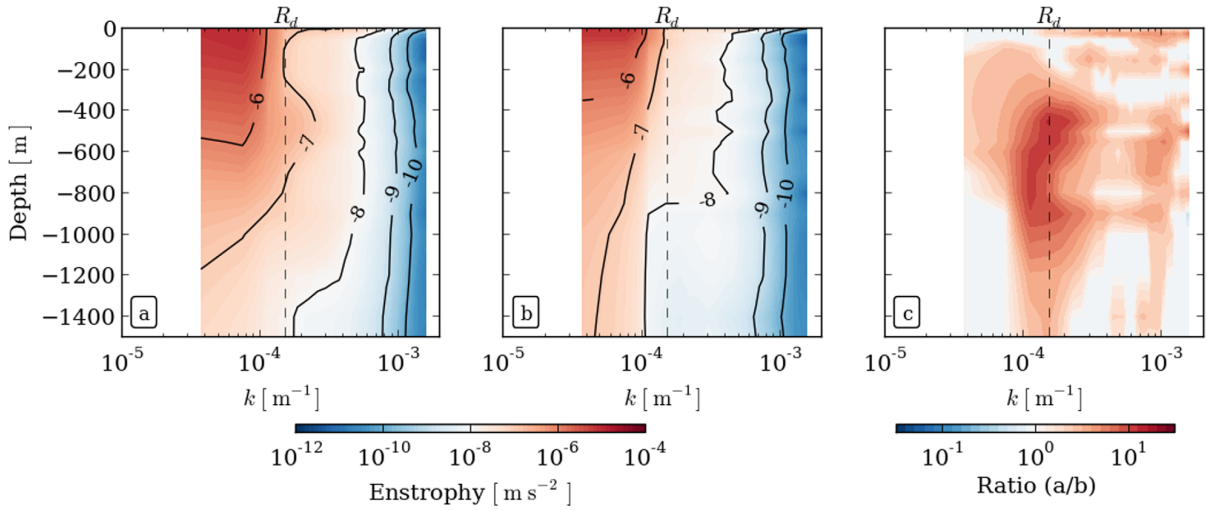

Figure 12. Enstrophy spectral density as a function of depth averaged over 1 month in the idealized experiments (a) with linear bottom stress and (b) with no bottom stress. Figure 12c is the ratio of (a)/(b). $k=(k_x^2+k_y^2)^{1/2}$ is the horizontal wave number. The vertical dashed line shows the deformation radius scale (R_d).

and its integrated value is very similar to the quadratic case with $C_D=2.5\,10^{-3}$ (Figure 13). This is not surprising since the bottom stress mainly acts around 400 m (see the large vorticity values in Figure 3 of the manuscript) and $C_D^{VonKarman}(\sim 400\,\mathrm{m}) \sim 2-4\,10^{-3}$. This more sophisticated formulation does not really bring changes in the simulations here.

To conclude, we can state that the velocity field is not sensitive to the bottom stress formulation and the drag coefficient used in our simulations. All sensitivity tests exhibit similar eddy-topography interactions, thus the phenomenology described in the manuscript is robust.

5. Turbulent Diffusion

In this section, we assess the efficiency of eddy-topography interactions described previously in diffusing the salinity in the Gulf of Oman.

5.1. Eulerian Perspective

We start with an Eulerian point of view that reveals the significance of eddy fluxes in distributing salinity in the Gulf. We separate the contributions of salt fluxes into a mean and an eddy part:

$$\underbrace{\nabla_{3D}\cdot\overline{u\bar{S}}}_{\text{total}} = \underbrace{\nabla_{3D}\cdot\bar{u}\,\bar{S}}_{\text{mean}} + \underbrace{\nabla_{3D}\cdot\overline{u'S'}}_{\text{eddy}}. \quad (3)$$

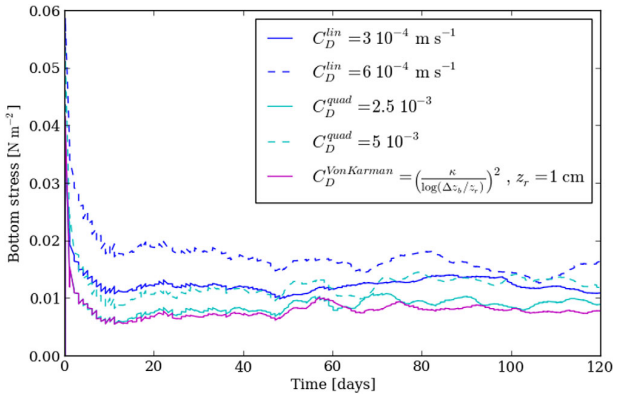

Figure 13. Horizontally integrated bottom stress as a function of time (120 days of simulation) with five different bottom stress parameterizations (see the legend for correspondence).

We average the *total* term computed online during 1 year, and compute offline the *mean* term from the averaged velocity and salinity fields. As such, we can estimate the *eddy* contribution as the difference between the total and the mean terms. In addition, contributions are vertically integrated over the salt tongue depth range (100–250 m). The first-order balance is between the mean and the eddy contributions, and the total advection term is weaker than both contributions. All other terms (mixing, rate, and forcing) are at least 1 order of magnitude smaller. As

AGU Journal of Geophysical Research: Oceans 10.1002/2015JC011033

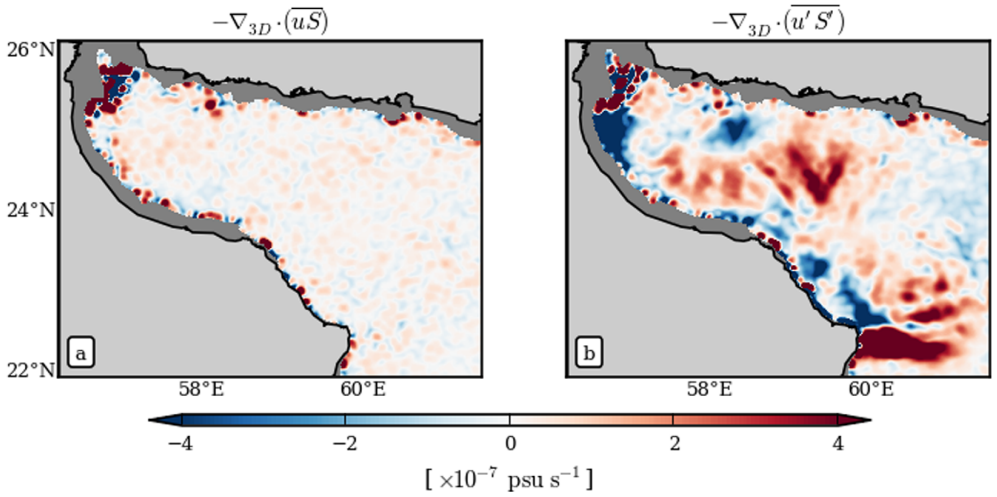

Figure 14. Convergence (i.e., minus divergence) of salt fluxes computed over 1 year and integrated between 100 and 250 m in the vertical. Figure 14a is the mean of total fluxes computed online and Figure 14b is the eddy salt flux divergence. Both fields have been spatially smoothed with a Gaussian filter of width 10 km.

such, we only show the total and the eddy terms in Figure 14 (the mean term is almost equal to the opposite of the eddy term). Displayed are opposite quantities of those in equation (3), i.e., convergence of fluxes. The most important contribution of eddy fluxes is done in the inner basin, where eddy fluxes contribute to the supply in salty waters (convergence of eddy fluxes). Values reach $\sim 2\times10^{-7}$ psu s^{-1}, i.e., 0.6 psu $month^{-1}$. Along the southern boundary, a dominance of negative convergence of eddy salt fluxes indicates that salt is *extracted* from the slope current at roughly similar rates. The role of eddy fluxes is thus to extract salinity from the boundaries (preferentially from the southern boundary where the slope current sits) and redistribute it in the interior of the Gulf. This provides a hint of explanation to understand how the almost isotropic salinity plume can form. In fact, the mean salinity gradient is directed in the along-gulf direction and the signature of the slope current is very weak (Figure 6a).

5.2. Lagrangian Perspective

We now examine synthetic particle trajectories released in the source of the outflow, in the Strait of Hormuz. This Lagrangian approach brings complementary information in terms of dispersion rate of particles during their journey through the Gulf of Oman which can under some assumptions and approximations be translated into eddy diffusivities (e.g., review on Lagrangian statistics in *LaCasce* [2008]). Particles are released off-line in the model solution, using the code described in *Gula et al.* [2014]. Neutrally buoyant particles are advected directly by the model velocity fields without any additional dispersion from the model's mixing processes. Model 12 hourly outputs are linearly interpolated in space and time. A time step of 7 min is chosen to respect the Friedrich-Courant-Levy condition imposed by $\Delta x = 2$ km and maximum model velocities of 1.8 m s^{-1}. A total of 120,000 particles are continuously injected in the outflow during 2 years to cover seasonal variations.

The mean trajectory of all released particles, i.e., the trajectory of their center of mass, is shown in Figure 15a. The trajectory is well centered in the cross-Gulf direction, from their release in the Strait until reaching the middle of the Gulf. This confirms the insignificant role played by the slope current. Examining an animation of their pathways confirms the role of mesoscale eddies in stirring them, northward (southward) when a cyclone (anticyclone) occupies the end of the Gulf.

On average, the PGW salt anomalies are diluted as they are transported toward the mouth of the Gulf. This is noticeable in particle's mean salinity (Figure 15a). To quantify this diffusion, we compute the absolute dispersion of particles around their mean position, that is, the mean square distance between particles and their center of mass $\langle d^2(t)\rangle$ at a function of time t, relative to the release absolute time ($\langle\cdot\rangle$ denotes an ensemble average). It reveals how a cloud of tracer spreads about its center of mass [*LaCasce*, 2008]. Figure 15b shows the dispersion evolution, computed with all particles released in the Strait. Three regimes are

AGU Journal of Geophysical Research: Oceans 10.1002/2015JC011033

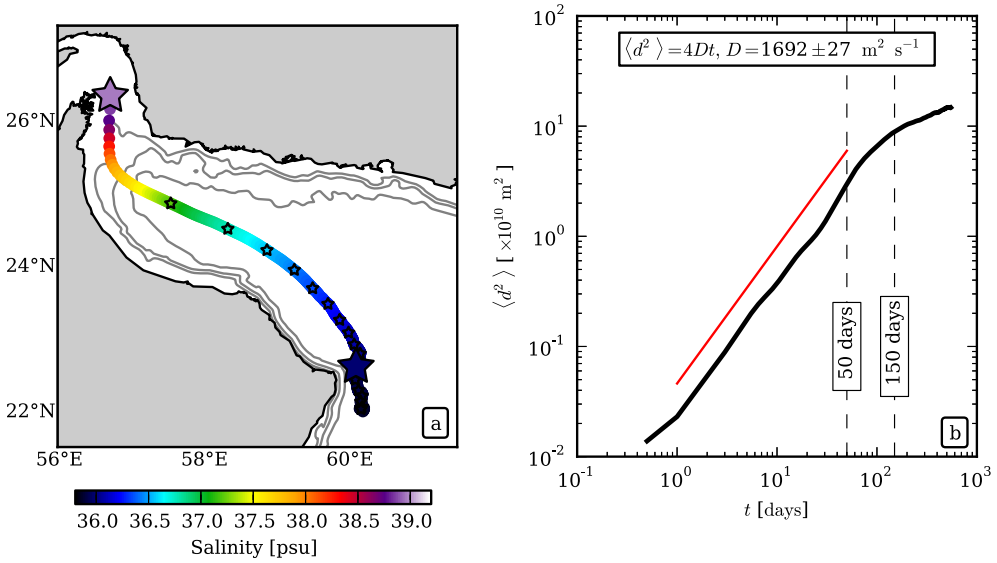

Figure 15. (a) Trajectory of the center of mass of 120,000 particles released in the outflow in the Strait of Hormuz during 2 years. There is one point per day, one small star every month, and one big star every year. Color is the mean salinity of the particles and isobaths 100, 250, and 1000 m are shown in gray lines. (b) Relative dispersion of particles relative to the center of mass as a function of time (black line) and linear regression computed between days 1 and 50 (red line). Correlation coefficient for linear fit is 0.98.

noticeable. First, from the release time to about 50 days, $\langle d^2(t) \rangle$ can be approximated by a linear function. $\langle d^2(t) \rangle \propto t$ suggests a diffusive behavior typical of a *random walk* process (same behavior was found in the surface and subsurface North Atlantic) [*Colin de Verdière*, 1983; *LaCasce and Bower*, 2000]. In a two-dimensional flow, in case of a linear dispersion, one can infer a diffusivity D:

$$\langle d^2(t) \rangle = 4D\,t. \tag{4}$$

Assuming this model is valid and using a linear regression, we obtain a diffusivity $D = 1692 \pm 27$ m^2 s^{-1}. This value accounts for a variety of 3-D dispersive processes. Excluding particles whose depth evolution deviates from that of the center of mass by more than $\pm d_0$ a priori leads to a lower value D_{d_0}. For small d_0 this estimate should be more directly comparable to classical quasi-2-D isopycnal diffusivity values because the influence of dispersive processes in the vertical direction is limited. For $d_0 = 50$ m, we find $D_{d_0} \sim 1600$ m^2 s^{-1} which is still large and comparable to those obtained for well-known highly diffusive environments, e.g., in the Antarctic Circumpolar Current (ACC). For comparison, *Abernathey et al.* [2010] find values reaching $\sim$2000 m^2 s^{-1} in the ACC (although the method is different, it is also representative of an eddy diffusivity) whereas *Colas et al.* [2013] obtain 300−750 m^2 s^{-1} in an eastern boundary regime (California Current System). Note that this diffusivity corresponds to the dispersion during almost the first 2 months (50 days, until the second star in Figure 15a). A slight deep is visible in the dispersion curve after t $\sim$ 20 days. It is due to a saturation of the across-gulf dispersion (not shown) component that is consistent with the elongated shape of the gulf. A transition occurs at 50 days, which corresponds to a standard deviation of $\sim$170 km of the particle distance to the center of mass. This makes a disk of diameter 340 km that fills the Gulf.

Between days 50–150, there is a second stage, which is subdiffusive ($\langle d^2 \rangle \sim t^\alpha$, $\alpha < 1$). As the majority of the particles fill the Gulf, their overall dispersion is slowed down in the cross-Gulf direction (dispersion is anisotropic due to the Gulf geometry, not shown). A transition occurs around 150 days and marks the beginning of a third stage, which is associated with an even slower dispersion (i.e., smaller diffusivities). We hesitate to dynamically interpret this regime during which particles progressively exit the computational domain.

6. Summary

The realistic simulation evidences the important role of mesoscale eddies in spreading PGW in the Gulf of Oman at seasonal time scales, similarly to the fate of the Red Sea outflow in the Gulf of

AGU Journal of Geophysical Research: Oceans 10.1002/2015JC011033

Aden [*Ilicak et al*., 2011]. Unlike in many other outflows, the slope current (along the southern coast) associated with outflowing waters is very intermittent and not instrumental in generating turbulence. The idealized simulations isolate the interaction of mesoscale eddies with the topography and reveal an enstrophy source at depth, located on the continental slope, that is produced by frictional effects in boundary layers. Friction is responsible for the formation of intense relative vorticity strips that detach from the continental slope and rapidly roll up into SCVs produced by instability. It is found in the realistic simulation that these SCVs trap PGW in their vicinity and contribute to PGW advection in the interior of the Gulf of Oman. SCVs are advected along the edges of the surrounding mesoscale eddies and do not live longer than 10 days due to the strong deformation rates there. Overall, this combination of processes mixes the salt input associated with PGW and produces a smooth large-scale salinity gradient in the Gulf. A release of virtual particles in the realistic simulation allowed to infer a diffusive regime with an estimated eddy diffusivity of $\sim$1700 $m^2 s^{-1}$, typical of highly turbulent and dispersive regimes. This study thus brings an additional dynamical ingredient to the observations in *L'Hégaret et al*. [2013]: PGW in the interior of the basin is partly contained into SCVs that participate actively to its spreading.

Furthermore, we suggest that eddy-topography interactions creating submesoscale structures may often occur on continental slopes. Water masses trapped into SCVs may be spread into inner basins (away from boundaries) through this mechanism of transport. Eddy-topography interactions may well be a frequent and important process along continental slopes and contribute to offshore advection, dispersion and mixing of slope current waters in many other ocean sectors. For instance, recent fine-scale measurements by gliders in the Mediterranean Sea revealed the importance of SCVs, generated on the continental slope, to spread Levantine Intermediate Waters [*Bosse et al*., 2015]. It is likely that the formation of SCVs by boundary layer detachment is not a rare process in the ocean. However, it is hard to observe because it is essentially a submesoscale process.

A step further in the study of the PGW spreading should be to focus on diabatic processes, especially on vertical mixing during the adjustment phase and horizontal mixing associated with SCVs collapse. The contribution of near Strait turbulence generated by pulses in the outflow could also lead to a richer variability in the spreading of PGW.

Acknowledgments
Eddy Available Potential Energy data set was downloaded from http://stockage.univ-brest.fr/~roullet/research.html. MODIS SST data are available (Level 2) at http://oceancolor.gsfc.nasa.gov/cgi/browse.pl. SRTM30-plus bathymetry data set is available at http://topex.ucsd.edu/www_html/srtm30_plus.html. The altimeter products were produced by Ssalto/Duacs and distributed by Aviso, with support from Cnes (http://www.aviso.altimetry.fr/duacs/). CV is supported by the Direction Générale de l'Armement (DGA) and the Région Bretagne in the form of a PhD scholarship. C.V. benefited from a mobility grant from LABEX-MER to do an internship at UCLA. This study is a contribution to the French ANR Synbios. We thank two anonymous reviewers for their constructive remarks.

References

Abernathey, R., J. Marshall, M. Mazloff, and E. Shuckburgh (2010), Enhancement of mesoscale eddy stirring at steering levels in the Southern Ocean, *J. Phys. Oceanogr.*, *40*(1), 170–184, doi:10.1175/2009JPO4201.1.

Akuetevi, C., and A. Wirth (2015), Dynamics of turbulent western-boundary currents at low latitude in a shallow-water model, *Ocean Sci.*, *11*(3), 471–481, doi:10.5194/os-11-471-2015.

Banse, K. (1997), Irregular flow of Persian (Arabian) Gulf water to the Arabian Sea, *J. Mar. Res.*, *55*(6), 1049–1067, doi:10.1357/0022240973224120.

Becker, J., et al. (2009), Global bathymetry and elevation data at 30 arc seconds resolution: SRTM30_PLUS, *Mar. Geod.*, *32*(4), 355–371.

Böhm, E., J. Morrison, V. Manghnani, H. Kim, and C. Flagg (1999), The Ras al Hadd Jet: Remotely sensed and acoustic Doppler current profiler observations in 1994–1995, *Deep Sea Res., Part II*, *46*(8), 1531–1549, doi:10.1016/S0967-0645(99)00034-X.

Bosse, A., P. Testor, L. Mortier, L. Prieur, V. Taillandier, F. d'Ortenzio, and L. Coppola (2015), Spreading of Levantine Intermediate Waters by submesoscale coherent vortices in the northwestern Mediterranean Sea as observed with gliders, *J. Geophys. Res. Oceans*, *120*, 1599–1622, doi:10.1002/2014JC010263.

Bower, A. S., and H. H. Furey (2012), Mesoscale eddies in the Gulf of Aden and their impact on the spreading of Red Sea Outflow Water, *Prog. Oceanogr.*, *96*(1), 14–39, doi:10.1016/j.pocean.2011.09.003.

Bower, A. S., H. D. Hunt, and J. F. Price (2000), Character and dynamics of the Red Sea and Persian Gulf outflows, *J. Geophys. Res.*, *105*(C3), 6387–6414, doi:10.1029/1999JC900297.

Capet, X., F. Colas, J. McWilliams, P. Penven, and P. Marchesiello (2008), Eddies in eastern boundary subtropical upwelling systems, in *Ocean Modeling in an Eddying Regime, Geophys. Monogr. Ser.*, edited by M. W. Hecht and H. Hasumi, pp. 131–147, AGU, Washington, D. C.

Carton, X., P. L'Hegaret, and R. Baraille (2012), Mesoscale variability of water masses in the Arabian Sea as revealed by ARGO floats, *Ocean Sci.*, *8*, 227–248, doi:10.5194/os-8-227-2012.

Colas, F., X. Capet, J. C. McWilliams, and Z. Li (2013), Mesoscale eddy buoyancy flux and eddy-induced circulation in Eastern Boundary Currents, *J. Phys. Oceanogr.*, *43*(6), 1073–1095, doi:10.1175/JPO-D-11-0241.1.

Colin de Verdière, A. (1983), Lagrangian eddy statistics from surface drifters in the eastern North Atlantic, *J. Mar. Res.*, *41*(3), 375–398.

D'Asaro, E. A. (1988), Generation of submesoscale vortices: A new mechanism, *J. Geophys. Res.*, *93*(C6), 6685–6693.

Dewar, W., J. McWilliams, and J. Molemaker (2015), Centrifugal instability and mixing in the California Undercurrent, *J. Phys. Oceanogr.*, *45*(5), 1224–1241, doi:10.1175/JPO-D-13-0269.1.

Dong, C., J. C. McWilliams, and A. F. Shchepetkin (2007), Island wakes in deep water, *J. Phys. Oceanogr.*, *37*(4), 962–981, doi:10.1175/JPO3047.1.

Frolov, S., G. Sutyrin, G. Rowe, and L. Rothstein (2004), Loop current eddy interaction with the western boundary in the Gulf of Mexico, *J. Phys. Oceanogr.*, *34*(10), 2223–2237, doi:10.1175/1520-0485(2004)034¡2223:LCEIWT¿2.0.CO;2.

Griffiths, R. (1986), Gravity currents in rotating systems, *Annu. Rev. Fluid Mech.*, *18*(1), 59–89.

AGU Journal of Geophysical Research: Oceans 10.1002/2015JC011033

Gula, J., M. J. Molemaker, and J. C. McWilliams (2014), Submesoscale cold filaments in the Gulf Stream, *J. Phys. Oceanogr.*, *44*(10), 2617–2643, doi:10.1175/JPO-D-14-0029.1.

Gula, J., M. J. Molemaker, and J. C. McWilliams (2015), Topographic vorticity generation, submesoscale instability and vortex street formation in the Gulf Stream, *Geophys. Res. Lett.*, *42*, 4054–4062, doi:10.1002/2015GL063731.

Ilicak, M., T. M. Özgökmen, and W. E. Johns (2011), How does the Red Sea outflow water interact with Gulf of Aden Eddies?, *Ocean Modell.*, *36*(1), 133–148, doi:10.1016/j.ocemod.2010.10.006.

Johns, W., F. Yao, D. Olson, S. Josey, J. Grist, and D. Smeed (2003), Observations of seasonal exchange through the straits of Hormuz and the inferred heat and freshwater budgets of the Persian Gulf, *J. Geophys. Res.*, *108*(C12), 3391, doi:10.1029/2003JC001881.

Laanaia, N., A. Wirth, J.-M. Molines, B. Barnier, and J. Verron (2010), On the numerical resolution of the bottom layer in simulations of oceanic gravity currents, *Ocean Sci.*, *6*(2), 563–572, doi:10.5194/os-6-563-2010.

LaCasce, J. (2008), Statistics from Lagrangian observations, *Prog. Oceanogr.*, *77*(1), 1–29, doi:10.1016/j.pocean.2008.02.002.

LaCasce, J., and A. Bower (2000), Relative dispersion in the subsurface North Atlantic, *J. Mar. Res.*, *58*(6), 863–894, doi:10.1357/002224000763485737.

Legg, S., et al. (2009), Improving oceanic overflow representation in climate models: The gravity current entrainment climate process team, *Bull. Am. Meteorol. Soc.*, *90*, 657–670, doi:10.1175/2008BAMS2667.1.

Lemarié, F., J. Kurian, A. F. Shchepetkin, M. Jeroen Molemaker, F. Colas, and J. C. McWilliams (2012), Are there inescapable issues prohibiting the use of terrain-following coordinates in climate models?, *Ocean Modell.*, *42*, 57–79, doi:10.1016/j.ocemod.2011.11.007.

L'Hégaret, P. (2015), Etude de la circulation de mésoéchelle et des sorties d'eaux du Golfe Persique dans l'Océan Indien Nord-Ouest, PhD thesis, Univ. de Bretagne Occidentale, Brest, France.

L'Hégaret, P., L. Lacour, X. Carton, G. Roullet, R. Baraille, and S. Corréard (2013), A seasonal dipolar eddy near Ras Al Hamra (Sea of Oman), *Ocean Dyn.*, *63*, 633–659, doi:10.1007/s10236-013-0616-2.

L'Hégaret, P., R. Duarte, X. Carton, C. Vic, D. Ciani, R. Baraille, and S. Corréard (2015), Mesoscale variability in the Arabian Sea from HYCOM model results and observations: Impact on the Persian Gulf Water path, *Ocean Sci.*, *11*, 667–693, doi:10.5194/os-11-667-2015.

Mason, E., J. Molemaker, A. F. Shchepetkin, F. Colas, J. C. McWilliams, and P. Sangrà (2010), Procedures for offline grid nesting in regional ocean models, *Ocean Modell.*, *35*(1), 1–15, doi:10.1016/j.ocemod.2010.05.007.

McWilliams, J. C. (1985), Submesoscale, coherent vortices in the ocean, *Rev. Geophys.*, *23*(2), 165–182.

Molemaker, M. J., J. C. McWilliams, and W. K. Dewar (2015), Submesoscale instability and generation of mesoscale anticyclones near a separation of the California Undercurrent, *J. Phys. Oceanogr.*, *45*(3), 613–629, doi:10.1175/JPO-D-13-0225.1.

Nof, D. (1983), The translation of isolated cold eddies on a sloping bottom, *Deep Sea Res., Part A*, *30*(2), 171–182.

Oey, L.-Y., and H. Zhang (2004), The generation of subsurface cyclones and jets through eddy–slope interaction, *Cont. Shelf Res.*, *24*(18), 2109–2131, doi:10.1016/j.csr.2004.07.007.

Peters, H., W. E. Johns, A. S. Bower, and D. M. Fratantoni (2005), Mixing and entrainment in the Red Sea outflow plume. Part I: Plume structure, *J. Phys. Oceanogr.*, *35*(5), 569–583, doi:10.1175/JPO2679.1.

Pous, S., X. Carton, and P. Lazure (2004), Hydrology and circulation in the Strait of Hormuz and the Gulf of Oman—Results from the GOGP99 Experiment: 2. Gulf of Oman, *J. Geophys. Res.*, *109*, C12038, doi:10.1029/2003JC002146.

Price, J. F., and M. O'Neil Baringer (1994), Outflows and deep water production by marginal seas, *Prog. Oceanogr.*, *33*(3), 161–200, doi:10.1016/0079-6611(94)90027-2.

Reverdin, G., J.-C. Gascard, B. Le Cann, L. Prieur, M. Assenbaum, and P. Lherminier (2009), A long-lasting mode water vortex in the Northeast Atlantic Ocean, *J. Phys. Oceanogr.*, *39*(3), 536–558, doi:10.1175/2008JPO3970.1.

Risien, C., and D. Chelton (2008), A global climatology of surface wind and wind stress fields from eight years of QuikSCAT scatterometer data, *J. Phys. Oceanogr.*, *38*(11), 2379–2413, doi:10.1175/2008JPO3881.1.

Robinson, S. K. (1991), Coherent motions in the turbulent boundary layer, *Annu. Rev. Fluid Mech.*, *23*(1), 601–639.

Roullet, G., X. Capet, and G. Maze (2014), Global interior eddy available potential energy diagnosed from Argo floats, *Geophys. Res. Lett.*, *41*, 1651–1656, doi:10.1002/2013GL059004.

Senjyu, T., T. Ishimaru, M. Matsuyama, and Y. Koike (1998), High salinity lens from the Strait of Hormuz, in *Offshore Environment of the ROPME Sea Area After the War-Related Oil Spill*, edited by A. Otsuki, M. Y. Abdulraheem, and R. M. Reynolds, pp. 35–48, Terra Science Pub., Tokyo.

Shchepetkin, A., and J. McWilliams (2005), The regional oceanic modeling system (ROMS): A split-explicit, free-surface, topography-following-coordinate oceanic model, *Ocean Modell.*, *9*(4), 347–404, doi:10.1016/j.ocemod.2004.08.002.

Smith, W., and D. Sandwell (1997), Global sea floor topography from satellite altimetry and ship depth soundings, *Science*, *277*(5334), 1956–1962, doi:10.1126/science.277.5334.1956.

Stephens, J. (1997), Linear stability analysis of a gravity current over topography, in *Double-Diffusive Processes: 1996 Summer Study Program in Geophysical Fluid Dynamics*, edited by S. Meacham, pp. 287–310, Woods Hole Oceanogr. Inst., Mass.

Sutyrin, G. G., and R. Grimshaw (2010), The long-time interaction of an eddy with shelf topography, *Ocean Modell.*, *32*(1), 25–35, doi:10.1016/j.ocemod.2009.08.001.

Thoppil, P. G., and P. J. Hogan (2009), On the mechanisms of episodic salinity outflow events in the Strait of Hormuz, *J. Phys. Oceanogr.*, *39*(6), 1340–1360, doi:10.1175/2008JPO3941.1.

Vic, C., G. Roullet, X. Carton, and X. Capet (2014), Mesoscale dynamics in the Arabian Sea and a focus on the Great Whirl life cycle: A numerical investigation using ROMS, *J. Geophys. Res. Oceans*, *119*, 6422–6443, doi:10.1002/2014JC009857.

Wei, J., and D.-P. Wang (2009), A three-dimensional model study of warm core ring interaction with continental shelf and slope, *Cont. Shelf Res.*, *29*(13), 1635–1642, doi:10.1016/j.csr.2009.05.009.

Wirth, A. (2009), On the basic structure of oceanic gravity currents, *Ocean Dyn.*, *59*(4), 551–563, doi:10.1007/s10236-009-0202-9.

Worley, S., S. Woodruff, R. Reynolds, S. Lubker, and N. Lott (2005), ICOADS release 2.1 data and products, *Int. J. Climatol.*, *25*(7), 823–842, doi:10.1002/joc.1166.

4.3 Supplementary Information

4.3.1 Parallel Shear Flow Instabilities

In this section, we test the hypothesis that the size of Submesoscale Coherent Vortices (SCVs) generated by friction in boundary layers (Figure 4.2) is compatible with the size of vortices generated by parallel shear flow instability (purely barotropic). We use the simple framework of Rayleigh (1880) for two-dimensional incompressible flow. We solve the linear instability problem for a piecewise linear flow (pages 251-256 in Vallis, 2006).

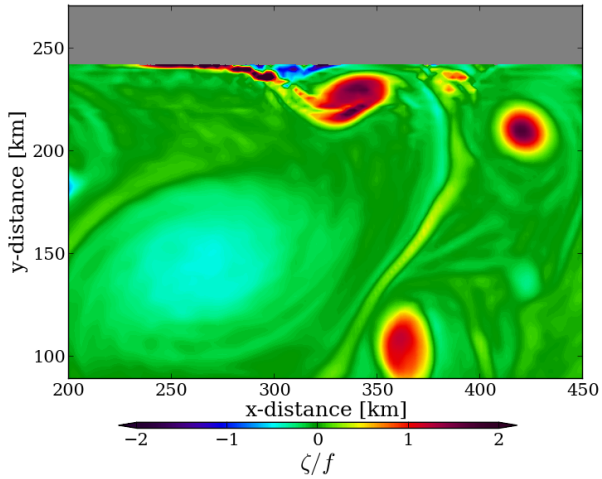

Figure 4.2: Snapshot at 400 m from the idealized experiment. A mesoscale anticyclone (blue core of negative relative vorticity) drags on the northern slope and generates opposite sign vorticity. The thin vorticity strip detaches from the slope and rolls up into submesoscale cyclones (red structures).

Analysis

We suppose the basic state to be a parallel flow in the x direction (Figure 4.3). It illustrates what occurs just after the vorticity strip detachment (Figure 4.2, $x \sim 300$ km, $y \sim 240$ km). The background velocity field ($y < -b$) is thus the one of the mesoscale eddy (except that it does not decrease going to the eddy center) that has been sheared in the boundary layer. Vorticity is concentrated in the shear layer of width d ($-b < y < -a$). The basic state is :

$$\begin{cases} U_1 = 0, & -a < y < 0 \\ U_2 = -\frac{U_0}{d}(y+b) + U_0, & -b < y < -a \\ U_3 = U_0, & y < -b \end{cases} \tag{4.1}$$

We assume a solution of Rayleigh's equation (linear vorticity equation for disturbances

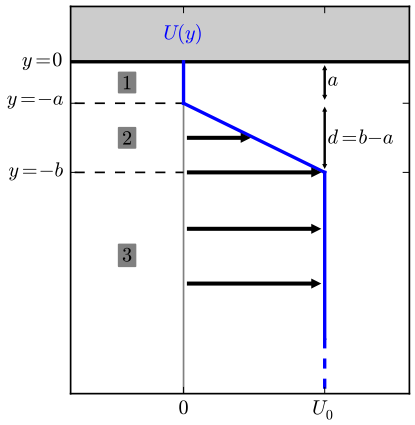

Figure 4.3: Barotropically unstable parallel shear flow $U(y)$ (blue line). The vorticity is concentrated in $-b < y < -a$ (layer of width $d = b - a$). Distance from the boundary layer (where vorticity has been created) is a.

to parallel shear flow) of the form :

$$\begin{cases} \psi_1 = A\,\mathrm{e}^{-k(y+a)} + B\,\mathrm{e}^{k(y+a)}, & -a < y < 0 \\ \psi_2 = C\,\mathrm{e}^{-k(y+a)} + D\,\mathrm{e}^{k(y+b)}, & -b < y < -a \\ \psi_3 = E\,\mathrm{e}^{k(y+b)}, & y < -b \end{cases} \tag{4.2}$$

Where total solutions for disturbances are written $\Psi_i' = \psi_i(y)\,\mathrm{e}^{ik(x-ct)}$, $i = 1, 2, 3$. The wavenumber of the disturbance is k and c is the phase speed of the wave if purely real (the disturbance is not a growing mode) and is related to the growth rate of the disturbance if it has a positive imaginary part (the growth rate is $k\Im(c)$). These solutions (4.2) must match two conditions :

1. Continuity of pressure across interfaces (namely, at $y = -a$ and $y = -b$) :

$$\Delta\left[(U-c)\frac{\partial\psi}{\partial y} - \psi\frac{\partial U}{\partial y}\right] = 0, \tag{4.3}$$

2. Continuity of normal velocity across interfaces :

$$\Delta\left[\frac{\psi}{U-c}\right] = 0, \tag{4.4}$$

where Δ is the difference between values across the interface.

We apply the jump conditions at the interfaces at $y = -a$ and $y = -b$ and obtain the

following relations between the coefficients :

$$\begin{array}{rl} A(kc) + B(-kc) + C\left(-kc - \frac{U_0}{d}\right) + D\left[\left(kc - \frac{U_0}{d}\right)\mathrm{e}^{kd}\right] & = 0 \\ A + B - C - D\,\mathrm{e}^{kd} & = 0 \\ C\left[\left(-(U_0 - c)k + \frac{U_0}{d}\right)\mathrm{e}^{kd}\right] + D\left((U_0 - c)k + \frac{U_0}{d}\right) + E\left(-(U_0 - c)k\right) & = 0 \\ C\,\mathrm{e}^{kd} + D - E & = 0 \end{array} \tag{4.5}$$

The second condition also applies to the northern boundary interface :

$$A\,\mathrm{e}^{-ka} + B\,\mathrm{e}^{ka} = 0 \tag{4.6}$$

This set of 5 homogeneous equations (4.5-4.6) may be written in the form of a matrix equation :

$$\mathbf{M}\ (A\ B\ C\ D\ E)^T = 0 \tag{4.7}$$

with :

$$\mathbf{M} = \begin{pmatrix} \mathrm{e}^{ka} & \mathrm{e}^{-ka} & 0 & 0 & 0 \\ kc & -kc & -kc - \frac{U_0}{d} & \left(kc - \frac{U_0}{d}\right)\mathrm{e}^{kd} & 0 \\ 1 & 1 & -1 & -\mathrm{e}^{kd} & 0 \\ 0 & 0 & \left(-(U_0 - c)k + \frac{U_0}{d}\right)\mathrm{e}^{kd} & (U_0 - c)k + \frac{U_0}{d} & -(U_0 - c)k \\ 0 & 0 & \mathrm{e}^{kd} & 1 & -1 \end{pmatrix} \tag{4.8}$$

The determinant of the matrix must be zero for non-trivial solutions. In the general case, $\det(\mathbf{M})$ has a (very) complicated form. If we assume that the boundary is far from the shear layer, $a \to \infty$, we have $\det(\mathbf{M}) \to \mathrm{e}^{ka}\det(\mathbf{M'})$, **M'** being the extraction of **M** from lines 2 to 5 and columns 2 to 5. In this case, we just solve $\det(\mathbf{M'}) = 0$.

$$\det(\mathbf{M'}) = \frac{4\,\mathrm{e}^{2dk}}{d^2}\left[d^2k^2c^2 + \frac{U_0^2}{4}\left(\mathrm{e}^{-2dk} - (1 - dk)^2\right)\right] \tag{4.9}$$

$$\det(\mathbf{M'}) = 0 \Longleftrightarrow c^2 = \frac{U_0^2}{4d^2k^2}\left[(1 - dk)^2 - \mathrm{e}^{-2dk}\right] \tag{4.10}$$

Results

From relation (4.10), one may find that instability occurs if $c^2 < 0$ and c has a positive imaginary part. It is the case for wavelengths ($\lambda = 2\pi/k$) that are long enough : $dk \lesssim 1.3$, i.e., $\lambda \gtrsim 4.8\,d$. Figure 4.4 shows the growth rate as function of wavenumber, computed from relation (4.10). The most unstable wavenumber is $dk \sim 0.78$, i.e., $\lambda \sim 8.1\,d$. This means that we can expect, in the limit of validity of the linear instability theory, that a characteristic length scale of the SCVs is 8 times the width of the boundary layer.

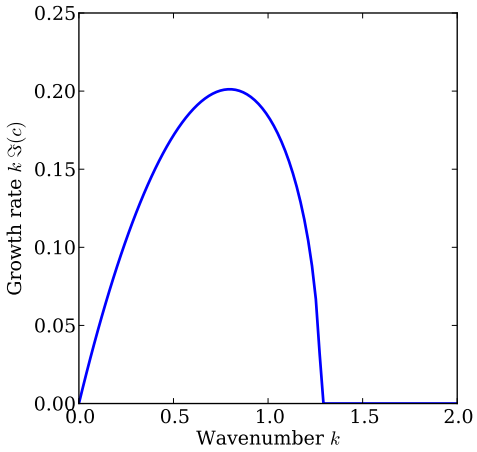

Figure 4.4: Growth rate $k\,\Im(c)$ as a function of wavenumber k. c and k are non-dimensionalized by U_0 and $1/d$ respectively.

Redimensionalizing the growth rate and the wavelength of the most unstable wave with $U_0 = 0.3$ m s^{-1} and $d = 5$ km gives a wavelength of 40 km and a growth rate of 1 day^{-1}. This is approximately the size of the SCVs (Figure 4.2) and the order of magnitude of time necessary for the shear layer to roll up into SCVs. Hence, the mechanism generating SCVs in our numerical experiments (once the vorticity strip, i.e. shear layer, is detached from the boundary) is compatible with the simple parallel shear flow instability theory.

To go further : in a course note by McIntyre (2005), the suppression of shear instabilities by boundary constraints is alluded. "These are cases with the side boundaries so close to the shear layer that the Rossby-wave propagation mechanism does not have room to operate sufficiently strongly to hold a phase-locked configuration."

Chapter 5

Dynamics of the Oman Upwelling

Contents

5.1 Introduction

The seasonal upwellings occuring along the coasts of Somalia and Oman have not been deeply examined compared to Eastern Boundary Upwelling Systems (EBUS, see the review of Capet et al., 2008a). Motivation to study the Arabian Sea upwellings is twofold. On the one hand, their impacts on regional climate[1] and ecosystems have been found to be strong. In fact, they were early revealed to be of primary importance in the heat budget of the Arabian Sea (Düing and Leetmaa, 1980). Besides, their role in the sustainment of ecosystems in driving the summer phytoplankton bloom has also been observed for a long time (Banse, 1987). On the other hand, there is a more theoretical motivation to study these upwellings as there are fundamental reasons to elaborate on a different functioning of western and eastern boundary upwelling systems. The principal one is the onshore vs. offshore propagation of Rossby waves that allow dissipating vs. delivering energy to the system (as mentioned in Marchesiello et al., 2000).

The following manuscript (to be submitted soon) focuses on the upwelling off Oman and has two main objectives. The first one is to provide a modeled description of the upwelling off Oman in terms of currents, temperature structure and eddy kinetic energy budget. This part is strongly inspired by the work done on EBUS by Marchesiello et al. (2003); Capet et al. (2008a,b); Colas et al. (2012, 2013). It thus allows a systematic comparison between eastern and western boundary upwellings, with dynamical interpretations. The second objective is to investigate closely the Rossby wave dynamics in the upwelling context. Therefore, we give a qualitative and quantitative description of the regional scale functioning of the upwelling. On the other hand, the study mostly leaves aside the ∼10-50 km details of the dynamics that is due to some small scales in the forcing : topographic irregularities, indented coastline and cape effects on wind stress curl. These details are resolved by the model. They certainly play a role on the continental shelf and shelf break dynamics and would deserve a study on their own right.

[1] They influence precipitations over the Indian continent for instance (Izumo et al., 2008; Xie et al., 2009)

5.2 Article in preparation

Western boundary upwelling dynamics off Oman

C. Vic,[1] X. Capet,[2] G. Roullet[1] and X. Carton[1]

[1]*Laboratoire de Physique des Océans, UMR 6523, CNRS/Ifremer/IRD/UBO, 6 Avenue Le Gorgeu, 29200 Brest, France.*

[2]*IPSL/LOCEAN, UMR 7159, CNRS/UPMC/IRD/MNHN, 4 Place Jussieu, 75252 Paris cedex 05, France.*

5.2.1 Abstract

Despite its climatic and ecosystemic significance, the coastal upwelling taking place off Oman is poorly known. The authors use a regional model forced by climatological wind stress to investigate its dynamics. The model is found to compare favorably with existing observations. In particular, the thermal structure, the surface circulation pattern (mean and turbulent) and the sea surface temperature (SST) seasonal cycle are well represented. The underlying dynamics is examined and it is demonstrated that : (i) EKE generation through baroclinic/barotropic instability of the upwelling jet has a contribution to EKE comparable to that of the remote open ocean sources (which tend to feed the western part of the basin through beta drift); (ii) Rossby wave field excited by wind stress curl, in an area situated $O(1-10)\,R_d$ from the coast, interacts with the western boundary and plays an essential role in sustaining the cooling of the upwelling area. Specifically, linear Rossby wave arguments allow the authors to explain the 1.5 month lag between SST minimum and forcing maximum (wind stress and wind stress curl). These results strongly contrast with those for eastern boundary upwelling systems where EKE essentially results from local instability of the upwelling system and SST is more tightly coupled to wind forcing. At smaller scales, ∼10–50 km major heterogeneities due to geomorphological irregularities are present in the system and would need further investigation.

5.2.2 Introduction

Currents in the Arabian Sea are primarily driven by monsoonal winds (Lee et al., 2000; Schott and McCreary, 2001). Along with the twice yearly reversal of the monsoonal

winds, surface boundary currents also reverse. During the summer monsoon, strong upwellings occur in the western Arabian Sea, over a wide area along Somali and the Arabian Peninsula. Their strong impact on the heat budget of the Arabian Sea was early revealed by Düing and Leetmaa (1980). The Somali upwelling was subsequently thoroughly investigated (e.g., Schott and Quadfasel, 1982; Schott, 1983; McCreary and Kundu, 1985; Fischer et al., 1996) while the upwelling sector situated further north offshore of Oman has received comparatively limited attention.

The Oman upwelling is of primary importance in the ecosystems of the Arabian Sea in driving the summer phytoplankton bloom (e.g., Banse, 1987; Lévy et al., 2007). It also plays a major role in the Indian monsoon rainfall variability, hence on the Asian continent climate, as revealed by global coupled ocean-atmosphere numerical models (Izumo et al., 2008). Only a few studies are dedicated to observation and understanding of this upwelling functioning but measures are sparse with a very limited temporal coverage (Elliott and Savidge, 1990; Savidge et al., 1990; Manghnani et al., 1998; Shi et al., 2000).

Elliott and Savidge (1990) highlight specific features of this upwelling. It is found to be (i) active only seasonally, roughly during the summer monsoon, being driven by alongshore reversing monsoonal winds and (ii) coupled with a very intense and turbulent surface circulation linked with its position on a western boundary. These make it being fundamentally different from more thoroughly studied Eastern Boundary Upwelling Systems (EBUS, composed of the Canary, Benguela, Peru-Chile and California upwelling systems, Capet et al., 2008a), which show less seasonal variability at similar or even higher latitudes and are dynamically more isolated because of their position on eastern boundaries. In fact, transient features in the ocean (except in the Antarctic Circumpolar Current), whether being coherent structures (eddies) or wave-like motions, mostly follow a westward propagation (e.g., Fu, 2004). Schematically, turbulence generated at eastern boundaries is radiated westward in the open ocean, whereas western boundaries can receive turbulent features generated far to the east in the inner basin (Chelton et al., 2011). As such, we expect the Oman upwelling to be influenced by remotely forced signals. Interactions between incoming Rossby waves and western boundary currents have been documented and analysed in several regions, including the East Australian Current (Marchesiello et al., 2000) and the Brazil Current (Azevedo et al., 2012). It has also been suggested to occur in the Somali Current by McCreary and Kundu (1985). Whereas "at eastern boundaries, coastal upwelling currents leak consistently offshore by means of the radiation of Rossby waves" (Marchesiello et al., 2000), energy transported by these waves tends to pile up at western boundaries (McCreary and Kundu, 1985).

The objective of this study is threefold. First, we aim to investigate the structure and dynamics of the Oman upwelling in light of what has been done for EBUS, with a

particular focus on eddy kinetic energy (EKE) distribution, generation and propagation. Second, we investigate specifically the impact of Rossby waves on the upwelling structure, as they are expected to influence its dynamics. Third, we assess the contribution of different mechanisms in the mixed layer cooling during the upwelling. We use a regional model to do so, with a sufficient resolution to fully resolve mesoscales (Δx=2 km). This rather high resolution ensures that the mesoscale is well resolved and that its accompanying frontal activity is in large part accounted for (Capet et al., 2008b; Marchesiello et al., 2011). In parallel, the use of a two-layer linear shallow-water model forced by a realistic wind stress curl allows to isolate wave mechanisms. It gives instructive insights on the reflection of waves in the upwelling context.

Our main findings can be summarized as follows : Similarly to EBUS, the coastal upwelling jet is found to generate significant EKE (mainly through baroclinic instability) but the upwelling area is also impacted by mesoscale turbulence generated offshore that drifts onshore. Besides, a lag of $\sim$ 1.5 month is found between the maximum of the upwelling favorable atmospheric conditions (wind stress and wind stress curl) and the peak of the associated oceanic response (when the surface temperature reaches its minimum). We argue that this is consistent with a Rossby wave propagation and reflection mechanism that traps anomalies at the coast, thus reinforcing and sustaining the wind-driven upwelling. Precisely, an upwelling long wave is triggered by an intense positive wind stress curl during the summer monsoon. It propagates westward and reflects at the western boundary into a shorter mode. This mode propagates eastward at a very slow speed, thus traps the upwelling anomaly at the coast at a seasonal scale. Finally, the mixed layer heat budget confirms the importance of vertical advection, thus of the wind stress curl, in cooling the surface layers during the upwelling.

The outline of the paper is as follows. The model configuration is presented in section 5.2.3 and an extensive characterization of the upwelling follows in section 5.2.4. EKE generation and propagation is quantified in section 5.2.5. The mechanisms of Rossby wave reflection are investigated in section 5.2.6 and a mixed-layer heat budget is performed in section 5.2.7. Finally, conclusions are drawn and perspectives on future work are elaborated in section 5.2.8.

5.2.3 Numerical framework

We use the Regional Oceanic Modelling System (ROMS, Shchepetkin and McWilliams, 2005). An off-line one-way nested configuration with a 2 km horizontal resolution is set up from a parent solution described in Vic et al. (2014b) at 6.6 km resolution. The fine-scale domain and topography are shown in Fig. 5.1. The nesting approach follows the procedure of Mason et al. (2010). Boundary conditions are extracted from the parent solution to

force the nested solution for 4 years. Topography is from the Shuttle Radar Topography Mission dataset at 30' of resolution (SRTM30-plus, Becker et al., 2009). Atmospheric forcing is monthly and climatological as we do not elaborate on interannual variability (that may involve ocean-atmosphere interactions, Izumo et al., 2008) but rather focus on the upwelling merely forced by the atmosphere. Wind stress is from the Scatterometer Climatology of Ocean Winds (SCOW, Risien and Chelton, 2008) and heat and water fluxes are from the International Comprehensive Ocean Atmosphere Dataset (ICOADS, Worley et al., 2005).

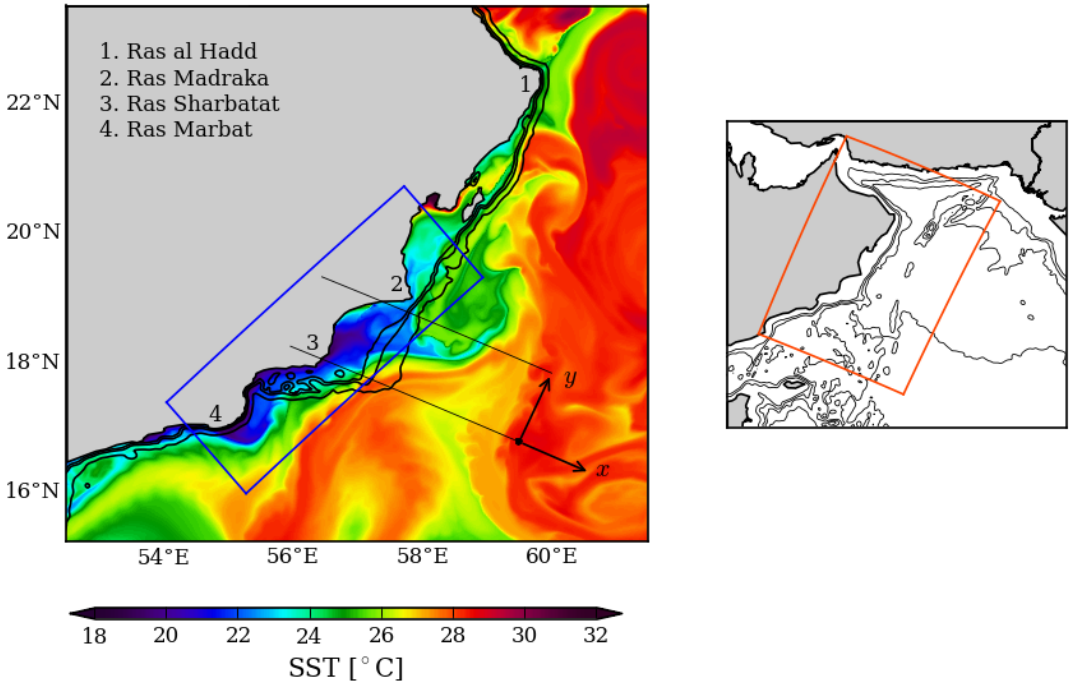

Figure 5.1: Snapshot of sea surface temperature during an upwelling event off the Oman coast. Thick black lines are isobaths 100, 200 and 1000 m. The blue rectangle is the area where variables in Fig. 5.2 are averaged. Thin parallel black lines limit a region where the shelf is almost alongshore invariant. The (x, y) arrows represent the coordinate system used to draw sections (e.g., Fig. 5.5). The inset map on the right shows the nested domain (orange rectangle) and isobaths 1000, 2000, 3000 and 4000 m (black lines).

The turbulent vertical mixing is parameterized by the K-profile parameterization (KPP, Large et al., 1994) for the surface and bottom boundary layers. The boundary layer thickness (used to compute mixed layer heat budget in section 5.2.7) is diagnosed by comparing a bulk Richardson number to a critical value. The boundary layer mixing scheme connects to an interior mixing scheme that takes into account three processes : static instability (convection), vertical shear and internal wave breaking (for details on interior and boundary layer mixing, see appendix in Jullien et al., 2012). The bottom stress is linear with a drag coefficient $C_d = 3 \times 10^{-4}$ m s^{-1} (in the range of values commonly used, e.g., Dong et al., 2007).

The simulation has already been used in a different context and the reader is refered

to Vic et al. (2015) for further information. In section 5.2.4, we assess the model ability to reproduce observational fields related to the upwelling season.

5.2.4 Model regional circulation and evaluation

In this section, we consider the seasonality of the dynamics off Oman which helps us define the upwelling season. We then examine some general characteristics of the mean circulation and hydrography during this period of interest. In parallel, we assess the model performance in comparison to observational datasets.

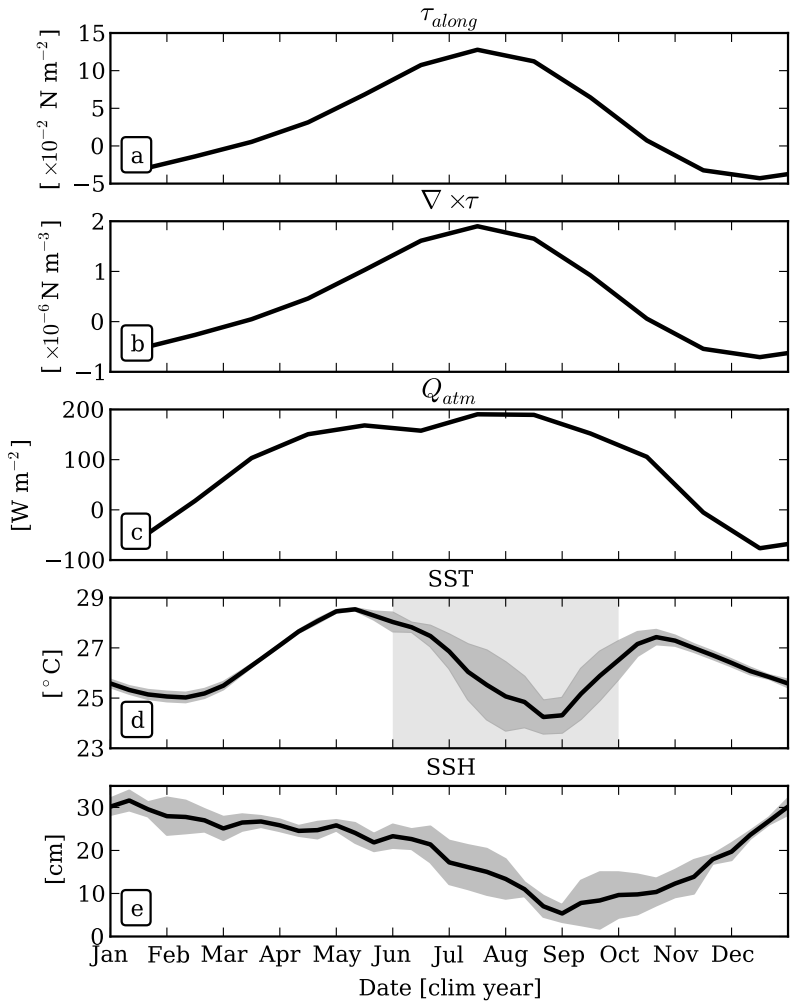

Figure 5.2: Time series of (a) alongshore wind stress, (b) wind stress curl, (c) atmospheric net heat flux, (d) sea surface temperature (SST) and (e) sea surface height (SSH). All variables are averaged in the blue rectangle in Fig. 5.1. SST and SSH are averaged over the 4 years of simulations and dark gray shaded areas represent one standard deviation on each part of the mean (biased estimator). Light gray area defines the upwelling season.

System seasonality

Due to the sparseness of observations in the region, literature is vague on the upwelling spin up and spin down periods. Figure 5.2a,b,c show a climatological time series of the surface atmospheric forcing relevant to describe the regional seasonal cycle : alongshore wind stress τ_{along}, wind stress curl $\nabla \times \tau$, and net heat flux Q_{atm}[2]. These fields are averaged in an area covering the upwelling (blue box in Fig. 5.1). Figure 5.2d,e show the modeled climatological sea surface temperature (SST) and sea surface height (SSH), averaged in the same area. All oceanic forcing display a dominant annual cycle, characteristic of the monsoonal pace in the Arabian Sea (e.g., Schott and McCreary, 2001). τ_{along} is approximately in the direction of the dominant monsoonal winds in this region, blowing northeastward during the summer monsoon (mid-May to mid-September) and southwestward during the winter monsoon (mid-November to March). The winds are stronger during the summer monsoon and τ_{along} partly reflects the signature of the Findlater Jet that is almost parallel to the Arabian Peninsula during this season (Findlater, 1969). The onshore side from the axis of the Findlater Jet is characterized by a strong positive wind stress curl extending on more than 200 km offshore the Oman coast (e.g., Fig. 1c in Vic et al., 2014b). Thus both τ_{along} and $\nabla \times \tau$ are upwelling favorable forcing during the summer monsoon (Manghnani et al., 1998), respectively triggering Ekman coastal divergence and Ekman pumping (e.g., Bakun and Nelson, 1991). This explains the weak SST from mid-May to mid-October that reveals the seasonal coastal upwelling (Fig. 5.2d). We define the upwelling season from June to September (4 months) using Fig. 5.2d, when SST is significantly lower (by $\sim 0.5°C$) than semi-annual maxima. In the following, the brackets denote an average on the upwelling season through the 4 years of simulation.

A remarkable feature of the annual cycle of SST is the ~ 1.5 month lag between the maximum of upwelling forcing (τ_{along} and $\nabla \times \tau$) and the response of the ocean (SST and SSH minima). Although not quantified, this phase difference has been noticed in observing SST derived from Advanced Very High Resolution Radiometer and SSH derived from satellite altimetry (Manghnani et al., 1998). In EBUS, it has been shown that the ocean's Ekman response to synoptic events of upwelling favorable winds has a lag of a few days (Wang, 1997; Renault et al., 2012). This raises the issue of a companion forcing to the wind in the upwelling sustainment that may be specific to western boundaries (we tackle this question in section 5.2.6). Another noticeable feature is the strong standard deviation in SST that occurs primarily during the upwelling season. It reveals an intense

[2]In the model, the wind stress is directly prescribed and the net heat flux is adjusted to better simulate SST. Notice that the adjustment is limited and the net heat flux received by the model is essentially identical to ICOADS observations presented in Fig. 5.2c.

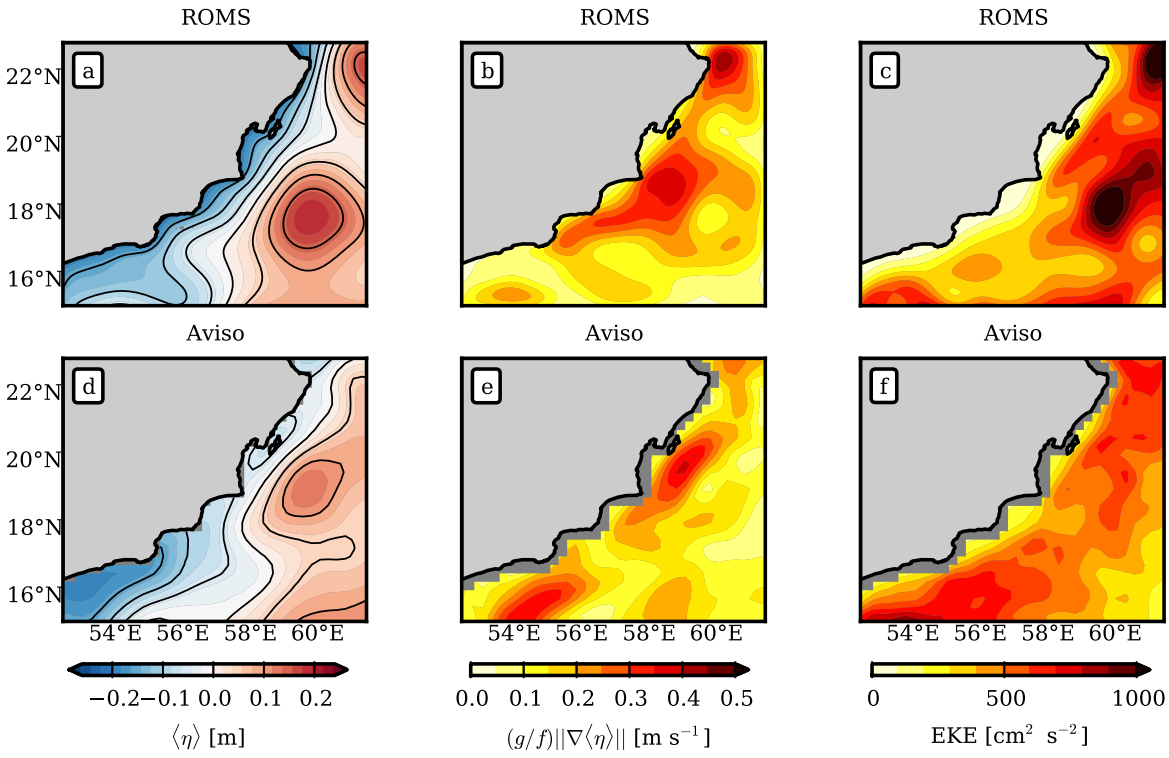

Figure 5.3: (left) Mean SSH $\langle\eta\rangle$, (center) surface geostrophic currents $(g/f)||\nabla\langle\eta\rangle||$ and (right) EKE during the upwelling season for (top) the ROMS simulation and (bottom) Aviso absolute dynamics topography (ADT). ROMS SSH has been low-pass filtered at 30 km (Gaussian filter) to be comparable to Aviso ADT (same technique is used in Capet et al., 2008a), and both field means have been set to zero to exhibit the same range of variation. Currents in ROMS have also been filtered to compute EKE.

intrinsic (forcing are climatological) interannual variability probably due to an enhanced mesoscale circulation (also noticed in Shi et al., 2000). In the remainder of the study we focus on the upwelling season.

Surface circulation

Figure 5.3 shows the mean SSH during the upwelling season $\langle\eta\rangle$ and the mean geostrophic current intensity derived from $\langle\eta\rangle$, $(g/f)||\nabla\langle\eta\rangle||$ (g is the acceleration of gravity and f is the local Coriolis frequency) for ROMS and Aviso's absolute dynamics topography gridded at a resolution of 1/4° (Rio et al., 2011). The mean geostrophic flow is directed northeastward along the coast, in the direction of the wind stress. Similarly to EBUS, the Ekman divergence at the coast drives an SSH low supporting a geostrophic coastal jet (Figs. 5.3a,d). The path of this current reaches the peninsula's easternmost cape (Ras al Hadd, Fig. 5.1), detaches and generates the Ras al Hadd Jet (Böhm et al., 1999). ROMS and Aviso $\langle\eta\rangle$ are comparable in the domain, with larger discrepancies nearshore where Aviso has difficulties to capture the SSH properly as commonly found (Vignudelli et al., 2005). Both fields display a persistent anticyclonic structure offshore Ras Madraka that

reinforces the northeastward circulation.

Intensity of the circulation is comparable in ROMS and in Aviso (Figs. 5.3b,e), with peak geostrophic velocity of 0.5 m s^{-1}. Although maxima are not exactly colocated, they are both located in the path of the upwelling jet where the circulation is intensified by the standing anticyclone.

Seasonal EKE also compares well (Figs. 5.3c,f) although ROMS is slightly more energetic even after filtering the currents (see caption of Fig. 5.3). Interestingly, both fields display a local increase of EKE downstream Ras Madraka, where the circulation is maximum. Notice that the annual EKE over the whole domain (not shown here) is higher in ROMS than in Aviso by $\sim 20\%$ (Fig. 3 in Vic et al., 2015).

Vertical structure

The indented coastline and shelf break and the relatively small upwelling area (Fig. 5.1) complicate the analysis compared to usual situations along EBUS with long and nearly straight stretches of coastlines (California and Peru-Chile coasts for instance). In this subsection, we focus on the central bay, located between Ras Madraka and Ras Sharbatat (Fig. 5.1), where the shelf is relatively alongshore invariant. Alongshore (y) and cross-shore (x) directions are defined in Fig. 5.1. For a variable X, $\overline{X}$ denotes an alongshore average in the bay area (Fig. 5.1) and $X_H = \int_H^\eta X \, \mathrm{d}z$, where H is the ocean depth. Recall that $\langle X \rangle$ is a time mean during the upwelling season.

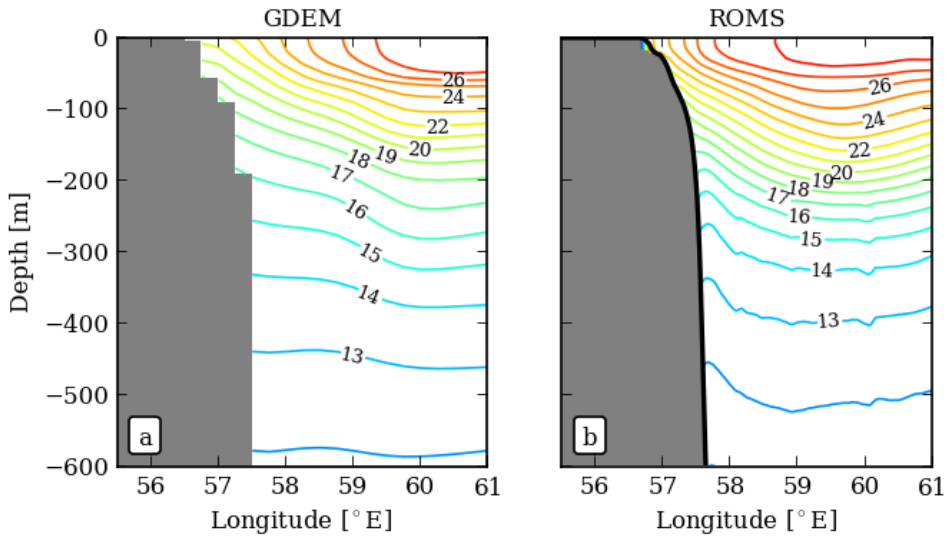

Figure 5.4: Alongshore and time averaged temperature $\langle \overline{T} \rangle$ during the upwelling season in (left) GDEM (Teague et al., 1990) and (right) ROMS.

The temperature structure of the upwelling is shown in Fig. 5.4 and evaluated against the Generalized Digital Environment Model observational dataset (GDEM, that has been

shown to better represent seasonal frequencies compared to other hydrographic climatologies, Teague et al., 1990). Overall, there is a good agreement between both fields, albeit with a global warm bias (all isotherms being shifted upward by 10 to 50 m compared to GDEM) that may be linked with a too strong net heat flux[3]. Isotherms tilt upward when approaching shore as expected in coastal upwellings. This tilt is present down to 300 m in agreement with the synoptic measurements in Elliott and Savidge (1990). This is much deeper than in EBUS, where the upward tilt is constrained to the upper 150 m in the Peru-Chile current system (Colas et al., 2012) and to the upper 100 m in the California current system (Capet et al., 2008b). This is consistent with the deepening of the main pycnocline westward at a basin scale (e.g., Chelton et al., 1998) and with the increasing depth of the wind's influence from eastern to western boundaries due to a weaker stratification (see section 14.8.1 in Vallis, 2006).

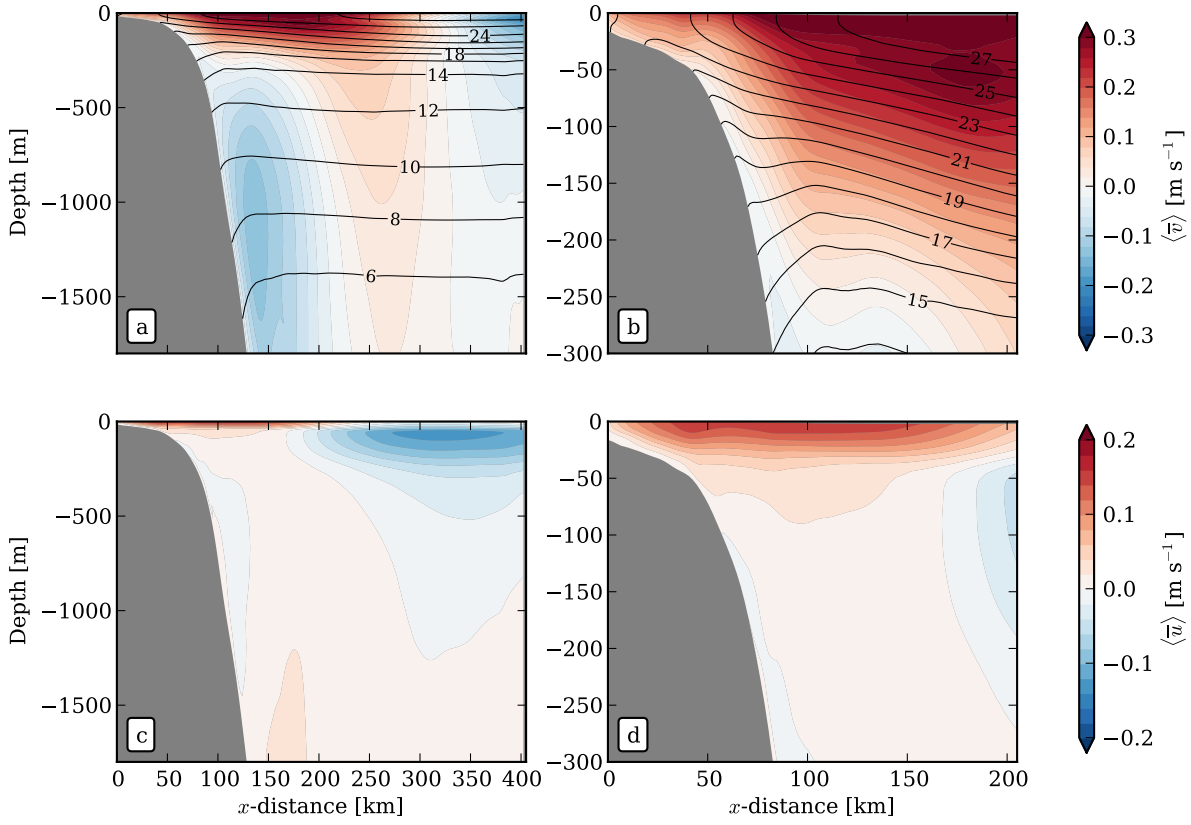

Figure 5.5: Sections of time and alongshore averaged (a,b) alongshore velocity $\langle\overline{v}\rangle$ and (c,d) cross-shore velocity $\langle\overline{u}\rangle$. Left panels are zoomed in on right panels. Black thin lines on panels (a,b) are the time and alongshore averaged temperature $\langle\overline{T}\rangle$. Notice that colorbars are differents for $\langle\overline{v}\rangle$ and $\langle\overline{u}\rangle$.

Figure 5.5 shows mean alongshore $\langle\overline{v}\rangle$ and across-shore $\langle\overline{u}\rangle$ currents. Because of limited averaging standing mesoscale patterns present in the region affect the offshore part of this

[3]Uncertainty in the net heat flux in this region is large. We compared short wave radiations from ICOADS (Worley et al., 2005), the Common Ocean-Ice Reference Experiment dataset (CORE2, Large and Yeager, 2009) and the Clouds and Earth's Radiant Energy System dataset (CERES, Kato et al., 2013) and found local discrepancies of up to 80 W m^{-2}.

cross-sections (e.g., circulation patterns 200 km offshore and more are influenced by the standing eddy visible in Fig. 5.3a centered at 18°N, 60°E). They nevertheless provide useful information on the vertical and cross-shore structure of the nearshore currents. The nearshore structure (∼200 km from shore) of $\langle\overline{v}\rangle$ is similar to EBUS with a surface intensified current flowing in the downwind direction (geostrophically balanced by the SSH low at the coast), and a weaker undercurrent in the opposite direction. Consistently with the deep isotherms tilt, the upper ocean poleward current reaches ∼250 m, deeper than in EBUS (50 m, Colas et al., 2012). Note that this flow is part of the regional circulation. In summer, the upper ocean circulation rotates clockwise in the Arabian Sea, as a consequence of the large scale wind patterns, with the Somali Current (Schott and McCreary, 2001) (resp. Ras Al Hadd Jet, Böhm et al., 1999) begin located upstream (resp. downstream) of our region of interest. The undercurrent is also part of the large-scale circulation. It is present in the parent domain in the latitude range 5°N–22°N. Notice that this undercurrent only exists during summer and that currents are much more barotropic during winter (not shown). The depth of its core is ∼1000 m, i.e., much deeper than found in EBUS (∼150–200 m). A similar structure, though not seasonal, is found in the Brazil Current system, with a deep undercurrent core at 800 m (Da Silveira et al., 2004), as well as in the Agulhas (Beal and Bryden, 1997; Beal, 2009) and East Australian (Mata et al., 2000) current systems.

Cross-shore velocity $\langle\overline{u}\rangle$ (Figs. 5.5c,d) consists of an offshore flow in the surface Ekman layer (upper 50 m) and an underlying onshore flow with a core around 75 m. Although currents are also stronger than in EBUS, the vertical structure of $\langle\overline{u}\rangle$ shares more similarities with EBUS than $\langle\overline{v}\rangle$, with depth ranges being comparable. Indeed, Ekman dynamics is supposedly independent of where the wind stress acts (interior, western or eastern boundary). The onshore return flow feeding the upwelling is not visible in this figure. Our interpretation supported by the description of bottom flow over the shelf offered in conclusion is that onshore advection induced by the coastal upwelling mainly takes place southwest of the section.

5.2.5 Eddy kinetic energy

In EBUS, upwelling dynamics coexists with its associated turbulent activity that is generated locally, mainly through baroclinic instability (Marchesiello et al., 2003). In particular, EKE in EBUS is strongly modulated by the seasonal cycle of upwelling winds (Kelly et al., 1998). Once generated, surface intensified EKE propagates offshore at roughly the speed of long baroclinic Rossby waves (Kelly et al., 1998; Marchesiello et al., 2003). It is also redistributed vertically, energizing the subsurface ocean (Haney et al., 2001). In contrast, western boundaries in the ocean are subjected to remotely forced mesoscale

turbulence that has drifted westward due to the planetary β effect. This turbulence then interacts with the coastal dynamics. To which extent the intense upwelling current system present off Oman contributes to the turbulence it is subjected to is thus an open question. Manghnani et al. (1998) hypothesized that upwelled water is passively advected offshore by incoming mesoscale eddies. Our simulation analysed below reveals a more complex situation.

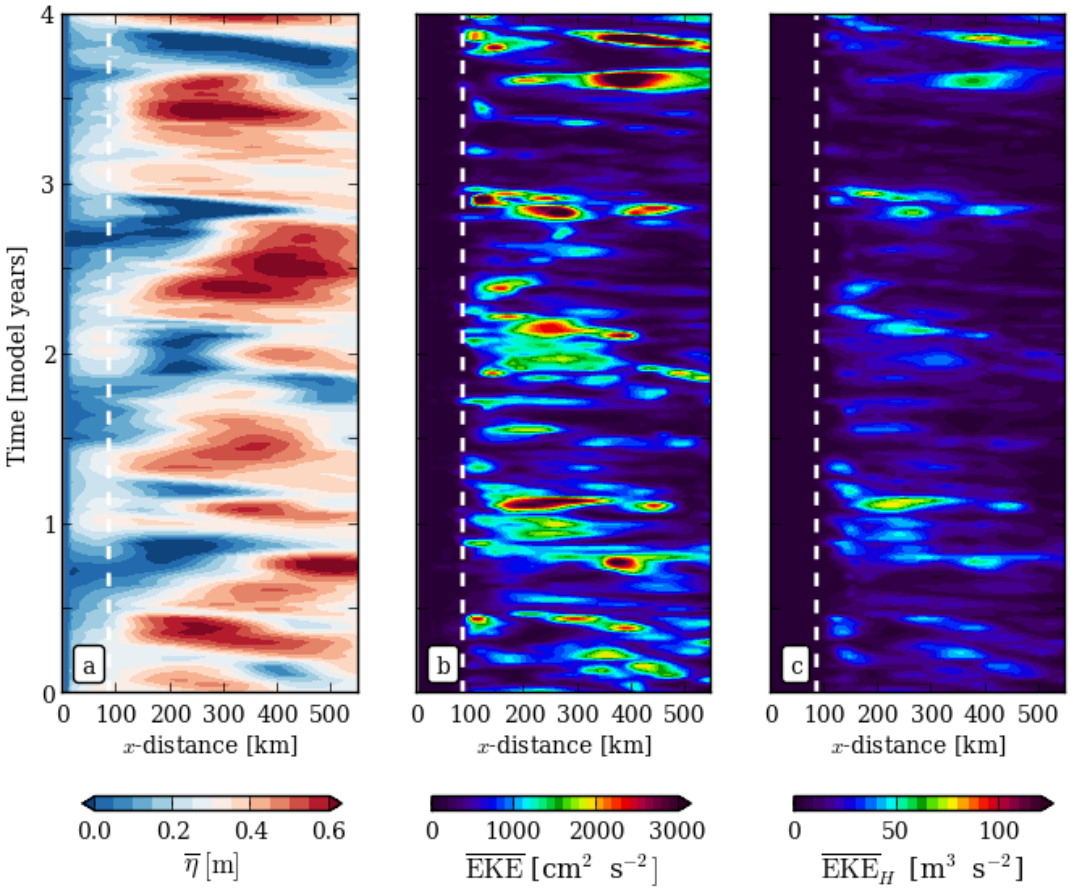

Figure 5.6: Longitude-time diagrams of alongshore averaged variables : (a) $\overline{\eta}$, (b) $\overline{\mathrm{EKE}}$ and (c) depth integrated $\overline{\mathrm{EKE}}_H$. EKE is computed relatively to a running mean on 6 months (seasonal EKE). The white dotted line is isobath 200 m.

Evolution of eddy kinetic energy

Figure 5.6 shows longitude-time diagrams of alongshore averaged SSH ($\overline{\eta}$), surface and depth integrated EKE ($\overline{\mathrm{EKE}}$ and $\overline{\mathrm{EKE}}_H$) during the 4 years of simulation. EKE is computed relatively to a 6-month running mean. As such, it represents a seasonal EKE[4]. Nearshore $\overline{\eta}$ (Fig. 5.6a, westward of 59°E) has a strong seasonal cycle, with a marked negative anomaly during the upwelling season and a positive anomaly during the rest of

[4]As western boundary currents in the Arabian Sea seasonally reverse, their annual mean is meaningless and do not represent an observable state. Consequently, EKE needs to be computed in relation to a seasonal basic state.

the year. This alternating pattern, geostrophic footprint of a coastal jet, is consistent with the seasonal reversing of the East Arabian Current (Schott and McCreary, 2001). This seasonal signal dominates over the propagation of remotely forced structures emerging from the inner basin that are noticeable in the eastern part of the diagram. EKE (Figs. 5.6b,c) displays random patterns, with local maxima emerging at every location and at any time of the year.

A westward propagation is noticeable although it is less clear than in EBUS (Kelly et al., 1998). Notice that not surprisingly, the level of turbulence is enhanced compared to EBUS (surface EKE reaches 3000 $\mathrm{cm^2\,s^{-2}}$ vs. 800 $\mathrm{cm^2\,s^{-2}}$). Interestingly, contrary to $\overline{\eta}$, neither $\overline{\mathrm{EKE}}$ (Fig. 5.6b) nor $\overline{\mathrm{EKE}}_H$ (Fig. 5.6c) display a seasonal cycle comparable to the California current system (Fig. 12 in Marchesiello et al., 2003). This is a clue to infer that the upwelling system is not the primary source of turbulence in this area.

Energy conversion

In order to investigate the mechanisms at play in the EKE generation, we compute the energy conversion terms relative to EKE, in the same fashion as Marchesiello et al. (2003). We recall that the brackets denote a time average during the upwelling season and we define primed quantities as deviations from those means. The wind work input into the oceanic perturbations $\mathrm{F_eK_e}$ is computed as :

$$\mathrm{F_eK_e} = \frac{1}{\rho_0}\left(\langle u'_s\tau'_{sx}\rangle + \langle v'_s\tau'_{sy}\rangle\right) \tag{5.1}$$

where (u'_s, v'_s) is the horizontal eddy velocity in the surface layer, (τ'_{sx}, τ'_{sy}) is the eddy wind stress and ρ_0 is a reference density. The conversion term from mean to eddy kinetic energy $\mathrm{K_mK_e}$ is decomposed in two parts. The two contributions arise from instabilities triggered by the horizontal (barotropic) and the vertical mean shears, commonly called horizontal and vertical Reynolds stresses (HRS and VRS, following Gula et al., 2015a) :

$$\mathrm{K_mK_e} = \mathrm{HRS} + \mathrm{VRS} \tag{5.2}$$

with:

$$\begin{aligned}\mathrm{HRS} = \; & -\langle u'u'\rangle\partial_x\langle u\rangle - \langle u'v'\rangle\partial_y\langle u\rangle \\ & -\langle u'v'\rangle\partial_x\langle v\rangle - \langle v'v'\rangle\partial_y\langle v\rangle\end{aligned} \tag{5.3}$$

and

$$\mathrm{VRS} = -\langle u'w'\rangle\partial_z\langle u\rangle - \langle v'w'\rangle\partial_z\langle v\rangle \tag{5.4}$$

The baroclinic conversion term P_eK_e transfers eddy potential energy to eddy kinetic energy through a vertical buoyancy flux :

$$P_eK_e = \langle w'b' \rangle \tag{5.5}$$

where $b' = -g\rho'/\rho_0$ is the local buoyancy anomaly. Finally, the eddy dissipation by friction at the bottom D_e is computed as :

$$D_e = \frac{1}{\rho_0} \left(\langle u'_b \tau'_{bx} \rangle + \langle v'_b \tau'_{by} \rangle \right) \tag{5.6}$$

where (u'_b, v'_b) is the horizontal eddy velocity in the bottom layer and (τ'_{bx}, τ'_{by}) is the eddy bottom stress.

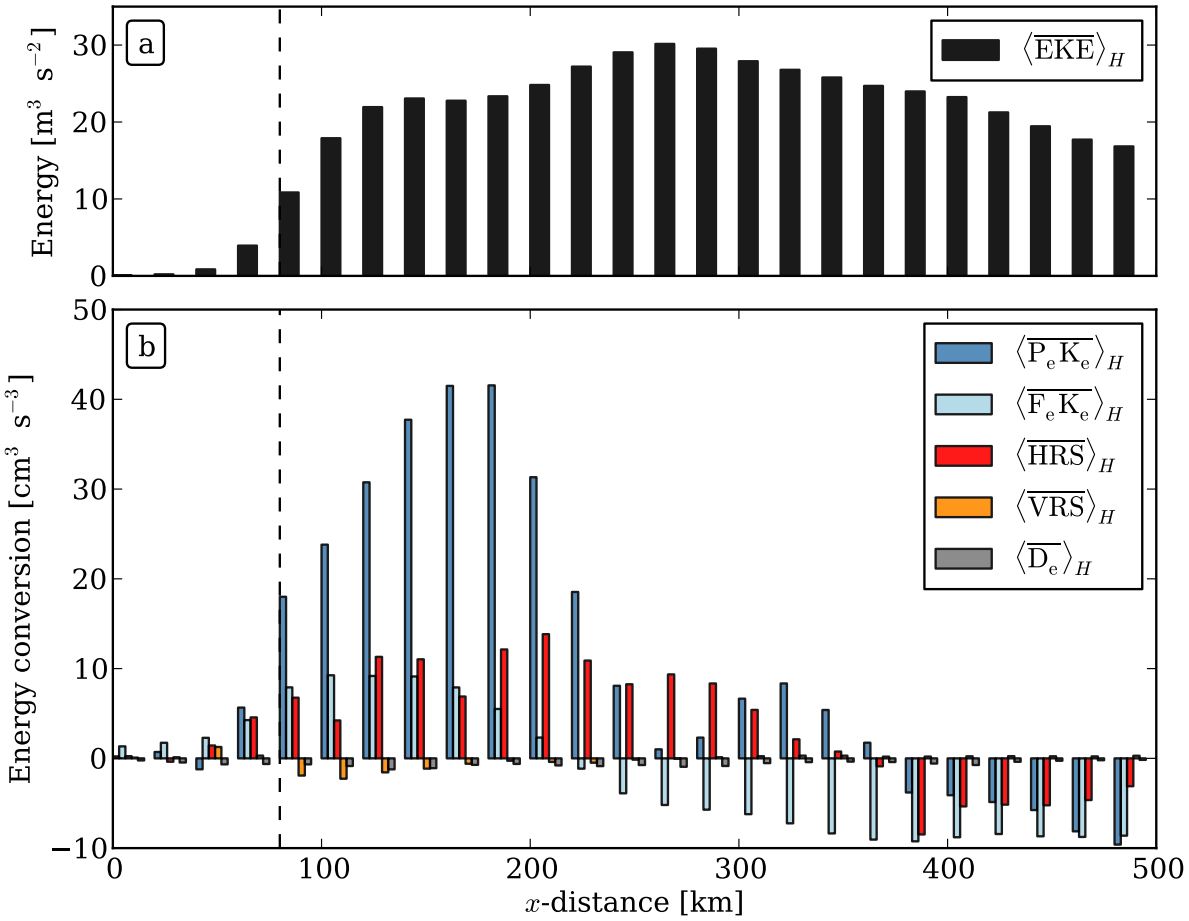

Figure 5.7: Depth-integrated, time and alongshore averaged (a) $\langle \overline{\mathrm{EKE}} \rangle_H$ and (b) energy conversion terms, cross-shore averaged over 20-km intervals. Dark blue is the baroclinic conversion term $\langle \overline{\mathrm{P_eK_e}} \rangle_H$, light blue is the wind energy input $\langle \overline{\mathrm{F_eKe}} \rangle_H$, red and orange are the horizontal and vertical Reynolds stresses $\langle \overline{\mathrm{HRS}} \rangle_H$ and $\langle \overline{\mathrm{VRS}} \rangle_H$, the two components of the barotropic conversion term $\langle \overline{\mathrm{K_mK_e}} \rangle_H$, and gray is the frictional dissipation term $\langle \overline{\mathrm{D_e}} \rangle_H$. The black dotted line is isobath 200 m.

Cross-shore variability Figure 5.7 shows a cross-shore profile of depth integrated and along-shore averaged EKE and energy conversion terms defined in Eqs. (5.1-5.6), binned over 20-km intervals (it is directly comparable to Fig. 15 in Marchesiello et al., 2003). The dominant sign of oceanic conversion terms (K_mK_e and P_eK_e) allows to separate two distinct regimes. First, in the inshore band (0-300 km), K_mK_e (dominated by HRS) and P_eK_e are positive. This band coincides with the area where the upwelling jet sits (Figs. 5.5a,b). Thus, conversion terms from mean potential energy and mean kinetic energy to eddy kinetic energy reveal that the jet is prone to both baroclinic and barotropic instabilities respectively (mixed instabilities are usually observed in oceanic jets, e.g., in the Gulf Stream, Gula et al., 2015a). The ratio between EKE values and the conversion terms provides a replenishment time scale τ_p for the mesoscale eddy activity, i.e., the time is takes for baroclinic/barotropic instability processes to produce the observed level of EKE. Using vertically integrated values we find $\tau_p \sim 5$ days over the continental slope. Intense EKE production in this particular area has direct consequences on EKE levels with large values being observed immediately to the north and east (Fig. 5.3c), i.e., along advection pathways.

Second, in the offshore band (300-500 km), oceanic conversion terms are negative, meaning that energy transfer occurs from the eddy to the mean. Notice that the wind input reinforces this transfer. This band is offshore the jet area, and although energy conversion terms are negative (thus acting to restore energy to the mean state), EKE is still important. As there is no local sources of EKE, we infer that EKE in this area has been generated offshore the upwelling system and has drifted westward due to β. This quantifies a distinguishing feature of western boundary upwellings that we suggested, which is the interaction of locally and remotely generated turbulence.

The dissipation of EKE through frictional processes at the bottom is very low compared to generation processes (D_e is one order of magnitude smaller than P_eK_e and K_mK_e, Fig. 5.7b). As such, EKE does not reach an equilibrium state in the upwelling system at a seasonal scale and must be radiated somewhere. The alongshore average is done on a rather small distance (130 km) so we cannot neglect advection through boundaries. Thus, we argue that EKE should leak alongshore.

Vertical structure The vertical structures of EKE and P_eK_e are shown in Fig. 5.8. The superposition of the alongshore current and isotherms confirms that the vertical buoyancy flux occurs in the core of the upwelling jet. This is also where the vertical tilt of isotherms is maximum (the mean current is in thermal wind balance), thus where baroclinic instability is the more likely to occur (restratification effect). Colas et al. (2013) make similar plot in the California and Peru-Chile current systems (their Figs. 3 and 4).

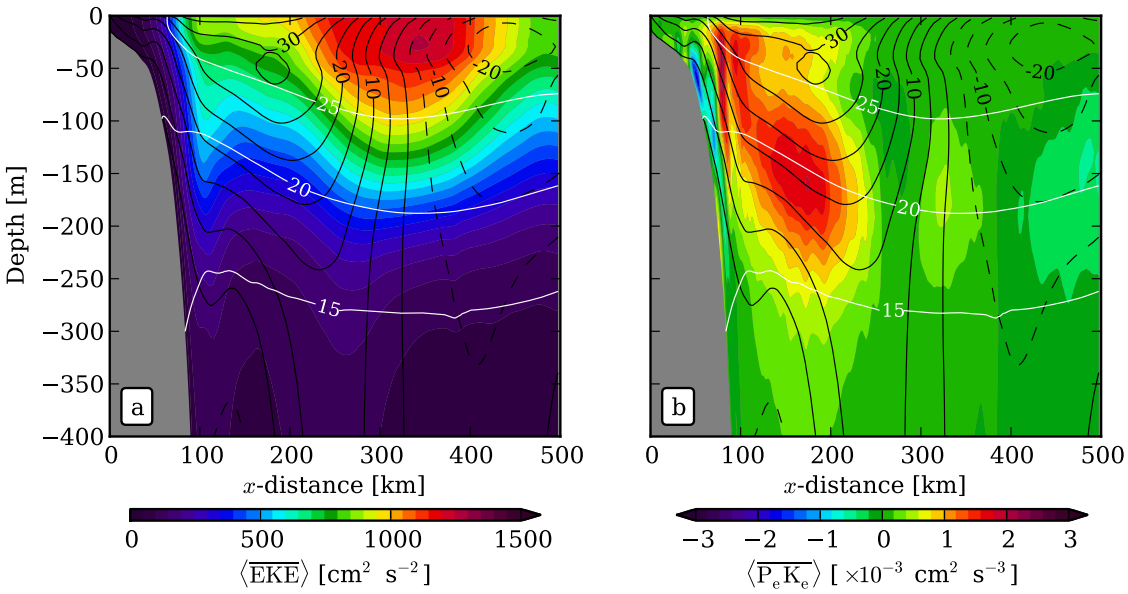

Figure 5.8: Time and alongshore averaged vertical sections of (a) $\langle\overline{\mathrm{EKE}}\rangle$ and (b) baroclinic conversion term $\langle\overline{\mathrm{P_eK_e}}\rangle$. The black lines are the alongshore velocity $\langle\overline{v}\rangle$ with CI=5 cm s^{-1}. The white lines are isotherms 15, 20 and 25°C.

Consistently with the deeper extent of the upwelling jet off Oman than in EBUS, $\mathrm{P_eK_e}$ significantly reaches larger depth (250 m vs. 100 m). It also has larger values by one order of magnitude, revealing the enhanced *frontality* of the western boundary upwelling. As previously noted, EKE is significantly larger, and reaches deeper levels.

Interestingly, $\mathrm{P_eK_e}$ is negative over a narrow band over the continental slope. This pattern is also present in EBUS and is associated with a change of sign of the isotherm slopes. Eddy fluxes here do not act to restratify the ocean.

5.2.6 Role of Rossby waves

Rossby wave dynamics plays an essential role in EBUS by radiating the upwelling signal away from the coast. In this section, we show that Rossby wave dynamics is also essential in western boundary upwelling systems, although reasons are fundamentally different. In this section, to highlight the role of Rossby waves, we make use of a simplified shallow-water model. This two-layer unidirectional (zonal) linear shallow-water model is forced by a realistic wind stress curl. It captures the barotropic and first mode baroclinic Rossby wave processes, that account for the dominant SSH variability (Wunsch, 1997). The equations solved are given in appendix and the parameters are chosen to correspond to the Oman situation (Table 5.1).

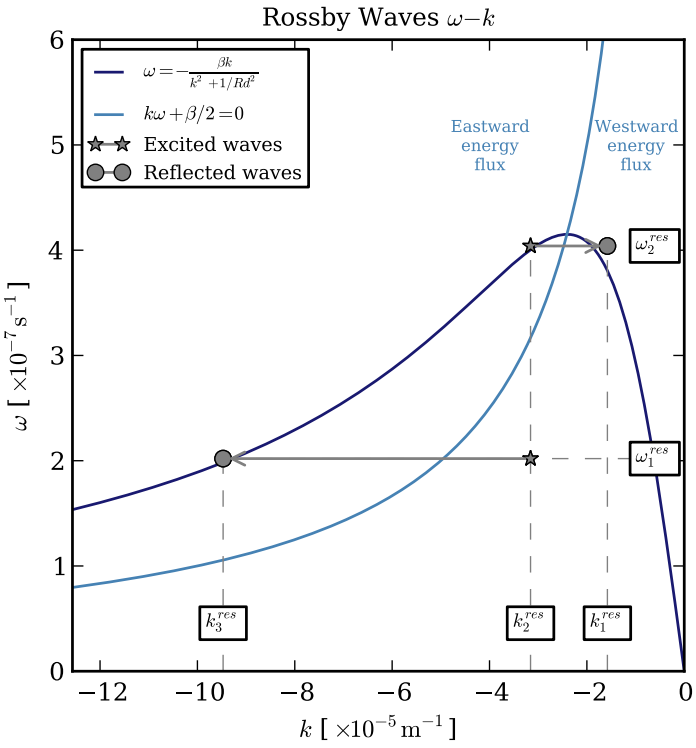

Figure 5.9: Spatiotemporal scales of the response η_{bc} as spectrally diagnosed in Fig. 5.10e,f. Gray stars correspond to waves excited at the forcing scales (ω_1^{res}, ω_2^{res} and k_2^{res}) and gray points correspond to waves reflected (details in text). Superimposed on these scales intersections are the Rossby wave dispersion relation corresponding to the model parameters (dark blue) and the separation line for waves with a westward energy flux (light blue). Above (below) this line, the wave energy flux is going eastward (westward).

Background

Fu and Qiu (2002) have shown that baroclinic Rossby waves in the inner Pacific (far enough from the eastern boundary) are primarily excited by the wind stress curl. In the northern Arabian Sea, this forcing mechanism has been clearly identified by analyzing wind stress curl derived from scatterometer winds and SSH derived from altimetry in longitude-time sections across the basin (see Fig. 7 in Beal et al., 2013). A positive wind stress curl causes an upwelling Rossby wave thus a negative anomaly of SSH (for the first mode, thermocline and SSH are mirrored, e.g., Killworth et al., 2004).

When a wave encounters a meridional boundary, reflection occurs. The reflected wave must satisfy two conditions : (i) it conserves the temporal frequency of the incident wave and (ii) propagates the zonal energy flux of the incident wave in the opposite direction. The zonal energy flux $\mathcal{F}^x$ for a Rossby wave can be written as :

$$\mathcal{F}^x = -\frac{A^2}{2}(k\omega + \beta/2), \tag{5.7}$$

where A is the wave amplitude (sections 3.21 and 3.23 in Pedlosky, 1987). When $k\omega +$

$\beta/2 > 0$ (< 0), the energy goes westward (eastward). In Fig. 5.9, the line $k\omega + \beta/2 = 0$ separates the two regions of opposite propagation for the energy flux. The dispersion relation for Rossby waves :

$$\omega = -\frac{\beta k}{(k^2 + 1/R_d^2)}, \tag{5.8}$$

is also shown (recall that we do not consider meridional propagation). For a given incident wave, the characteristics of the reflected wave can be retrieved in crossing the line $k\omega + \beta/2 = 0$ at constant ω. The intersection of this line with the dispersion relation gives the characteristics of the reflected (free) wave. A well-known particular case is the long wave (thus westward propagating) reflection at a western boundary into a shorter mode, propagating slowly eastward (Longuet-Higgins, 1966).

Analysis

Figures 5.10a,d show the model forcing (wind stress curl) and response (SSH) evolution throughout the 4 years of integration. SSH is decomposed into baroclinic and barotropic components, η_{bc} and η_{bt}. We only show η_{bc} as it clearly dominates the response ($\eta_{bt} = O(10^{-1})\eta_{bc}$; a same order of magnitude of the ratio is found in Qiu, 2002). During the northeast monsoon (roughly between November and March), the forcing is relatively weak ($|\nabla \times \boldsymbol{\tau}| < 2 \times 10^{-7}$ N m^{-3}) and spatially smooth whereas it has a high amplitude ($\nabla \times \boldsymbol{\tau}$ reaches 10^{-6} N m^{-3}) and a locally intensified positive pattern with a maximum around 100 km from the coast during the southwest monsoon (embedding the upwelling season, from May to September). The spectral analysis of the wind stress curl isolate two dominating temporal scales, $\omega_1^{frc} = 2.020 \times 10^{-7}$ s^{-1} and $\omega_2^{frc} = 4.040 \times 10^{-7}$ s^{-1}, corresponding to annual (the most energetic) and semi-annual periods respectively (Fig. 5.10b), and one spatial scale $k_1^{frc} = 3.157 \times 10^{-5}$ m^{-1}. It corresponds to a wavelength of ∼200 km (Fig. 5.10c), consistent with the dominant pattern scale of $\nabla \times \boldsymbol{\tau}$ (Fig. 5.10a). The dominant signal in the response (η_{bc}, Fig. 5.10d) is the long-wave annually forced by this seasonal burst of positive wind stress curl. This propagation is easily identified in Fig. 5.11b showing the low-pass filtered η_{bc}.

The reflection of the long wave at the western boundary actually occurs in the model and scales smaller than the incident wave emerge near the coast (Fig. 5.10d). Indeed, the spectral analysis of η_{bc} reveals the emergence of a high wavenumber $k_3^{res} = 9.472 \times 10^{-5}$ m (Fig. 5.10e), corresponding to a wavelength of ∼66 km, consistent with the scale of coastal patterns of η_{bc} (Fig. 5.11c). Notice that a shorter wavenumber emerges too, $k_3^{res} = 1.579 \times 10^{-5}$ m corresponding to a wavelength of ∼398 km, almost equal to the size of the domain. The spatial spectrum also contains some signal at the frequency of the forcing ($k_2^{res} \equiv k_1^{frc}$), thus this signal must be associated with forced waves. The temporal

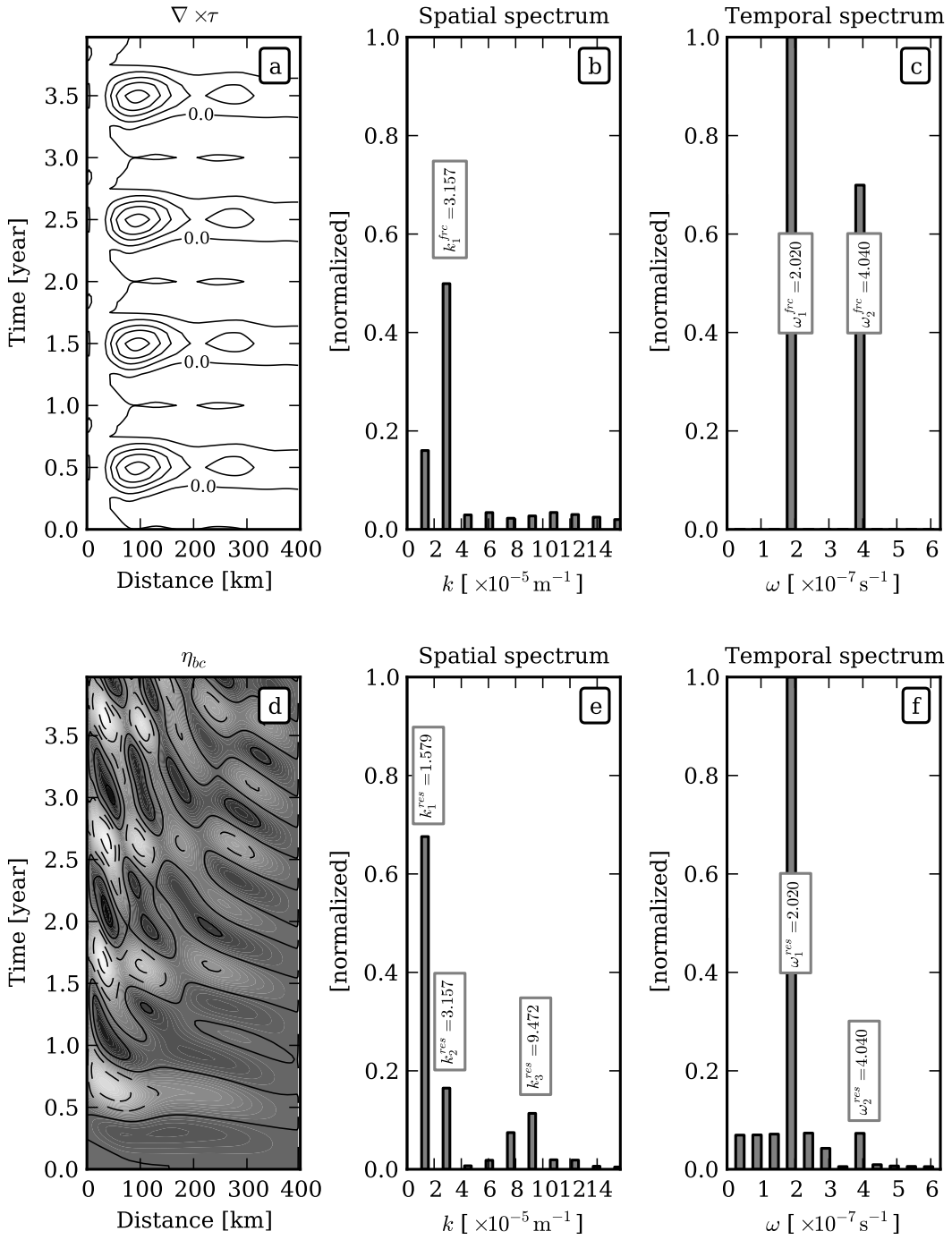

Figure 5.10: Longitude-time diagrams (left) and spatial (middle) and temporal (right) spectra of the wind stress curl $\nabla \times \boldsymbol{\tau}$ forcing the shallow-water model (top) and the baroclinic response in SSH anomaly, η_{bc} (bottom). CI for $\nabla \times \boldsymbol{\tau}$ is 2×10^{-7}N m^{-3} and CI for η_{bc} is 3 cm (dashed lines are for negative values and superimposed gray shadows are used to emphasize the alternating η_{bc}). Spectra indicate the spatiotemporal scales of the forcing $k_1^{frc}, \omega_1^{frc}, \omega_2^{frc}$ and of the response $k_1^{res}, k_2^{res}, k_3^{res}, \omega_1^{res}, \omega_2^{res}$. Notice that spatiotemporal scales of the forcing are conserved in the response ($\omega_1^{frc} = \omega_1^{res}$, $\omega_2^{frc} = \omega_2^{res}$ and $k_2^{res} = k_1^{frc}$) and that some spatial scales emerge in the response (k_1^{res} and k_3^{res}).

spectrum of the response keeps the same peaks as the spectrum of the forcing, $\omega_1^{res} \equiv \omega_1^{frc}$ and $\omega_2^{res} \equiv \omega_2^{frc}$, although the semi-annual signal has been importantly damped (it was originally weaker).

In Fig. 5.9 we report in the ω–k space the dominating scales of the response. The two forced waves $(k_2^{res}, \omega_1^{res})$ and $(k_2^{res}, \omega_2^{res})$ are not supposed to project onto the dispersion relation (valid for free waves) and the fact that $(k_2^{res}, \omega_2^{res})$ satisfies the relation is fortuitous. As reviewed in section 1.2.15.2.6, incident waves conserve their temporal frequency at the reflection and reverse their energy flux. Hence, we can identify their associated reflected waves. One of them can be clearly projected onto the Rossby wave dispersion relation (ω_1^{res},k_3^{res}) and the other (ω_2^{res},k_1^{res}) may also be projected. This is not surprising since the reflected waves are freely propagating, thus correspond to Rossby waves.

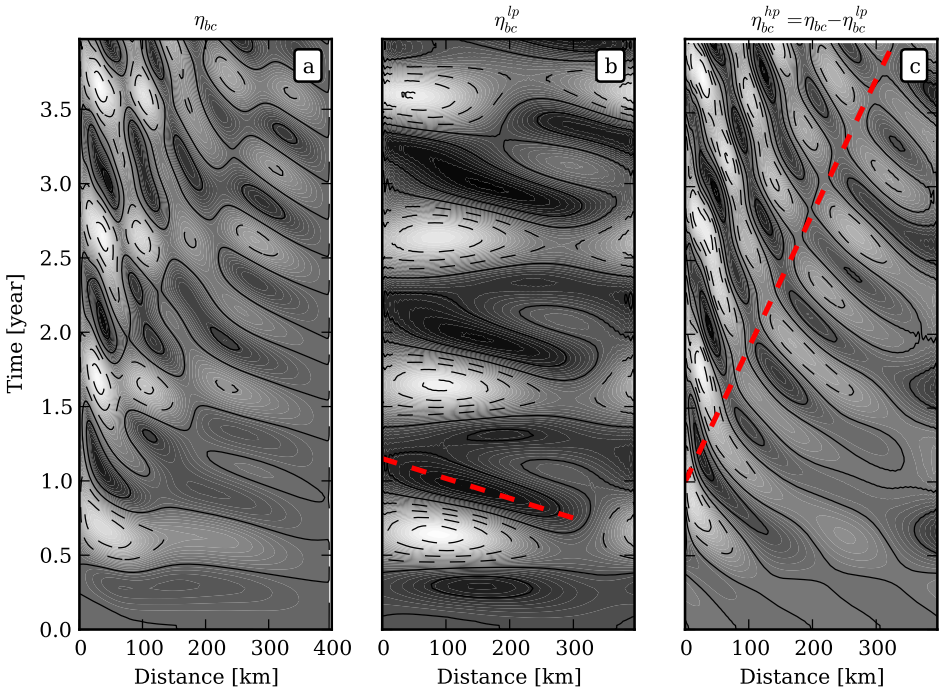

Figure 5.11: Baroclinic response in SSH anomaly for the shallow-water model, (a) η_{bc} (same as in Fig. 5.10d), (b) low-pass filtered SSH η_{bc}^{lp} and (c) high-pass component of SSH η_{bc}^{hp}. Filtering is done using a fast Fourier transform. Red dashed lines show the estimated propagation speed for long and short waves.

Interpretation and discussion

In the following, we focus on the forced wave $(k_2^{res}, \omega_1^{res})$ and its reflected wave $(k_3^{res}, \omega_1^{res})$ as they dominate the response. The energy contained at ω_1^{res} (annual period) is one order of magnitude greater than the energy contained at ω_2^{res} (semi-annual period, Fig. 5.10f). The energy of the reflected mode propagates eastward very slowly with a group velocity (at which energy travels) $c_g(k_3^{res}) = \partial\omega/\partial k|_{k=k_3^{res}} \sim 2 \times 10^{-3}$ m s^{-1} ~ 5 km mon^{-1} (comparable to rough estimates in Fig. 5.11c). Thus, energy is almost trapped at the coast at a seasonal time scale. In a linear theory, the amplitude of the superposition of two waves is the sum of the wave amplitudes. Here, as the reflected wave carries the same anomaly as

the incident wave (negative SSH), their superposition in a coastal fringe (0–100 km) has an increased amplitude. This is consistent with the idea that energy is coastally trapped. Moreover, the minimum of η_{bc} is reached between 50 and 70 days after the maximum of $\nabla \times \boldsymbol{\tau}$. Interestingly, this range is similar to the lag between the maximum of the upwelling favourable forcing and minimum of SST diagnosed in the realistic simulation ($\sim$1.5 month).

Assuming that SSH is a good proxy for the upwelling intensity, we argue that the wave reflection mechanism put forward by the shallow-water model is insightful for the understanding of the Oman western boundary upwelling. Overall, this illustrates the fundamentally different role played by Rossby waves between EBUS and western boundary upwellings. In the former, they act to propagate the coastally upwelled waters offshore (Marchesiello et al., 2003) whereas in the latter, they concentrate at the coast and amplify the wind stress curl-driven upwelling.

A limitation of the 1D shallow-water model is that the wave propagation can be only zonal. Even if it is not very restrictive for Rossby waves whose propagation is mostly zonal, we miss the propagation of coastal Kelvin waves and here discuss their potential impact. Grimshaw and Allen (1988) show that high frequency forcing and high latitude favor trapped motions (coastal Kelvin waves) whereas low frequency and low latitude favor interior motions (mainly Rossby waves). More specifically, at a given latitude, a critical frequency ω_c exists such that for $\omega < \omega_c$, energy leaks in the interior while it is coastally trapped for $\omega > \omega_c$. ω_c also depends on the angle of the coast with the meridional direction θ and Clarke and Shi (1991) derived an expression for ω_c that takes into account this angle : $\omega_c = \frac{1}{2}\beta R_d \cos\theta$. Using the realistic parameters mentioned in appendix, we find $\omega_c|_{\theta=0^\circ} = 5.5 \times 10^{-7}$ s^{-1}. This is much larger than the characteristic frequencies of η_{bc} so that motions are favourably reflected into the interior and the shallow-water model probably captures the essence of the physics. In the case of a slanted coastline, considering a mean shelf break line in the upwelling region (as advocated by Clarke and Shi, 1991) that make an angle of $\theta \sim 30^\circ$ with the meridional direction, we find $\omega_c|_{\theta=30^\circ} = 4.8 \times 10^{-7}$ s^{-1}. In the world atlas of ω_c derived by Clarke and Shi (1991), we read $2\pi/\omega_c^{atlas} = 167.6$ days (their Table 1), which gives $\omega_c^{atlas} = 4.3 \times 10^{-7}$ s^{-1}. Both values are higher than the dominating annual frequency of η_{bc} so we are confident with the fact that coastal Kelvin waves certainly play a minor role in the reflection process.

5.2.7 Mixed layer heat budget

We now investigate the mechanisms by which the oceanic mixed layer temperature cools during the seasonal upwelling. To that end, we compute a heat budget on the mixed layer (in the same fashion as Vialard and Delecluse, 1998; Vialard et al., 2001) averaged over

an area covering the upwelling system. We start from the pointwise heat balance in which we introduce the 3D averaged mixed layer temperature T_{ML} for the domain of interest :

$$\partial_t T = \quad -\partial_x \left[u(T-T_{ML})\right] - \partial_y \left[v(T-T_{ML})\right] - \partial_z \left[w(T-T_{ML})\right] + \partial_z \left(\kappa \partial_z T\right) + \frac{Q_{atm}}{\rho_0 C_p} \partial_z f(z) \tag{5.9}$$

where κ is the vertical diffusivity coefficient determined by the KPP scheme, Q_{atm} is the net solar surface heat flux and $f(z)$ is the the attenuation factor that determines the fraction of solar radiation that reaches depth z (Jullien et al., 2012). We do not explicit the horizontal diffusion here (done implicitely by the upstream biased advective scheme, without the need for an explicit diffusion operator, Shchepetkin and McWilliams, 1998). We computed it and found that it is at least one order of magnitude smaller than other terms, thus we neglect it in the following. Equation (5.9) holds because T_{ML} does not depend on spatial coordinates and the flow is 3D non divergent. This formulation with T being replaced by $T-T_{ML}$ allows to better quantify the cooling/heating done by advection terms, relatively to a reference temperature. Then we integrate Eq. (5.9) horizontally over the domain of interest and vertically over the mixed layer depth h_{ML} diagnosed by KPP :

$$\begin{aligned} \underbrace{\partial_t T_{ML}}_{\text{RATE}} = \quad & \underbrace{-\frac{1}{h_{ML}} \left\{ \left[u(T-T_{ML})\right]_{dA} + \left[v(T-T_{ML})\right]_{dA} \right\}}_{\text{HADV}} + \underbrace{\frac{1}{h_{ML}} \left[w(T-T_{ML})\right]_{z=h_{ML}}}_{\text{VADV}} \\ & \underbrace{-\frac{1}{h_{ML}} \left[\kappa \partial_z T\right]_{z=h_{ML}}}_{\text{VMIX}} + \underbrace{\frac{Q_{atm}}{\rho_0 C_p h_{ML}}}_{\text{FORC}} \underbrace{-\frac{1}{h_{ML}} \partial_t h_{ML} \left(T_{ML} - T_{z=h_{ML}}\right)}_{\text{ED}} \end{aligned} \tag{5.10}$$

where the first two terms on rhs are evaluated on the lateral boundaries dA of the domain A. The different terms are labeled as : RATE for the temporal tendency of the mixed layer temperature, HADV for the horizontal advection of heat through lateral boundaries of A, VADV for the vertical advection of heat at the bottom of the mixed layer, VMIX for the mixing occuring at the base of the mixed layer, FORC for the atmospheric heating and ED for entrainment/detrainment at the base of the mixed layer (due to temporal variations in h_{ML}). The time series of these terms averaged on two years of simulation are shown in Fig. 5.12. We do not represent ED since it is found to be two orders of magnitude smaller than RATE, thus it can be neglected in the heat balance.

The annual cycle of T_{ML} is consistent with the larger scale variation of SST in the western Arabian Sea. Using a global model, de Boyer Montégut et al. (2007) show that SST averaged in the western Arabian Sea (in a box whose southern and eastern boundaries are latitude 6°N and longitude 65°E respectively) experiences two seasons of warming during intermonsoon phases and two seasons of cooling during both monsoons. In the following, we analyse which processes are responsible for the temperature evolution during

the different phases.

From the end of February to May (spring intermonsoon), T_{ML} increases under the influence of several processes. The mixed layer strongly shallows from 60 m at the end of February to 10–20 m in May as the wind stress fades out (end of the winter monsoon) and the spring restratification occurs. During this time, vertical mixing instigates heating. From April onward, the atmosphere starts to heat the mixed layer. It progressively overcomes the vertical mixing, which changes sign at mid-May, under the influence of the raising summer monsoon winds (deepening the mixed layer).

At the beginning of June, the upwelling favorable winds blow, triggering a decrease of T_{ML}. During all the upwelling season (shadow areas in Figs. 5.12a-c), the atmosphere keeps on heating the mixed layer and the vertical mixing at the base of the mixed layer is opposed to it with the same magnitude. In fact, because the mixed layer is shallow (< 30 m), solar heating penetrates to its base and the vertical mixing acts to redistribute the heat (this is not the case in winter when the mixed layer is deep). Thus, there is almost a balance between these two terms. The vertical advection plays an important role during the upwelling period. It brings cold waters at the base of the mixed layer through Ekman pumping. The horizontal advection does not counterbalance the cooling by vertical advection (Fig. 5.12b). Thus, vertical advection seemingly explains the cooling of the mixed layer during the upwelling season (in Fig. 5.12c, HADV+VADV and RATE follow the same evolution with similar magnitudes).

At the end of the upwelling season, the mixed layer shallows when the summer monsoon winds fade out. As soon as the upwelling shuts down, T_{ML} increases, mainly driven by the atmospheric heating and horizontal advection that brings warm waters (outside from the upwelling area). From the end of October onward, the winter conditions evoked earlier are retrieved with a domination of atmospheric cooling.

Notice that the standard deviation of the terms in Figs 5.12a,b,c is related to year to year variability of the system. We are tempted to associate it with the mesoscale circulation (eddies entering and exiting the computational area) that strongly modulates the heat transport : using arrays of moorings deployed off the Oman coast (500 km offshore) during one year, Fischer et al. (2002) and Weller et al. (2002) find that advection of heat by mesoscale eddies is responsible for strong variability in the surface layer heat budget.

The contribution of each term to the cooling tendency during the upwelling season is represented in Fig. 5.12d. The near-equilibrium between vertical mixing and atmosphering forcing is confirmed (VERT$\simeq$115% FORC). This local balance is known to occur when the mixed layer is shallow and one-dimensional processes dominate (e.g., Spall et al., 2000; Jullien et al., 2012). The important contribution of the vertical advection was also

highlighted in a broader area of the Arabian Sea embedding both upwellings off Somalia and Oman (Shenoi et al., 2002). However, it contrasts with other mixed layer heat budgets in EBUS (coastal or offshore regions) where the vertical mixing is often found to be the major cooling contributor (Takahashi, 2005; Colbo and Weller, 2007; Renault et al., 2012). Vertical velocity at the base of the mixed layed is triggered by both Ekman pumping and Rossby waves, hence these mechanisms are important to explain mixed layer temperature variability during the upwelling. Consequently, we state that the wind stress curl is of paramount importance in the sustainment of the cooling tendency of the northwestern Arabian Sea in summer.

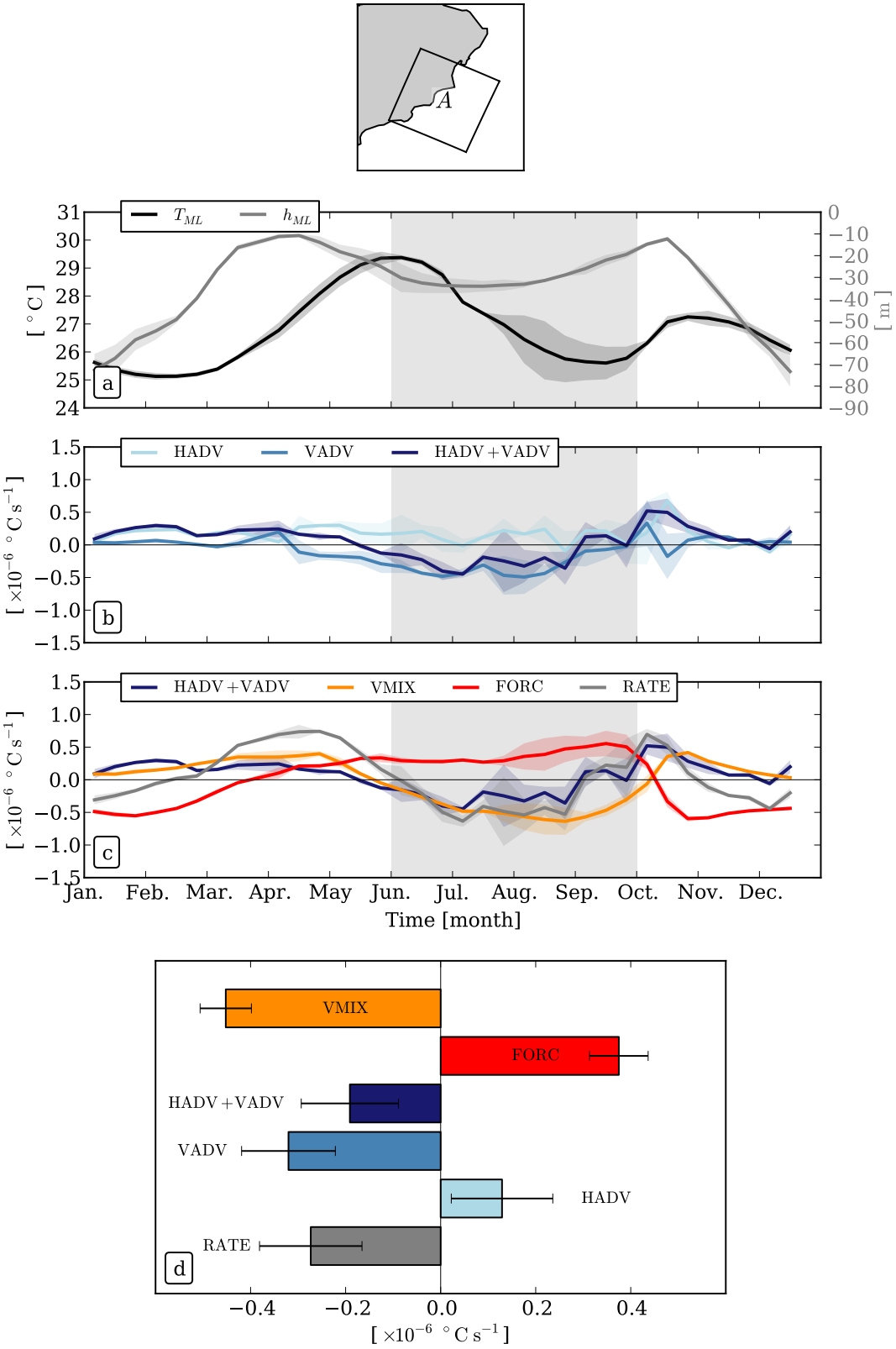

Figure 5.12: (a),(b) and (c) Time series of variables averaged over the mixed layer and over the domain A shown in inset map : (a) temperature (black) and mixed layer depth (gray), (b) HADV (light blue), VADV (steel blue) and HADV+VADV (dark blue), (c) HADV+VADV (dark blue), VMIX (yellow), FORC (red) and RATE (gray). Gray area on panels (a),(b) and (c) is the upwelling season. Bold lines and shaded areas are means and standard deviations computed on two years of simulation. (d) time averaged variables (same color code) during the upwelling season. Error bars are the standard deviations.

5.2.8 Conclusions and perspectives

Dynamics of the seasonal upwelling off Oman is analyzed using a realistic regional numerical simulation. The vertical structure of the upwelling is found to contrast with EBUS : isotherm upward tilt goes deeper (300 m vs. 100-150 m) and the surface jet associated (thermal wind balance) is therefore deeper. The core of the undercurrent, flowing in the opposite direction, is also much deeper (1000 m vs 150-200 m). The upwelling system is found to release EKE in a nearshore band, mainly through baroclinic instability of the jet (like in EBUS, Marchesiello et al., 2003). The level of EKE produced by the upwelling is significantly larger than in EBUS. However, the level of EKE offshore the jet area, where conversion terms do not act to increase EKE, is still very high and comparable to mean values in the nearshore band. We argue that mesoscale turbulence remotely forced enters the upwelling area and interacts with the system. It is consistent with previous observations made that mesoscale eddies peel off upwelled waters from the shore (Manghnani et al., 1998).

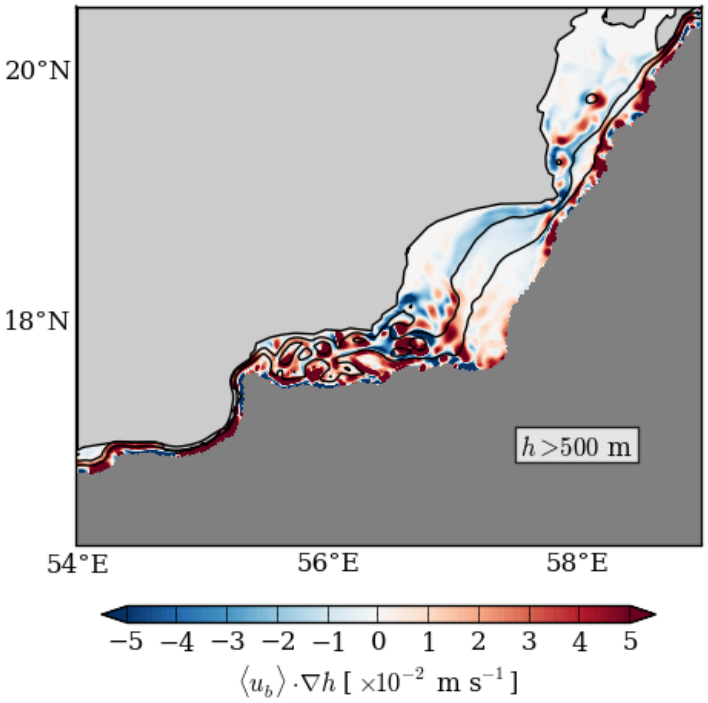

Figure 5.13: Map of $\langle \boldsymbol{u_b} \rangle \cdot \nabla h$ in the upwelling area. $\boldsymbol{u_b}$ is the horizontal velocity in the bottom layer and h is the bathymetry. Areas where $h > 500$ m are masked.

The use of a linear shallow-water model highlighted the role of Rossby waves in the upwelling system. Upwelling long waves triggered by a strong positive wind stress curl travel westward and reflect into short modes propagating eastward. Their propagation speed is so slow that waves are almost trapped in a coastal area at a seasonal time scale. Consequently, they increase the upwelling and are even responsible for a lag in the SST

response to seasonal wind forcing. More generally, unlike in EBUS where they act to leak upwelling perturbations in the open ocean, Rossby waves in western boundary systems trap anomalies nearshore.

A mixed layer heat budget reveals that the cooling contribution in the upwelling area is dominated by vertical mixing and vertical advection of cold waters. This result contrasts with EBUS where vertical mixing is the overwhelming contributor. This result underpins the importance of the wind stress curl in sustaining the cooling of the northwestern Arabian Sea in summer.

Finally, notice that this study shows principally integrated quantities (area averaged) and proposes mechanisms with rather large space scales, comparable to the area of the upwelling. However, the complex geomorphology (indented coastline and wide shelf) of the system involves small atmospheric and oceanic scales, and the system is heterogeneous. Figure 5.13 shows $\langle u_b \rangle \cdot \nabla h$ in the upwelling area, where bathymetry h is shallower than 500 m. This quantity roughly measures where water climbs on the shelf ($\langle u_b \rangle \cdot \nabla h > 0$) and where it sinks ($\langle u_b \rangle \cdot \nabla h < 0$). Patterns are rather complex and alternating but there is seemingly a tendency for water to be preferentially upwelled on the upstream side of Ras Sharbatat where the shelf is steeper. On the contrary, on the downstream side where the shelf is wider, water is found to sink. Release of synthetic particles in the model confirm this tendency (not shown). Therefore, the upwelling off Oman requires further investigation to elucidate its fine scale structure.

Acknowledgments

The altimeter products were produced by Ssalto/Duacs and distributed by Aviso, with support from Cnes (http://www.aviso.altimetry.fr/duacs/). CV is supported by the Direction Générale de l'Armement (DGA) and the Région Bretagne in the form of a PhD scolarship. We thank Antoine Hochet (UBO, Brest) for fruitful discussions.

Appendix : shallow-water framework

We use the same framework as Qiu (2002) without the long-wave approximation, solving separately the baroclinic mode :

$$\frac{\partial}{\partial t}\left(\nabla^2 \eta_{bc} - \frac{f_0^2}{g' H_e}\eta_{bc}\right) + \beta \frac{\partial \eta_{bc}}{\partial x} = \frac{f_0 H_e \nabla \times \boldsymbol{\tau}}{\rho_0 g H_1^2}, \tag{5.11}$$

and the barotropic mode :

$$\frac{\partial}{\partial t}\left(\nabla^2 \eta_{bt}\right) + \beta \frac{\partial \eta_{bt}}{\partial x} = \frac{f_0 \nabla \times \boldsymbol{\tau}}{\rho_0 g (H_1 + H_2)}, \tag{5.12}$$

where the SSH anomaly is $\eta_{bc} + \eta_{bt}$ and all parameters designation and values are given in Table 5.1. The domain has an extent of 400 km and no normal-flow conditions are set at both boundaries. As we are interested in the reflection of Rossby wave, we only solve these equations in the zonal direction (x-axis). Therefore, we impede the propagation of waves in the meridional direction. This effect is discussed in section 1.2.15.2.6. The wind stress curl is exactly derived from the forcing of the realistic simulation, alongshore averaged in the bay area of Fig. 5.1. We integrate equations (5.11) and (5.12) during 4 years, using a periodic forcing. Parameters are chosen to represent the mode 1 in the western Arabian Sea at the mean latitude of the upwelling region. Given a mean profile of the Brunt-Vaisala frequency, we solve the eigenvalue problem for vertical modes.

Table 5.1: Parameters used in the shallow-water model.

Parameter	Description	Value
H_1	Thickness of the upper layer	444 m
H_2	Thickness of the bottom layer	3056 m
$H_e = H_1 H_2/(H_1 + H_2)$	Equivalent depth	387 m
ρ_0	Reference density	1025 kg m^{-3}
g	Gravity	9.81 m s^{-2}
$g' = (\rho_2 - \rho_1)g/\rho_0$	Reduced gravity	1.6×10^{-2} m s^{-2}
f_0	Reference Coriolis frequency	5.0×10^{-5} s^{-1}
β	Meridional derivative of f	2.2×10^{-11} m^{-1}s^{-1}
$R_d = \sqrt{g' H_e}/f_0$	First Rossby radius of deformation	50 km

Chapter 6

Conclusions and Perspectives

Contents

6.1 Conclusions

This chapter recalls the specific issues tackled in this dissertation and the results associated. Each chapter is self consistent and is summarized individually. Then, we give overall conclusions of this dissertation before presenting some perspectives that could be adressed in future work.

6.1.1 Summary of Chapter 3

In Chapter 3, we investigated the life cycle of the Great Whirl, a mesoscale anticyclone that remains at a quasi-steady place during the summer monsoon. Among the unresolved issues, the questions of generation and demise remained debated. In particular, the impact of local (wind stress and wind stress curl) vs. remote (waves remotely generated) forcing were still lacking a quantification. We found that the onset of the Great Whirl is highly infuenced by an annual downwelling Rossby wave. Indeed, the wave sets its location and timing of initiation as revealed by sensitivity tests. Nonetheless, the strong wind stress and wind stress curl remain of crucial importance to explain the maintenance and barotropization of the Great Whirl all along the summer monsoon. At the end of the monsoon, it shrinks and progressively vanishes, sitting in a very turbulent environment at a western boundary. The arrival of a Rossby wave of opposed polarity seemingly causes the shut down of the eddy. Sensitivity experiments highlighted the importance of Rossby waves to pace the life cycle of the Great Whirl. The role of these waves has been underestimated compared to local high winds and this study helped to clarify their respective influence.

Far from being exclusive to this eddy, this study underscores the importance of wave-eddy interactions. It also quantifies the role of the wind stress curl in energizing eddies, a subject about which L'Hégaret et al. (2015) further elaborate on the northern Arabian Sea.

6.1.2 Summary of Chapter 4

In Chapter 4, we tackled the general question of the spreading of Persian Gulf Water (PGW) in the Gulf of Oman. A realistic simulation evidences the important role of mesoscale eddies in spreading PGW at seasonal time scales, similarly to the fate of the Red Sea outflow in the Gulf of Aden (Bower and Furey, 2012). Unlike for many other outflows taking place at greater depth in more quiescent environments, the slope current is very weak and intermittent and not instrumental in generating turbulence. Idealized simulations isolated the interaction of mesoscale eddies with topography. They revealed an important source of enstrophy at depths where the eddies drag on the continental slope.

High vorticity strips, generated by friction, detach from the boundary and roll up into submesoscale coherent vortices (SCVs). These SCVs are then advected along the edges of their *parent* mesoscale eddies. In the realistic simulation, these SCVs are found to trap PGW. They are thus a mean to transport PGW seaward. This result complements the observations of L'Hégaret et al. (2013) that allowed to infer an important role of eddies in spreading PGW.

These processes ultimately lead to mixing of salt and produce a large-scale smooth gradient of salinity in the northern Arabian Sea. A release of virtual particles in the realistic simulation allowed to infer a diffusive regime with an estimated eddy diffusivity typical of highly turbulent and dispersive regimes.

More generally, the frictional interaction of eddies with topography leading to the formation of intense submesoscale structures may often occur on continental slopes. Thus, it would be an important process for offshore advection, dispersion and mixing of slope current waters. We further argue that this process is intensified at western boundaries because of the westward drift of mesoscale eddies.

6.1.3 Summary of Chapter 5

In Chapter 5, we studied the structure and variability of the seasonal upwelling off Oman. We were interested in comparing this western boundary upwelling with more deeply studied eastern boundary upwelling systems (EBUS). More specifically, the impact of Rossby waves, propagating offshore in EBUS vs. onshore in western boundary upwellings was of particular interest as suggested by Marchesiello et al. (2000).

The structure of the Oman upwelling is found to strongly contrast with EBUS, with isotherm tilting and the surface intensified upwelling jet reaching deeper. An undercurrent flowing in the opposite direction is also found to reach deeper, similarly to the baroclinic structure of the western boundary Brazil current system (Da Silveira et al., 2004). The forcing of this undercurrent remains unexplained as Sverdrup transport (that explains the structure of the undercurrent in EBUS) can not be invoked in this western boundary system.

The energetics of the system is more complex than in EBUS. The surface intensified jet produces more eddy kinetic energy (EKE), mainly through baroclinic instability (enhanced frontality). However, EKE produced by the upwelling itself is comparable to EKE remotely generated that drifts onshore. This qualitatively explains the general observations of former studies (e.g., Manghnani et al., 1998) reporting a passive advection of upwelled waters by mesoscale eddies entering the upwelling area.

The use of a linear shallow-water model revealed the role of Rossby waves in the upwelling system. Upwelling long waves triggered by a strong positive wind stress curl travel

westward and reflect into short modes propagating eastward. Their offshore propagation is so slow that waves are almost trapped in the coastal area on a seasonal time scale. Consequently, they enhance the upwelling and contribute to a lag in the sea surface temperature response to seasonal wind forcing. More generally, unlike in EBUS where they act to leak upwelling perturbations in the open ocean, Rossby waves in western boundary systems are unable to evacuate nearshore anomalies.

A mixed layer heat budget is performed, revealing that the cooling contribution in the upwelling area is dominated by vertical mixing and vertical advection of cold waters. This result contrasts with EBUS where vertical mixing is the overwhelming contributor. It also underpins the importance of the wind stress curl in sustaining the cooling of the northwestern Arabian Sea in summer.

6.1.4 Overall conclusions

In this dissertation, we studied the dynamics of three different phenomena occuring in the western Arabian Sea; namely, the life cycle of a remarkable eddy, the spreading of marginal sea outflowing waters and a seasonal upwelling. Each phenomenon deserves its own chapter but some dynamical ingredients are common to these chapters. As presented in Chapter 1, the similarity of the Great Whirl, the Persian Gulf outflow and the upwelling off Oman is that they all occur at a western boundary. The low-latitude of the Arabian Sea implies a fast propagation of Rossby waves and mesoscale eddies. As such, dynamics at the western boundary is strongly impacted by these remote forcing. Consequently, there is a competition between local and remote forcing as summarized in Table 6.1.

Table 6.1: Overview of local and remote forcing involved in the different phenomena studied in this dissertation.

	local forcing	remote influence
Chapter 3 Life cycle of the GW	wind stress curl topography	Rossby waves
Chapter 4 Spreading of PGW	slope current	incoming mesoscale eddies
Chapter 5 Upwelling	wind stress wind stress curl	Rossby waves (incident & reflected)

In this context, regarding the Great Whirl life cycle, Rossby waves and wind stress curl are the dominant players driving its dynamics. The spreading of PGW is almost entirely explained by the stirring done by remotely formed eddies; the slope current is indeed very weak and intermittent unlike in other major outflows. In the upwelling system, although the main contributor is the wind stress, Rossby waves modulate the response of sea surface temperature to the wind forcing.

Despite the similarity of the remote influence on these processes, the regimes of oceanic turbulence are different. In Chapter 3, turbulence is at mesoscales and is highly influenced by seasonal waves and also sustained by the wind stress curl. In Chapter 4, eddy-topography frictional interactions act as a source of enstrophy at depth and create turbulence at submesoscales. In Chapter 5, we have shown that the mesoscale turbulence locally forced by the upwelling surface jet has a comparable intensity to the remotely forced turbulence that interacts with the upwelling site.

Overall, these results contrast with the general functioning of large-scale subtropical and subpolar oceanic gyres. These gyres are forced by basin-scale winds and earth's rotation setting western boundary currents, themselves generating turbulence through instability processes (e.g., Smith, 2007). Waves and winds are not known to impact significantly on the mesoscale variability in these gyres. The short zonal extent and the low-latitude of the Arabian Sea, as well as the seasonally reversing wind forcing, make it being particular. Fast waves and drifting eddies significantly shape the western boundary turbulent regimes.

6.2 Perspectives

Many mechanisms in this dissertation were investigated in the context of issues inherent to the Arabian Sea. However, they would deserve further investigation. Here is a non exhaustive list of points I would like to examinate more closely :

- *Eddy-topography interactions.* The promising results on the eddy-topography interactions presented in Chapter 4 would require further investigation. In fact, we designed the idealized experiment to match with the reality of Gulf of Oman eddies and bathymetry. But some results were not discussed : in particular, what sets the depth of enstrophy creation (Figure 12 in Chapter 4) ? Is there a vertical decay scale of the mesoscale eddies associated with the creation of enstrophy ? How sensitive is this vertical scale to the slope of topography and to the eddy's vertical structure ? How sensitive is the size of SCVs to the grid size of the model ? Furthermore, the formation process of SCVs differs for cyclones and anticyclones (Molemaker et al., 2015; Gula et al., 2015b). It seems that in our simulations, submesoscale cyclones are more robust than submesoscale anticyclones. What explains this characteristic ?

- *Energy budget in upwellings.* The interesting comparison of western vs. eastern boundary upwelling systems is seemingly the first of this kind. However, we did not fully close the budget because we did not investigate the energy sinks. These must be associated with energy radiation out of the domain that would need a specific

analysis. The use of idealized experiments with a simplified setup (strait coastline, alongshore invariant shelf and wind forcing, ...) and upwellings occuring either at western or eastern boundary would allow to derive closed EKE budgets.

Other issues relative to the Arabian Sea would also require further investigation :

- *Sensitivity to bursts in PGW.* Observations suggest that the Persian Gulf outflow is very intermittent at intraseasonal time scales (e.g., Banse, 1997; Pous et al., 2004a). This mechanism involves rapid mixing and adjustment and may be responsible for the formation of SCVs (McWilliams, 1988). Designing an idealized experiment with a sudden intrusion of a homogeneous fluid into a stratified environment could be effective to describe closely this mechanism. In the context of the Persian Gulf outflow, adding temporal variability to the boundary prescription of the outflow could also lead to a richer variability of the spreading.

- *Small scale dynamics in the upwelling off Oman.* As acknowledged at the end of Chapter 5, we described only the large scale functioning of the upwelling. The indented coastline and the complex shelf geometry certainly lead to local forcing of vertical velocities (as compared to vertical velocities forced by wind stress curl). A proper description of the system would require to account for its alongshore heterogeneities. In particular, the description of upwelling water pathways provide a natural follow-up study.

- *Air-sea interactions during the summer monsoon.* The monsoon is a typical phenomenon involving air-sea interactions (e.g., Vecchi et al., 2004). The use of a forced model thus severly limits our understanding of the monsoonal processes. Using general circulation models, Izumo et al. (2008) showed that upwellings in the Arabian Sea impact the rainfall variability on the Asian Continent. The details of these interactions are parameterized in global models and would require a fine scale investigation. For instance, turbulent air-sea fluxes at mesoscales were investigated recently in the southern Atlantic Ocean (Villas Bôas et al., 2015). Furthermore, at interannual time scales, retroactions of the ocean on the atmosphere also play an important role and oceanic interannual variability is fundamentally triggered by these interactions (Beal et al., 2013). Our climatological forcing impedes this variability and studying year-to-year covariability of ocean and atmosphere could be interesting.

Appendix A

Meanwhile, in the Gulf of Guinea

Contents

A.1 Foreword

I did my Master II's internship at the Laboratoire de Physique des Océans, under the supervision of Anne-Marie Tréguier and one of her PhD student, Henrick Berger. The topic of research was the study of the Congo River plume in the Gulf of Guinea[1]. I carried on working on this subject during the first year of my PhD and this is the main reason why I wished to enclose the final product (i.e., the article, Vic et al., 2014a) in the dissertation. Now that this work has been digested and that I have switched to other topics in other regions, I have found another reasons to enclose it. Indeed, this study shares a similar objective with Chapter 4 that is the spreading of an outflow, but a with conceptually different dynamical framework.

A.1.1 An Outflow Problem ...

The Congo River has the second largest rate of flow on Earth ($\sim 40\,000$ m^3 s^{-1}, behind the Amazon River, $\sim 200\,000$ m^3 s^{-1}). This freshwater discharge spreads in the Gulf of Guinea and stays at the surface, being lighter than background waters. It clearly impacts the salinity budget of the surface layer in the Gulf of Guinea and more widely in the Tropical Atlantic (Berger et al., 2014). However, the spreading of the outflow had not been thoroughly examined yet. Similarly to Chapter 4, the objective of this study is understand the mechanisms at play in the spreading of the outflow.

A.1.2 ... With a Different Dynamical Framework

The two main differences between the Persian Gulf outflow and the Congo River outflow are the equilibrium depth and the location of spreading. The Persian Gulf outflow spreads at a western boundary and equilibrates around 200 m whereas the Congo River outflow spreads at an eastern boundary and equilibrates at the surface. A major consequence of the location is the background eddy kinetic energy (EKE). Figure A.1 shows EKE in the regions where both outflows spread. It highlights the important difference between both regions, the Gulf of Oman being 3 to 4 times more energetic than the southern Gulf of Guinea. Thus, frameworks used to study both outflows are fundamentally different. In the Persian Gulf outflow case, we considered the dispersion caused by background eddies whereas for the Congo River, we could consider the background flow to be at rest. Indeed, inviscid theories focused on the spreading of outflows (always considered to spread in quiescent environments) were found to apply well to the Congo River outflow

[1] Henrick's thesis dealt with salinity budgets in the surface layers in the Tropical Atlantic, highly influenced by the Congo River freshwater discharge.

(e.g., Yankovsky and Chapman, 1997; Garvine, 1999; Nof and Pichevin, 2001; Nof et al., 2002).

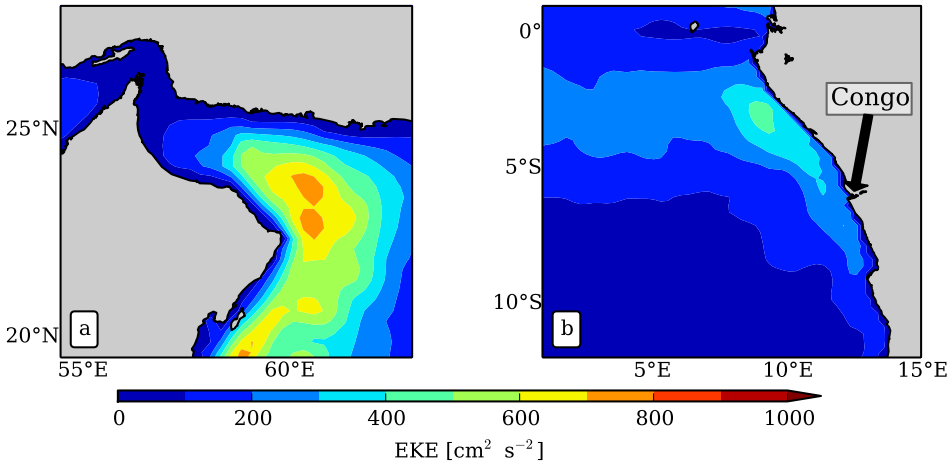

Figure A.1: Eddy kinetic energy (EKE) computed with Aviso's absolute dynamic topography derived geostrophic currents for the period 2000-2012. Maps are (a) the Gulf of Oman where the Persian Gulf outflow spreads and (b) the southern Gulf of Guinea where the Congo River spreads.

A.2 Article published in Journal of Physical Oceanography

Appendix A. Meanwhile, in the Gulf of Guinea

Dynamics of an Equatorial River Plume: Theory and Numerical Experiments Applied to the Congo Plume Case

CLÉMENT VIC

Laboratoire de Physique des Océans, UMR6523, UBO/IFREMER/CNRS/IRD, Brest, France

HENRICK BERGER

Actimar, Brest, France

ANNE-MARIE TRÉGUIER AND XAVIER COUVELARD

Laboratoire de Physique des Océans, UMR6523, UBO/IFREMER/CNRS/IRD, Brest, France

(Manuscript received 14 June 2013, in final form 18 October 2013)

ABSTRACT

The Congo River has the second largest rate of flow in the world and is mainly responsible for the broad tongue of low-salinity water that is observed in the Gulf of Guinea. Despite their importance, near-equatorial river plumes have not been studied as thoroughly as midlatitude plumes and their dynamics remain unclear. Using both theory and idealized numerical experiments that reproduce the major characteristics of the region, the authors have investigated the dynamics of the Congo River plume and examine its sensitivity to different forcing mechanisms. It is found that near-equatorial plumes are more likely to be surface trapped than midlatitude plumes, and the importance of the β effect in describing the strong offshore extent of the low-salinity tongue during most of the year is demonstrated. It is shown that the buoyant plume constrained by the geomorphology is subject to the β pulling of nonlinear structures and wavelike equatorial dynamics. The wind is found to strengthen the intrinsic buoyancy-driven dynamics and impede the development of the coastal southward current, in coherence with observations.

1. Introduction

The outflow of the Congo River is the second largest in the world with a mean rate of flow of about $40\,000\,m^3\,s^{-1}$ (Dai and Trenberth 2002). As such, it is a major contributor to the mean state and the variability of the surface salinity in the Gulf of Guinea (Signorini et al. 1999), and it has been recently shown that it may have a strong impact on climate variability in the region (Materia et al. 2012). Moreover, rivers are important sources of carbon in the ocean (Schlünz and Schneider 2000), and the Congo River is one of the greatest contributors (Coynel et al. 2005). Its signature can be seen very far offshore of the river mouth (Hopkins et al. 2013) as highlighted by Fig. 1, which presents the sea surface salinity (SSS) and the colored, dissolved, and detrital organic matter (CDM) absorption length in the Gulf of Guinea. CDM, which is well correlated with SSS, has been demonstrated to be a useful indicator of the trophic chain and has been successfully used to track the Amazon River plume (Salisbury et al. 2011).

Despite its importance, the Congo River plume dynamics has not been much studied. Even if the role of environmental factors such as the geomorphology, the wind, and the ambient currents have been recently assessed in a realistic model (Denamiel et al. 2013, hereafter D13), the strong northwestward offshore extent of the low-salinity waters during most of the year remains misunderstood. Indeed, it is not a common feature as it opposes the predicted extent of the coastal current in the direction of the coastal Kelvin wave propagation (Chao 1988a) and is abnormally large [reaching 850 km according to Hopkins et al. (2013)]. Many theoretical (Yankovsky and Chapman 1997; Nof and Pichevin 2001) and numerical studies (Chao and Boicourt 1986; Chao 1988a; Kourafalou et al. 1996; Garvine 1999; Schiller

Corresponding author address: Clément Vic, Laboratoire de Physique des Océans, 6 Avenue Victor Le Gorgeu, 29200 Brest, France.
E-mail: clement.vic@univ-brest.fr

DOI: 10.1175/JPO-D-13-0132.1

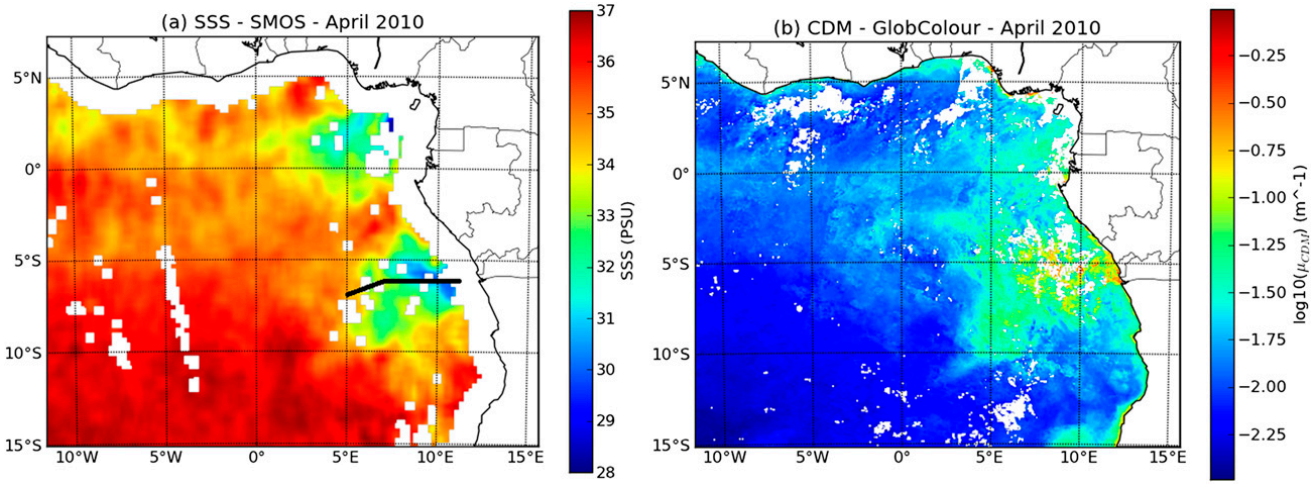

FIG. 1. Satellite visualizations of the Congo plume at the same date (mean over April 2010) during the period of the largest spread of the plume. The Congo mouth is at 6°S. (a) The SSS from Soil Moisture Ocean Salinity (SMOS); the black line represents the section along which the BIOZAIRE section is drawn in Fig. 2. (b) The CDM absorption length scale from GlobColour data.

and Kourafalou 2010) have described the dynamics of midlatitude river plumes and the associated mechanisms of advection and diffusion of freshwater in the unforced case. They have also evaluated the impact of external forcing such as the wind or the bottom topography on plumes. Nonetheless, no study is dedicated to low-latitude river plumes, and the Congo River mouth position, where f is very low and its gradient β is at its maximum, could play a role in the self-induced buoyancy dynamics of the outflow.

Parallel to D13, we have carried out research on the Congo plume with a different strategy. We have situated the Congo River in a theoretical framework in order to predict what could be the dynamics of a near-equatorial plume in an unforced case and explore its fate at longer time scales. Then, we have used idealized numerical experiments to verify our theoretical assumptions and clarify the near-equatorial specific characteristic. Making the study more complex step by step, some sensitivity experiments have been carried out to estimate the impact of the geomorphology (bottom topography and coastline) and the wind on the plume.

In this paper, we aim to provide a new physical explanation for the northwestward extent of the Congo plume. We first describe what is the expected dynamics and morphology of the Congo plume by interpreting some nondimensional numbers associated with the problem in a physical parameter space. After a description of the model and the configuration used, we then discuss the impact of Earth's rotation on the plume as well as other forcings. Finally, we draw the main conclusions on the dynamics of near-equatorial plumes and discuss our results within the context of the realistic study of D13.

2. Theoretical framework

In this section, we review some theoretical and numerical studies that are relevant to near-equatorial river plumes. We also develop a theory of the Congo plume based on the dichotomous distinction of surface-trapped and bottom-influenced plumes made by Yankovsky and Chapman (1997), and then incorporate the major results of Garvine (1999) that reveal the importance of the physical and geometrical parameter range in the near-field dynamics of river plumes. As the Congo River inflow is very important in comparison with standard values of midlatitudes rivers (basically two orders of magnitude of difference), we expect the inflow to reach a significant extent off the river mouth (this is supported by observations; Fig. 1). As such, the fate of the inflow in its far field is also evaluated by considering the theory of Nof and Pichevin (2001) and adapting the quantitative results of Nof et al. (2002b) as their study framework is close to ours.

a. General background

Observations of river inflows into the ocean commonly reveal two types of structures (Chao 1988a; Kourafalou et al. 1996; Yankovsky and Chapman 1997): an anticyclonic circulation at the river mouth and a coastal current that propagates in the direction of coastal Kelvin waves. The anticyclonic circulation is induced by the input of river water that perturbs the vorticity balance. To help describe this, we consider a shallow layer of rotating fluid of a mean depth H, bounded by a flat, rigid surface at either the top or bottom and on the other side by a fluid of different density, forming an interface that deviates from the mean state by η (positive if increasing the layer depth).

TABLE 1. Observed and computed parameters of the Congo River. They are also used in the model in the REF experiment. List based on the Garvine (1999) study.

Parameter	Name	Value
f	Coriolis frequency	$-1.52 \times 10^{-5}\,\mathrm{s}^{-1}$
L	River width	27 km
h_0	River mouth depth	30 m
h_1	Inlet depth	10 m
$S_a - S_i$	Salinity difference	15
v_i	Inlet velocity	$0.148\,\mathrm{m\,s}^{-1}$
T_i	Rate of flow	$40\,000\,\mathrm{m}^3\,\mathrm{s}^{-1}$
A	Tidal height amplitude	0 m (1.1 m observed)
g'	Reduced gravity	$0.113\,\mathrm{m\,s}^{-2}$
c_i	Internal wave speed	$1.063\,\mathrm{m\,s}^{-1}$
r_i	Rossby radius of deformation	70.0 km
α	Shelf bottom slope	0

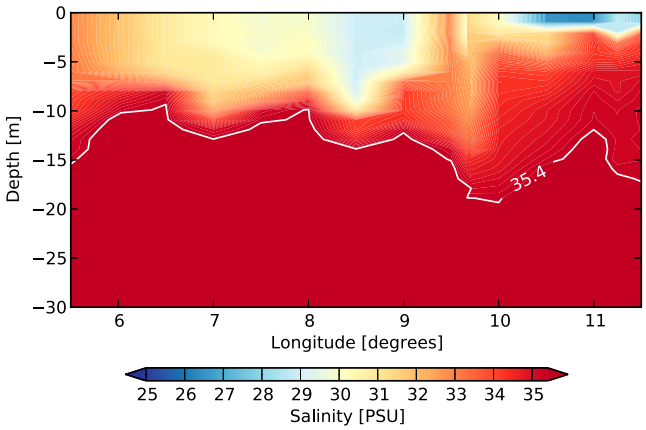

FIG. 2. Vertical salinity section (BIOZAIRE data, stations 22–38), along the path drawn in Fig. 1a. The white line is isohaline 35.4 psu, which can be approximated as the limit of the desalinated waters, as the max of salinity in the region is about 35.5 psu.

We cross differentiate the linear, shallow water momentum equations, which leads to

$$\frac{\partial}{\partial t}\left(\zeta - \frac{f\eta}{H}\right) = -\frac{fQ}{H}, \tag{1}$$

where f and ζ are, respectively, the planetary and relative vorticity; η is the interface displacement; and Q is the rate of flow that enters the conservation equation (positive for a source and negative for a sink). Considering that the layer depth is nearly constant and neglecting variations of the interface, we can deduce that a riverine source will induce a negative relative vorticity at a river mouth. In the case of the Congo River, whose mouth is at 6°S, observations reveal an anticlockwise circulation with a disk shape and a coastal current propagating to the south, leaving the coast to its left, as expected in the Southern Hemisphere (D13, their Fig. 10.1). We will verify this in idealized numerical simulations as described later.

Beyond this theory, model-based works on the river inflows initiated in the 1970s (Garvine 1974; Kao et al. 1977, 1978) pointed out the dependency of the plume on numerous physical and numerical parameters such as the estuarine slope or the estuary width, influencing its shape, size, and stability. Many studies build up a plume classification based on these parameters, according to various criteria such as the relative offshore extension of the bulge compared to the coastal current (Chao 1988a) or the meanders and instabilities developed by the coastal current (Schiller and Kourafalou 2010). Garvine (1999) appears to be the first to provide the quasi-exhaustive list of physical parameters that influence the plume shape.

b. The Congo River parameters

Table 1 presents the real geometrical and physical parameters of the Congo River used to set up the reference experiment (REF) described later. Here, we comment on how we choose these parameters. The Coriolis parameter is calculated at the river mouth (6°S). The width and depth of the estuary are approximated as mean values out of the canyon area because of their spatial high variability. Based on the observation of Eisma et al. (1978) and Vangriesheim et al. (2009), we estimate the depth h_1 of the freshwater surface layer (Fig. 2) and the salinity difference ΔS between the inflow and the ambient shelf water. Depending on the location and naturally decreasing when going downstream, ΔS is about 15 psu [in a range that is consistent with the usual values for coastal plumes, as Kao et al. (1977) notice a salinity difference of 16 psu, for instance]. The inlet velocity v_i is computed as the ratio of the freshwater flux to the section of the estuary, as Lh_1v_i is the rate of flow. To compute a reduced gravity g' representative of the plume, we use a linear model of density calculation varying with the salinity: $\Delta\rho = r_\beta \times \Delta S$, with $r_\beta = 0.824\,\mathrm{kg\,m}^{-3}\,\mathrm{psu}^{-1}$. In fact, in its first approximation, the temperature would not influence density much, as the thermocline is not very marked and lies under a sharp halocline due to the freshwater discharge (Jourdin et al. 2006; Vangriesheim et al. 2009). The propagation speed of the gravity internal waves in a two-layer model is formally $c_i = [g'h_1h_2/(h_1 + h_2)]^{1/2}$, which is frequently approximated to $(g'h_1)^{1/2}$ if the upper layer is much thinner than the bottom layer, as is the case for the Congo plume (see Fig. 2). The shelf bottom slope α is neglected at first. Later on we carry out sensitivity experiments to determine the impact of the slope on the dynamics.

c. Nondimensionalized parameters

Defining seven geometrical and physical parameters (f, L, h_1, $S_a - S_i$, T_i, and A; see Table 1) holding two

TABLE 2. Nondimensional parameters computed from Table 1. List based on the Garvine (1999) study.

	Name	Value
Nondimensional parameters		
$\tau = \frac{2T_i f}{g' h_1^2}$	Scaled inlet transport	0.108
$K_i = \frac{L}{r_i}$	Kelvin number	0.38
α	Shelf bottom slope	0
$\epsilon = \frac{A}{h_1}$	Scaled tidal amplitude	0 (0.11 observed)
$\frac{L}{h_1}$	Aspect ratio	2700
Alternative parameters		
$F_i = \frac{v_i}{c_i} = \frac{\tau}{2K_i}$	Froude number	0.139
$\mathrm{Ro}_i = \frac{v_i}{fL} = \frac{\tau}{2K_i^2}$	Rossby number	0.289

independent dimensions (time and length), one can determine five nondimensional, independent parameters (τ, K_i, α, ϵ, and L/h_1; see Table 2) driving the dynamics. We can interpret them separately, deducing some expected theoretical characteristics of the Congo plume (the role of the shelf slope α is discussed later):

(i) The scaled inlet transport τ satisfies $\tau \ll 1$. This implies that the river transport is far less important than the geostrophic flow induced by the gravity current. The river dynamics can therefore be neglected in the setup of the intrinsic buoyancy-driven dynamics of the plume. Independently, this parameter is also used by Yankovsky and Chapman (1997), who associate $\tau \ll 1$ with surface plumes, leading to consistency with what we found.

(ii) The inlet Kelvin number verifies $K_i < 1$, which shows that Earth's rotation does not play an important role in the dynamics. This is due to the near-equatorial position of the river mouth and implies that the coastal current does not transport much freshwater in comparison with the lens.

(iii) The scaled tidal amplitude is very weak as suggested by the parameter $\epsilon \ll 1$ (from Eisma et al. 1978), which means that the tidal effect has a negligible importance over the near-field plume dynamics. As such, we do not take the tide into account in our experiments.

(iv) The aspect ratio $L/h_1 \gg 1$ shows that the outflow is mainly horizontal and that we can use the hydrostatic approximation in further simulations [this aspect ratio has an importance for laboratory tank experiments (Sutherland and Cenedese 2009)].

The first two nondimensional parameters τ and K_i are both linked with other parameters: the inlet Froude number $F_i = v_i/c_i = \tau/(2K_i)$ and the inlet Rossby number $\mathrm{Ro}_i = v_i/(fL) = \tau/(2K_i^2)$. The inlet Froude number $F_i < 1$ can be interpreted as a prevailing input of potential energy rather than kinetic energy (Garvine 1999). The inlet Rossby number $\mathrm{Ro}_i = O(1)$ indicates that the flow is not completely geostrophic at the river mouth and presents nonlinearities in the near-field plume development as we expect advection to play a role in the salt transport.

Even if the theoretical results of Yankovsky and Chapman (1997) place the Congo plume as surface trapped, D13 notice that the geomorphology of the estuary (partly represented through the shelf slope α) plays an important role in the plume morphology. This is why we further dedicate sensitivity experiments to the influence of the bottom slope, taking into account previous idealized studies such as the ones of Kourafalou et al. (1996) and Chao (1988a) that reveal that the slope has a trapping effect on the bulge at the coast, slowing down its offshore extension.

In summary, the major theories of unforced plumes indicate that the Congo River parameters are in a range that induces a surface-trapped plume without any influence of the bottom slope and a large-scale, horizontal, anticlockwise geostrophic circulation with an offshore spreading bulge largely dominating a small coastal current going southward. Furthermore, the dynamics should be dominated by the gravity current rather than by the transport generated by the river inflow. Concerning the tidal impact, observations show that it is negligible (Eisma et al. 1978).

d. Near-field plume morphology

Here, we concentrate on the Yankovsky and Chapman (1997) study that appeared to be the most relevant for the near-equatorial case to describe the near-field plume morphology. Their theory classifies the plume in two distinct categories. On the one hand, the plume can be surface trapped, which means that the freshwater thin surface layer does not have any interaction with the bottom and the anticyclonic bulge extends offshore with a disk shape. On the other hand, it can be bottom influenced, which means that in this parameter range, the plume feels the bottom friction and its offshore extent is compromised by its vertical and coastal spread. This theory is based on simple hypotheses such as the cyclogeostrophic equilibrium on an f plane in the bulge that involves a balance between the pressure force, the Coriolis force, and the centrifugal force:

$$-v^2/r - fv = -g' \frac{\partial h_1}{\partial r}, \tag{2}$$

where v is the azimuthal velocity, r is the bulge radius, f is the planetary vorticity, and g' is the reduced gravity

between the upper thin layer of freshwater of depth h_1 and the bottom layer of ambient shelf water (values are found in Table 1). Considering a constant vertical shear of the horizontal velocities, Yankovsky and Chapman (1997) calculate the depth at which the plume should be trapped:

$$h_b = (2Lv_i h_1 f/g')^{1/2}. \quad (3)$$

Within the real Congo River parameters that are also used in the model (Table 1), we have $h_b = 3\,\text{m} < h_1$. The predicted equilibrium depth for the bottom-influenced plume is shallower than the real depth of the buoyant inflow so the plume is surface trapped. In Eq. (3), the Coriolis frequency acts in favor of trapping by the surface for a near-equatorial plume. This feature is observed in the BIOZAIRE cruises (see salinity section of Fig. 2) carried out by L'Institut Français de Recherche pour l'Exploitation de la Mer (IFREMER) between 2000 and 2005 (Vangriesheim et al. 2009) and OPTIC–CONGO carried out by the Service Hydrographique et Océanographique de la Marine (SHOM) in March 2005 (Jourdin et al. 2006), where the Congo plume is surface trapped with no evidence of coastal current (it would have been necessarily noticeable if the plume was bottom influenced). The shape of the surface bulge is also observed to spread like a lens in the satellite observations of CDM absorption length of GlobColour data (Maritorena et al. 2010) and sea surface salinity of SMOS data (Boutin et al. 2012) (see Fig. 1). The realistic simulations of D13 confirm these aspects of the observations. However, the strongest hypothesis of Yankovsky and Chapman (1997) is that the flow is in dynamical balance with no growth of the bulge radius at the equilibrium state. This implicitly hides the fact that a balance is reached between advection and diffusion of buoyancy after a certain period (Garvine 1999). Dynamics of inviscid outflow leads to different results.

e. *High rate of flow plume dynamics at long time scales*

Studies of Pichevin and Nof (1997), Nof and Pichevin (2001), Nof et al. (2002a,b), and Nof (2005) focus on inviscid outflows, inflows, and throughflows spreading in a β-plane ocean through straits or archipelagos. The first paper of this list highlights the fact that the outflowing bulge cannot be in momentum balance (under the assumption of no momentum viscosity nor diffusivity) as nothing can counterbalance the force exerted by the alongshore current. Consequently, the plume is shedding eddies that are moving contrary or at a right angle to the coastal current, depending on the coast orientation. These theory- and attendant-derived cases (depending on the geometry of the configuration) give general features of some real outflows (Indonesian Throughflow, Red Sea outflow, and Loop Current, for instance). Although this framework is useful for studying outflows with high rates of flow [greater than 0.1 Sverdrups (Sv; $1\,\text{Sv} \equiv 10^6\,\text{m}^3\,\text{s}^{-1}$), as the ones cited], it has never been referred to when dealing with river inflows, as their rates of flow are generally much lower (order of magnitude of 0.001 Sv). In fact, the bulge has to reach a certain size defined by the theory before being sheared by the planetary vorticity gradient and relaxing eddies that drift westward due to β. Basically, if the rate of flow is not important enough, diffusion processes of buoyancy due to the wind or tidal mixing effects impede a sufficient development of the lens.

The Congo River presents a mean outflow of 0.04 Sv and is seemingly not topographically controlled (Yankovsky and Chapman 1997), which is a necessary assumption to use this theory, so we could expect its associated bulge in a nonforced case (without wind and tide) to grow sufficiently to shed eddies. To describe the expected behavior, we use the framework of Nof et al. (2002b) applied to the Indonesian Throughflow that has the same configuration as the African west coast at the Congo River latitude with its meridional coastline oriented westward.

The detachment condition of the eddy is that its westward drift just exceeds its growth rate (Nof et al. 2002b), and then the vortex detaches from the coast and migrates westward. Equating the growth rate of the eddy dR/dt, where R is the eddy radius, with the drifting velocity of nonlinear eddies $(2/3)\beta R d^2$ (Nof 1981) gives the final eddy radius. Adding an assumption on the vorticity profile of the growing lens, Nof et al. (2002b) find an analytical solution for the eddy radius and their frequency of ejection. For a linear orbital speed of $v_\theta = (-\alpha/2)fR$ (meaning that the relative vorticity is $\zeta = -\alpha f$, α being a nonlinearity parameter), the final radius of the eddy at detachment is

$$R_f = \frac{2\sqrt{2}}{[(2-\alpha)\alpha]^{1/2}}\left[\frac{3\alpha^{1/2}(2-\alpha)^{3/2}}{8\sqrt{2}\pi}\frac{g' T_i}{\beta f^2}\right]^{1/5}, \quad (4)$$

and the period of ejection is

$$T = \frac{48\ (1-\alpha/2)}{(2-\alpha)\alpha}(\beta R_f)^{-1}. \quad (5)$$

Figure 3 shows that the radius and period of ejection of eddies are very sensitive to the vorticity profile. The smallest period is reached for highly nonlinear eddies ($\alpha = 1$) and is greater than 100 days at the Congo latitude (bold lines). The "Baseline" run performed by D13

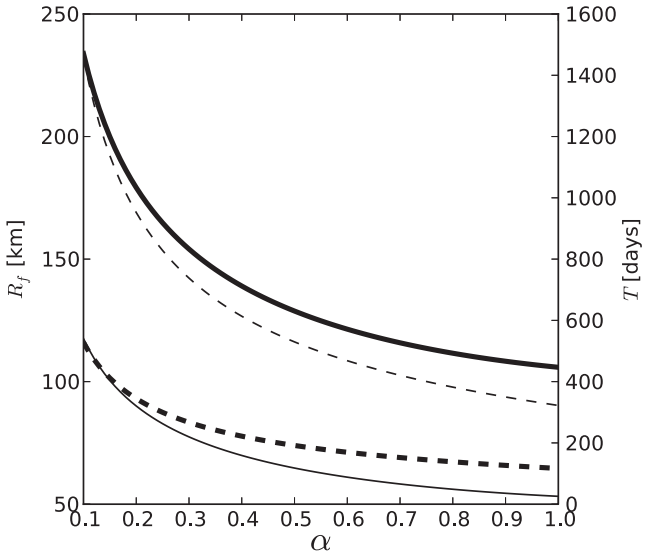

FIG. 3. Max radius R_f (plain) and period of ejection T (dashed) of the eddies at the Congo lat (bold) and at 46°S (thin), depending on the nonlinearity parameter α. See Eqs. (4) and (5).

(i.e., with no forcing but a realistic coastline and bathymetry) was only run for 40 days to avoid spurious interactions between currents in the plume and boundaries of the domain, so they were not able to observe β pulling of nonlinear structures offshore.

In conclusion, this theory applied to our case study reveals that the high rate of flow of the Congo River combined with its equatorial position imposing small f (thus large radius of deformation) and high β acts in favor of an important westward β pulling of nonlinear vortical structures according to Eq. (5) derived from Nof et al. (2002b).

3. Model description

To verify our theoretical results concerning the Congo plume classification, we carry out numerical experiments. We use idealized configurations, starting from a simplified unforced problem with different assumptions on the Coriolis parameter, and then evaluate the role of wind and topography through sensitivity experiments. Here, we describe the reference experiment (hereafter REF). In contrary to the Baseline unforced simulation of D13 performed for 40 days to see the near-field extent, we ran the simulations for 1500 days to see the fate of the plume at long time scales, testing the validity of the Nof et al. (2002b) theory.

We use the Regional Ocean Modeling System [ROMS; see Shchepetkin and McWilliams (2005) for a complete description] in its version 3.0. ROMS solves the primitive equations on an orthogonal curvilinear coordinate system. The latter is terrain following to better represent the effect of topography on the fluid. The advection scheme is third-order upstream biased, has low numerical dissipation, and is assessed to be strong enough not to add physical explicit eddy viscosity nor tracer diffusivity in the interior of the domain. The diffusive part of the advection scheme is rotated along the iso-geopotential surfaces to avoid spurious diapycnal mixing as explained in Marchesiello et al. (2009). Subgrid-scale vertical mixing processes are parameterized using the K-profile planetary (KPP) boundary formulation (Large et al. 1994).

Our configuration is based on a 1/12° grid with idealized meridional coastline and a waterway at the Congo River mouth latitude at 6°S. Bathymetry is constant in the basin (1000 m) and the waterway (30 m). Between the basin and the waterway, topography follows a slope of approximately 1%. The grid has 40 vertical levels with refinement only at the surface using stretching parameters $\theta_s = 6.5$ and $\theta_b = 0$ (Haidvogel and Beckmann 1999) with geometrical transformation parameter Vtransform = 2. The minimum depth at which stretching occurs is defined in the parameter h_c = 300 m, and the minimum depth represented is 15 m. The western, southern, and northern boundaries are open with viscosity coefficient of 300 m s^{-2} on a sponge layer of width 100 km. The river runoff is prescribed at the end of the waterway, and steady stratification on the column is effective on the waterway. Temperature is taken uniform on the domain as well as salinity of 35.5 psu, which is the maximum reached in the subsurface in this region according to the Levitus climatology (Levitus 1982). Temperature and salinity are taken as constant to isolate the influence of the river inflow on the buoyancy in the basin.

The topography used for the TOPO and WIND sensitivity experiments (deeply described later) is from the 2-Minute Gridded Global Relief Data (ETOPO2) (Smith and Sandwell 1997). It has been smoothed under the constraint $\Delta h/2h < 0.2$. The wind stress of the WIND experiment is an annual mean computed from the Scatterometer Climatology of Ocean Winds (SCOW) monthly climatological dataset (Risien and Chelton 2008) computed for 122 months (September 1999–October 2009) of Quick Scatterometer (QuikSCAT) data (dataset is available at a 1/4° resolution at http://cioss.coas.oregonstate.edu/scow/) (Fig. 4).

4. Buoyancy-driven dynamics of the REF experiment

During the first 150 days of the simulation, we observe the growth of the surface lens with its anticyclonic circulation (Fig. 5) and the spreading of a coastal current in the direction of the coastal Kelvin wave propagation, in

Appendix A. Meanwhile, in the Gulf of Guinea

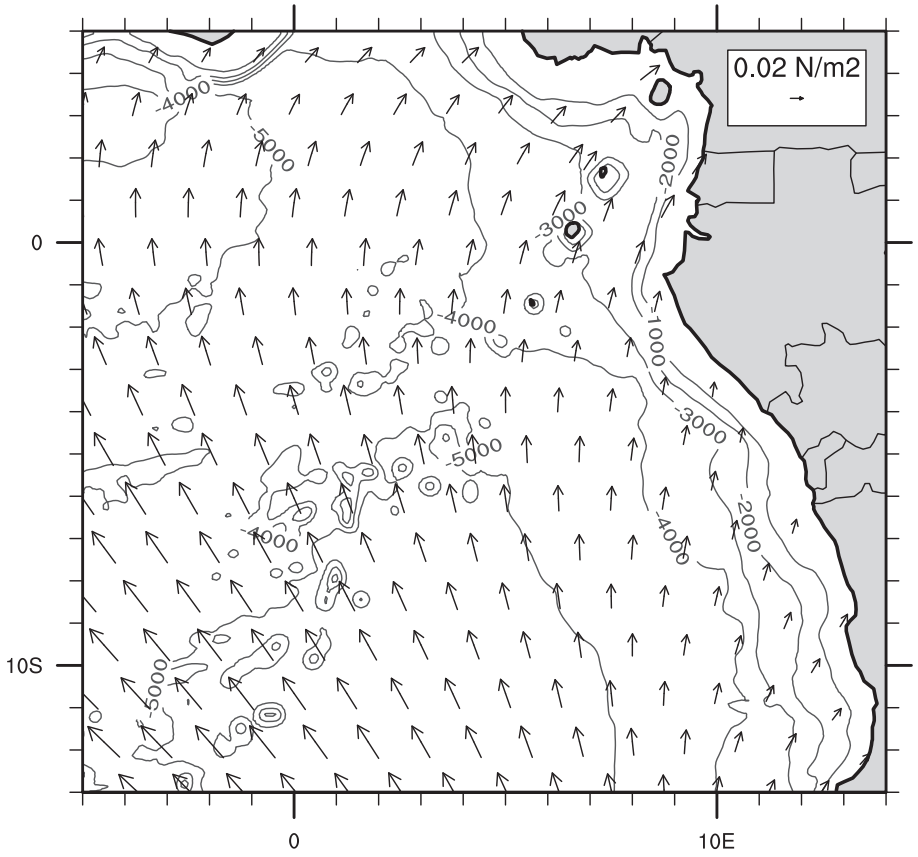

FIG. 4. Bathymetry and wind stress fields used in TOPO and WIND experiments (see text for details). Topography contour interval is 1000 m. Wind stress is an annual mean (SCOW climatology).

coherence with the theory. Compared to the low Kelvin number experiments of Garvine (1999) (cf. his Figs. 7 and 8 with our Fig. 5a), the plume develops in a predicted way, with a huge anticyclonic bulge (see map of surface relative vorticity in Fig. 6a at 100 days of simulation) containing most of the desalinated waters and a narrow coastal current. This is due to the weak impact of the Coriolis force on the dynamics near the equator, as deduced from the low Kelvin number K_i. The nondimensionalized, surface relative vorticity $\zeta/|f|$ scales as the Rossby number and is a good indicator of the degree of geostrophy of the flow. Figure 6a displays relatively high vorticity patterns ($\zeta/|f| > 0.7$) that indicate that the flow departs from geostrophy just at the waterway mouth. The Rossby number found in the theory (Table 2) reveals an important part of the advection in the plume dynamics that is verified in simulations.

Figure 7a presents a vertical section of salinity in the axis of the waterway at 500 days of simulation for the REF experiment. We verify that the layer of low-salinity water is contained at the surface and does not reach the bottom in the waterway, as anticipated by the theory. The plume classification as surface trapped is validated by both the section and the morphology of the surface bulge [see schematics of Figs. 1 and 2 of the Yankovsky and Chapman (1997) study]. This is seemingly a robust result of equatorial plumes as we show that a weak Coriolis frequency acts in surface trapping the bulge [Eq. (3)]. The depth of the surface layer is between 10 m at the river mouth and 40 m in the core of the plume according to the white line representative of isohaline 35.4 psu (background salinity is 35.5 psu). It is difficult to determine its depth precisely because the bottom limit of the plume is not as marked as in the observations. Nonetheless, we notice that this depth range includes the one of the BIOZAIRE section (Fig. 2), which is around 20 m.

As demonstrated by Pichevin and Nof (1997) and Nof and Pichevin (2001), and noticed by Fong and Geyer (2002), the lens cannot reach a stationary state and its offshore-oriented growth is the result of a balance between three alongshore forces: the ''jet'' force (Nof et al. 2002b) resulting from the downstream current, the integrated Coriolis force resulting from the offshore displacement of the eddy center, and the β-induced force pulling it equatorward. The bulge reaches a critical size

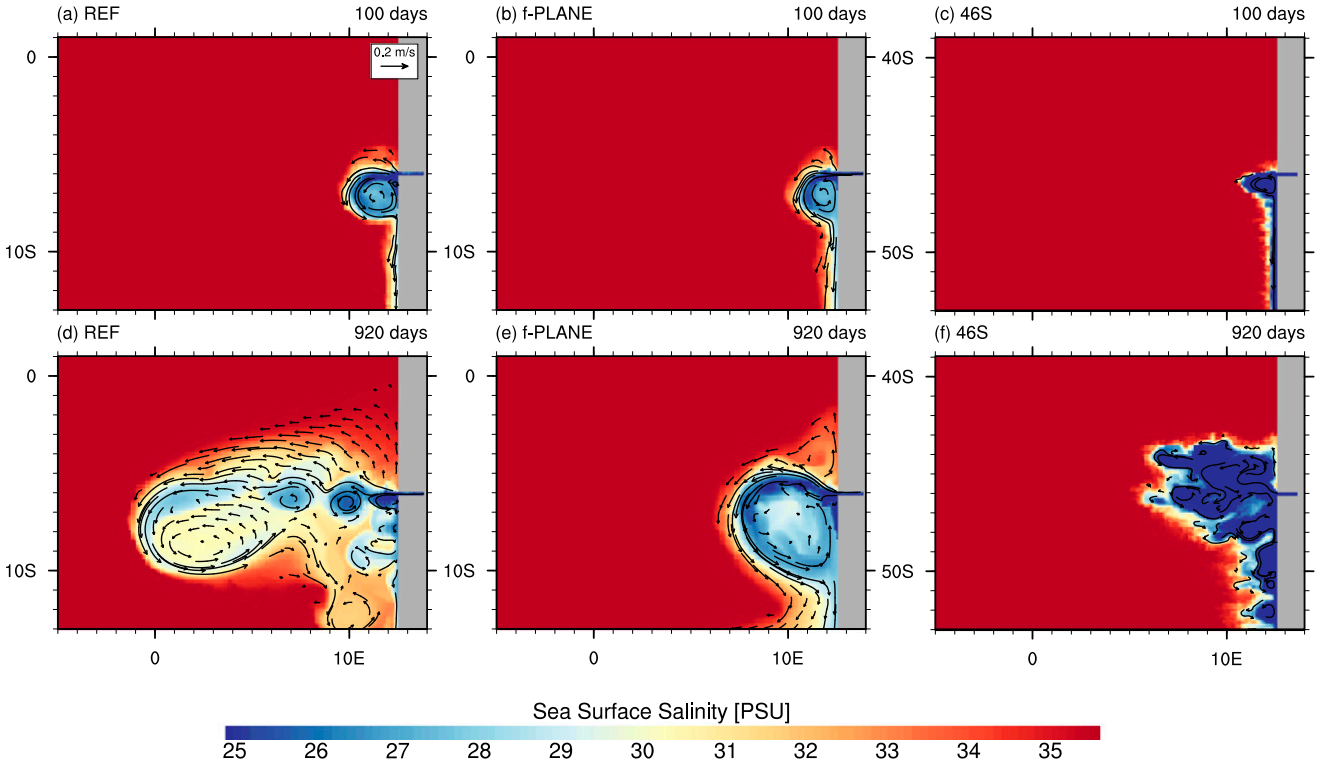

FIG. 5. SSS and surface velocity field at 100 and 920 days of simulation for the REF experiment with no assumption on the (a),(d) Coriolis frequency, for the (b),(e) *f*-plane experiment, and the (c),(f) midlatitude experiment 46°S.

as discussed in the previous section, and mesoscale anticyclonic eddies are ejected, transporting low-salinity waters offshore (Fig. 5d). Figure 8 is a time–latitude diagram of sea surface height (SSH) at longitude 10°E. This representation allows one to visualize separately the eddies' shed, thus assessing their averaged size and period of shedding. The size of eddies is about 200 km (we exclude the first structure displaying high SSH that is formed by aggregation of eddies), and their averaged period of ejection is 42 days. High values of $\zeta/|f|$ in vortex cores (Fig. 6b) are representative of nonlinear eddies, and according to Fig. 3, we should observe shedding periods of about 110 days. However, Nof et al. (2002b) find a similar discrepancy of a factor of 2 between their theoretical and experimental periods of ejection. Nevertheless, the size of eddies is in good agreement with the theory as their radius is estimated to 110 km (Fig. 3).

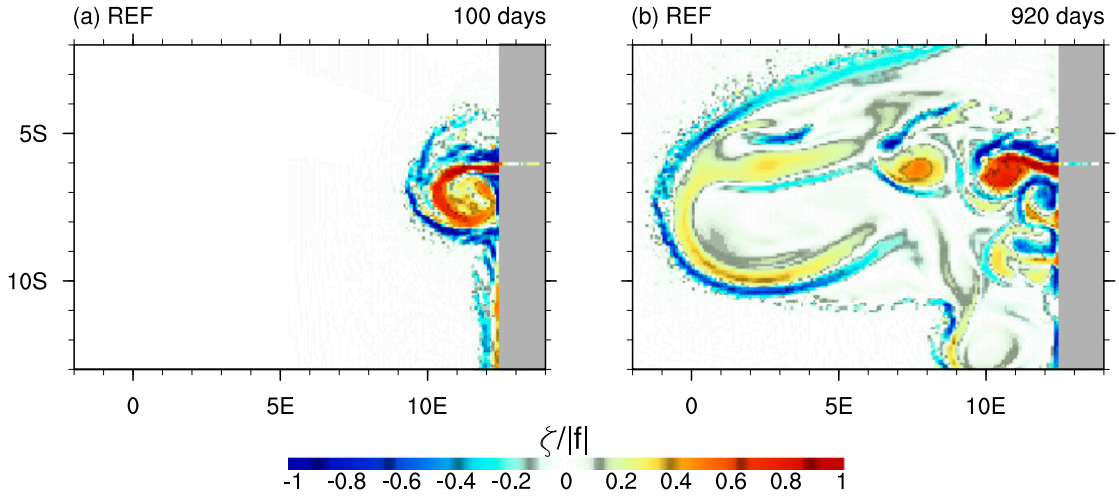

FIG. 6. Surface relative vorticity ζ nondimensionalized by the Coriolis frequency $|f|$ for the REF experiment at (a) 100 and (b) 920 days of simulation.

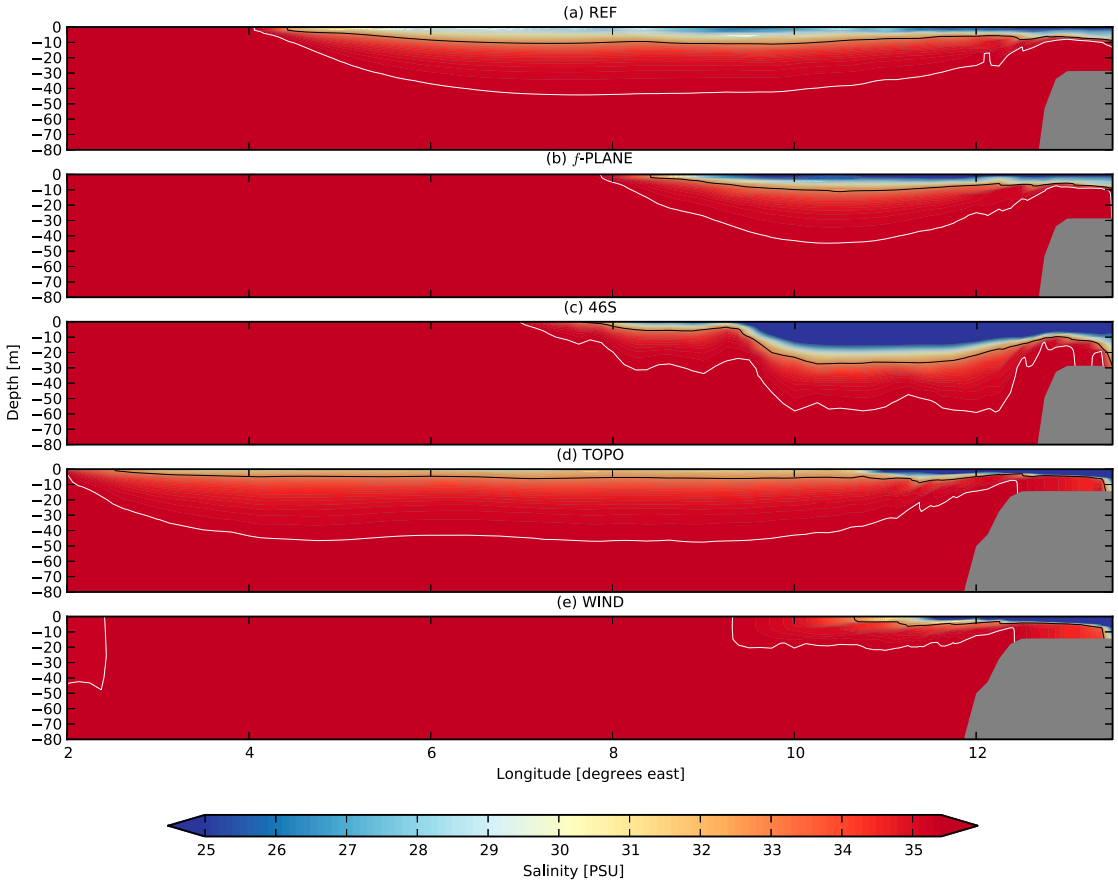

FIG. 7. Vertical zonal sections in the axis of the middle of the waterway at 500 days of simulation. (a) REF experiment, (b) *f* PLANE, (c) 46°S, (d) TOPO, and (e) WIND. The white (black) line is the isohaline 35.4 psu (33 psu), which determines the limit of the plume, as the salinity in the basin is taken constant of 35.5 psu.

As vortical structures shed are anticyclonic, they are expected to move equatorward (Sutyrin and Flierl 1994; Morrow et al. 2004). Surprisingly, this behavior does not occur and seems to be overwhelmed by another process very active in our experiments, that is, the interaction between like-sign vortices (Carton 2001). Indeed, the distance separating the eddies of the REF simulation (identified in surface relative vorticity; Fig. 6b) is less than the critical merger distance that is approximately 3.3 times the vortex radius (Carton 2001), and this is why merging occurs. This phenomenon is often preceded by a rotation of the eddy centers around each other in a direction depending on their polarity. Two anticyclonic vortices move around each other in an anticyclonic

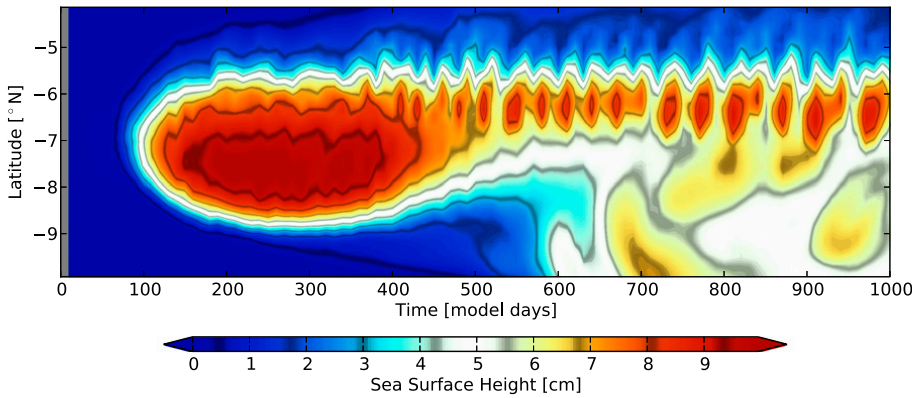

FIG. 8. Time–lat diagram of the SSH for the REF experiment at 10°E.

motion, and this is what we observe before merging the structures. The closeness of the eddies is therefore a prevailing condition that makes them interact strongly and impedes their westward drift to be deflected equatorward. The large-scale bulge (Fig. 5) of low-salinity water is the result of merging smaller anticyclones. The downstream coastal current also becomes unstable and develops meandering patterns and recirculation cells close to the coast, but we do not focus on these instabilities.

The REF experiment verifies the main characteristics of the plume developed in the theoretical part, in its near field as well as in its fate at long time scales. In terms of near-field plume morphology, theory and experiment confirm that it is surface trapped and that the large anticyclonic circulation overwhelms the weak coastal current. The Congo River high rate of flow associated with its near-equatorial position seem to be a sufficient condition for the shedding of eddies transporting low-salinity waters far offshore of the river mouth, as commonly observed in the real case (Fig. 1). To test the robustness of this explanation for the large offshore extent of the plume, we carry out sensitivity experiments on Earth's rotation effect and on wind and topographic forcing on the plume.

5. Sensitivity of the plume

We use two sensitivity experiments to evaluate the role of the near-equatorial position on the dynamics. The 46°S experiment is derived from the REF experiment by shifting every grid point by 40° poleward. As a consequence, the river mouth that is normally situated at 6°S is now at 46°S. The *f*-plane experiment differs from the REF experiment by the *f*-plane approximation made on the domain. The Coriolis frequency is taken as constant everywhere at the value it has at the river mouth (Table 1).

According to D13 findings, the geomorphology of the Congo River plume environment plays an important role in its development in the upstream direction. In addition, many studies [see Kourafalou et al. (1996) and Chao (1988a), for instance] reveal that the estuarine slope and the continental shelf have an impact on midlatitude plumes, which is why we measure the sensitivity of the plume on a real bathymetry in the TOPO experiment.

The Congo River enters the ocean at a latitude where steady trade winds blow during the majority of the year and develop coastal upwellings (Verstraete 1992). To assess the effect of the wind on the plume, we use a real forcing by wind stress in the WIND simulation. Winds are parallel to the coast and upwelling favorable in the Congo mouth vicinity.

a. Effect of Earth rotation

The 46°S experiment confirms that some of the distinguishing features of the near-equatorial plume cannot be reproduced at midlatitudes. In Figs. 5c and 5f, we see that the extent of the bulge is far less important than in the REF experiment, and the coastal current is much better developed, containing more low-salinity water, in coherence with the high Kelvin number experiment of Garvine (1999) (cf. his Fig. 7 with the current Fig. 5f). As the Coriolis force is about 7 times stronger in midlatitudes (at 46°S; $f = 1.05 \times 10^{-4}\,\mathrm{s}^{-1}$), the flow is more tilted to the left directly at the river mouth, and the anticyclonic circulation cannot spin up as smoothly as it does in the near-equatorial case. We also notice in Fig. 7c that the depth of the plume is greater than in the REF case, as suggested by the theory of Yankovsky and Chapman (1997) that implies a larger influence of the bottom at higher latitudes. The freshwater layer in the waterway is also deeper because the Coriolis force creates a meridional slope of the low-salinity layer depth, thinning it northerly and deepening it southerly.

At midlatitudes, the minimal period required to shed eddies is more than 300 days (Fig. 3, thin lines) for the highest nonlinear eddies ($\alpha = 1$). This time scale is much higher than the characteristic time of baroclinic and frontal instabilities developing in the bulge. For instance, Fong and Geyer (2002) and Kourafalou et al. (1996) found the order of magnitude of destabilization times of about 10 days. Small anticyclonic eddies sometimes detach from the lens, but they are drifting westward too slowly and merge with other anticyclonic structures of the plume. In fact, with an equivalent stratification (that is the case of our simulations), their drifting velocity $\propto \beta(g'h_1/f^2)$ is reduced by nearly two orders of magnitude.[1] As a consequence, even with an important rate of flow, β pulling of nonlinear structures is not an active mechanism for transporting low-salinity waters off the river mouth at midlatitudes, and this may be a reason why, to the authors' knowledge, no study dedicated to the midlatitudes' river plume describes the ejection of eddies.

On the *f*-plane experiment, we confirm that the near-field plume has the same shape as in the REF simulation (Figs. 5a,b). The growth of the bulge does not show any difference with the REF until about 150 days when it reaches a sufficient diameter that makes it feel the gradient of *f*. On the sphere, the lens detaches from the coast due to the β effect, whereas on the *f* plane, its growth is unlimited as an outflow can never be steady

[1] Divided by 1.4×7^2 as $f_{46°S} \approx 7 \times f_{REF}$ and $\beta_{46°S} \approx \beta_{REF}/1.4$.

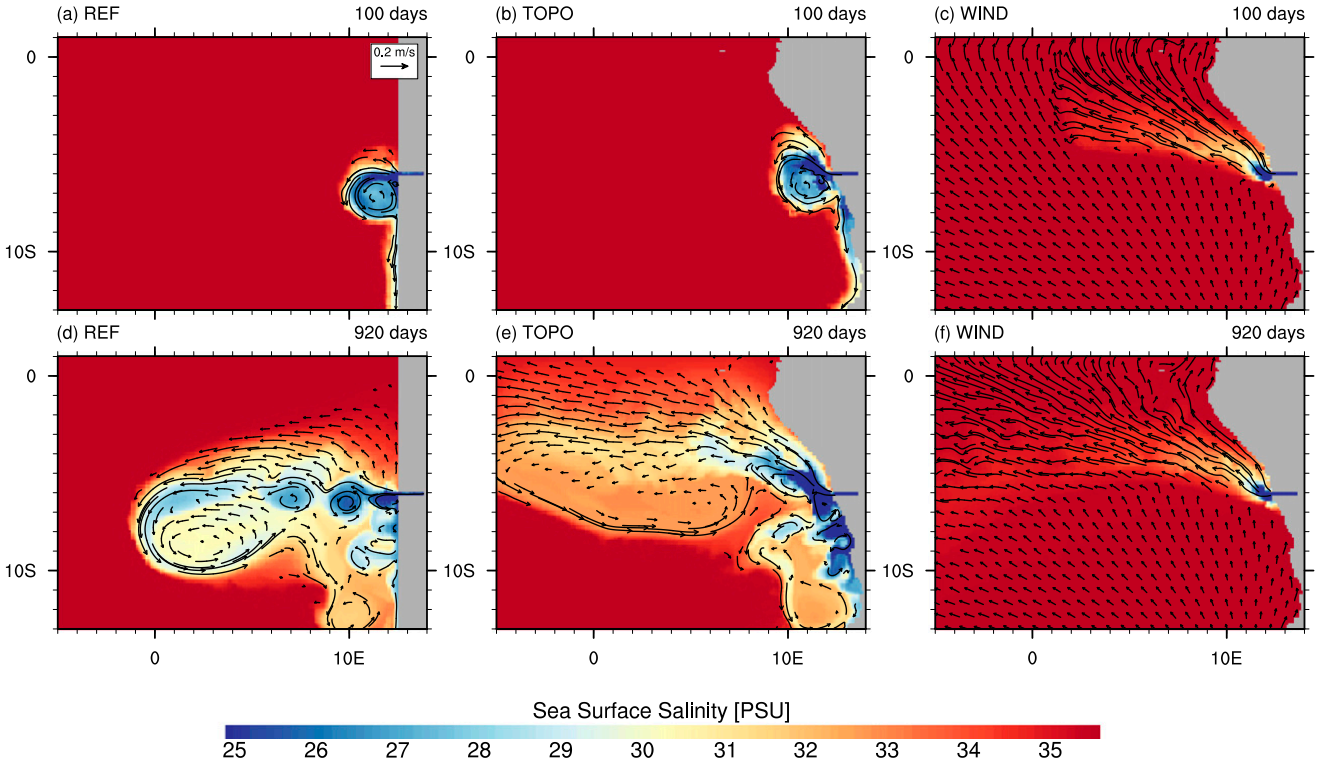

FIG. 9. SSS and surface velocity field at 80 and 300 days of simulation for the (a),(d) REF experiment, for the (b),(e) TOPO experiment, and the (c),(f) WIND experiment.

(Nof et al. 2002b). The impact of β on the transport of low-salinity waters is clearly seen on the sections of Fig. 7 where the offshore extent of the bulge nearly doubles between REF and f plane.

Those experiments clearly underline the importance of the β effect to reproduce the offshore drift of low-salinity waters observed in satellite measurements (Fig. 1) and modeled in the realistic numerical simulations of D13. In fact, because of the huge rate of flow and the near-equatorial position of the river mouth, the meridional length scale of the plume is larger than in previously published experiments carried out at mid-latitudes with weaker rates of flow. This allows the development of westward β pulling of nonlinear structures.

b. *Impact of the geomorphology*

The estuarine and the shelf slopes tend to trap the plume at the coast and limit its offshore extension (Kourafalou et al. 1996; Chao 1988a). Shallow waters are also more inclined to be bottom influenced (Yankovsky and Chapman 1997). Nevertheless, these results apply mainly to midlatitude plumes, which are more likely to feel the influence of the topography and the bottom Ekman layer as reviewed before. This can be seen in the computation of h_b [Eq. (3)] that varies as $f^{1/2}$, which means that the greater f, the more likely the plume to be bottom influenced. The TOPO experiment is set up to assess the impact of the real geomorphology and topography of the Congo River environment on its plume.

The scenario of the plume spreading is threefold. From the onset of the plume until about 130 days, its growth does not show any major difference with the REF experiment (Figs. 9a,b), developing an anticyclonic circulation and a downstream coastal current. The only small difference can be seen in the vertical structure of the plume whose isohaline 35.4 psu intersects the bottom (Fig. 7; although the figure is at 500 days and stratification in the waterway does not vary after 40 days of simulation), which is a distinguishing feature of bottom-influenced plumes. This trapping is certainly due to the shallower estuarine bathymetry and the smoother shelf slope, divided by almost three compared to the REF configuration.

As such, from 130 to about 300 days, the plume develops an upstream, coastally trapped current (Chapman and Lentz 1994) that has been shown to be a robust feature of bottom-influenced plumes (Matano and Palma 2010). The excursion of this current reaches a critical latitude at which dynamics can be interpreted in terms of wave propagations in a more linear regime than the geostrophic turbulence of midlatitudes (Theiss 2004).

This critical latitude has been noticed to be around 3° in regional primitive equation simulations (Penven et al. 2005). An important part of low-salinity waters seem to be pulled by the upstream current forming a large tongue northwestward of the river mouth.

Onward, two mechanisms modulate the transport of low-salinity waters. Examining Fig. 10 (SSH Hovmöller diagram at 2°S) leads to the distinction of two phenomena that seem to be trapped in the equatorial band. First, the propagation of the front of the tongue is noticeable by the most important SSH gradient that crosses the basin at a nearly constant speed of $3\,\mathrm{cm\,s^{-1}}$. This advective speed is associated with the movement induced by the baroclinic pressure of the constantly refilled upper layer (Nof et al. 2002b). Second, westward-propagating waves behind the front are generated near the coast and travel at a speed of about $12\,\mathrm{cm\,s^{-1}}$. These waves stop propagating at the front, which means that they need the plume-like stratification to exist (Nash and Moum 2005) and cannot be projected on classical equatorial wave modes that propagate on the background stratification of the model. Many crests of these waves can be observed in the signal and allows a dominating period of 32 days to be distinguished. Figure 11 can be compared to Fig. 8, as it shows the same eddy propagation field for the TOPO experiment at a latitude shifted by 1° northward. This northward shift between both simulations is certainly due to the northward-oriented estuary that deflects the flow in this direction. The same eddies are observed as in the REF experiment, but the signal is a bit noisier and attenuated (note the different color scales). The detaching period of eddies is found to be approximately 40 days, and even if they are not apparent in the surface tracer maps (Fig. 9), they are the footprint of a characteristic free mode of the dynamical system [Eq. (5)]. This period is close to the one of the wave generation occurring a few degrees of latitude equatorward, and the Congo River inflow could be seen as a wave maker, exciting signals that modulate the spreading of low-salinity water. The geomorphology thus plays an important role in driving the near-field plume northward, then reaching the equatorial band where wave signals are dominating.

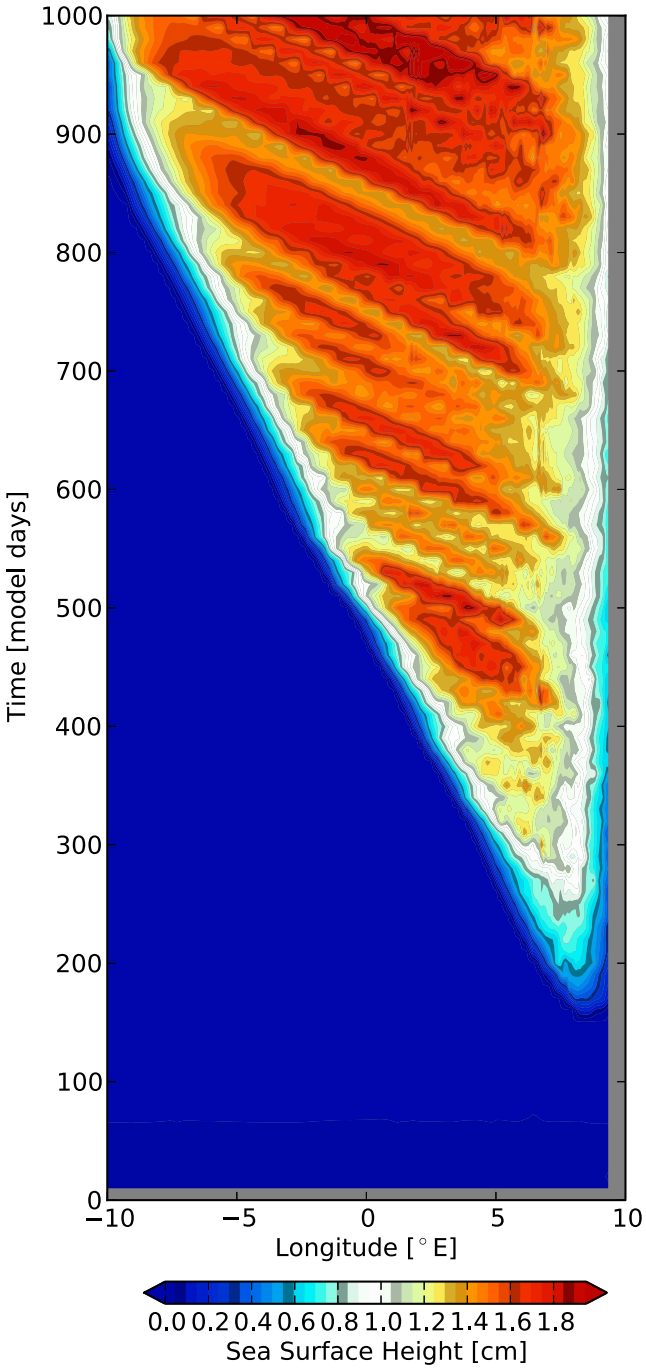

FIG. 10. Time–lon diagram of the SSH for the TOPO experiment at 2°S.

c. *Impact of other forcing*

Many studies have focused on the role of the wind on buoyant coastal currents and river plumes. The first numerical experiments were carried out by Chao (1988b), who concluded that the most important response was the wind-induced surface Ekman drift. Upwelling favorable winds cause the seaward excursion of the plume and tend to increase the vertical mixing and reduce stratification. Lentz (2004) developed a two-dimensional theory to quantify the effect of the wind on an existing plume by calculating the entrainment rate and the offshore drift of the coastal current.

Figures 9c and 9f show the response of the plume to the steady wind field at 100 and 920 days of simulation. The wind-driven surface Ekman current at about 45° to the left of the wind direction (Fig. 4) largely dominates the dynamics outside the plume. The plume core is

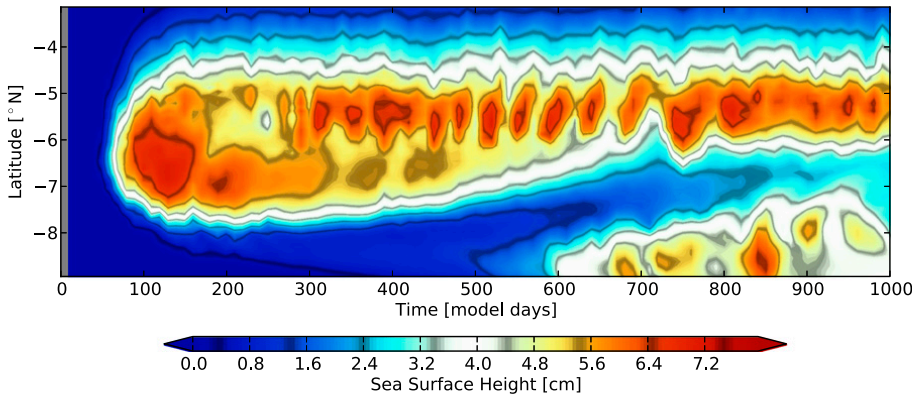

FIG. 11. Time–lat diagram of the SSH for the TOPO experiment at 10°E.

transported northwestward under the influence of this Ekman drift (Chao 1988b). The salinity section of Fig. 7e does not represent the core of low-salinity water that is situated more northward, but we can notice the effect of containment of the plume height on the Ekman depth (Fong and Geyer 2001) $h_{\mathrm{Ek}} = (2A/|f|)^{1/2}$, where A is the vertical eddy diffusivity. With $A \approx 5 \times 10^{-3}\,\mathrm{m^2\,s^{-1}}$ in the surface layers of the model in the plume area, we have $h_{\mathrm{Ek}} \approx 26\,\mathrm{m}$, not far from the WIND plume depth (Fig. 7). This constraint on the plume depth is mainly due to enhanced vertical mixing in the surface layer caused by the important horizontal velocity shear in the Ekman layer (Lentz 2004). This leads to a more homogeneous and shallow mixed layer than in the REF simulation.

The southward coastal current does not develop at all. This is brought to the fore in simulations of Chao (1988b) where the wind inhibits the development of the downstream coastal current that opposes the coastal northward geostrophic jet developed in response to the pressure gradient induced by the offshore Ekman drift. This is a plausible explanation for the weakness or absence of the southward coastal current (Fig. 1), even if seasonality is not explored in our study and is marked in this current extension (D13).

Although plume stratification changes between WIND and TOPO experiments, surface velocity fields are not much different in terms of direction (Fig. 9) in a strip containing most of the low-salinity waters (between 5° and 1°S). Indeed, even if the winds increase the velocity in this band by nearly 60%, the mean current direction is deflected northward by only 13°. As such, we conclude on a reinforcement of the naturally buoyancy-driven circulation by the annually averaged winds.

An important seasonality of the plume axis and extent has been highlighted in remote sensing data (Hopkins et al. 2013) and is reproduced in simulations of D13, shown on their seasonally averaged salinity maps. This may be associated with the complex regional current variability in the plume vicinity (Stramma and Schott 1999; Lumpkin and Garzoli 2005) mainly presented through the South Equatorial Current, the Angola Current, and the Benguela Coastal Current. This issue is beyond the scope of our study, as we aim to simplify the framework to explore mechanisms.

6. Discussion and concluding remarks

The impact of the Congo River on the salinity field in the Gulf of Guinea has been described from observational datasets (Eisma et al. 1978; Signorini et al. 1999). Mechanisms that govern the low-salinity water transport were recently studied by D13, who concluded on a high impact of environmental factors such as the wind, the geomorphology of the coast, and the bottom topography on the plume dynamics. However, the buoyancy-driven dynamics of near-equatorial plumes at long time scales had never been explored for huge rates of flow.

In this article, we have situated the Congo River in a theoretical framework examining what kind of dynamics and plume morphology we could expect from the river parameters. We have confirmed that near-equatorial plumes are more likely to be surface trapped than midlatitude plumes (Yankovsky and Chapman 1997) and that the amount of freshwater would be mostly contained in the offshore bulge rather than in the narrow coastal current, in coherence with observations. The nonlinear outflow at long time scale is expected to shed eddies whose size and shedding period are almost determined by the river parameters (Nof et al. 2002b).

Our idealized numerical experiments agree with the theory regarding the near-field plume morphology. They reveal an unusual behavior of the plume at a long time scale that had not been explored before, that is, the shedding of eddies due to β. These eddies strongly interact with each other leading to the extent of a low-salinity tongue far offshore of the river mouth. We

believe that this is a characteristic feature of low-latitude outflow and is seemingly not observed in the midlatitude as the shedding period is longer and the drifting speed of eventually formed eddies is lower (Fig. 3).

The joint effect of β (Nof et al. 2002b) and topography (Matano and Palma 2010) deflects the plume equatorward, roughly reproducing the observed (SMOS and GlobColour) tongue of low-salinity water during its most important extent. This extent can only be reproduced by taking into account the β effect and could not have been observed with the *f*-plane assumption of most of the idealized simulations carried out before [even with the low Kelvin number near-equatorial experiments of Garvine (1999)]. The mechanisms governing this extent are twofold, developed through β pulling of nonlinear structures (Nof and Pichevin 2001) and excitation of waves that propagate on the plume stratification (Nash and Moum 2005). This gives a new physical explanation of the equatorward extent of the Congo River plume that could be relevant to other near-equatorial rivers.

The impact of the wind is qualitatively comparable in our idealized simulations and in realistic simulations of D13 as the Ekman northwestward drift strengthens the buoyancy-driven circulation. The upwelling favorable winds act by impeding the southward development of the coastal current by setting a geostrophic current settled in the Ekman-induced low SSH at the coast. We have not evaluated the role of the ambient circulation on the plume or the seasonality of the winds, which can only be tested in realistic simulations to be compared with observations (D13). Because of the large scale of the plume and the complex circulation in the region (Stramma and Schott 1999), the basin-scale circulation is likely to influence the far field as commonly suggested. These issues could be explored in future high-resolution regional experiments to assess the mechanisms that drive the plume seasonality. For instance, Chang and Oey (2010) found a decrease in the eddy shedding of the Loop Current due to the winds.

In conclusion, we argue that the β-induced self-advection of the plume is one of the mechanisms that could explain, in part, the nonintuitive development of the low-salinity Congo plume in the Gulf of Guinea. Our idealized model experiments complement the more realistic ones of D13 and provide a new theoretical explanation for the behavior observed in their complex simulations.

Acknowledgments. SMOS data were provided by the Laboratory of Spatial Oceanography, and simulations were performed at the computing center CAPARMOR (IFREMER). This work was supported by IFREMER, Actimar, Total, and Mercator Ocean. A.-M. Treguier is supported by CNRS. X. Couvelard is supported by ANR Project COMODO (ANR-11-MONU-005). We appreciated discussion with Bernard Bourles (IRD) that helped linking theory with the reality of the Congo River and suggestions from Guillaume Roullet (UBO) about the wavelike dynamics. We thank two reviewers for insightful remarks and especially the first reviewer who pointed out the relevance of the Nof and Pichevin theory to the Congo plume.

REFERENCES

Boutin, J., N. Martin, X. Yin, J. Font, N. Reul, and P. Spurgeon, 2012: First assessment of SMOS data over open ocean: Part II—Sea surface salinity. *IEEE Trans. Geosci. Remote Sens.,* **50,** 1662–1675.

Carton, X., 2001: Hydrodynamical modeling of oceanic vortices. *Surv. Geophys.,* **22,** 179–263.

Chang, Y.-L., and L.-Y. Oey, 2010: Why can wind delay the shedding of loop current eddies? *J. Phys. Oceanogr.,* **40,** 2481–2495.

Chao, S., 1988a: River-forced estuarine plumes. *J. Phys. Oceanogr.,* **18,** 72–88.

——, 1988b: Wind-driven motion of estuarine plumes. *J. Phys. Oceanogr.,* **18,** 1144–1166.

——, and W. Boicourt, 1986: Onset of estuarine plumes. *J. Phys. Oceanogr.,* **16,** 2137–2149.

Chapman, D. C., and S. J. Lentz, 1994: Trapping of a coastal density front by the bottom boundary layer. *J. Phys. Oceanogr.,* **24,** 1464–1479.

Coynel, A., P. Seyler, H. Etcheber, M. Meybeck, and D. Orange, 2005: Spatial and seasonal dynamics of total suspended sediment and organic carbon species in the Congo River. *Global Biogeochem. Cycles,* **19,** GB4019, doi:10.1029/2004GB002335.

Dai, A., and K. Trenberth, 2002: Estimates of freshwater discharge from continents: Latitudinal and seasonal variations. *J. Hydrometeor.,* **3,** 660–687.

Denamiel, C., W. Budgell, and R. Toumi, 2013: The Congo River plume: Impact of the forcing on the far-field and near-field dynamics. *J. Geophys. Res. Oceans,* **118,** 964–989, doi:10.1002/jgrc.20062.

Eisma, D., and A. Van Bennekom, 1978: The Zaire River and estuary and the Zaire outflow in the Atlantic Ocean. *Neth. J. Sea Res.,* **12,** 255–272.

Fong, D., and W. Geyer, 2001: Response of a river plume during an upwelling favorable wind event. *J. Geophys. Res.,* **106** (C1), 1067–1084.

——, and ——, 2002: The alongshore transport of freshwater in a surface-trapped river plume. *J. Phys. Oceanogr.,* **32,** 957–972.

Garvine, R., 1974: Dynamics of small-scale oceanic fronts. *J. Phys. Oceanogr.,* **4,** 557–569.

——, 1999: Penetration of buoyant coastal discharge onto the continental shelf: A numerical model experiment. *J. Phys. Oceanogr.,* **29,** 1892–1909.

Haidvogel, D. B., and A. Beckmann, 1999: *Numerical Ocean Circulation Modeling.* Series on Environmental Science and Management, Vol. 344, Imperial College Press London, 300 pp.

Hopkins, J., M. Lucas, C. Dufau, M. Sutton, J. Stum, O. Lauret, and C. Channelliere, 2013: Detection and variability of the Congo River plume from satellite derived sea surface temperature,

salinity, ocean colour and sea level. *Remote Sens. Environ.,* **139,** 365–385.

Jourdin, F., J. Froidefond, S. Loyer, C. Lefèvre, Y. Mayoyas, C. Vrignaud, and N. Kolodziejczyk, 2006: Measuring upper ocean turbidity off Congo and Gabon coasts. *Proc. CMM'06 Caractérisation du Milieu Marin,* Brest, France, SHOM.

Kao, T., C. Park, and H. Pao, 1977: Buoyant surface discharge and small-scale oceanic fronts: A numerical study. *J. Geophys. Res.,* **82** (12), 1747–1752.

——, ——, and ——, 1978: Inflows, density currents, and fronts. *Phys. Fluids,* **21,** 1912–1922.

Kourafalou, V., L. Oey, J. Wang, and T. Lee, 1996: The fate of river discharge on the continental shelf: 1. Modeling the river plume and the inner shelf coastal current. *J. Geophys. Res.,* **101** (C2), 3415–3434.

Large, W. G., J. C. McWilliams, and S. C. Doney, 1994: Oceanic vertical mixing: A review and a model with a nonlocal boundary layer parameterization. *Rev. Geophys.,* **32,** 363–403.

Lentz, S., 2004: The response of buoyant coastal plumes to upwelling-favorable winds. *J. Phys. Oceanogr.,* **34,** 2458–2469.

Levitus, S., 1982: Climatological atlas of the world ocean. NOAA/ERL GFDL Professional Paper 13, 173 pp.

Lumpkin, R., and S. L. Garzoli, 2005: Near-surface circulation in the tropical Atlantic Ocean. *Deep-Sea Res.,* **52,** 495–518.

Marchesiello, P., L. Debreu, and X. Couvelard, 2009: Spurious diapycnal mixing in terrain-following coordinate models: The problem and a solution. *Ocean Modell.,* **26,** 156–169.

Maritorena, S., O. d'Andon, A. Mangin, and D. Siegel, 2010: Merged satellite ocean color data products using a bio-optical model: Characteristics, benefits and issues. *Remote Sens. Environ.,* **114,** 1791–1804.

Matano, R. P., and E. D. Palma, 2010: The upstream spreading of bottom-trapped plumes. *J. Phys. Oceanogr.,* **40,** 1631–1650.

Materia, S., S. Gualdi, A. Navarra, and L. Terray, 2012: The effect of Congo River freshwater discharge on eastern equatorial Atlantic climate variability. *Climate Dyn.,* **39,** 2109–2125.

Morrow, R., F. Birol, D. Griffin, and J. Sudre, 2004: Divergent pathways of cyclonic and anti-cyclonic ocean eddies. *Geophys. Res. Lett.,* **31,** L24311, doi:10.1029/2004GL020974.

Nash, J. D., and J. N. Moum, 2005: River plumes as a source of large-amplitude internal waves in the coastal ocean. *Nature,* **437,** 400–403.

Nof, D., 1981: On the β-induced movement of isolated baroclinic eddies. *J. Phys. Oceanogr.,* **11,** 1662–1672.

——, 2005: The momentum imbalance paradox revisited. *J. Phys. Oceanogr.,* **35,** 1928–1939.

——, and T. Pichevin, 2001: The ballooning of outflows. *J. Phys. Oceanogr.,* **31,** 3045–3058.

——, N. Paldor, and S. V. Gorder, 2002a: The Reddy maker. *Deep-Sea Res.,* **49,** 1531–1549.

——, T. Pichevin, and J. Sprintall, 2002b: ''Teddies'' and the origin of the Leeuwin Current. *J. Phys. Oceanogr.,* **32,** 2571–2588.

Penven, P., V. Echevin, J. Pasapera, F. Colas, and J. Tam, 2005: Average circulation, seasonal cycle, and mesoscale dynamics of the Peru Current system: A modeling approach. *J. Geophys. Res.,* **110,** C10021, doi:10.1029/2005JC002945.

Pichevin, T., and D. Nof, 1997: The momentum imbalance paradox. *Tellus,* **49A,** 298–319.

Risien, C., and D. Chelton, 2008: A global climatology of surface wind and wind stress fields from eight years of QuikSCAT scatterometer data. *J. Phys. Oceanogr.,* **38,** 2379–2413.

Salisbury, J., D. Vandemark, J. Campbell, C. Hunt, D. Wisser, N. Reul, and B. Chapron, 2011: Spatial and temporal coherence between Amazon River discharge, salinity, and light absorption by colored organic carbon in western tropical Atlantic surface waters. *J. Geophys. Res.,* **116,** C00H02, doi:10.1029/2011JC006989.

Schiller, R., and V. Kourafalou, 2010: Modeling river plume dynamics with the hybrid coordinate ocean model. *Ocean Modell.,* **33,** 101–117.

Schlünz, B., and R. Schneider, 2000: Transport of terrestrial organic carbon to the oceans by rivers: Re-estimating flux- and burial rates. *Int. J. Earth Sci.,* **88,** 599–606.

Shchepetkin, A. F., and J. C. McWilliams, 2005: The regional oceanic modeling system (ROMS): A split-explicit, free-surface, topography-following-coordinate oceanic model. *Ocean Modell.,* **9,** 347–404.

Signorini, S. R., R. Murtugudde, C. McClain, J. Christian, J. Picaut, and A. Busalacchi, 1999: Biological and physical signatures in the tropical and subtropical Atlantic. *J. Geophys. Res.,* **104** (C8), 18 367–18 382.

Smith, W., and D. Sandwell, 1997: Global sea floor topography from satellite altimetry and ship depth soundings. *Science,* **277,** 1956–1962.

Stramma, L., and F. Schott, 1999: The mean flow field of the tropical Atlantic Ocean. *Deep-Sea Res.,* **46,** 279–303.

Sutherland, D., and C. Cenedese, 2009: Laboratory experiment on the interaction of a buoyant coastal current with a canyon: Application to the East Greenland Current. *J. Phys. Oceanogr.,* **39,** 1258–1271.

Sutyrin, G. G., and G. R. Flierl, 1994: Intense vortex motion on the beta plane: Development of the beta gyres. *J. Atmos. Sci.,* **51,** 773–790.

Theiss, J., 2004: Equatorward energy cascade, critical latitude, and the predominance of cyclonic vortices in geostrophic turbulence. *J. Phys. Oceanogr.,* **34,** 1663–1678.

Vangriesheim, A., C. Pierre, A. Aminot, N. Metzl, F. Baurand, and J. Caprais, 2009: The influence of Congo River discharges in the surface and deep layers of the Gulf of Guinea. *Deep-Sea Res.,* **56,** 2183–2196.

Verstraete, J., 1992: The seasonal upwellings in the Gulf of Guinea. *Prog. Oceanogr.,* **29,** 1–60.

Yankovsky, A., and D. Chapman, 1997: A simple theory for the fate of buoyant coastal discharges. *J. Phys. Oceanogr.,* **27,** 1386–1401.

Bibliography

Anderson, D. L., Bryan, K., Gill, A., and Pacanowski, R. (1979). The transient response of the North Atlantic: Some model studies. *J. Geophys. Res.*, 84(C8):4795–4815.

Anderson, D. L. and Gill, A. (1975). Spin-up of a stratified ocean, with applications to upwelling. *Deep Sea Res.*, 22(9):583–596.

Antonov, J., Seidov, D., Boyer, T., Locarnini, R., Mishonov, A., Garcia, H., Baranova, O., Zweng, M., and Johnson, D. (2010). World Ocean Atlas 2009, vol. 2, Salinity. *NOAA Atlas NESDIS*, 69.

Arakawa, A. and Lamb, V. R. (1977). Computational design of the basic dynamical processes of the UCLA general circulation model. *Methods in Computational Physics*, 17:173–265.

Azevedo, J. L. L. d., Nof, D., and Mata, M. M. (2012). Eddy train encounters with a continental boundary: a South Atlantic case study. *J. Phys. Oceanogr.*, 42(9):1548–1565.

Bakun, A. and Nelson, C. S. (1991). The seasonal cycle of wind-stress curl in subtropical eastern boundary current regions. *J. Phys. Oceanogr.*, 21(12):1815–1834.

Banse, K. (1987). Seasonality of phytoplankton chlorophyll in the central and northern Arabian Sea. *Deep Sea Res.*, 34(5):713–723.

Banse, K. (1997). Irregular flow of Persian (Arabian) Gulf water to the Arabian Sea. *J. Mar. Res.*, 55(6):1049–1067.

Baringer, M. O. and Price, J. F. (1997). Mixing and spreading of the Mediterranean outflow. *J. Phys. Oceanogr.*, 27(8):1654–1677.

Bauer, S., Hitchcock, G. L., and Olson, D. B. (1991). Influence of monsoonally-forced Ekman dynamics upon surface layer depth and plankton biomass distribution in the Arabian Sea. *Deep Sea Res.*, 38(5):531–553.

Beal, L. and Donohue, K. (2013). The Great Whirl: Observations of its seasonal development and interannual variability. *J. Geophys. Res.*, 118(1):1–13.

Beal, L., Ffield, A., and Gordon, A. (2000). Spreading of Red Sea overflow waters. *J. Geophys. Res.*, 105:8549–8564.

Beal, L., Hormann, V., Lumpkin, R., and Foltz, G. (2013). The response of the surface circulation of the Arabian Sea to monsoonal forcing. *J. Phys. Oceanogr.*, 43(9):2008–2022.

Beal, L. M. (2009). A time series of Agulhas Undercurrent transport. *J. Phys. Oceanogr.*, 39(10):2436–2450.

Beal, L. M. and Bryden, H. L. (1997). Observations of an Agulhas undercurrent. *Deep Sea Res.*, 44(9):1715–1724.

Becker, J., Sandwell, D., Smith, W., Braud, J., Binder, B., Depner, J., Fabre, D., Factor, J., Ingalls, S., Kim, S., et al. (2009). Global bathymetry and elevation data at 30 arc seconds resolution: SRTM30_PLUS. *Marine Geodesy*, 32(4):355–371.

Beckmann, A. and Haidvogel, D. B. (1993). Numerical simulation of flow around a tall isolated seamount. Part I: Problem formulation and model accuracy. *J. Phys. Oceanogr.*, 23(8):1736–1753.

Berger, H., Treguier, A. M., Perenne, N., and Talandier, C. (2014). Dynamical contribution to sea surface salinity variations in the eastern Gulf of Guinea based on numerical modelling. *Climate Dyn.*, 43(11):3105–3122.

Böhm, E., Morrison, J., Manghnani, V., Kim, H., and Flagg, C. (1999). The Ras al Hadd Jet: remotely sensed and acoustic Doppler current profiler observations in 1994–1995. *Deep Sea Res.*, 46(8):1531–1549.

Bower, A. S., Armi, L., and Ambar, I. (1997). Lagrangian observations of meddy formation during a mediterranean undercurrent seeding experiment. *J. Phys. Oceanogr.*, 27(12):2545–2575.

Bower, A. S., Fratantoni, D. M., Johns, W. E., and Peters, H. (2002). Gulf of Aden eddies and their impact on Red Sea Water. *Geophys. Res. Lett.*, 29(21):21–1.

Bower, A. S. and Furey, H. H. (2012). Mesoscale eddies in the Gulf of Aden and their impact on the spreading of Red Sea Outflow Water. *Prog. Oceanogr.*, 96(1):14–39.

Bower, A. S., Hunt, H. D., and Price, J. F. (2000). Character and dynamics of the Red Sea and Persian Gulf outflows. *J. Geophys. Res.*, 105(C3):6387–6414.

Bower, A. S., Johns, W. E., Fratantoni, D. M., and Peters, H. (2005). Equilibration and circulation of Red Sea Outflow Water in the western Gulf of Aden. *J. Phys. Oceanogr.*, 35(11).

Brandt, P., Stramma, L., Schott, F., Fischer, J., Dengler, M., and Quadfasel, D. (2002). Annual Rossby waves in the Arabian Sea from TOPEX/POSEIDON altimeter and in situ data. *Deep Sea Res.*, 49(7):1197–1210.

Brewer, P. G. and Dyrssen, D. (1985). Chemical oceanography of the Persian Gulf. *Prog. Oceanogr.*, 14:41–55.

Bruce, J. (1983). The wind field in the western Indian Ocean and the related ocean circulation. *Mon. Wea. Rev.*, 111(7):1442–1452.

Capet, X., Colas, F., McWilliams, J., Penven, P., and Marchesiello, P. (2008a). Eddies in eastern boundary subtropical upwelling systems. *Ocean Modeling in an Eddying Regime*, pages 131–147.

Capet, X., McWilliams, J., Molemaker, M., and Shchepetkin, A. (2008b). Mesoscale to submesoscale transition in the California Current System. part i: Flow structure, eddy flux, and observational tests. *J. Phys. Oceanogr.*, 38(1):29–43.

Carton, X., L'Hegaret, P., and Baraille, R. (2012). Mesoscale variability of water masses in the Arabian Sea as revealed by ARGO floats. *Ocean Sci.*, 8:227–248.

Chelton, D., DeSzoeke, R., Schlax, M., El Naggar, K., and Siwertz, N. (1998). Geographical variability of the first baroclinic Rossby radius of deformation. *J. Phys. Oceanogr.*, 28(3):433–460.

Chelton, D., Schlax, M., Freilich, M., and Milliff, R. (2004). Satellite measurements reveal persistent small-scale features in ocean winds. *Science*, 303(5660):978–983.

Chelton, D. B. and Schlax, M. G. (1996). Global observations of oceanic rossby waves. *Science*, 272(5259):234–238.

Chelton, D. B., Schlax, M. G., and Samelson, R. M. (2011). Global observations of nonlinear mesoscale eddies. *Prog. Oceanogr.*, 91(2):167–216.

Chelton, D. B., Schlax, M. G., Samelson, R. M., and de Szoeke, R. A. (2007). Global observations of large oceanic eddies. *Geophys. Res. Lett.*, 34(15).

Cherubin, L., Carton, X., Paillet, J., Morel, Y., and Serpette, A. (2000). Instability of the Mediterranean Water undercurrents southwest of Portugal: effects of baroclinicity and of topography. *Oceanologica Acta*, 23(5):551–573.

Cipollini, P., Cromwell, D., Challenor, P. G., Raffaglio, S., et al. (2001). Rossby waves detected in global ocean colour data. *Geophys. Res. Lett*, 28(2):323–326.

Clarke, A. J. and Shi, C. (1991). Critical frequencies at ocean boundaries. *J. Geophys. Res.*, 96(C6):10731–10738.

Colas, F., Capet, X., McWilliams, J. C., and Li, Z. (2013). Mesoscale eddy buoyancy flux and eddy-induced circulation in Eastern Boundary Currents. *J. Phys. Oceanogr.*, 43(6):1073–1095.

Colas, F., McWilliams, J. C., Capet, X., and Kurian, J. (2012). Heat balance and eddies in the Peru-Chile current system. *Climate Dyn.*, 39(1-2):509–529.

Colbo, K. and Weller, R. (2007). The variability and heat budget of the upper ocean under the Chile-Peru stratus. *J. Mar. Res.*, 65(5):607–637.

Couvelard, X., Marchesiello, P., Gourdeau, L., and Lefèvre, J. (2008). Barotropic zonal jets induced by islands in the southwest Pacific. *J. Phys. Oceanogr.*, 38(10):2185–2204.

Da Silveira, I., Calado, L., Castro, B., Cirano, M., Lima, J., and Mascarenhas, A. d. S. (2004). On the baroclinic structure of the Brazil Current–Intermediate Western Boundary Current system at 22–23 S. *Geophys. Res. Lett.*, 31(14).

Dai, A. and Trenberth, K. (2002). Estimates of freshwater discharge from continents: Latitudinal and seasonal variations. *J. Hydrometeor.*, 3(6):660–687.

D'Asaro, E. A. (1988). Generation of submesoscale vortices: A new mechanism. *J. Geophys. Res.*, 93(C6):6685–6693.

de Boyer Montégut, C., Vialard, J., Shenoi, S. S., Shankar, D., Durand, F., Ethé, C., and Madec, G. (2007). Simulated seasonal and interannual variability of the mixed layer heat budget in the northern Indian Ocean. *J. Climate*, 20(13):3249–3268.

Debreu, L. and Blayo, E. (2008). Two-way embedding algorithms: a review. *Ocean Dynamics*, 58(5-6):415–428.

Debreu, L., Marchesiello, P., Penven, P., and Cambon, G. (2012). Two-way nesting in split-explicit ocean models: algorithms, implementation and validation. *Ocean Modell.*, 49:1–21.

Desbiolles, F., Blanke, B., Bentamy, A., and Grima, N. (2014). Origin of fine-scale wind stress curl structures in the Benguela and Canary upwelling systems. *J. Geophys. Res.*, 119(11):7931–7948.

Dong, C., McWilliams, J. C., and Shchepetkin, A. F. (2007). Island wakes in deep water. *J. Phys. Oceanogr.*, 37(4):962–981.

Ducet, N., Le Traon, P.-Y., and Reverdin, G. (2000). Global high-resolution mapping of ocean circulation from TOPEX/Poseidon and ERS-1 and-2. *J. Geophys. Res.*, 105(C8):19477–19498.

Düing, W. and Leetmaa, A. (1980). Arabian Sea cooling: A preliminary heat budget. *J. Phys. Oceanogr.*, 10(2):307–312.

Elliott, A. J. and Savidge, G. (1990). Some features of the upwelling off Oman. *J. Mar. Res.*, 48(2):319–333.

Fieux, M. and Stommel, H. (1977). Onset of the southwest monsoon over the Arabian Sea from marine reports of surface winds: structure and variability. *Mon. Wea. Rev.*, 105(2):231–236.

Findlater, J. (1969). A major low-level air current near the Indian Ocean during the northern summer. *Quart. J. Roy. Meteor. Soc.*, 95(404):362–380.

Findlay, A. G. (1876). *A directory for the navigation of the Indian Ocean: with descriptions of its coasts, islands, etc., from the Cape of Good Hope to the Strait of Sunda and Western Australia, including also the Red Sea and the Persian Gulf; the winds, monsoons, and currents, and the passages from Europe to its various ports*. RH Laurie.

Fischer, A. S., Weller, R. A., Rudnick, D. L., Eriksen, C. C., Lee, C. M., Brink, K. H., Fox, C. A., and Leben, R. R. (2002). Mesoscale eddies, coastal upwelling, and the upper-ocean heat budget in the Arabian Sea. *Deep Sea Res.*, 49(12):2231–2264.

Fischer, J., Schott, F., and Stramma, L. (1996). Currents and transports of the Great Whirl-Socotra Gyre system during the summer monsoon, August 1993. *J. Geophys. Res.*, 101(C2):3573–3587.

Flagg, C. N. and Kim, H.-S. (1998). Upper ocean currents in the northern Arabian Sea from shipboard ADCP measurements collected during the 1994–1996 us jgofs and onr programs. *Deep Sea Res.*, 45(10-11):1917–1959.

Fu, L.-L. (2004). Latitudinal and frequency characteristics of the westward propagation of large-scale oceanic variability. *J. Phys. Oceanogr*, 34(8):1907–1921.

Fu, L.-L., Christensen, E. J., Yamarone, C. A., Lefebvre, M., Menard, Y., Dorrer, M., and Escudier, P. (1994). TOPEX/POSEIDON mission overview. *J. Geophys. Res.*, 99(C12):24369–24381.

Fu, L.-L. and Qiu, B. (2002). Low-frequency variability of the North Pacific Ocean: The roles of boundary- and wind-driven baroclinic Rossby waves. *J. Geophys. Res.*, 107(C12):13–1.

Garvine, R. W. (1999). Penetration of buoyant coastal discharge onto the continental shelf: A numerical model experiment. *J. Phys. Oceanogr.*, 29(8):1892–1909.

Godfrey, J. and Golding, T. (1981). The Sverdrup relation in the Indian Ocean, and the effect of Pacific-Indian Ocean throughflow on Indian Ocean circulation and on the East Australian Current. *J. Phys. Oceanogr.*, 11(6):771–779.

Griffiths, R. (1986). Gravity currents in rotating systems. *Annu. Rev. Fluid Mech.*, 18(1):59–89.

Grimshaw, R. and Allen, J. S. (1988). Low-frequency baroclinic waves off coastal boundaries. *J. Phys. Oceanogr.*, 18(8):1124–1143.

Gula, J., Molemaker, M. J., and McWilliams, J. C. (2014). Submesoscale cold filaments in the Gulf Stream. *J. Phys. Oceanogr.*, 44(10):2617–2643.

Gula, J., Molemaker, M. J., and McWilliams, J. C. (2015a). Gulf Stream dynamics along the Southeastern US Seaboard. *J. Phys. Oceanogr.*, 45(3):690–715.

Gula, J., Molemaker, M. J., and McWilliams, J. C. (2015b). Topographic vorticity generation, submesoscale instability and vortex street formation in the Gulf Stream. *Geophys. Res. Lett.*, 42.

Haney, R. L., Hale, R. A., and Dietrich, D. E. (2001). Offshore propagation of eddy kinetic energy in the California Current. *J. Geophys. Res.*, 106(C6):11709–11717.

Hastenrath, S. and Greischar, L. (1991). The monsoonal current regimes of the tropical Indian Ocean: Observed surface flow fields and their geostrophic and wind-driven components. *J. Geophys. Res.*, 96(C7):12619–12.

Ilıcak, M., Özgökmen, T. M., and Johns, W. E. (2011). How does the Red Sea outflow water interact with Gulf of Aden Eddies? *Ocean Modell.*, 36(1):133–148.

Izumo, T., Montégut, C. B., Luo, J.-J., Behera, S. K., Masson, S., and Yamagata, T. (2008). The role of the western Arabian Sea upwelling in Indian monsoon rainfall variability. *J. Climate*, 21(21):5603–5623.

Jacobs, G., Hurlburt, H., Kindle, J., Metzger, E., Mitchell, J., Teague, W., and Wallcraft, A. (1994). Decade-scale trans-Pacific propagation and warming effects of an El Nino anomaly. *Nature*, 370:360–363.

Jensen, T. G. (1993). Equatorial variability and resonance in a wind-driven Indian Ocean model. *J. Geophys. Res.*, 98(C12):22533–22552.

Johns, W., Yao, F., Olson, D., Josey, S., Grist, J., and Smeed, D. (2003). Observations of seasonal exchange through the straits of Hormuz and the inferred heat and freshwater budgets of the Persian Gulf. *J. Geophys. Res.*, 108(C12).

Jullien, S., Menkes, C. E., Marchesiello, P., Jourdain, N. C., Lengaigne, M., Koch-Larrouy, A., Lefevre, J., Vincent, E. M., and Faure, V. (2012). Impact of tropical cyclones on the heat budget of the South Pacific Ocean. *J. Phys. Oceanogr.*, 42(11):1882–1906.

Kato, S., Loeb, N. G., Rose, F. G., Doelling, D. R., Rutan, D. A., Caldwell, T. E., Yu, L., and Weller, R. A. (2013). Surface irradiances consistent with CERES-derived top-of-atmosphere shortwave and longwave irradiances. *J. Climate*, 26(9):2719–2740.

Kelly, K. A., Beardsley, R. C., Limeburner, R., Brink, K. H., Paduan, J. D., and Chereskin, T. K. (1998). Variability of the near-surface eddy kinetic energy in the California Current based on altimetric, drifter, and moored current data. *J. Geophys. Res.*, 103(C6):13067–13083.

Kessler, W. S. (1990). Observations of long Rossby waves in the northern tropical Pacific. *J. Geophys. Res.*, 95(C4):5183–5217.

Killworth, P. D., Cipollini, P., Uz, B. M., and Blundell, J. R. (2004). Physical and biological mechanisms for planetary waves observed in satellite-derived chlorophyll. *J. Geophys. Res.*, 109(C7).

Kim, H.-S., Flagg, C. N., and Howden, S. D. (2001). Northern Arabian Sea variability from TOPEX/-POSEIDON altimetry data: an extension of the US JGOFS/ONR shipboard ADCP study. *Deep Sea Res.*, 48(6):1069–1096.

Kuzmin, D. (2010). *A guide to numerical methods for transport equations*. Dortmund University of Technology, available at http://www.mathematik.uni-dortmund.de/ kuzmin/Transport.pdf.

Large, W. and Danabasoglu, G. (2006). Attribution and impacts of upper-ocean biases in CCSM3. *J. Climate*, 19(11):2325–2346.

Large, W., McWilliams, J., and Doney, S. (1994). Oceanic vertical mixing: A review and a model with a nonlocal boundary layer parameterization. *Rev. Geophys.*, 32(4):363–403.

Large, W. and Yeager, S. (2009). The global climatology of an interannually varying air–sea flux data set. *Climate Dyn.*, 33(2-3):341–364.

Le Traon, P.-Y. and Minster, J.-F. (1993). Sea level variability and semiannual Rossby waves in the South Atlantic subtropical gyre. *J. Geophys. Res.*, 98(C7):12315–12326.

Le Traon, P.-Y. and Ogor, F. (1998). ERS-1/2 orbit improvement using TOPEX/POSEIDON: The 2cm challenge. *J. Geophys. Res.*, 103(C4):8045–8057.

LeBlond, P. H. and Mysak, L. A. (1981). *Waves in the Ocean*. Elsevier.

Lee, C., Jones, B., Brink, K., and Fischer, A. (2000). The upper-ocean response to monsoonal forcing in the Arabian Sea: seasonal and spatial variability. *Deep Sea Res.*, 47(7):1177–1226.

Legg, S., Ezer, T., Jackson, L., Briegleb, B. P., Danabasoglu, G., Large, W. G., Wu, W., Chang, Y., Ozgokmen, T. M., Peters, H., et al. (2009). Improving oceanic overflow representation in climate models: the gravity current entrainment climate process team. *Bull. Amer. Meteor. Soc.*, 90:657–670.

Lemarié, F., Kurian, J., Shchepetkin, A. F., Jeroen Molemaker, M., Colas, F., and McWilliams, J. C. (2012). Are there inescapable issues prohibiting the use of terrain-following coordinates in climate models? *Ocean Modell.*, 42:57–79.

Lévy, M., Shankar, D., André, J.-M., Shenoi, S., Durand, F., and de Boyer Montégut, C. (2007). Basin-wide seasonal evolution of the Indian Ocean's phytoplankton blooms. *J. Geophys. Res.*, 112(C12).

L'Hégaret, P. (2015). *Etude de la circulation de mésoéchelle et des sorties d'eaux du Golfe Persique dans l'Océan Indien Nord-Ouest*. PhD thesis, Université de Bretagne occidentale-Brest.

L'Hégaret, P., Duarte, R., Carton, X., Vic, C., Ciani, D., Baraille, R., and Corréard, S. (2015). Mesoscale variability in the Arabian Sea from HYCOM model results and observations: impact on the Persian Gulf Water path. *Ocean Sci.*, 11:667–693.

L'Hégaret, P., Lacour, L., Carton, X., Roullet, G., Baraille, R., and Corréard, S. (2013). A seasonal dipolar eddy near Ras Al Hamra (Sea of Oman). *Ocean Dynamics*, pages 1–27.

Lighthill, M. J. (1969). Dynamic response of the Indian Ocean to onset of the southwest monsoon. *Philos. Trans. Roy. Soc. London*, pages 45–92.

Locarnini, R., Mishonov, A., Antonov, J., Boyer, T., Garcia, H., Baranova, O., Zweng, M., and Johnson, D. (2010). World Ocean Atlas 2009, vol. 1, Temperature. *US Gov. Print. Off., Washington, DC*.

Longuet-Higgins, M. S. (1966). Planetary waves on a hemisphere bounded by meridians of longitude. *Phil. Trans. Roy. Soc. London*, 260(1111):317–350.

Luther, M. E. and O'Brien, J. J. (1985). A model of the seasonal circulation in the Arabian Sea forced by observed winds. *Prog. Oceanogr.*, 14:353–385.

Luther, M. E. and O'Brien, J. J. (1989). Modelling the variability in the Somali Current. *Mesoscale/Synoptic Coherent Structures in Geophysical Turbulence, Elsevier, Amsterdam*, pages 373–386.

Manghnani, V., Morrison, J. M., Hopkins, T. S., and Böhm, E. (1998). Advection of upwelled waters in the form of plumes off Oman during the Southwest Monsoon. *Deep Sea Res.*, 45(10):2027–2052.

Marchesiello, P., Capet, X., Menkes, C., and Kennan, S. C. (2011). Submesoscale dynamics in tropical instability waves. *Ocean Modell.*, 39(1):31–46.

Marchesiello, P., Debreu, L., and Couvelard, X. (2009). Spurious diapycnal mixing in terrain-following coordinate models: The problem and a solution. *Ocean Modell.*, 26(3):156–169.

Marchesiello, P., Gibbs, M. T., and Middleton, J. H. (2000). Simulations of coastal upwelling on the Sydney continental shelf. *Mar. Freshwater Res.*, 51(6):577–588.

Marchesiello, P., McWilliams, J., and Shchepetkin, A. (2003). Equilibrium structure and dynamics of the California Current System. *J. Phys. Oceanogr.*, 33(4):753–783.

Marchesiello, P., McWilliams, J. C., and Shchepetkin, A. (2001). Open boundary conditions for long-term integration of regional oceanic models. *Ocean Modell.*, 3(1):1–20.

Mason, E., Colas, F., Molemaker, J., Shchepetkin, A. F., Troupin, C., McWilliams, J. C., and Sangrà, P. (2011). Seasonal variability of the Canary Current: a numerical study. *J. Geophys. Res.*, 116(C6).

Mason, E., Molemaker, J., Shchepetkin, A. F., Colas, F., McWilliams, J. C., and Sangrà, P. (2010). Procedures for offline grid nesting in regional ocean models. *Ocean Modell.*, 35(1):1–15.

Mata, M. M., Tomczak, M., Wijffels, S., and Church, J. A. (2000). East Australian Current volume transports at 30 S: Estimates from the World Ocean Circulation Experiment hydrographic sections PR11/P6 and the PCM3 current meter array. *J. Geophys. Res.*, 105(C12):28509–28526.

McCreary, J. and Kundu, P. (1985). Western boundary circulation driven by an alongshore wind: With application to the Somali Current system. *J. Mar. Res.*, 43(3):493–516.

McCreary, J. and Kundu, P. (1988). A numerical investigation of the Somali Current during the Southwest Monsoon. *J. Mar. Res.*, 46(1):25–58.

McCreary, J., Kundu, P., and Molinari, R. (1993). A numerical investigation of dynamics, thermodynamics and mixed-layer processes in the Indian Ocean. *Prog. Oceanogr.*, 31(3):181–244.

McDowell, S. E. and Rossby, H. T. (1978). Mediterranean water: An intense mesoscale eddy off the Bahamas. *Science*, 202(4372):1085–1087.

McWilliams, J. C. (1985). Submesoscale, coherent vortices in the ocean. *Rev. Geophys.*, 23(2):165–182.

McWilliams, J. C. (1988). Vortex generation through balanced adjustment. *J. Phys. Oceanogr.*, 18(8):1178–1192.

Meacham, S. (1997). Double-diffusive processes. Technical report, Woods Hole Oceanog. Inst.

Molemaker, M. J., McWilliams, J. C., and Dewar, W. K. (2015). Submesoscale instability and generation of mesoscale anticyclones near a separation of the California Undercurrent. *J. Phys. Oceanogr.*, 45(3):613–629.

Morrow, R., Birol, F., Griffin, D., and Sudre, J. (2004). Divergent pathways of cyclonic and anti-cyclonic ocean eddies. *Geophys. Res. Lett.*, 31(24).

Nof, D. and Pichevin, T. (2001). The ballooning of outflows. *J. Phys. Oceanogr.*, 31(10):3045–3058.

Nof, D., Pichevin, T., and Sprintall, J. (2002). "teddies" and the origin of the leeuwin current. *J. Phys. Oceanogr.*, 32(9):2571–2588.

Olbers, D., Willebrand, J., and Eden, C. (2012). *Ocean dynamics*. Springer Science & Business Media.

Özgökmen, T. M., Johns, W. E., Peters, H., and Matt, S. (2003). Turbulent mixing in the Red Sea outflow plume from a high-resolution nonhydrostatic model. *J. Phys. Oceanogr.*, 33(8):1846–1869.

Pedlosky, J. (1987). *Geophysical fluid dynamics, 2nd edition*. Springer Science - Verlag.

Penven, P., Debreu, L., Marchesiello, P., and McWilliams, J. C. (2006). Evaluation and application of the ROMS 1-way embedding procedure to the central California upwelling system. *Ocean Modell.*, 12(1):157–187.

Penven, P., Echevin, V., Pasapera, J., Colas, F., and Tam, J. (2005). Average circulation, seasonal cycle, and mesoscale dynamics of the Peru Current System: A modeling approach. *J. Geophys. Res.*, 110(C10):C10021.

Penven, P., Marchesiello, P., Debreu, L., and Lefèvre, J. (2008). Software tools for pre-and post-processing of oceanic regional simulations. *Environmental Modelling & Software*, 23(5):660–662.

Peters, H. and Johns, W. E. (2005). Mixing and entrainment in the Red Sea outflow plume. Part II: Turbulence characteristics. *J. Phys. Oceanogr.*, 35(5):584–600.

Peters, H., Johns, W. E., Bower, A. S., and Fratantoni, D. M. (2005). Mixing and entrainment in the Red Sea outflow plume. Part I: Plume structure. *J. Phys. Oceanogr.*, 35(5):569–583.

Polito, P. S. and Cornillon, P. (1997). Long baroclinic Rossby waves detected by TOPEX/POSEIDON. *J. Geophys. Res.*, 102(C2):3215–3235.

Polito, P. S. and Sato, O. T. (2015). Do eddies ride on Rossby waves? *J. Geophys. Res.*, in press.

Pous, S., Carton, X., and Lazure, P. (2004a). Hydrology and circulation in the Strait of Hormuz and the Gulf of Oman—Results from the GOGP99 Experiment: 1. Strait of Hormuz. *J. Geophys Res.*, 109(C12):C12037.

Pous, S., Carton, X., and Lazure, P. (2004b). Hydrology and circulation in the Strait of Hormuz and the Gulf of Oman—Results from the GOGP99 Experiment: 2. Gulf of Oman. *J. Geophys. Res.*, 109(C12).

Price, J. F. and O'Neil Baringer, M. (1994). Outflows and deep water production by marginal seas. *Prog. Oceanogr.*, 33(3):161–200.

Privett, D. (1959). Monthly charts of evaporation from the N. Indian Ocean (including the Red Sea and the Persian Gulf). *Q. J. R. Meteorol. Soc.*, 85(366):424–428.

Qiu, B. (2002). Large-scale variability in the midlatitude subtropical and subpolar North Pacific Ocean: Observations and causes. *J. Phys. Oceanogr.*, 32(1):353–375.

Qiu, B., Miao, W., and Müller, P. (1997). Propagation and decay of forced and free baroclinic Rossby waves in off-equatorial oceans. *J. Phys. Oceanogr.*, 27(11):2405–2417.

Rayleigh, L. (1880). On the stability, or instability, of certain fluid motions. *Proc. London Math. Soc.*, 11:57–70.

Renault, L., Dewitte, B., Marchesiello, P., Illig, S., Echevin, V., Cambon, G., Ramos, M., Astudillo, O., Minnis, P., and Ayers, J. K. (2012). Upwelling response to atmospheric coastal jets off central Chile: A modeling study of the October 2000 event. *J. Geophys. Res.*, 117(C2).

Renault, L., Hall, A., and McWilliams, J. C. (2015). Orographic shaping of US West Coast wind profiles during the upwelling season. *Climate Dyn.*, in press.

Resplandy, L., Lévy, M., Madec, G., Pous, S., Aumont, O., and Kumar, D. (2011). Contribution of mesoscale processes to nutrient budgets in the Arabian Sea. *J. Geophys. Res.*, 116(C11):C11007.

Reynolds, R. M. (1993). Physical oceanography of the Gulf, Strait of Hormuz, and the Gulf of Oman—Results from the Mt Mitchell expedition. *Mar. Pollut. Bull.*, 27:35–59.

Rio, M., Guinehut, S., and Larnicol, G. (2011). New CNES-CLS09 global mean dynamic topography computed from the combination of GRACE data, altimetry, and in situ measurements. *J. Geophys. Res.*, 116(C7).

Risien, C. and Chelton, D. (2008). A global climatology of surface wind and wind stress fields from eight years of QuikSCAT scatterometer data. *J. Phys. Oceanogr.*, 38(11):2379–2413.

Rossby, C. (1940). Planetary flow patterns in the atmosphere. *Quart. J. Roy. Meteor. Soc.*, 66:68–97.

Saji, N., Goswami, B. N., Vinayachandran, P., and Yamagata, T. (1999). A dipole mode in the tropical Indian Ocean. *Nature*, 401(6751):360–363.

Sandwell, D. T. and Smith, W. H. (2009). Global marine gravity from retracked Geosat and ERS-1 altimetry: Ridge segmentation versus spreading rate. *J. Geophys. Res.*, 114(B1).

Savidge, G., Lennon, J., and Matthews, A. J. (1990). A shore-based survey of upwelling along the coast of Dhofar region, southern Oman. *Cont. Shelf Res.*, 10(3):259–275.

Schott, F. (1983). Monsoon response of the Somali Current and associated upwelling. *Prog. Oceanogr.*, 12(3):357–381.

Schott, F. and McCreary, J. (2001). The monsoon circulation of the Indian Ocean. *Prog. Oceanogr.*, 51(1):1–123.

Schott, F. and Quadfasel, D. R. (1982). Variability of the Somali Current system during the onset of the southwest monsoon, 1979. *J. Phys. Oceanogr.*, 12(12).

Schott, F., Swallow, J. C., and Fieux, M. (1990). The Somali Current at the equator: annual cycle of currents and transports in the upper 1000 m and connection to neighbouring latitudes. *Deep Sea Res.*, 37(12):1825–1848.

Senjyu, T., Ishimaru, T., Matsuyama, M., and Koike, Y. (1998). High salinity lens from the strait of hormuz. *Offshore Environment of the ROPME Sea Area after the War-Related Oil Spill*, pages 35–48.

Shchepetkin, A. and McWilliams, J. (1998). Quasi-monotone advection schemes based on explicit locally adaptive dissipation. *Mon. Wea. Rev.*, 126(6):1541–1580.

Shchepetkin, A. and McWilliams, J. (2005). The regional oceanic modeling system (ROMS): a split-explicit, free-surface, topography-following-coordinate oceanic model. *Ocean Modell.*, 9(4):347–404.

Shenoi, S., Shankar, D., and Shetye, S. (2002). Differences in heat budgets of the near-surface Arabian Sea and Bay of Bengal: Implications for the summer monsoon. *J. Geophys. Res.*, 107(C6):1–14.

Shetye, S., Gouveia, A., and Shenoi, S. (1994). Circulation and water masses of the Arabian Sea. *Journal of Earth System Science*, 103(2):107–123.

Shetye, S., Gouveia, A., Shenoi, S., Michael, G., Sundar, D., Almeida, A., and Santanam, K. (1991). The coastal current off western India during the northeast monsoon. *Deep Sea Res.*, 38(12):1517–1529.

Shetye, S., Gouveia, A., Shenoi, S., Sundar, D., Michael, G., Almeida, A., and Santanam, K. (1990). Hydrography and circulation off the west coast of India during the southwest monsoon 1987. *J. Mar. Res.*, 48(2):359–378.

Shi, W., Morrison, J. M., Böhm, E., and Manghnani, V. (2000). The Oman upwelling zone during 1993, 1994 and 1995. *Deep Sea Res.*, 47(7):1227–1247.

Smith, K. S. (2007). The geography of linear baroclinic instability in Earth's oceans. *J. Mar. Res.*, 65(5):655–683.

Smith, W. and Sandwell, D. (1997). Global sea floor topography from satellite altimetry and ship depth soundings. *Science*, 277(5334):1956–1962.

Spall, M. A. (2000). Generation of strong mesoscale eddies by weak ocean gyres. *J. Mar. Res.*, 58(1):97–116.

Spall, M. A., Weller, R. A., and Furey, P. W. (2000). Modeling the three-dimensional upper ocean heat budget and subduction rate during the Subduction Experiment. *J. Geophys. Res.*, 105(26,151).

Subrahmanyam, S. (1998). *The career and legend of Vasco da Gama.* Cambridge University Press.

Takahashi, K. (2005). The annual cycle of heat content in the Peru Current Region. *J. Climate*, 18(23):4937–4954.

Teague, W. J., Carron, M. J., and Hogan, P. J. (1990). A comparison between the Generalized Digital Environmental Model and Levitus climatologies. *J. Geophys. Res.*, 95(C5):7167–7183.

Tulloch, R., Marshall, J., Hill, C., and Smith, K. S. (2011). Scales, growth rates, and spectral fluxes of baroclinic instability in the ocean. *J. Phys. Oceanogr.*, 41(6):1057–1076.

Vallis, G. K. (2006). *Atmospheric and oceanic fluid dynamics: fundamentals and large-scale circulation.* Cambridge University Press.

Vecchi, G., Xie, S., and Fischer, A. (2004). Ocean-atmosphere covariability in the western Arabian Sea. *J. Climate*, 17(6):1213–1224.

Vialard, J. and Delecluse, P. (1998). An OGCM study for the TOGA decade. Part I: Role of salinity in the physics of the western Pacific fresh pool. *J. Phys. Oceanogr.*, 28(6):1071–1088.

Vialard, J., Jayakumar, A., Gnanaseelan, C., Lengaigne, M., Sengupta, D., and Goswami, B. (2012). Processes of 30–90 days sea surface temperature variability in the northern Indian Ocean during boreal summer. *Climate Dyn.*, 38(9-10):1901–1916.

Vialard, J., Menkes, C., Boulanger, J.-P., Delecluse, P., Guilyardi, E., McPhaden, M. J., and Madec, G. (2001). A model study of oceanic mechanisms affecting equatorial Pacific sea surface temperature during the 1997-98 El Niño. *J. Phys. Oceanogr.*, 31(7):1649–1675.

Vic, C., Berger, H., Tréguier, A.-M., and Couvelard, X. (2014a). Dynamics of an equatorial river plume: theory and numerical experiments applied to the Congo plume case. *J. Phys. Oceanogr.*, 44(3):980–994.

Vic, C., Roullet, G., Capet, X., Carton, X., Molemaker, M. J., and Gula, J. (2015). Eddy-topography interactions and the fate of the Persian Gulf Outflow. *J. Geophys. Res.*, 120(10):6700–6717.

Vic, C., Roullet, G., Carton, X., and Capet, X. (2014b). Mesoscale dynamics in the Arabian Sea and a focus on the Great Whirl life cycle : a numerical investigation using ROMS. *J. Geophys. Res.*, 119(9):6422–6443.

Vignudelli, S., Cipollini, P., Roblou, L., Lyard, F., Gasparini, G., Manzella, G., and Astraldi, M. (2005). Improved satellite altimetry in coastal systems: Case study of the Corsica Channel (Mediterranean Sea). *Geophys. Res. Lett.*, 32(7).

Villas Bôas, A., Sato, O., Chaigneau, A., and Castelão, G. (2015). The signature of mesoscale eddies on the air-sea turbulent heat fluxes in the South Atlantic Ocean. *Geophys. Res. Lett.*, 42(6):1856–1862.

Wang, D.-P. (1997). Effects of small-scale wind on coastal upwelling with application to Point Conception. *J. Geophys. Res.*, 102(C7):15555–15566.

Weller, R., Fischer, A., Rudnick, D., Eriksen, C., Dickey, T., Marra, J., Fox, C., and Leben, R. (2002). Moored observations of upper-ocean response to the monsoons in the Arabian Sea during 1994–1995. *Deep Sea Res.*, 49(12):2195–2230.

White, W. B. (1977). Annual forcing of baroclinic long waves in the tropical North Pacific Ocean. *J. Phys. Oceanogr.*, 7(1):50–61.

Wirth, A., Willebrand, J., and Schott, F. (2002). Variability of the Great Whirl from observations and models. *Deep Sea Res.*, 49(7):1279–1295.

Worley, S., Woodruff, S., Reynolds, R., Lubker, S., and Lott, N. (2005). ICOADS release 2.1 data and products. *Int. J. Climatol.*, 25(7):823–842.

Wunsch, C. (1997). The vertical partition of oceanic horizontal kinetic energy. *J. Phys. Oceanogr.*, 27(8):1770–1794.

Wunsch, C. (2011). The decadal mean ocean circulation and Sverdrup balance. *J. Mar. Res.*, 69(2-3):2–3.

Wyrtki, K. (1973). An equatorial jet in the Indian Ocean. *Science*, 181(4096):262.

Xie, S.-P., Hu, K., Hafner, J., Tokinaga, H., Du, Y., Huang, G., and Sampe, T. (2009). Indian Ocean capacitor effect on Indo-western Pacific climate during the summer following El Niño. *J. Climate*, 22(3):730–747.

Yankovsky, A. E. and Chapman, D. C. (1997). A simple theory for the fate of buoyant coastal discharges. *J. Phys. Oceanogr.*, 27(7):1386–1401.

Dynamique de bord ouest en Mer d'Arabie

Le but de cette thèse est d'analyser plusieurs phénomènes de bord ouest de la Mer d'Arabie : (i) le cycle de vie d'un tourbillon de mésoéchelle persistant, le Great Whirl; (ii) la dynamique d'un écoulement d'eau dense (*outflow*) formée dans une mer adjacente, l'outflow du Golfe Persique; et (iii) une remontée d'eau profonde (*upwelling*) saisonnière dans la zone côtière d'Oman. Le point commun entre ces phénomènes est leur localisation sur un bord ouest océanique. Ils sont donc influencés par des forçages locaux (notamment les vents de mousson) et des forçages à distance (ondes de Rossby et tourbillons dérivant vers l'ouest). En particulier, ces derniers vont jouer un rôle particulier car la Mer d'Arabie est située à basses latitudes, ce qui implique une propagation rapide des ondes longues et tourbillons. De plus, des ondes sont continuellement excitées par le régime saisonnier des moussons. Nous avons mis au point des expériences numériques de différentes complexités en utilisant un modèle aux équations primitives. Ces expériences permettent soit de simuler de manière réaliste la dynamique complexe de la Mer d'Arabie, soit d'isoler un processus en particulier.

Les résultats principaux peuvent se résumer comme suit : (i) le cycle de vie du Great Whirl est significativement impacté par les ondes de Rossby annuelles. Le rotationnel de la tension de vent joue un role important dans le maintien, le renforcement et la barotropisation du tourbillon. (ii) La dispersion de l'Eau du Golfe Persique (*Persian Gulf Water*, PGW) est determinée par le mélange induit par les tourbillons de mésoéchelle. Précisément, ces tourbillons entrent dans le Golfe d'Oman (où se deverse la PGW), et interagissent avec la topographie. Ces interactions frictionnelles produisent des bandes de vorticité très intenses dans la couche limite du fond. Celles-ci sont arrachées et forment des tourbillons de sous-mésoéchelle. Ces tourbillons capturent de la PGW initialement située sur la pente continentale et la redistribuent dans le Golfe d'Oman. Ce mécanisme donne finalement lieu à du mélange, permettant d'expliquer le gradient de salinité climatologique observé en profondeur. (iii) La dynamique de l'upwelling saisonnier au large d'Oman contraste fortement avec la dynamique des upwellings de bord est (*Eastern Boundary Upwelling Systems*, EBUS). En effet, les ondes de Rossby se propagent vers le large dans les EBUS et vers la côte dans l'upwelling de bord ouest d'Oman. Ces ondes modulent la réponse en température de l'upwelling forcé par le vent.

Dans l'ensemble, ces résultats sont relativement spécifiques à la Mer d'Arabie. La faible extension zonale et la basse latitude de la Mer d'Arabie, ainsi que le régime de mousson des vents saisonniers en font une région particulière. La propagation rapide des ondes et tourbillons, et leurs interactions avec le bord ouest façonnent les régimes de turbulence de la Mer d'Arabie.

Mots-clés : Mer d'Arabie, Great Whirl, outflow, Golfe d'Oman, Golfe Persique, ondes de Rossby, upwelling, dynamique de mésoéchelle et sous-mésoéchelle, modélisation réaliste, interactions tourbillon-topographie

Western boundary dynamics in the Arabian Sea

This PhD aims to investigate some western boundary processes in the Arabian Sea : (i) the life cycle of the so-called Great Whirl, a persistent mesoscale eddy; (ii) the dynamics of the Persian Gulf outflow, a marginal sea dense outflow; and (iii) the seasonal Oman upwelling, a coastal upwelling forced by summer monsoonal winds. The cornerstone of all these phenomena is their location at a western boundary, which makes them being influenced by both local forcing (e.g., monsoonal winds) and remote forcing (Rossby waves and westward drifting eddies). Specifically, the latter are expected to impact the western boundary dynamics since the low latitude of the Arabian Sea implies a fast westward propagation of long Rossby waves and eddies. Moreover, waves are continously excited by the reversing monsoonal winds. Based on a primitive equation model, we designed numerical experiments of different complexity that allowed to either realistically simulate the dynamics in the Arabian Sea or to isolate some processes.

Major findings can be summarized as follows : (i) The Great Whirl life cycle is found to be significantly paced by annual Rossby waves, although the strong monsoonal wind stress curl is of major importance to sustain the structure. (ii) The Persian Gulf Water (PGW) spreading in the Gulf of Oman and the northern Arabian Sea can be explained by the stirring done by eddies entering the Gulf. These remotely formed surface intensified mesoscale eddies propagate into the Gulf and interact with the topography. Frictional interactions produce intense vorticity strips at the boundary that detach and roll up in the interior, forming submesoscale coherent vortices (SCV). These SCV trap PGW initially located on the slope and redistribute it in the interior. This mechanism of transport ultimately produces mixing that explains the large-scale gradient of salinity in the Gulf. (iii) We find that the dynamics of the seasonal upwelling off Oman contrasts with the more deeply studied Eastern Boundary Upwelling Systems (EBUS). In particular, Rossby waves, propagating offshore in EBUS vs. onshore in this western boundary upwelling, are found to modulate the wind driven upwelling and its sea surface temperature response.

Overall, these results appear to be rather specific to the Arabian Sea. The short zonal extent and the low-latitude of the Arabian Sea, as well as the seasonally reversing wind forcing are the distinguishing features of this region. Fast waves and drifting eddies and their interactions with the western boundary significantly shape the turbulent regimes of the western Arabian Sea.

Key words : Arabian Sea, Great Whirl, outflow, Gulf of Oman, Persian Gulf, Rossby waves, upwelling, mesoscale and submesoscale dynamics, ocean modelling, eddy-topography interactions